CRANFIELD UNIVERSITY

CRANFIELD DEFENCE AND SECURITY

Department of Engineering Systems and Management,
Aeromechanical Systems Group

PhD

2009

Tanmay J Tipnis

Effects of Upstream Nozzle Geometry on Rectangular Free Jets

Supervisors:
Dr Derek Bray and Professor Kevin Knowles

July 2010

Abstract

This study is aimed at understanding the effects of changing the upstream nozzle geometry on the development of rectangular free jets. An existing converging rectangular nozzle with an exit aspect ratio of 4 and a circular inlet ($AR4$ nozzle) has been used as the basic configuration for this work. The study is primarily based on the results of numerical simulations wherein the internal geometry variation is accomplished by changing the inlet aspect ratio (AR_i) and the length of the converging section, expressed as a ratio with respect to the length of the nozzle (called 'converging section ratio', CSR); all the other parameters are kept constant. The results from LDA experiments done on the $AR4$ nozzle are presented and used as validation data for the CFD simulations. Analyses of the numerical results help in understanding the variation of the jet spreading for different combinations of AR_i and CSR. Two parameters are identified for describing the jet development: the cross-over point (X_c), defined as the location downstream of the exit where the jet half-velocity-widths (B) along the major and minor axes are equal, and the difference in the half-velocity-widths at 30 nozzle equivalent diameters (D_{eq}) from the exit (ΔB_{30}), to ascertain the occurrence of axis-switching. For a given AR_i, X_c varies linearly with CSR; the variation of X_c is non-linear with AR_i for a constant CSR. The ΔB_{30} variation is non-linear with both AR_i and CSR; the other variable being kept constant. The data obtained from the simulations are further used to propose two parametric models which can be used to predict the occurrence of axis-switching, within the scope of this work. The parametric models are validated and future work is proposed.

To

Aai, Baba,
Dada and *Madhavi*

Acknowledgements

I would like to thank everyone who has knowingly and unknowingly helped me and wished me the best in successfully completing this research.

I would like to thank my supervisors, Dr Derek Bray and Prof Kevin Knowles. Their guidance and encouragement at all times has been crucial. I want to thank Prof Knowles, in particular, for providing me this wonderful opportunity in the first place and being patient and understanding with my work. I would also like to thank Dr Mark Finnis for his help regarding various issues ranging from numerical coding to experiments. A special thanks also goes out to Mr Dave Wasley without whom the setup of experiments would not have been possible (and also for some entertaining conversations!). Everyone at the Barrington Library; thank you all for getting the necessary literature articles for me in time. The same goes to the staff at the workshop who also deserve a thanks for getting the necessary machined components ready whenever I needed them.

Throughout the project, Dr Graham Stabler had been instrumental in providing interesting comments and insights about many different things - thanks dude! Also, most of my knowledge about experiments, and the LDA in particular, is due to Dr Simon Ritchie, who has always been very helpful during all this time. I am extremely grateful for that for without his guidance and tips, experiments would've been a distant reality!

I also take this opportunity to thank all my good friends here at Shrivenham. Bidur and Nathan have been especially very crucial for the discussions, including and not limited to work-related stuff, over all this time—not to mention the quintessential coffee breaks! I know for sure that things would've been different for worse without you guys. Also, all the inhabitants of the Watchfield bubble, Moh, Georgios; you guys made living in this countryside bearable (knowing that people left this place within six months to go somewhere else in search of a social life). Thanks for all the good times. To all my family and friends back home in India, US and Australia; thanks for believing in me and supporting me through all this time!

A very special thanks to my best friends here who have definitely contributed more than they can probably imagine. Rahul, all the encouragement and support you've provided has been extremely valuable. I definitely can't thank you enough for this. You have looked out for me as a younger brother and I am extremely grateful for that! And Nicki!!!–you've been there for me through thick and thin of everything I've gone through in the past three

and a half (almost four) years. For my best friend, little sister (and elder at times!), housemate, all rolled into one, any amount of words to thank you for bearing with me would be insufficient, so here's just a simple: "Thanks!"

Finally, but not the very least, my family: Aai, Baba, Dada and Madhavi... I could not have been here if not for you all. Thanks for being there all the time to support and trust me for this fantastic opportunity. Your confidence in my abilities definitely gave me more strength to go past the final hurdle. More importantly, thanks for being all that you are; wouldn't want it any other way!

I'm a bigger believer of Destiny rather than the Almighty, but thanks also to that Someone/Something that's looked after me all this time!!

Contents

List of Tables

List of Figures

Nomenclature

All units are in SI unless otherwise stated

Alphanumeric

$\dot{m}$	Mass flow rate
AR_e	Exit aspect ratio
AR_i	Inlet aspect ratio
B	Jet half-velocity-width
b	Width of the nozzle exit
c	Speed of light
D_{eq}	Nozzle equivalent diameter; $D_{eq} = \sqrt{4bh/\pi}$
f_i	Predicted values (mathematical function)
$G(\lambda)$	Gladstone-Dale constant
h	Height of the nozzle exit
$k-\omega$	Turbulence model based on turbulence kinetic energy (k) and specific dissipation rate (ω)
$k-\varepsilon$	Turbulence model based on turbulence kinetic energy (k) and turbulence dissipation rate (ε)
M_j	Jet Mach number
P_s	Static pressure
R^2	Coefficient of Determination; $R^2 = 1 - \frac{SS_{err}}{SS_{tot}}$
R_{eq}	Nozzle equivalent radius; $R_{eq} = \sqrt{bh/\pi}$
Re	Reynolds number

SS_{err}	Sum of squares of residuals; $SS_{err} = \sum_i (y_i - f_i)^2$
SS_{reg}	Regression sum of squares; $SS_{reg} = \sum_i \left(f_i - \bar{f}\right)^2$
SS_{tot}	Total sum of squares; $SS_{tot} = \sum_i (y_i - \bar{y})^2$
T_i	Turbulence Intensity
U	Velocity in $x-$direction
U_c	Centreline jet velocity in $x-$direction
V_{yz}	Resultant of normalised spanwise velocities, V_y/V_{exit} and V_z/V_{exit}
x, y, z	Cartesian coordinates, x indicates streamwise direction
X_c	Normalised location of the cross-over point
y^+	Non-dimensional wall distance; $y^+ = \frac{y}{\mu_T}\sqrt{\rho\,\tau_w}$
y_i	Observed values (response variable)
B_y, B_z	Jet half-velocity-width along $y-$ and $z-$directions, respectively
P_∞, P_a	Free stream (ambient) pressure
U_j, V_{exit}	Centreline jet velocity in $x-$direction at the nozzle exit
V_x, V_y, V_z	Velocity components in Cartesian coordinates

Greek Symbols

γ	Ratio of specific heats; $\gamma = c_p/c_v$
λ	Wavelength of the incident laser light
μ_T	Turbulent viscosity
ω_x	Vorticity in $x-$direction (streamwise)
ρ	Density of the fluid
τ_w	Wall shear stress
θ	Momentum thickness

ε_i	Residual error; $\varepsilon_i = y_i - f_i$
μ, σ	Mean and standard deviation of a probability distribution

Abbreviations

$2-D$	Two-dimensional
$3-D$	Three-dimensional
AIAA	American Institute of Aeronautics and Astronautics
BOS	Background-Oriented Schlieren
BSA	Burst Spectrum Analyser
CFD	Computational Fluid Dynamics
CSR	Converging Section Ratio
DES	Detached Eddy Simulation
LDA	Laser Doppler Anemometry
LES	Large Eddy Simulation
NPR	Nozzle pressure ratio; P_0/P_∞
PDE	Partial Differential Equation
PIV	Particle Image Velocimetry
RANS	Reynolds-Averaged Navier-Stokes
RNG	Re-Normalization Group
SST	Shear-stress transport

Chapter 1

Introduction

This chapter introduces the rectangular nozzle and its applications. Its aims are to provide the background and motivations for undertaking the current study.

1.1 Background

Fluid flow through nozzles has been comprehensively studied for various configurations applicable to numerous liquids and gases for many years. Nozzle flows pertaining to air and water as the fluids, have been particularly extensively researched, primarily due to their ease of availability and widespread applications. That said, the property changes associated with nozzle flows have always been interesting to the scientific and engineering communities. Over the past many years, the flow regimes and properties of simple converging and diverging nozzles have been well established. The study was boosted with the advent of jet engines and their subsequent implementation as propulsive units for aircraft. At the beginning, however, the study was focussed on circular nozzles due to its well-defined, uniform jet development. Besides this, the ease of manufacture and incorporation into the gas turbine engines used by their host aircraft meant that it was favoured over other types of nozzles.

The scenario changed slightly with the demand for enhanced fighter aircraft technology. Air superiority was of prime importance and required the aircraft to be highly manoeuvrable and stealthy. This, and potential applications of nozzle flows in other areas, led to investigations into the feasibility of non-circular nozzles. The basic circular nozzle proved inadequate by itself as the preferred unit for providing thrust and control nozzle and required additional features to make it usable. Besides, towards the end of the 20^{th} century, the focus also began to shift towards understanding the impact of noise generated by the aircraft. These factors combined together to lead to the research and development of usable configurations of non-axisymmetric nozzles; mainly of triangular, elliptic and rectangular exits.

The thrust associated with these nozzles is fractionally less than the corresponding thrust from a circular nozzle for the same cross sectional area, but the loss is sometimes acceptable due to the other advantages offered by these shapes (Tam (1998)). One of the most important advantages is the enhanced mixing properties of the non-axisymmetric nozzle compared with its circular counterpart. This is also generally accompanied by a higher spreading rate for the jet. It is, however, interesting to note that the noise generated by the non-axisymmetric nozzle is usually lower than that for the circular nozzle of the same exit cross-sectional area, though this may not always be the case (Knowles & Saddington (2006)).

The study of rectangular nozzles assumes more importance than other nozzle configurations due to its inherent advantages for enhanced jet mixing and thrust vectoring. The requirements for the current generation of fighter aircraft emphasises the need for agility and stealth. The rectangular nozzle is able to score higher than most of its counterparts in this area (Grinstein (1993)). In its simplest configuration with fixed side walls, the rectangular nozzle may provide one-dimensional thrust vectoring capabilities. Additionally, the nozzle profile could be easily altered so that the jet is always ideally expanded at all flight conditions to minimise the thrust losses. For improved stealth capabilities, the infra-red (*IR*) signature of the jet should be as low as possible. This is achieved by reducing the jet plume, leading to an improved mixing of the jet. The circular nozzle requires the use of external mechanisms such as tabs, vortex generators, etc. whereas such devices need not be used on non-axisymmetric nozzles. As mentioned earlier, there is a thrust penalty associated with the use of non-axisymmetric nozzle but it is expected to be of the order of around 5% for a 6:1 aspect ratio rectangular nozzle (Knowles & Saddington (2006)).

The need to develop and integrate the use of non-axisymmetric nozzles into aircraft has led to many researchers attempting to develop an extensive database for the properties of free jets emanating from such nozzles. Rectangular nozzles have already been incorporated on current production aircraft like the F-22 and B-2 as thrust nozzles. Rectangular jets are also used as roll-posts, i.e. roll control ducts, in the F-35 (Joint Strike Fighter) and these experience conditions of high *NPR* during vertical take-off and landing. This may affect the under-wing stores if the jet spreads faster in that direction. It thus becomes important to understand

the flow field of a rectangular jet and if possible, determine accurately how it behaves under different conditions. It is known that the characteristics of the flow field issuing from the rectangular nozzles depend upon various factors such as the exit aspect ratio (AR_e), inlet geometry of the nozzle, type of exit velocity profile, magnitude of the turbulence intensity (T_i) at the exit, the Reynolds number (Re) at the nozzle exit and the condition of the ambient medium into which the jet is issuing (Krothapalli et al. (1981)).

1.2 Motivations

The rectangular nozzle will probably soon be accepted as one of the most commonly preferred component of a propulsion system for both aircraft and spacecraft. Besides, its ease of manufacture and maintenance makes it an economical choice compared to the circular nozzle of similar capabilities. The increased current need to understand the properties of the rectangular nozzle is primarily due to the wide range of applications that are now being realised in the aerospace design sector.

All the factors affecting the rectangular free jet mentioned above, have been studied with varying degree of success over the last three-four decades. The exit aspect ratio of the nozzle is known to affect axis-switching (which will be discussed in Section 2.2) (Gutmark & Ho (1983); Grinstein (1993); Tsuchiya & Horikoshi (1986); Ho & Gutmark (1987)). The turbulence intensity also affects the spread of the jet; the higher the turbulence intensity, the greater the spreading of the jet (Grinstein (1997)). For supersonic jets, the temperature and scale of the nozzle affects screech production (details in Section 2.2.4) which has a further effect on jet development (Anufriev et al. (1969); Raman (1998)). Amongst these, the least understood is probably the dependence of the jet development on the internal geometry of the nozzle. The focus of this study is, therefore, to understand and investigate further the effects of the upstream nozzle geometry that seem to have a significant influence on the development of the jet downstream of the exit. This effect has not yet been qualitatively analysed nor quantified regarding its impact on the jet development and in particular, axis-switching.

Chapter 2

Review of Research Studies: Past and Present

The information gathered from various research studies in the relevant areas of jet spreading and axis-switching are presented in this chapter. This information has served as the building blocks for the current study. The mechanisms involved and the factors affecting axis-switching are discussed. The understanding behind vorticity dynamics effects and the presence of turbulent structures in the jet, along with the screech production mechanism and its relevance, are reviewed. The summary of the literature review culminates in confirming the aims and objectives for this study, followed by a brief outline of the thesis explaining the layout of the different sections of the current study.

2.1 Study of Free Jets

As the title of the current study suggests, the focus is on free jet development for a jet issuing from a rectangular nozzle. It is, thus, important to understand how the structure of a free jet develops and the factors it is dependent upon. Free jets are one of most elementary nozzle flows for understanding since even the development of an impinging jet depends significantly on its initial development as a free jet from the nozzle exit. Numerous studies have been carried out over the past half-century or so to explain the free jet structure and development but no specific literature review to condense these findings has been found. Mathieu & Charnay (1981) contains a literature survey providing information about the behaviour and modelling of turbulent flows, while Kassab et al. (1996) provides a list of literature that deals with experimental investigations of turbulent free jets. Zaman (1999) presents a comparison for the spreading characteristics of jets in the range of M_j = 0.3–2.0. The factors that generally affect the development of the free jet are presented here. Primarily, free jet development may be defined using two parameters, *jet spreading* and *centreline velocity decay*.

2.1.1 Nozzle Pressure Ratio Effects

For any given nozzle, the Nozzle Pressure Ratio (*NPR*) is defined as the ratio of the nozzle stagnation pressure to the ambient pressure. Donaldson & Snedeker (1971) describes the effect of changing the *NPR* for an axisymmetric convergent nozzle. Depending on the nozzle pressure ratio, four jet variations are possible: subsonic, sonic, moderately under-expanded, and highly under-expanded. The three non-sonic variations with their idealised flow structure are shown in Figure 2.1.

For air, a subsonic jet exists for isentropic nozzle pressure ratio range of $1 > NPR > 1.895$ (Figure 2.1(*a*)). Such a jet is characterised by the presence of two distinct regions: the *potential core*, where the axial velocity of the jet remains constant, and the *mixing region* that surrounds the core and extends downstream, formed due to the viscous mixing between the jet and the ambient fluid. The mixing region spreading continues as the velocity decays at a rate required to conserve the axial momentum. In the meantime, the mean velocity profiles in the mixing region approach the general self-similar shape of a fully-developed jet. The jet usually attains self-similarity for axial turbulences by 40 diameters downstream while the spanwise/radial turbulences become self-similar around 70 diameters downstream of the exit (Wygnanski & Fiedler (1969)). Thus, based on the streamwise velocity profiles, the mixing region downstream of the potential core may be divided into a transition region and the fully developed region. The critical *NPR* for air ($\gamma = 1.403$) at isentropic conditions is 1.895, below which the nozzle exhibits subsonic flow.

When the critical or sonic *NPR* is reached, a very weak normal shock forms at the exit. With an increasing pressure ratio, however, this shock changes rapidly to form a 'shock-cell' structure within the core for $NPR \approx 2$. For a simple converging nozzle, this structure continues to exist until $NPR \approx 4$. The structure is believed to form due to the presence of intersecting oblique shocks. Since the jet still needs to expand beyond the nozzle exit, the potential core boundaries are defined by the pressure equilibrium between the outermost portion of the flow within the shock structure and the ambient air surrounding it. The mixing region, meanwhile, continues to diffuse inwards until the core is dissipated. Beyond the core, the jet is subsonic and is expected to behave similar to a normal subsonic jet. The

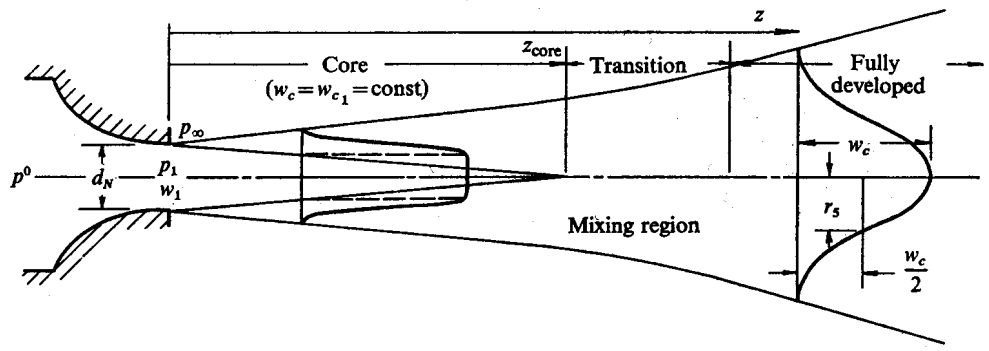

(a) Subsonic Jet

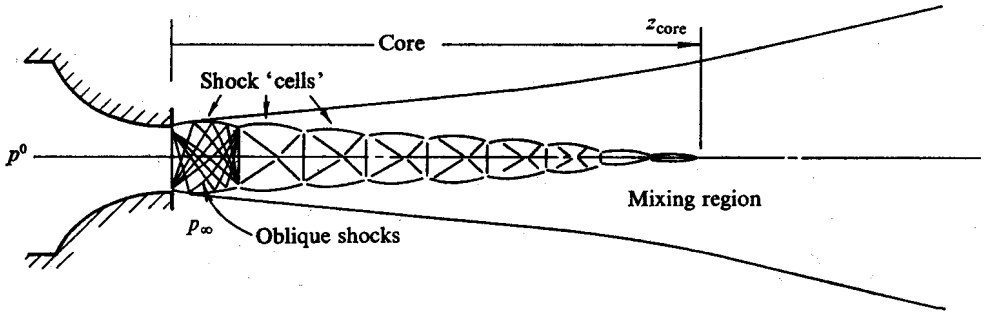

(b) Moderately under-expanded jet

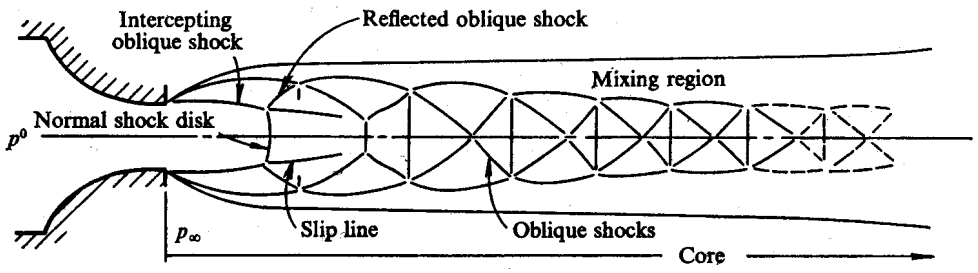

(c) Highly under-expanded jet

Figure 2.1: Three non-sonic variations of the jet issuing from an axisymmetric convergent nozzle illustrating the dependence of jet structure on NPR (Donaldson & Snedeker (1971))

jets corresponding to a nozzle pressure ratio interval of $2 \leq NPR \leq 4$, for a sonic nozzle are termed as 'moderately under-expanded' (Figure 2.1(*b*)).

As the *NPR* for a sonic nozzle increases beyond 4, the centreline pressure falls due to maximum expansion of the shock-cell, becoming so low compared to the ambient pressure such that the compression waves join together to form a normal shock disc (also known as a 'Mach disc'). The formation of this disc is indicative of a 'highly under-expanded' flow (Figure 2.1(*c*)). A further increase in the pressure ratio increases the strength and diameter of the shock disc. The region immediately behind the shock disc is subsonic; since the surrounding flow in the oblique shock region still remains supersonic, a slip line exists at the boundary between these concentric regions. For a fairly high degree of under-expansion ($NPR \approx 7$), this subsonic core region is quickly accelerated and becomes supersonic once again at the beginning of the second shock-cell. Consequently, the second cell may resemble the first cell and could also possess a normal shock similar to the first cell. The structure for a highly under-expanded jet, however, is usually characterised by the presence of a single very strong normal shock present in the first cell; no other normal shocks are present and the structure downstream of the first cell is dominated by the normal shock in the first cell. Beyond this, the flow decays through a structure of oblique shocks. The mixing region, although surrounding the core, shows only small levels of radial diffusion. Consequently, the core of a highly under-expanded jet is generally very long. The usual subsonic decay takes place further downstream, after the core is diffused.

It can be clearly seen from the above description that the potential core length of the jet is directly proportional to the *NPR* of the jet whilst the spreading rate is inversely proportional to it. This observation was also concluded by some studies such as Lau et al. (1979), Curtis (1987) and Moustafa (1993), etc. The Laser-Doppler Anemometry (*LDA*) studies by Lau et al. (1979) on subsonic and supersonic free jets also found that these parameters vary with the square of the jet Mach number. Also, the entrainment rate of the jets decreases with an increase in the *NPR* in the subsonic regime while increasing again in the supersonic regime with increasing *NPR* (Curtis (1987)).

2.1.2 Nozzle Geometry Effects

A circular, rectangular and four-slot nozzle was tested by Hammond (1966) to study the effect of changing the nozzle exit geometry on their decay rates (Figure 2.2). It can be clearly seen that the rectangular nozzle displays higher decay compared to the circular nozzle with the slot nozzle showing the highest decay amongst the three. A comparison of difference in performances of a conical nozzle and a Stratford nozzle are provided by Curtis (1987). The Stratford nozzle is characterised by a smoothly profiled converging section which minimises flow separation and hence the exit turbulence intensity. It was found that the potential core length was independent of the geometry variation between these nozzles; instead being affected by the *NPR* and temperature. There was, however, a difference in the spreading rate of the nozzle downstream, this being affected by the exit turbulence intensity. A comparison carried out by Kassab et al. (1996) for understanding the effects of upstream conditions, also shows that the nozzle profile does not alter the potential core length. For a supersonic configuration involving castellated nozzles, streamwise vortices generated due to the differential expansion at the nozzle lip give rise to increased mixing and correspondingly, shorter shock-cells (Knowles & Saddington (2002)).

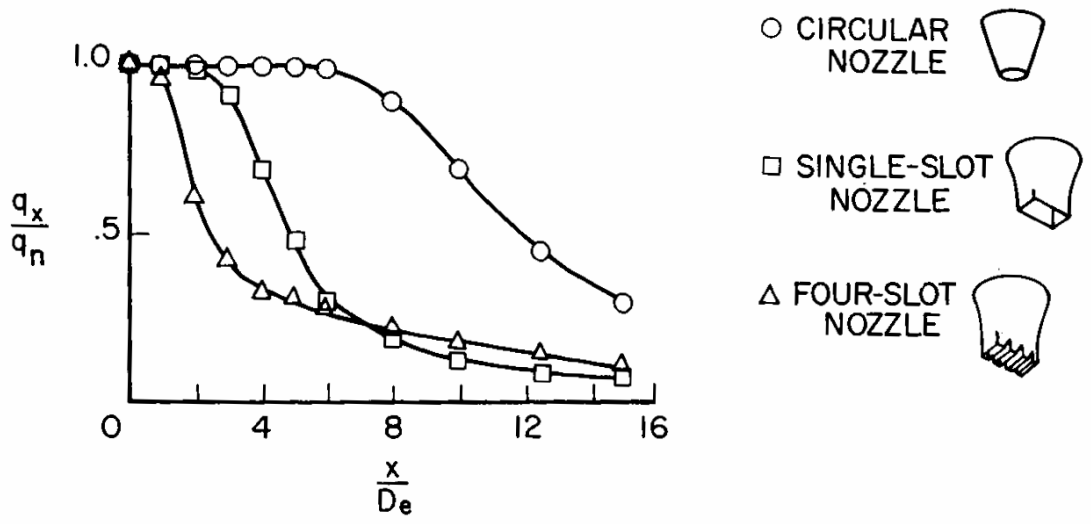

Figure 2.2: Effect of nozzle geometry on jet velocity decay (Hammond (1966))

2.1.3 Temperature Effects

The influence of temperature on the structure of round jets has been investigated by a number of authors, notably Lau (1981), Curtis (1987) and Lepicovsky (1990). Lau (1981) observed that the spreading rate initially falls for increasing M_j for a fixed temperature ratio (T_J/T_0, where T_J is the static jet temperature at the exit plane and T_0 is the ambient temperature). For jets with T_J/T_0 = 1.0 to 1.5, it reaches a minimum and begins to rise when the conditions of the jet promote the convection velocity of the large-scale structure of the jet to be equal to the ambient speed of sound. In general, the spreading rate falls with an increase in T_J/T_0 for subsonic flows and rises for supersonic flows. The potential core generally contracts with increasing jet-exit temperature or a decrease in the exit Mach number. This observation, also confirmed by Curtis (1987), is believed to be due to higher viscosity of the heated jet. It thus reduces the characteristic turbulence length. It was also found that an increase in the jet temperature from 300 K to 600 K resulted in an increase in the entrainment rate by anywhere between 5% to 11%. Studies by Lepicovsky (1990) indicate that the effects of temperature variation are not as straight-forward as they may seem at first inspection but can in fact be classified according to two factors. The heat transfer and momentum interchange due to viscous stresses may be a direct influence on the jet development; this is only one aspect of the temperature variation. The other aspect, due to the effects of jet operating conditions (i.e. heated jets) on the nozzle exit boundary-layer characteristics, indirectly affects the jet plume development. This indirect effect is believed to be the dominant factor. He thus observed that the comparison of experimental data on free jet development is meaningless, if acquired at different test facilities, unless the nozzle exit boundary-layer characteristics are taken into consideration.

2.1.4 Effects of Swirl

Compared to the other effects affecting the free jet development, effects of swirl have not be documented extensively. Ribeiro & Whitelaw (1980) present a review related to the study of swirling jet. A swirling round jet experiences a rapid increase in the flow width and the momentum balance associated with the jet is influenced more by the pressure field set up by the inertial forces associated with the swirl. The far region of the swirling flow then depends upon the axial fluxes

of angular and linear momentum since these are conserved. Consequently, the simplicity associated with the flow of plane and round jets is lost. The ratio of the non-dimensionalised axial fluxes of angular and linear momentum is called the swirl number. The centreline velocity decay increases with increasing swirl number, i.e. the potential core length decreases. For an under-expanded circular flow, Neemeh et al. (1999) found that a small flow rotation weakens the internal shock strength. This reduces the shock-cell length, and in turn the potential core, and also decreases the screech noise generated; higher flow rotations, however, did not have any additional benefits in terms of screech noise reduction.

2.1.5 Non-axisymmetric Nozzles

Gutmark & Grinstein (1999) have reviewed the research carried out in the field of non-circular jets, especially related to flow control and noise suppression. The structure of non-axisymmetric jets has been explained in works carried out by Krothapalli et al. (1981) and Hussain & Husain (1989), amongst others. Sfeir (1976) reports studies on incompressible rectangular nozzles carried out at Polytechnic Institute of Brooklyn[1] which show that the flow-field may be subdivided into three main regions:

- The potential core region, where the centreline velocity, U_c is constant;
- The two-dimensional transition region, where $(U_c)^2 \propto x^{-n}$ with $n \approx 1$;
- The region extending to infinity, where the centreline velocity decay is characteristic of axisymmetric jets, i.e. $U_c \propto x^{-1}$.

The above subdivision is similar to that found for the subsonic jet as described by Donaldson & Snedeker (1971) (Figure 2.1(*a*)). According to Sfeir (1976) the extents of these regions and the exponent n are shown to be a function of the nozzle aspect ratio. The flow in the transition and axisymmetric regions was also found to be dependent on the initial nozzle geometry. A rectangular flow-field can be schematically represented (Krothapalli et al. (1981)) as shown in Figure 2.3. The variation of the centreline velocity U_c normalised with the mean velocity

[1]Researches carried out by Sforza et al. (1966), Trentacoste & Sforza (1967) and Sforza (1969)

at the centre of the nozzle exit U_0 has been shown in the lower left corner of the figure. The description of the three regions matches that observed by Sfeir (1976).

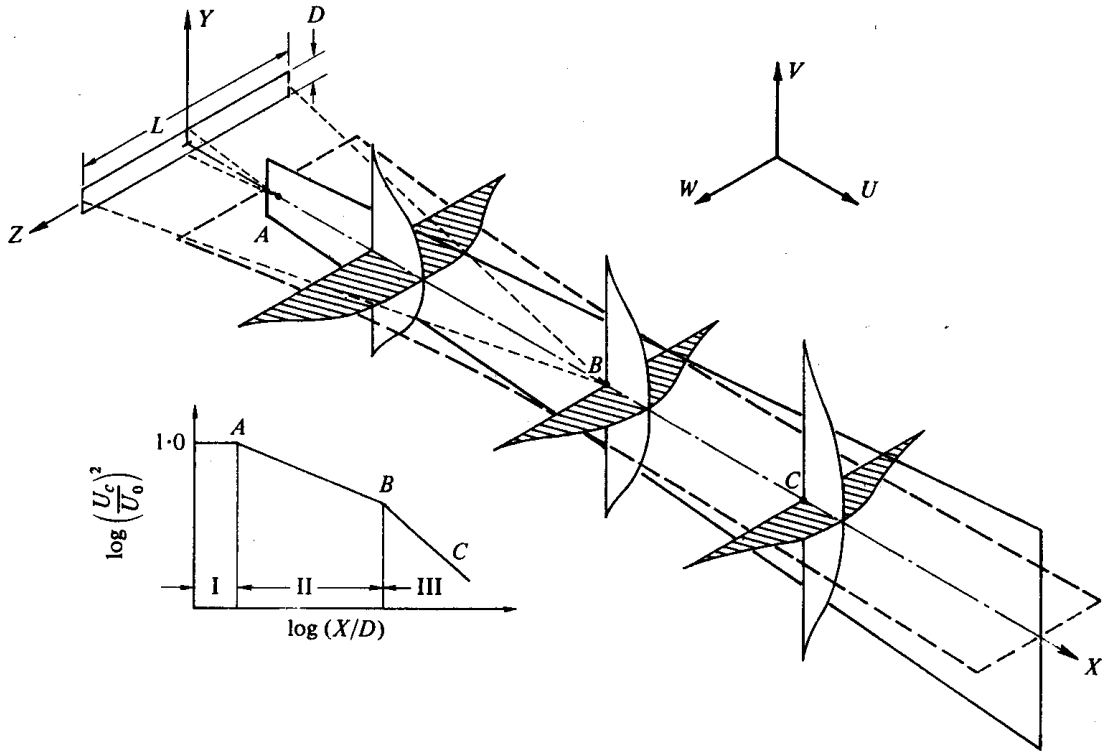

Figure 2.3: Schematic representation of a subsonic rectangular free jet flow-field (Krothapalli et al. (1981))

Zaman (1999) presents a comparison between the spreading characteristics for nozzles with different exit geometries: circular, rectangular, elliptic and 'lobed'. In subsonic conditions, the circular nozzle exhibits the lowest spreading rate, while the lobed nozzle had the highest spreading rate, although the difference was very small. At supersonic conditions of M_j = 1.63, while all nozzles show elevated spreading rates, the elliptic and rectangular nozzles, however, spread much faster compared to the circular and lobed nozzles; the lobed nozzle displaying the lowest spreading rate of all four configurations. The higher mixing rate of the elliptic jet also results in the reduction of the potential jet core by approximately one to two equivalent diameters compared to that of a circular jet of the same exit cross-sectional area (Gutmark & Grinstein (1999)). It is also reported that the introduction of sharp corners in a nozzle can significantly increase the fine-scale turbulence at the corners relative to the flat segments of the nozzle and

enhance mass entrainment (Schadow et al. (1988); Vandsburger & Ding (1995)). The vertices of the rectangular jet thus reduced the coherence of the large-scale structures and consequently lowered the spreading rate to less than that of the elliptic jet. A non-circular jet is also reported to have larger spreading rates compared to jets with circular geometry, especially at jet sections with a larger radius of curvature (Gutmark et al. (1989)). This leads to what is commonly referred to as 'axis-switching'.

2.2 The Axis-switching Phenomenon

Non-axisymmetric nozzles are generally well-known to exhibit the peculiar phenomenon of 'axis-switching'. It is understood to be due to the effect of non-uniform vorticity distribution along the edges of the non-axisymmetric cross-section at the nozzle exit. It has been widely observed for nozzles with elliptic, square, triangular and rectangular cross-sections.

2.2.1 Definition

The spreading rates of the jet column issuing from such nozzles are not equal in all directions. This results in the eventual development of the jet being aligned such that at some point downstream of the nozzle, it appears that the jet column has rotated through a certain angle while spreading (Grinstein (1997)). It is usually termed as 'axis-switching' since the orientation of the axes as seen along the nozzle exit cross-section appears to 'turn' through an angle as it evolves downstream.

Axis-switching is thus defined as "the phenomenon in which the cross-section of an asymmetric jet evolves in such a manner that, after a certain distance from the nozzle, the major and minor axes are interchanged" (Zaman (1996a)). An example for the axis-switching sequence depicted through the deformations of non-axisymmetric vortex rings is shown in Figure 2.4[2].

[2]Although originally found in Hussain & Husain (1989), this figure is as taken from Zaman (1996a)

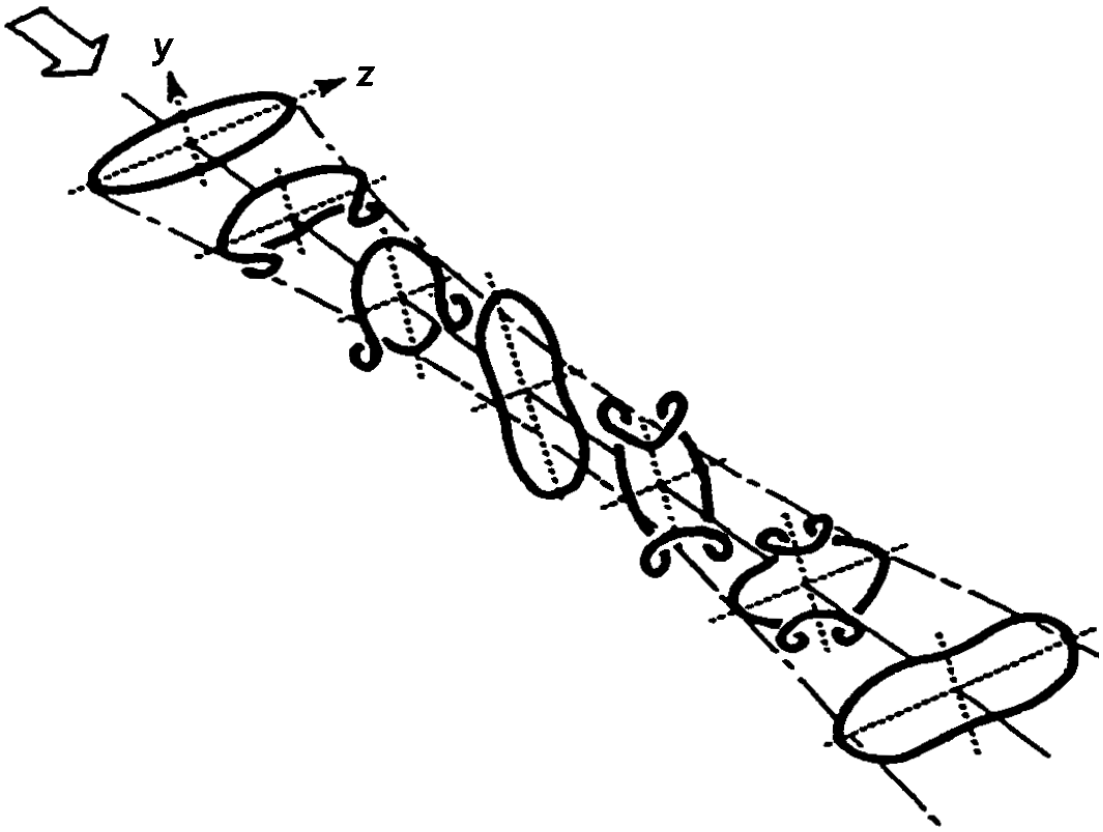

Figure 2.4: An example for the axis-switching sequence depicted through the deformations of non-axisymmetric vortex rings (Zaman (1996a))

2.2.2 Mechanisms Associated

Axis-switching for non-axisymmetric nozzles has been increasingly studied in line with an increased need to understand these nozzle flow-fields. It is believed that the principal mechanism responsible for axis-switching is the presence of vortical structures and the dynamics associated with their development. It is considered to be the reason behind the unequal spreading rates along the major and minor axes of the jet cross section.

The elliptic jet and its characteristics have been studied elsewhere in detail and compared to the properties associated with circular and plane jets. It has been found that coherent structures dominate the jet far field of the elliptic jet and the axis-switching (which continues for about hundred equivalent diameters downstream) with the locations and number of switch-overs strongly dependent on a number of factors. These include the initial conditions, the aspect ratio and

(in cases concerning excited jets), the Strouhal number and the level of excitation (Hussain & Husain (1989)). Numerical studies carried out in the early 1970s and 1980s show that the elliptic ring is inherently unstable due to the variation of self-induction in the azimuthal direction (Viets & Sforza (1972); Dhanak & Bernardinis (1981)). It was established that the advection velocity of a local segment belonging to a curved vortex filament is along the normal to the plane of the segment, i.e. the bi-normal. It is also proportional to the curvature of the segment, so that a segment with greater curvature moves faster than a segment with a smaller curvature (Arms & Hama (1965)). During its motion, the elliptic vortex ring does not retain its shape or remain in a plane, but deforms such that the two axes are interchanged after some time (Figure 2.5). Because of the breakdown of the vortex rings, azimuthal instability and decay, and viscosity and 'shedding' of fluid, it is not possible for this process to continue indefinitely.

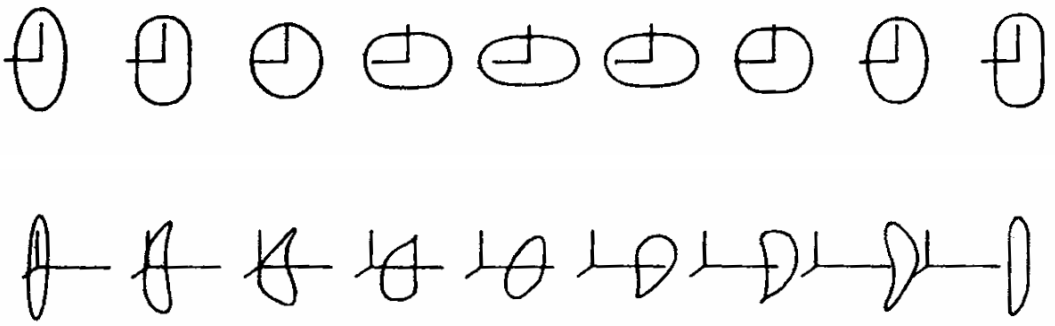

Figure 2.5: The advection of an elliptic vortex ring as it moves downstream of the exit (numerically computed); vortex ring cross-section indicating axis-switching (top); corresponding side-view indicating advection of the ring (bottom); increasing time from left to right (Hussain & Husain (1989))

The elliptic jet also exhibits similar behaviour to that of the elliptic ring deformation. The situation is somewhat more complex, however, due to shear, entrainment, development of azimuthal instability and interactions such as pairing, tearing and cross-linking. During the advection of the elliptic vortex, the vortex ring is deformed due to differential induction velocity; the ends of the major axis tend to move faster than the minor axis ends. In a jet, however, the core

radius increases due to diffusion which leads to reduced self-induced velocity and an induced deformation of the elliptic vortical structures in the jet. This also delays the axis-switching process (Hussain & Husain (1989)). The self-induction of the asymmetrical distribution of the vorticity in the elliptic jet is thus responsible for the deformation of the coherent structures and subsequent development of axis-switching, causing differences in the roll-up locations (Husain & Hussain (1983)).

The role of vorticity dynamics was further explored by introducing tabs along the edges of a rectangular jet (Zaman (1996a)). Two mechanisms were identified for axis-switching. The first, which was previously studied by other researchers such as Viets & Sforza (1972), Ho & Gutmark (1987), and Hertzberg & Ho (1992), amongst others, is due to the deformation and reorientation of rolled-up azimuthal vortices (named ω_θ-induced dynamics), which always tends to cause axis-switching. Periodic excitation tends to enhance this mechanism; thus faster axis-switching in screeching jets can be accounted for, since screech is periodic in nature. The other mechanism is due to the induced velocities of streamwise vortex pairs (named ω_x-induced dynamics). The two pairs of streamwise vortices, if situated at the ends of the major axis and having the 'out-flow' sense, tend to resist axis-switching, whereas those with an 'in-flow' sense tend to assist axis-switching (Figure2.6). Such vortex pairs are encountered in jets due to secondary flows within the nozzle, e.g. when the nozzle involves transition from different cross-section geometries, wherein the axis-switching is either delayed or may not even occur at all. It is also, however, interesting to note that since both these mechanisms occur in natural non-axisymmetric jets, depending on the streamwise vorticity distribution, the tendency of axis-switching due to the ω_θ-induced dynamics is either resisted or enhanced by the ω_x-induced dynamics.

At high enough Reynolds number, the large-scale coherent vortical structures are intrinsic features of the jet and control the development of jet mixing layers (Brown & Roshko (1974)). The jet growth and entrainment at moderately high Reynolds number, in the simplest axisymmetric configuration, is dominated by the dynamics of the vortex rings (Crow & Champagne (1971)). However, when there is a non-axisymmetric flow or a high Reynolds number flow, the three-dimensionality becomes a crucial feature and the streamwise vorticity is able to entrain fluid from the surroundings more efficiently (Liepmann & Gharib

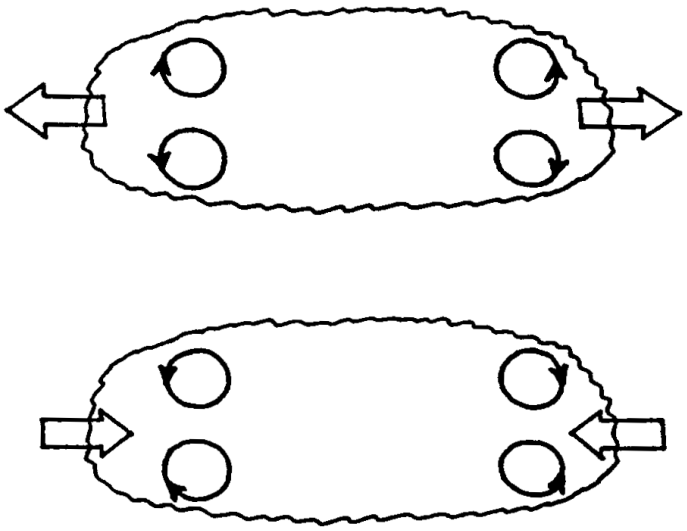

Figure 2.6: Illustration depicting the 'out-flow' pair (top) and the 'in-flow' pair (bottom), resisting and assisting axis-switching, respectively (Zaman (1996a))

(1992)) with the dominant fluid-dynamical mechanisms being self-induction, vortex stretching and vortex reconnection (Hussain (1986)).

Axis-switching for a rectangular jet can also be explained by the means of the self-induced Biot-Savart deformation of the vortex rings with non-uniform azimuthal curvature and interaction between the spanwise and streamwise vorticity (Abramovich (1982)). On the basis of theoretical incompressible flow analysis, it can be argued that, for a rectangular jet, the successive axis-switchings are a result of pressure differentials on the plane of the rectangular vortex ring. The pressure on the short, more separated sides of the nominally rectangular ring is higher than that on the long, less separated sides. This induces a gradual deformation of the transverse section of the jet (Grinstein (1997)).

2.2.3 Factors Affecting Axis-switching

Early studies on the mixing properties of a rectangular jet focussed on the understanding of the flow-field characteristics. It was realised that these characteristics are dependent on various factors; primarily, the exit aspect ratio (AR_e), inlet geometry, the type of exit velocity profile, the magnitude of the turbulence intensity at the exit plane ($T_{i,e}$), the exit Reynolds number and the condition of the ambient

medium into which the jet issues (Krothapalli et al. (1981)). The variation of the cross-over point with aspect ratio is shown in Figure 2.7. The results indicate that the nozzle geometry alters the cross-over point location; for a given aspect ratio, the location of the cross-over point is further downstream for a jet from a long channel compared to that issuing from an orifice (Sfeir (1976)). It can be seen that the distance of the cross-over location downstream of the exit is directly proportional to the exit aspect ratio of the nozzle. Studies also showed that the spreading rate for a jet could be altered by varying the conditions at the initiation of the shear layer, i.e. either by making it turbulent or laminar (Gutmark & Ho (1983)).

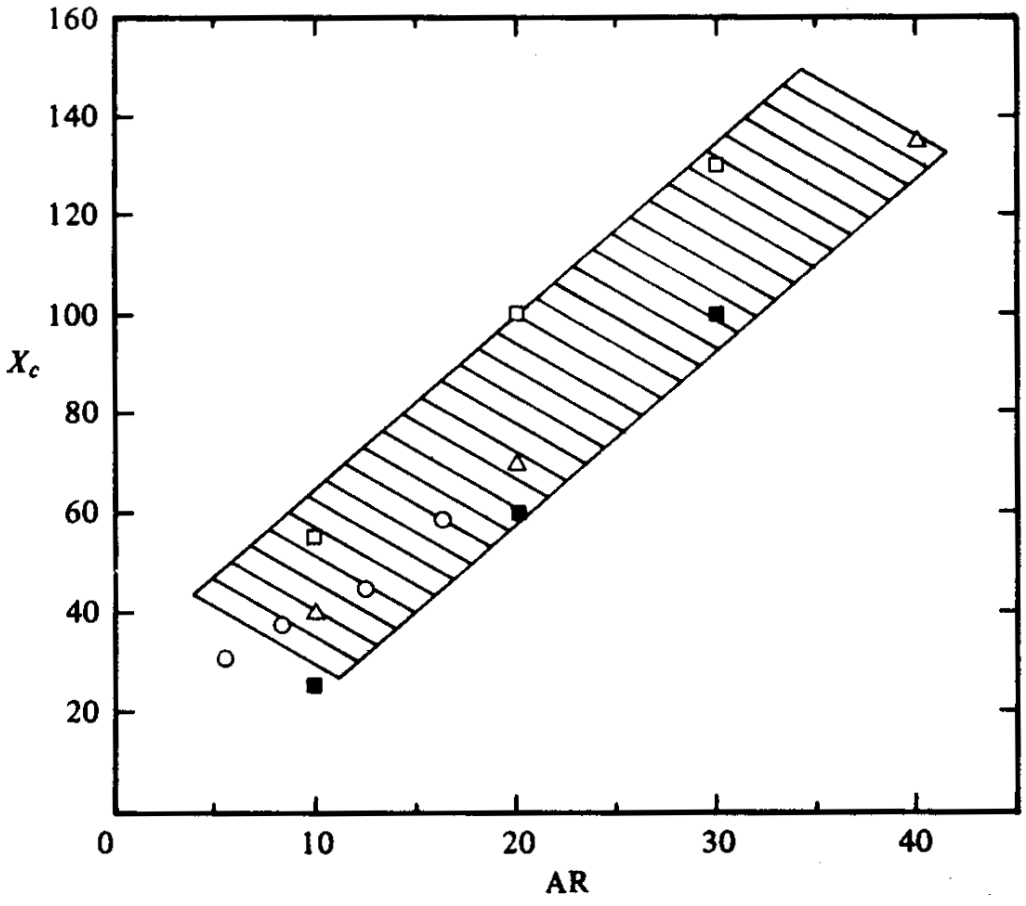

Figure 2.7: Variation of the cross-over point with aspect ratio (Krothapalli et al. (1981)); ○, Krothapalli et al. (1981); △, Sforza et al. (1966); □, ■, Sfeir (1976) (filled square indicates orifice jet)

The development of vorticity dynamics theory for non-axisymmetric jets and its application for a periodic forced jet has shown that the process occurs due to the roll up of the azimuthal vorticity. This process also occurs for a natural asymmetric jet due to the inherent natural roll up of the azimuthal vortices, but the formation and subsequent evolution of these vortices is arbitrary. This randomness generally results in delayed axis-switching or in a simple transition to the round shape without axis-switching (Zaman (1996a)).

The initial jet conditions are responsible for the occurrence of axis-switching in any given non-axisymmetric nozzle. These conditions include azimuthal distribution of the momentum thickness (θ), the ratio of the equivalent diameter to θ, turbulence level and jet forcing, and also on the presence of streamwise vorticity at the jet exit (due to either the secondary flows within the nozzle or the vortex generators placed at the rim of the nozzle). The streamwise vorticity may be effectively absent at the nozzle exit, but it still plays an important part in the jet development downstream (Grinstein (1997)).

It was also found that the non-axisymmetric nozzle does not spread faster in comparison to an axisymmetric nozzle at subsonic conditions, but only in supersonic conditions. This can be attributed to the presence of screech; this is known to increase the jet spreading in case of almost all the nozzles, the amount of increase varying with the various stages of screech (Zaman et al. (1997)). Although the presence of screech promotes axis-switching, it is interesting to note that at higher Mach numbers, the spreading decreases with increasing compressibility (Papamoschou & Roshko (1988)).

2.2.4 Screech and its Impact

Screech is the discrete component of shock-associated noise. Thus, it can exist only if there is an over- or under-expanded flow through the nozzle. As mentioned in the earlier section, screech plays an important role in the flow-field characteristics of a non-axisymmetric jet. The phenomena associated with screech production are, however, still not very well understood (Raman (1998)). The earliest known work in the field of screech is the contribution of Powell (1953). He defined screech as: "a very powerful noise of completely different character, described as a 'whistle' or 'screech', rather harsh and of a confused nature, becoming much

more like a pure note, usually of increased intensity, over certain ranges of pressure ratio".

The production of screech is essentially a cyclic process, as shown in Figure 2.8. If any one element of the loop is missing, the feedback is broken and screech cannot be produced. The cyclic process originates at the nozzle exit with the sound waves giving rise to embryonic disturbances on passing the orifice (1). These grow and amplify as they travel downstream, interacting with the shock cells to produce sound (2). The sound generated then propagates upstream (3) to be received at the nozzle lip (4), thus closing the feedback loop.

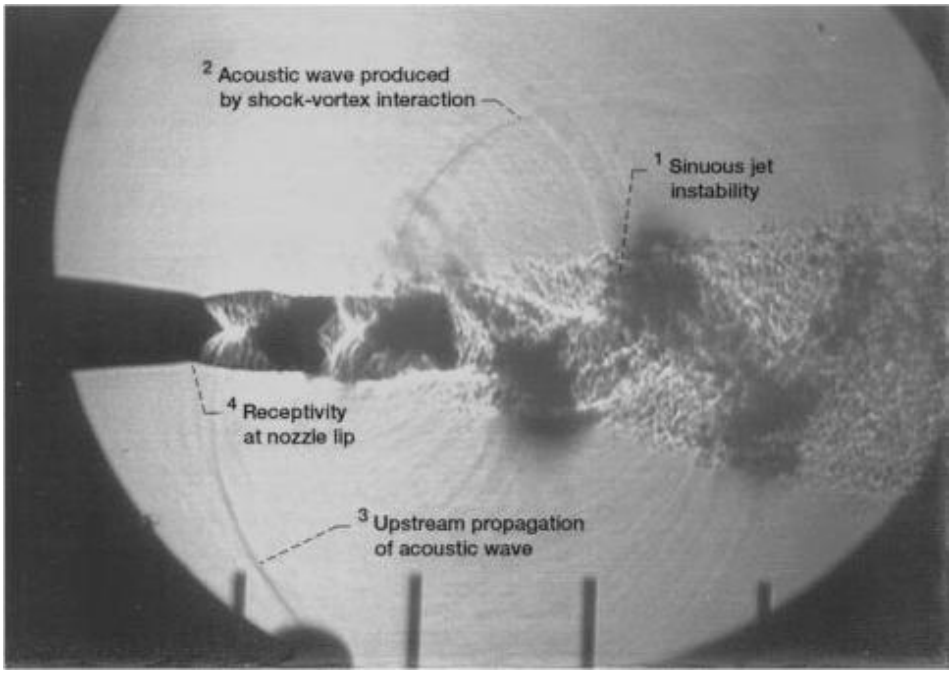

Figure 2.8: Mechanisms operating in a resonant screech loop for a 5 : 1 *rectangular nozzle at* $M_j = 1.5$*; image taken normal to the minor plane, the rod spacing at the bottom of the image is* $3.5h$ *(Raman (1997))*

A jet exhibiting screech is strongly excited by the feedback received at the nozzle lip since the jet is most susceptible to external disturbances here. Consequently, it enhances jet mixing. The nozzle pressure ratio determines the screech frequency and mode of screech of a circular jet, so we can say that the mixing enhancement depends on the *NPR* of the nozzle (Glass (1968)). Some studies have, however, also reported irregular changes with an increase in Mach number

(Gutmark et al. (1989)). The screech frequency also depends on the presence of reflecting surfaces in the near-field region, e.g. the thickness of the nozzle lip, since it affects screech and thus jet mixing. Besides the screech amplitude, the mode of screech also determines the mixing enhancement. It is interesting to note that the presence of screech has been shown to promote faster axis-switching (Zaman (1996b); Zaman et al. (1997)).

2.3 Secondary Flows

In a three-dimensional flow field, secondary flow is the motion in the plane normal to the main streamwise flow direction, whose magnitude is one order or more smaller than that of the main flow and generally characterised by the presence of mean streamwise vorticity (Demuren (1993)). The secondary flows induced within ducts with corners can be attributed to cause the axis-switching-inhibiting features in pipe or contoured non-axisymmetric nozzle jets (Gutmark & Grinstein (1999)). In orifice jets, the initial bending of the corner sections is accompanied by jet-width reduction in the corners and hence promotion of axis-switching; the secondary flows in the pipe nozzle, however, are characteristically directed away from the jet axis and towards the corners, thus leading to a growth of the jet-width in the corners at the nozzle exit. Studies showing behaviour promoting axis-switching has also been reported, notably by Quinn (1992) and Zaman (1996a). The latter showed the effective use of the appropriate location of external tabs to alter the streamwise vortices to promote axis-switching.

2.3.1 Types of Secondary Flows

Ludwig Prandtl (1875–1953) separated secondary flows into three kinds, based on the mechanisms that produced them (Prandtl (1952)):

- The generation of streamwise vorticity induced due to skewness of the mean flow was classified under *secondary flow of the first kind*. This is essentially an inviscid process.
- A turbulent flow through a straight channel of non-circular cross section is characterised by the presence of another kind of secondary flow called

secondary flow of the second kind. These are caused by non-uniformities in wall turbulence (Perkins (1970)) and the streamwise vorticities can, in fact, be generated by the Reynolds stresses (Bradshaw (1987)).

- Small oscillations of solid bodies in fluids can set up a peculiar flow phenomenon which is referred to as *secondary flow of the third kind*. It is attributed to the second-order effect, related to the interaction of the mean pressures, momenta and frictional forces. This may be particularly observed in cases involving experiments with ultrasonic waves.

Amongst these, the first two kinds of secondary flow are associated with steady fluid flows. Assuming the streamwise direction to be denoted by x, the mean streamwise vorticity equation for an incompressible steady-state flow is given by (Perkins (1970)) as:

$$\begin{aligned} U\frac{\partial \xi}{\partial x} + V\frac{\partial \xi}{\partial y} + W\frac{\partial \xi}{\partial z} &= \nu\nabla^2\xi + \xi\frac{\partial U}{\partial x} + \eta\frac{\partial U}{\partial y} + \zeta\frac{\partial U}{\partial z} \\ &+ \frac{\partial}{\partial x}\left(-\frac{\partial \overline{uw}}{\partial y} + \frac{\partial \overline{uv}}{\partial z}\right) + \left(\frac{\partial^2}{\partial y^2} - \frac{\partial^2}{\partial z^2}\right)(-\overline{vw}) + \frac{\partial^2}{\partial y \partial z}\left(\overline{v^2} - \overline{w^2}\right) \end{aligned} \tag{2.1}$$

where,

$$\xi = \left(\frac{\partial W}{\partial y} - \frac{\partial V}{\partial z}\right); \quad \eta = \left(-\frac{\partial W}{\partial x} + \frac{\partial U}{\partial z}\right); \quad \zeta = \left(\frac{\partial V}{\partial x} - \frac{\partial U}{\partial y}\right)$$

in standard notations.

The left side of Equation 2.1 represents the total convection of streamwise vorticity. On the right side, the first term accounts for the viscous diffusion of the streamwise vorticity while the second term represents vortex stretching in the streamwise direction. The next two terms taken together describe the production of streamwise vorticity through deflection or skewing of the mean shear by a transverse pressure gradient. This produces secondary flows of Prandtl's first kind. These flows are pressure driven and usually of a magnitude of the order of 10 to 40% of the bulk streamwise velocity (Demuren (1991)). The remaining three terms of Equation 2.1 are responsible for maintaining the secondary flows of Prandtl's second kind. These terms collectively represent the effective sum of the time-averaged convection of turbulent vorticity by the the turbulence and the

time-averaged production of turbulent vorticity (Perkins (1970)). Such flows can also be found in the presence of streamwise corners. For most straight channels with non-circular cross section, these flows have a velocity magnitude of 1 to 4% of the bulk streamwise velocity. Their effects on wall shear stress distribution and heat transfer, however, are quite significant (Demuren (1991)).

Examples of the three kinds of Prandtl's secondary flows are shown in Figure 2.9. A fluid flow through a curved pipe experiences straight flow at the core due to greater velocity compared to the slower layers at the boundary which are markedly deflected, and hence tend towards the inner side of the curve. The main flow is thus parallel to the central line of the pipe but experiences the presence of secondary flow superimposed onto it; it is outwards at the centre of the pipe and inwards in the wall-neighbourhood region (Figure 2.9(*a*), left). Secondary flows of the first kind are also experienced at the bottom of a rotating flow in a cylindrical vessel. The flow in the layer next to the bottom of the fluid in the cylinder is directed inwards due to its smaller centrifugal force (Figure 2.9(*a*), right). The secondary flows of second kind are depicted in Figure 2.9(*b*) for straight channels with non-circular cross-sections. Both the channels show the flow moving away from the wall centres where the shearing stress at the boundary is greater. Similarly, the flow can be seen moving towards the corners where the shear stress at the boundary is less. This has an overall effect to even out the shear stresses at the boundary by lowering the velocity in the first instance (near wall centres) and raising it at the latter (near corners). The secondary flows of the third kind, as mentioned previously, are produced by a cyclic motion in the flow. Figure 2.9(*c*) shows the image obtained with an experiment performed by Schlichting (1932)[3] with a cylinder swinging to and fro in a water tank, the camera moving along with the cylinder. The flow visualising particles move to and fro during the long exposure shots giving rise to the broad bands seen in the image.

2.3.2 Application to Current Study

Turbulent stresses existing in a jet issuing from a non-circular cross-section drive the mean flow into approximate axisymmetry. All this while, these stresses are non-axisymmetric in nature (Bradshaw (1987)). Such stresses are also responsible

[3] As mentioned in Prandtl (1952)

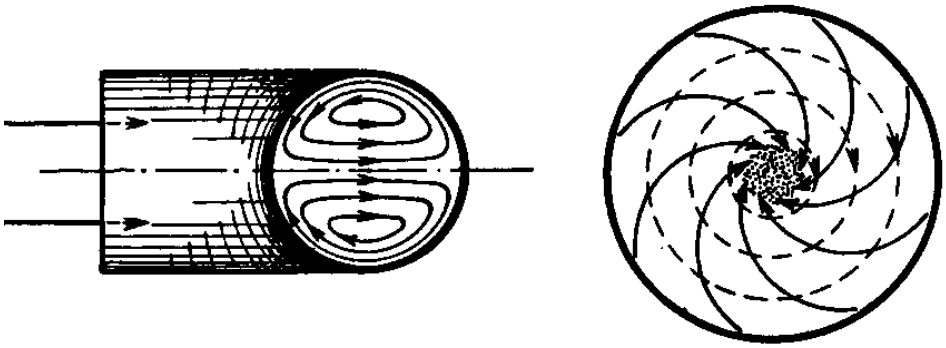

(a) Secondary flows of the first kind due to skewness

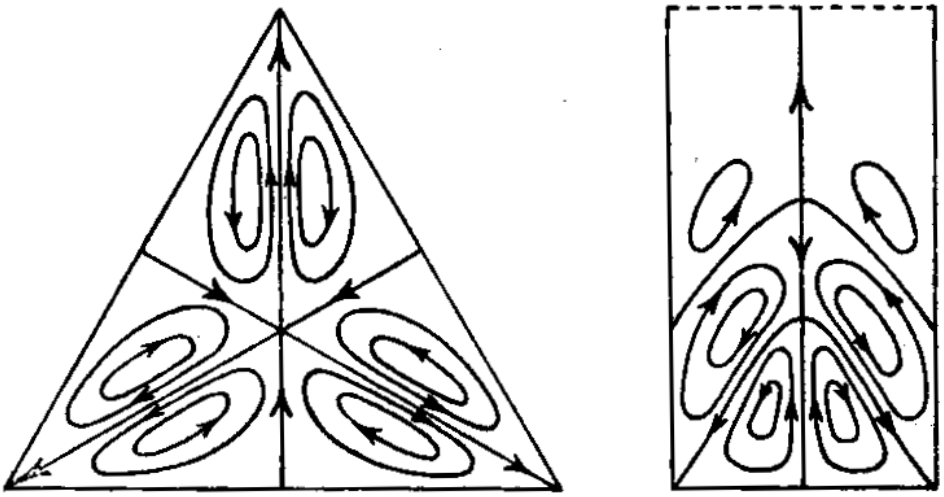

(b) Secondary flows of the second kind due to turbulent stresses

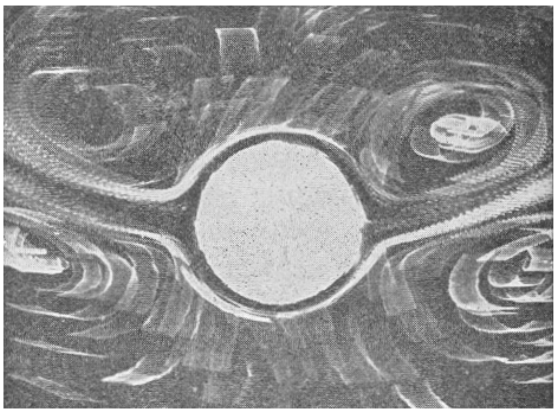

(c) Secondary flows of the third kind due to oscillatory motion

Figure 2.9: Examples of Prandtl's secondary flows (Prandtl (1952))

for producing secondary flows of Prandtl's second kind. As such, understanding the production and development of these secondary flows can be an important aid to understanding the flow development of the rectangular free jet. Since the secondary flows of Prandtl's second kind are a magnitude of one order weaker than those of the first kind (Demuren (1991)), they are more difficult to measure. Both of these flows are capable of inducing cross-flows and identifiable streamwise vortices, but the presence of secondary flows of second kind is identified only when it produces identifiable vortices (Bradshaw (1987)). Demuren (1991) also notes that differences in the treatments of secondary shear stress between various analyses are responsible for different strengths of the predicted secondary motion. Besides this, it is extremely important to ensure that the near-wall modelling of the flow is highly accurate, especially for complex geometries, so that the secondary flows may be resolved effectively.

2.4 Summary of the Literature Review

A summary of the important points of the literature review are provided here:

- Free jets, especially in cases concerning axisymmetric nozzles, have been extensively studied. Jet spreading and centreline velocity decay—the two parameters that can describe a jet flow-field effectively—are well understood.
- The primary factors affecting the development of the jet are identified as the nozzle pressure ratio, nozzle geometry, operating temperature and the presence of swirling flows.
- Non-axisymmetric nozzles have also received substantial attention due to their inherent properties of enhanced jet mixing which is important in varied applications including aircraft propulsion. The increased jet mixing reduces the infra-red signature of the thrust, in addition to reducing the noise levels of the jet.
- Such non-axisymmetric jets, especially elliptic and rectangular, are sometimes known to exhibit the peculiar phenomenon of axis-switching, where the spreading rate along the minor axis of the jet is faster than that along the

major axis, resulting in the jet cross-section appearing as 'turning' through an angle as it evolves downstream.

- The complete understanding of axis-switching is essential for future generations of aircraft which are known to employ rectangular nozzles for their advantages over the circular nozzles in providing better stealth and manoeuvrability characteristics.

- The occurrence of axis-switching can be explained through different mechanisms; vorticity dynamics being able to describe it comprehensively. It has been established that the factors primarily affecting axis-switching are exit aspect ratio, inlet geometry, type of exit velocity profile, magnitude of exit turbulence intensity, exit Reynolds number and the condition of the ambient medium into which the jet issues.

- All these factors are also responsible for the development of secondary flows in the nozzle. Out of these, the secondary flows of Prandtl's second kind are of interest since these are produced in straight channels of non-circular cross-sections due to different shear stresses acting along the boundary. Consequently, the occurrence of axis-switching may be attributed to the presence of the streamwise vorticity associated with these secondary flows, their orientation and strength.

- In addition to this, at supersonic conditions for a convergent nozzle, screech could play an important role in assisting or delaying axis-switching. Screech is the discrete component of shock-associated jet noise and depending on its mode (which in turn depends upon the *NPR* and the nozzle geometry), is known to promote or resist axis-switching.

- An area of interest that has yet to be thoroughly investigated is the dependence of axis-switching based on variation of the inlet geometry. Studies have pointed to understanding the effects of changing a contoured or pipe nozzle jet to an orifice jet (Sfeir (1976)) but no further variation has been taken into account.

2.5 Aims and Objectives

Based on the summary presented earlier, it is identified that the effects of changing the upstream nozzle geometry have not been effectively understood. An effective comparison to realise this variation involves keeping constant the nozzle dimensional parameters such as inlet area, exit area, nozzle length and exit aspect ratio. Also, a further constraint is introduced by ensuring that the exterior shape of the nozzle is maintained as fixed throughout the study. Furthermore, the operating conditions for all the nozzle designs should be identical so that the comparison of the results is on a completely even ground. A converging nozzle with a circular inlet and a rectangular exit of aspect ratio 4 was identified as a basis for this study. Additional details regarding the nozzle geometry are provided in further chapters. Thus, effectively, we have two principal design parameters for understanding the effects of changing the nozzle geometry: *inlet aspect ratio* AR_i and *the length of the converging section*. The study aims to achieve the following objectives:

- Understanding the variation of AR_i and converging section length on the production of axis-switching. In particular, for determining the downstream location where the jet axis in both the width-wise and height-wise directions is equal (i.e. the cross-over point X_c).
- Undertaking a parametric study to quantify the above observations for a given range of the two parameters under investigation.
- Understanding the generation of secondary flows for the given nozzle designs and their effect on the production of streamwise vortices and subsequent jet spreading.
- Proposing methods based on inlet geometry variation that may be implemented for assisting or resisting axis-switching, as required by the situation.

2.6 Outline of the Thesis

Chapter 3 deals with the numerical methodology applicable for the current study. The intended use of Computational Fluid Dynamics is explained in Section 3.1

followed by the criteria applied for acceptance of the *CFD* solutions (Section 3.2). The next section (3.3) describes the process of simulation setup and the use of preliminary studies, especially those of a rectangular nozzle (Section 3.3.1) based on a *Journal of Fluid Mechanics* article by Zaman (1996a). A brief account of the different variables used for creating the parametric model along with their range and constraints is provided in Section 3.4.1, while Section 3.4.2 attempts to provide a statistical basis to this study including the validation of the model. No numerical study can be considered acceptable without appropriate validation; the experimental methods employed to validate the *CFD* simulations have been discussed in Chapter 4. The experimental facilities available at Cranfield University, Shrivenham are explained briefly in Section 4.1, while the experimental techniques utilised are described in Section 4.2. This is followed by a brief coverage of the error estimation related to the experimental work (Section 4.3).

The results of this work are provided in Chapter 5 along with the corresponding comments and discussions. The scope of the various techniques is also provided here, followed by the grid independence and validation results for the *CFD* simulations (Section 5.1). The results and discussions pertaining to the rectangular nozzle flow simulation are then detailed in Section 5.2. These results are analysed and formulated into the parametric model which is discussed in Section 5.3. Following this, the experimental and simulation results pertaining to the supersonic case are discussed as Additional Results in Section 5.5. Chapter 6 deals with the conclusions of the current study and proposes possible future work that may be carried out after this work.

Chapter 3

Numerical Methods

This chapter details the computational fluid dynamics (*CFD*) setup that forms the major part of this study. The simulations were setup and analysed using commercially available software. The pre-processing, i.e. mesh generation, was handled by Gambit™, while the processing was performed using Fluent™. The data was then exported into a favourable format and post-processed using Tecplot 360™and Matlab™.

3.1 CFD and its Intended Application

Computational Fluid Dynamics (*CFD*) uses various numerical methods and approximations to solve the fluid flow problem. A fluid flow problem is governed by three fundamental principles: (1) conservation of mass, (2) conservation of momentum, and (3) conservation of energy. These principles can be expressed in the form of mathematical equations, usually as partial differential equations (*PDEs*). These equations are together represented as a Navier-Stokes Equation (Equations 3.1 - 3.3) which can effectively be used to depict any single phase fluid flow problem. The equations below represent instantaneous continuity, momentum and energy for a compressible fluid.

$$\frac{\partial \rho}{\partial t} + \frac{\partial}{\partial x_j}\left[\rho u_j\right] = 0 \tag{3.1}$$

$$\frac{\partial}{\partial t}\left[\rho u_i\right] + \frac{\partial}{\partial x_j}\left[\rho u_i u_j + p\delta_{ij} - \tau_{ji}\right] = 0 \tag{3.2}$$

$$\frac{\partial}{\partial t}\left[\rho e_0\right] + \frac{\partial}{\partial x_j}\left[\rho u_j e_0 + u_j p + q_j - u_i \tau_{ij}\right] = 0 \tag{3.3}$$

where, x_j indicates Cartesian co-ordinates (j =1, 2, 3), u_j indicates Cartesian velocity components, p is pressure, ρ is density, τ_{ji} indicates viscous stress terms, e_0 is the energy term, q_j indicates heat flux, and δ_{ij} is the Kronecker delta term.

Various algorithms are then employed to discretise this Navier-Stokes equation to convert the continuous flow problem to be solved efficiently using numerical

methods. The advances in computers and the available computing power have enabled enormous development in the field of Computational Fluid Dynamics. Fluent™uses the finite-volume method for solving the fluid flow problem. The meshing essentially breaks down the domain into small finite volumes which are then used for integrating the governing equations (Equations 3.1-3.3) to produce the equations that conserve the primary variables in each control volume. These governing equations, i.e. the Navier-Stokes equation in its integral, cartesian form (Equation 3.4) for a control volume **V** with a differential surface area **S** is generally represented as[4]:

$$\frac{\partial}{\partial t}\int_V \mathbf{W}dV + \int_S [\mathbf{F} - \mathbf{G}].dS = \int_V \mathbf{H}dV \tag{3.4}$$

where,

$$W = \begin{pmatrix} \rho \\ \rho u \\ \rho v \\ \rho w \\ \rho E \end{pmatrix}; \quad F = \begin{pmatrix} \rho\mathbf{v} \\ \rho\mathbf{v}u + p\mathbf{i} \\ \rho\mathbf{v}v + p\mathbf{j} \\ \rho\mathbf{v}w + p\mathbf{k} \\ \rho E + p\mathbf{v} \end{pmatrix}; \quad G = \begin{pmatrix} 0 \\ \tau_{xi} \\ \tau_{yi} \\ \tau_{zi} \\ \tau_{ij}u_j + q \end{pmatrix}$$

W indicates the conservation terms, F denotes the convective terms, and G denotes the dissipation, or stress terms. The source term, H is generally equal to zero for unforced flows.

The three steps involved in CFD, as mentioned earlier, are pre-processing, processing and post-processing.

- *Pre-processing*: The physical setup of the model is created along with the specification of the different boundaries, their nature and fluid types. It can be sub-divided into:
  - Volume creation, where the physical dimensions of the model are defined.
  - Meshing of the volume, where the domain is divided into cells for solving the discretised problem.

[4]The author would like to thank Mr B. Khanal for pointing out the use of this form of the Navier-Stokes equation as used by Fluent™

  - Specification of the physical model, which includes specifying the governing equations for the given fluid flow.
  - Specification of the boundary conditions, where the initial conditions and the behaviour of the fluid at the physical bounds of the model are specified.

- *Processing*: The simulation is initiated and the *PDEs* are solved as a steady-state or as an unsteady flow problem, as required.

- *Post-processing*: The solution thus obtained is then analysed, generally by exporting the data for further calculations or by using different visualising techniques.

Since the solution obtained from a CFD simulation is based on solving the PDEs, it inherently introduces a very small error at every iteration stage of the solution. As long as this residual error is kept to a minimum or a constant over a significant number of iterations, the solution can be said to have converged. To ensure that the final results are able to depict the solutions to the real life problems, two principles are used to establish the credentials of a simulation: *verification* and *validation*.

The U.S. department of Defense, Modelling and Simulation defines verification and validation (AIAA (1998)) as follows:

- *Verification*: "The process of determining that a model implementation accurately represents the developer's conceptual description of the model and the solution to the model."

- *Validation*: "The process of determining the degree to which a model is an accurate representation of the real world from the perspective of the intended uses of the model."

The current study deals with understanding the effects of upstream geometry changes on rectangular jets. If the study is conducted using physical models, it will be extremely expensive to manufacture the required nozzle configurations. Besides, the current setup available for performing the experiments will have to undergo extensive modifications to accommodate these nozzles. This all adds

up to additional costs. The feasible option then is to verify and validate one simulation based on a physical model. This simulation model is then altered for the required parameters keeping all the initialising parameters and boundary conditions the same. Consequently, the results can then be compared on an even ground and since these results include a validated simulation result, we can reasonably concur that the simulation results thus obtained are all valid.

3.2 Solution Convergence Criteria

Since a simulation is essentially a numerical approximation derived from solving the partial differential equations iteratively, every resultant step produces a residual error. If this error is high, it implies that the solution has not reached convergence, i.e. it can be refined further to produce better, accurate results. The easiest way of determining if the solution has converged is to check the residuals at every step of iteration. Fluent^{TM}is able to provide such a facility; we can check the convergence of a solution by monitoring the residuals for various calculated quantities for every iteration. A minimum limit may be set for the residuals (depending on the desired accuracy) so that, as soon as all the monitored residuals reach these specified values, the solution stops and is said to have converged to the required level of accuracy.

This works well for a simple fluid flow problem. Simulation of a nozzle flow is not as simple a problem as it may seem. This is especially true for supersonic nozzle flows where the monitors usually show a higher residual value, albeit constant. In such a case, it might become necessary to specify other criteria to determine the convergence of the solution. During the preliminary work for the current study, it was found that the residual monitors tend to show a constant value for the different residuals (up to a maximum of the order of 10^{-2}). The solution results, however, showed a consistent comparison with other data available for the same problem. As such, it was decided that the solution convergence will have to be based on some other criteria.

For the current simulation, six different monitors were set up. Three of these monitors generated the total mass flux of the simulation, mass flow rate of the nozzle ($\dot{m}$) and the mass flux of the nozzle, each at an interval of 1,000 iterations.

The other three monitors generated the velocity magnitude at three different locations downstream of the exit at: 2 D_{eq}, 25 D_{eq} and 50 D_{eq}, each at an interval of 500 iterations. The error margins chosen were very narrow such that the simulation results could be perceived as accurate as possible. From these monitors, the solution convergence was set as follows:

- The total mass flux of the domain and the mass flux of the nozzle should be consistently less than 0.5% of the mass flow rate of the nozzle over a period of 3,000 iterations, and
- The variation of the velocity over the 3,000 iterations should be less than 0.5% of the average velocity over these 3,000 iterations.

3.3 Simulation Setup

The initial simulation for validation was based on the physical model of the nozzle available for experimental work. The rectangular nozzle used for experiments is shown in Figure 3.1(*a*), along with its dimensions in Figure 3.1(*b*). The rectangular nozzle has an aspect ratio 4, an exit area of 400 mm^2 and a circular inlet of 35 *mm* diameter. The cross-section area starts converging at 65 *mm* upstream of the nozzle exit. During the initial part of the study, the experimental setup was unavailable for use for a significant time. This meant that the simulations, if performed, could not be verified or validated since there was no established data available for comparision. Consequently, time was devoted to tuning the simulation setup as required for the current nozzle problem. This work of tuning the simulation setup formed a part of the preliminary work that, although providing an insight into different important aspects of *CFD* simulations, and for nozzle flows in particular, was outside the primary aims and scope of this study. For this reason, it is not presented in this thesis.

Some data regarding the use of a circular-to-rectangular nozzle for studying axis-switching was found from an article published in the *Journal of Fluid Mechanics* by Zaman (1996a). This nozzle (henceforth referred to as '*AR*3 nozzle') was physically bigger and used a different contraction profile than the rectangular nozzle used for the current studies (henceforth referred to as '*AR*4 nozzle'). The

flow conditions were, however, similar and it was decided that it would be appropriate to determine the optimum simulation conditions for the current study based on the results obtained from the $AR3$ nozzle simulations.

3.3.1 Validation Results using $AR3$ Nozzle

The first step for a CFD simulation involves the creation of a grid that is able to resolve all the necessary flow structures. The nozzle used for the current study presented a significant challenge during meshing of the nozzle domain. For the flow to develop satisfactorily, it was essential that the boundary layer development of the flow from the inlet was modelled correctly. This was done by ensuring that the wall y^+ values were maintained within acceptable limits for the given turbulence model. This peculiarly challenging problem was also faced when meshing the $AR3$ nozzle.

The $AR3$ nozzle had a 3:1 rectangular exit with an equivalent diameter, D_{eq} = 6.35 cm. The inlet of the nozzle was circular with a diameter of 41 cm. It contracted from this round cross-section to the rectangular exit within a length of 23 cm, the transition of the geometry starting at 12.7 cm upstream of the exit. The total length of the nozzle was 15.2 cm and the lip thickness at the exit was 1.27 cm. The outside of the nozzle essentially comprised of four tapered sides, starting from round cross-section and ending into the rectangular shape at the lip, with wall thickness no less than 1.27cm anywhere[5]. The nozzle was run at an NPR corresponding to a jet Mach number, M_j = 0.31. The centreline turbulence intensity at the jet exit was approximately 0.15%.

3.3.1.1 Grid Creation

The requirement for ensuring the boundary layer flow development meant that the meshing would have to be done with quadrilateral/hexahedral cells along the wall of the nozzle (Figure 3.2(a)). On extending this to the rectangular exit, however, the cells become highly skewed (Figure 3.2(b)). This can introduce errors

[5]Additional details regarding the nozzle geometry were received via email communication between the author and Dr. K. B. M. Q. Zaman. The author would like to thank Dr. Zaman for the same

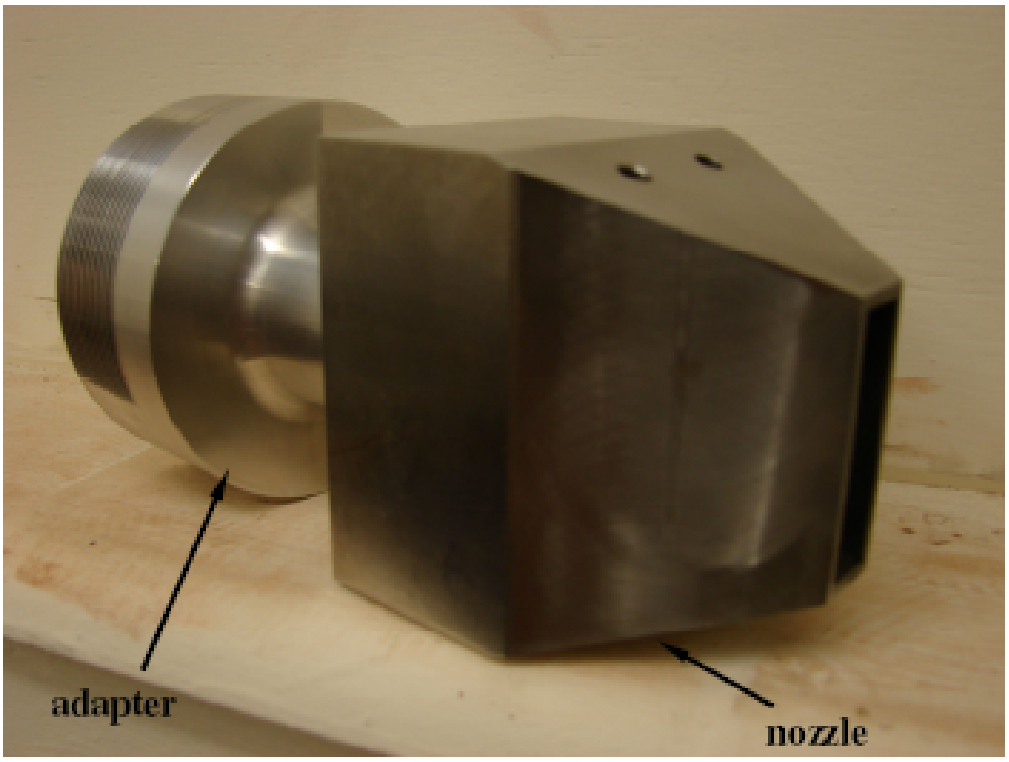

(a) The aspect ratio 4 rectangular nozzle used for experiments

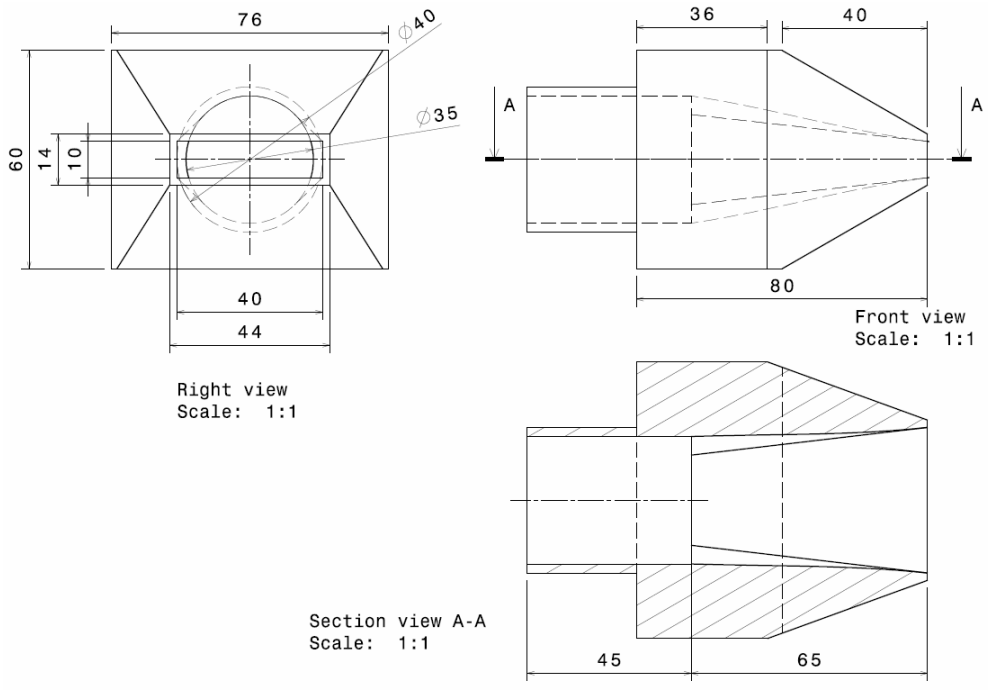

(b) Dimensions of the nozzle

Figure 3.1: Aspect Ratio 4 Rectangular Nozzle used for experimental work

into the solution. The flow coming out of the nozzle would also not be depicted properly. It thus became necessary to maintain a rectangular grid at the nozzle exit (Figure 3.2(*c*)). This, too, had its drawbacks since the resulting grid at the inlet would have highly skewed cells (Figure 3.2(*d*)) and would present the very same problem of introducing grid error into the solution. A compromise was reached by introducing an interface at an appropriate location upstream of the nozzle exit. This location was selected such that the skewness of the cells would be within acceptable limits for both the mesh configurations mentioned previously. It was also checked that the flow development would have been uniform at the specified location in the absence of the interface. The grid before the interface (on the inlet side) was modelled with hexahedral cells along the wall up to a certain distance towards the centre, followed by prismatic (triangular bases and five faces) cells to fill up the volume (Figure 3.2(*e*)). On the other side, the rectangular grid from the exit was extended up to the interface (Figure 3.2(*f*)). The minimum cell height of the wall-adjacent cells was equal in both the cases, as seen in Figure 3.3. These two sections of the nozzle were then interfaced together in Fluent^{TM}. The nozzle exit was also specified as an interface so that it could be coupled seamlessly with the corresponding surface of the exterior domain. It is to be noted that the grids on both sides of this interface at the nozzle exit were identical.

It is important to mention here that the grid creation for the simulations based on the *AR*4 nozzle with rectangular inlet, on the other hand, was straightforward with no need to have any interfaces. The minimum cell height at the inlet, start of the converging section and the exit were specified such that the wall y^+ values were within 1 to 5. The explanation for using these values is presented later in Section 3.3.1.3.

The grid spacing along the streamwise and spanwise directions outside the nozzle was non-uniform. This helped in reducing the number of cells in the simulation and thus in minimising the necessary computation time. The cells were closely spaced near the nozzle exit to capture the flow development as accurately as possible. Towards the domain extents, this was relaxed and the cell spacing was kept sparse. The coarse cell spacing also helps towards stabilising the simulation. The grid spacing along the streamwise direction and the dimensions of the domain are shown in Figure 3.4.

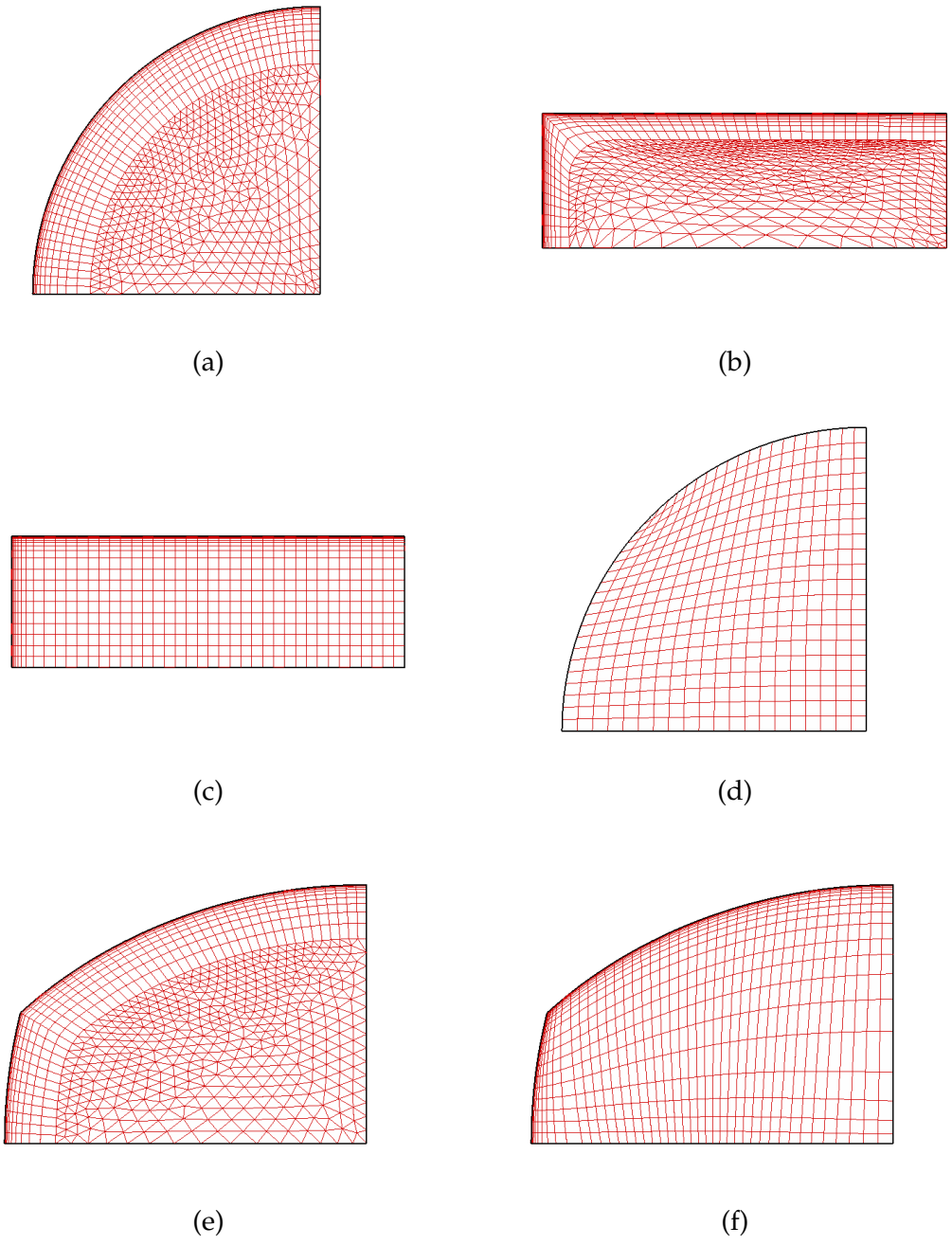

Figure 3.2: Meshing difficulties for the circular-to-rectangular nozzle geometry: (a) Ideal mesh for the circular inlet; (b) Exit mesh showing highly skewed cells; (c) Ideal mesh for the rectangular nozzle exit; (d) Distorted mesh for the inlet; the ideal exit mesh is extended upto the inlet; (e) Interface mesh on the inlet side; (f) Interface mesh on the exit side

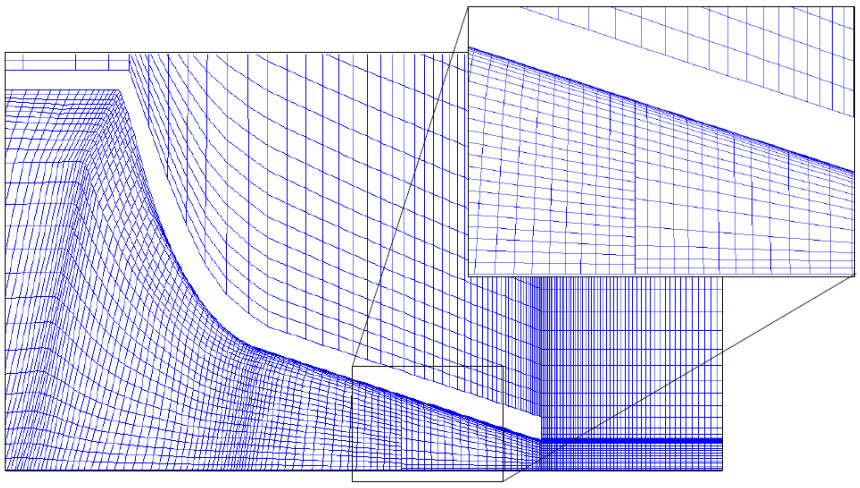

Figure 3.3: Minimum cell-height matching at the interface; zoomed in (inset)

3.3.1.2 Turbulence Model Selection

Fluent™, being commercial software, aims to provide a range of options to cater for different fluid flow problems. For additional flexibility and control, it also lets the user specify different values for the constants used in the different equations based on the problem under consideration. With a variety of options at hand, however, it is also easy to select the wrong parameters for a given problem. One of the most important parameters for solving a CFD problem is the specification of the turbulence model.

The options available in Fluent™vary from an inviscid model to a laminar model, single-equation model (Spalart-Allmaras) to various Reynolds-Averaged Navier-Stokes models (*RANS*) and even Detached Eddy Simulation (*DES*) and Large Eddy Simulation (*LES*). The most popular models for nozzle flow simulations were found to be the k-ε, two-equation models. Since the preliminary studies for the nozzle flow problem had identified the need to study supersonic flow, the *RNG* k-ε model was initially selected as it is the most suitable amongst the k-ε models for modelling under-expanded turbulent jets (Knowles & Saddington (2002)).

With the subsequent redefining of the problem at hand; i.e. the core of the study being focussed on subsonic flows, it was deemed necessary to perform a comparison between the different *RANS* models. A comparison was made between the Spalart-Allmaras model (Spalart & Allmaras (1992)), the standard

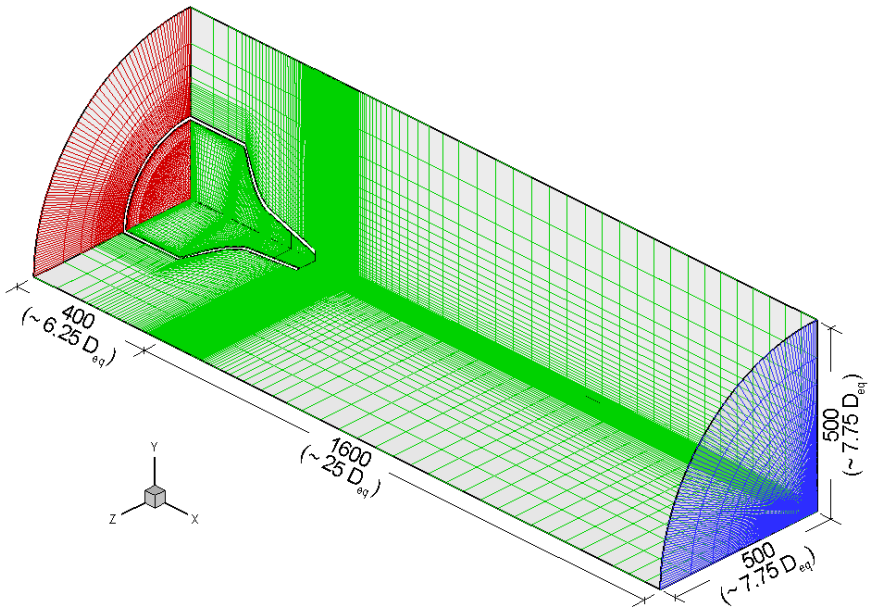

Figure 3.4: Grid spacing and domain extents for the AR3 nozzle simulation

k-ε model (Launder & Spalding (1972)), the *RNG* k-ε model (Yakhot & Orszag (1986)), and the k-ω models (standard (Wilcox (1998)) and shear-stress transport (*SST*) (Menter (1994))). More details about the specific turbulence models and the calculations involved can be found from the references mentioned alongside each model stated above. The results for the normalised jet half-velocity-width were compared with the experimental data published by Zaman (1996a). The relevant results and discussions are mentioned in the next section (3.3.1.3).

3.3.1.3 *AR3* Nozzle Results and Discussions

One of the methods used to ensure that the grid errors are kept to a minimum is to minimise the wall y^+ values in the cells close to the walls. The y^+ values can be calculated using Equation 3.5 given below.

$$y^+ = \frac{y}{\mu_T}\sqrt{\rho\,\tau_w} \tag{3.5}$$

where, y is the wall distance, τ_w is the wall shear stress, ρ is the density, and μ_T is the turbulent viscosity.

The y^+ values are not only dependent on the resolution of the grid but also on the flow Reynolds number. Also, these values are only meaningful in the

boundary layers (Spalart (2003)). It is therefore clear that for a simple estimation of the first cell height, Equation 3.5 may be used by substituting the initial free-stream conditions. The above equation, however, cannot be used for determining the absolute values of y^+ since it is dependent on τ_w, ρ and μ_T, all of which are dynamic properties in a compressible flow.

The mesh for the *AR*3 nozzle simulation was created such that the wall y^+ values lie between the recommended ranges. In equilibrium turbulent boundary layers, y^* and y^+ are approximately equal. The standard wall functions incorporate the logarithmic law-of-the-wall which is valid for $30<y^*<300$ (Launder & Spalding (1974)).Thus, although the most desirable value for y^+ is approximately equal to 30 for standard wall functions, this was difficult to achieve because of the complexity of the nozzle geometry. Besides, a fine mesh was necessary to understand and resolve the flow mechanisms. If the grid was coarse, flow structures might not have developed correctly. Consequently, enhanced wall functions based on blending of laminar and logarithmic laws-of-the-wall suggested by Kader (1981) can be effectively applied in the near-wall region. The mesh was, therefore, modelled such that the y^+ values at most locations along the wall were approximately between 1 and 5 (Figure 3.5). Since the geometry of the nozzle was complex, for keeping the wall y^+ values within acceptable limits, the cell height of the wall-adjacent cell was varied depending on its streamwise location. For instance, the minimum cell height at the inlet boundary was 0.325 *mm*, at the interface was 0.0375 *mm* and at the nozzle exit was 0.02 *mm*. As stated earlier (Section 3.3.1.1), it was ensured that the flow development across the interface remained unaffected by its location, as can be seen by the velocity contours in Figure 3.6.

Another important aspect of the *AR*3 simulation results was the selection of an appropriate turbulence model for the current study. As mentioned in section 3.3.1.2, four different turbulence models were compared with the available results from Zaman (1996a). The inlet and outlet boundaries were specified in each case, using the turbulence intensity and length scale method. This also partly ensured that the comparison was done on an even basis. The turbulence intensity was specified at 0.3% in all cases. The length scale was taken as 7.5% of the equivalent radius (R_{eq}) of the nozzle exit (Rodi (1984)). The jet half-velocity-widths for the different simulations were then compared with the experimental data from the

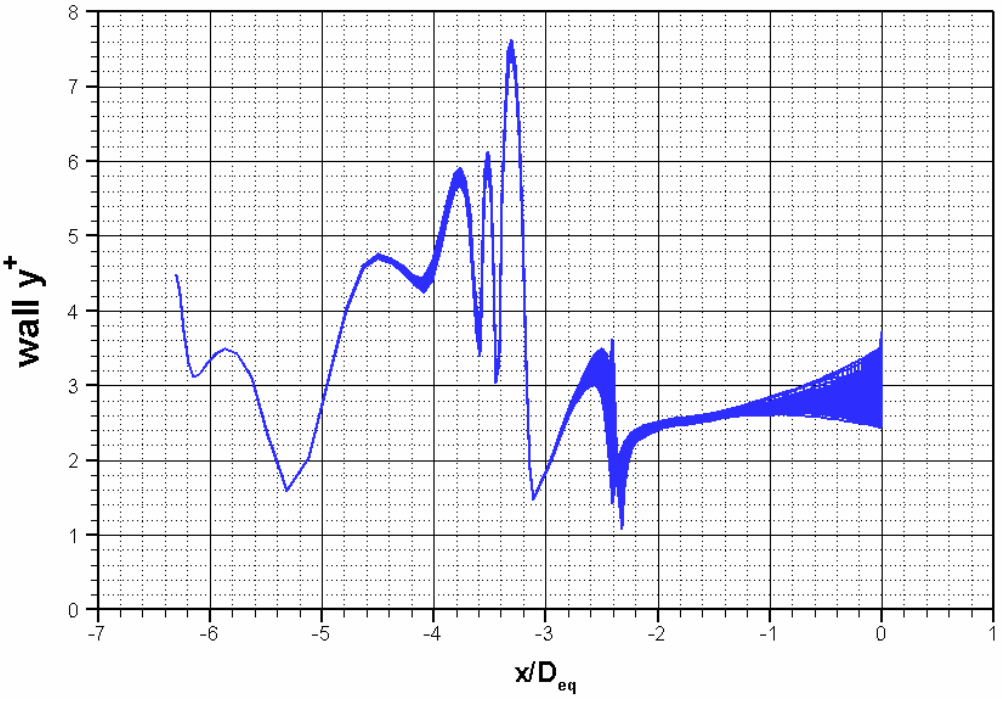

Figure 3.5: The wall y^+ values for the AR3 nozzle using variable cell heights for the wall-adjacent cells

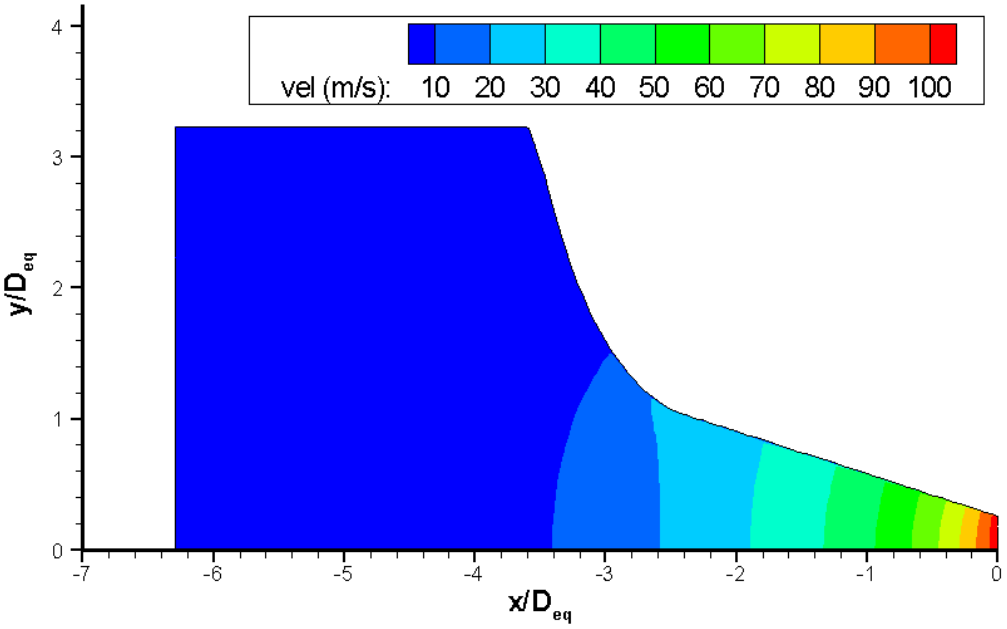

Figure 3.6: Velocity contours for AR3 nozzle at M_j = 0.31; the grid interface does not distort flow development

published article. It can be seen from Figure 3.7 that amongst all the simulation results, those obtained from the *SST k-ω* model show the closest match with the experimental results. Figures 3.8(*a*) and (*b*) further illustrate that the *SST k-ω* model was able to produce comparable results with those of the published experimental data from Zaman (1996a). Since the nozzle used for the current study was comparable to the nozzle used by Zaman, it was deemed that the *SST k-ω* turbulence model would be adequate for the given simulations.

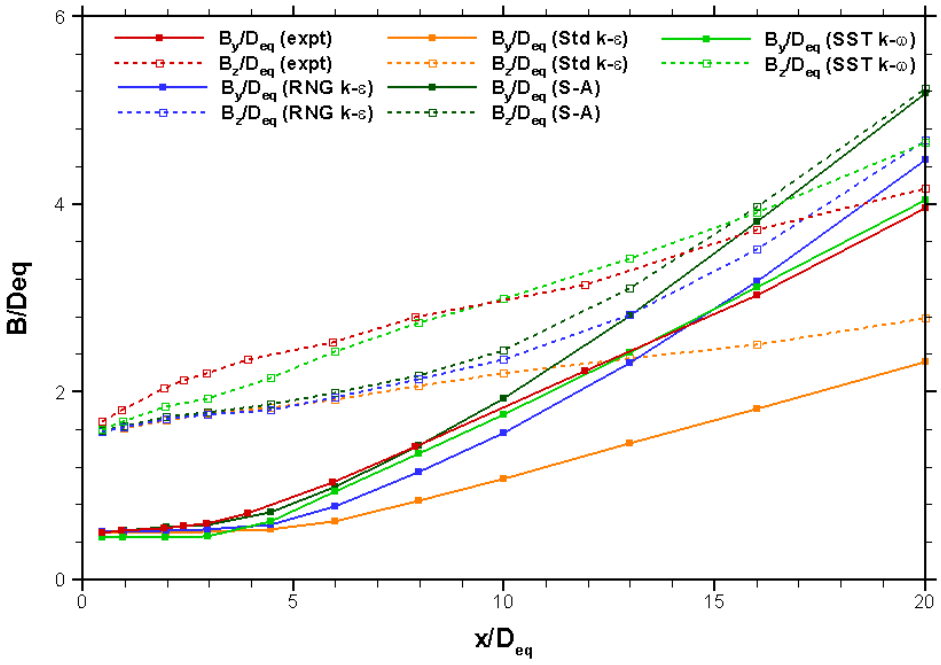

Figure 3.7: Comparison of jet half-velocity-widths (B/D_{eq}) for various turbulence models with the experimental results from Zaman (1996a); the SST k-*ω model shows maximum promise*

3.3.2 Initialisation Parameters

Following the selection of the meshing technique and the appropriate turbulence model, it was necessary to specify the initialisation parameters for the simulations. Since the flow was highly subsonic, a pressure-based implicit solver was sufficient for analysing the flow correctly. However, the compressibility effects still had to be taken into account. The specification of density calculations based on ideal gas laws and viscosity calculations utilising the three-coefficient Sutherland method take care of this. The default values for constants are maintained for the *SST k-ω*

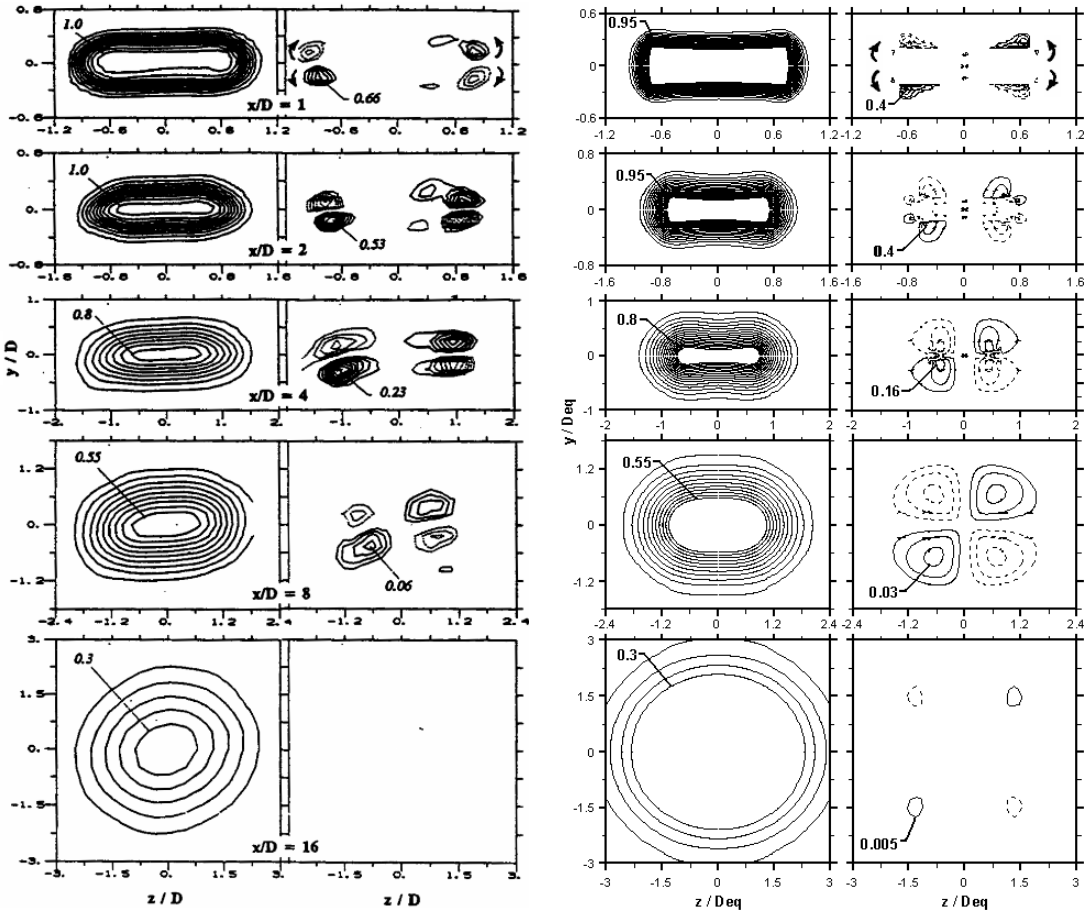

Figure 3.8: Comparison of normalised velocity (U/U_j) contours (left column in each) and normalised streamwise vorticity ($\omega_x D_{eq}/U_j$) contours (right column); the published results from Zaman (1996a) are shown in (a), while the simulation results using the SST k-ω *model are shown in (b); the location of the measurement planes is stated in (a)*

turbulence model. The operating pressure was set at 0 *kPa* so that the pressures specified at the boundaries were absolute. The under-relaxation factors for the different parameters were kept at the default value. The discretisation schemes, however, were changed to second-order for pressure and second-order upwind for the other parameters of density, momentum, turbulent kinetic energy (k), specific dissipation rate (ω) and energy. The SIMPLEC (SIMPLE-Consistent) algorithm was employed for the pressure-velocity coupling with a skewness correction of zero. SIMPLEC provides better under-relaxation compared to the SIMPLE algorithm and may provide a quicker converged solution if the pressure-velocity coupling is the limiting factor (Van Doormaal & Raithby (1984)).

Since the convergence of the solution was based on the user-defined monitor points (see Section 3.2 for details) rather than the residual monitors, all the residual monitors were turned off. Surface monitors were set up for tracking the total mass flux of the domain, the nozzle mass flux, mass flow rate of the nozzle ($\dot{m}$) and velocity convergence at centreline points 2, 25 and 50 D_{eq} downstream of the nozzle exit. The boundary conditions of the domain were then set, details of which are provided in Section 3.3.3. After ensuring that the simulation was setup as required, it was initialised using the values at the inlet. The final step before iteration was to partition the grid so that parallelising of the simulation was possible. The interfaces were encapsulated so that they were maintained within a single partition each. The number of iterations was specified and the simulations run on the High Throughput Computing Cluster (*HTCC*) facility at Cranfield University, Shrivenham.

3.3.3 Boundary Conditions

The tests were intended for subsonic conditions with a nozzle pressure ratio of 1.05, corresponding to a jet Mach number of 0.265. The averaged flow properties were of interest to determine how much the jet would spread along the different directions with respect to its location downstream of the exit. To this extent, the simulation was modelled for a quarter-domain with symmetry boundary conditions imposed on the *xy*- and *xz*- planes.

The physical dimensions of the nozzle were transferred to the simulation model. The length of the nozzle was taken to be the distance of the nozzle exit from the end of the settling chamber; this was found out to be 110 mm. The domain was set as 500 *mm* from the end of the nozzle exit in the lateral direction and 2000 *mm* from the exit plane in the downstream direction. To capture the upstream entrainment effects, the boundary outside the nozzle was extended up to the rear outer edge of the nozzle.

The ambient conditions for the simulation were set at 101.325 *kPa* and 288.16 *K* by default. The inlet of the nozzle was specified as a pressure inlet with the total and supersonic pressure adjusted to give an *NPR* of 1.05. The boundary outside the nozzle, upstream of the exit (called the 'free inlet') was also specified as a pressure inlet but the *NPR* was set at 1.00. This was to ensure that the

flow through this boundary was not forced into the domain but present only due to entrainment. The planes xy and xz were specified as symmetry boundaries. The remaining three boundaries were specified as pressure outlets at ambient pressure. The turbulence was specified in the inlet and outlet boundaries in terms of the turbulence intensity and the length scale. The length scale was taken as 7.5% of the R_{eq} as mentioned in Section 3.3.1.3. The free inlet and the outlets were specified at a turbulence intensity of 1%. The inlet turbulence intensity ($T_{i,i}$) was specified such that the exit turbulence intensity of the simulations matched that of the experiments. This value of $T_{i,i}$ was found to be 5%. The walls of the nozzle were set as walls with no-slip boundary condition. Figure 3.9 shows the dimensions of the domain and the different types of boundaries set in the $AR4$ simulation.

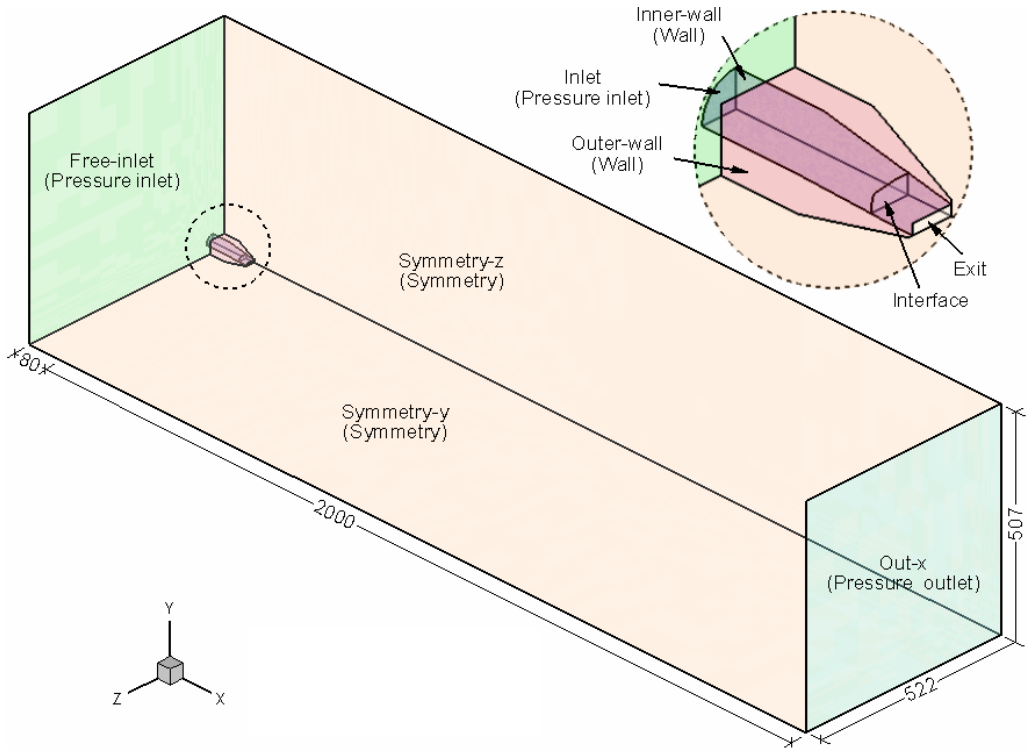

Figure 3.9: Domain extents and boundary types for the AR4 simulation; the lateral pressure outlets (Out − y and Out − z) are not shown in the figure; dimensions are in mm

The simulation results obtained after this only hold true if it is established that the grid used for the simulations does not introduce any errors into the solution. This is confirmed by performing grid independence checks for the given domain. Along with validation of the model, this forms an important step in confidently

accepting the simulated results as being valid and consistent. These are discussed in Chapter 5 under Grid Independence and Validation (Section 5.1).

3.4 Parametric Model

One of the aims of this study, as outlined in section 2.5, is to develop a parametric model that can effectively predict the occurrence of axis-switching for a given nozzle geometry upstream of the exit. Such a model was intended to be developed by incorporating statistical studies such as the appropriate design of experiments and curve-fitting.

3.4.1 Variables of Interest

The prediction of axis-switching could be achieved based on the calculated values of two parameters: location of the cross-over point (X_c), and difference in the normalised spanwise jet half-velocity-widths along the major and minor axes of the jet (ΔB). A cross-over point is defined as the distance downstream of the nozzle exit where the normalised spanwise jet half-velocity-widths along the major and minor axes of the jet are equal to each other. Henceforth in this study, the use of the symbol X_c indicates the distance of the cross-over point from the nozzle exit, normalised using the equivalent diameter, D_{eq}. Since the determination of axis-switching was important within 30 D_{eq} from the exit, the difference in the half-velocity-widths was considered at this location and called as ΔB_{30}. A positive difference would indicate greater spread along the major axis and hence, no axis-switching.

The upstream nozzle geometry is mainly dependent on the inlet area (A_i), inlet aspect ratio (AR_i), the cross-sectional geometry (i.e. circular, rectangular, etc.), and the length of the converging section. Since the simulations are based on the assumption that A_i and the length of the nozzle remain constant, the random variables available for changing the upstream nozzle geometry are: AR_i, cross-sectional geometry and length of the converging section. The cross-sectional geometry, however, was limited to two different types: elliptic (this also includes circular), and rectangular (including square). Within these two types, the effects

of varying the AR_i and length of the cross-section was studied. For simplification, the length of the cross-section was defined in the form of a ratio of the length of the converging section to the length of the nozzle. This ratio was called the 'Contraction Section Ratio' (*CSR*).

3.4.1.1 Range Selection

The two variables thus selected, AR_i and *CSR*, were varied over a range of values to understand their effects on the location of X_c and the corresponding value of ΔB_{30}. Initially, the variation of both these variables was chosen to vary for five different values, giving a matrix of 25 different combinations. This range though was constrained by the physical dimensions of the nozzle used for experiments. Since the exterior shape and geometry of the nozzle was also used for the simulations to incorporate the upstream entrainment effects, the interior nozzle dimensions were limited. The range of AR_i and *CSR* was therefore restricted from 1 to 4 and 0.4 to 1, respectively. The selections were made such that both the types of inlet geometries would have an identical number of simulations. The table 3.1 below shows the possible combinations for the nozzle simulations. The higlighted cells indicate the selected combinations. The *CSR* value of 0.59 implies a converging section of length 65 *mm*, corresponding to the physical dimension of the rectangular nozzle used for experiments. Thus in this case, an elliptic nozzle with $AR_i = 1$ and *CSR* = 0.59 corresponds to the nozzle used for experiments.

Table 3.1: Range of variation for AR_i and CSR; ⊡ indicates the physical possibility for a rectangular inlet with the given AR_i and CSR, and ⊙ indicates the same for an elliptic inlet; the highlighted cells indicate the selected combinations

$CSR \backslash AR_i$	1	2	3	4	5
0.20	⊡ ⊙	⊡ ⊙	⊡	⊡	
0.40	⊡ ⊙	⊡ ⊙	⊡ ⊙	⊡ ⊙	⊡
0.59	⊡ ⊙	⊡ ⊙	⊡ ⊙	⊡ ⊙	⊡
0.80	⊡ ⊙	⊡ ⊙	⊡ ⊙	⊡ ⊙	⊡
1.00	⊡ ⊙	⊡ ⊙	⊡ ⊙	⊡ ⊙	⊡ ⊙

3.4.1.2 Nozzle Designations

The nozzles are classified as belonging to either the $R-$series, if they have rectangular inlets, or the $E-$series, if they have elliptic inlets. The AR_i values are indicated by adding a number corresponding to the inlet aspect ratio after the letter 'A' in the designation. Furthermore, the CSR values are indicated by assigning 1 to 4 for the four values in ascending order and indicated by the letter 'C'. Thus, as per the designation, the nozzles are indicated as either $RAmCn$ or $EAmCn$ where, m and n are numbers between 1 and 4. For example:

EA1C2: corresponds to the experimental nozzle with elliptic inlet of aspect ratio 1 (i.e. circular inlet) and $CSR = 0.59$

RA3C1: corresponds to a nozzle with rectangular inlet of aspect ratio 3 and $CSR = 0.4$

EA4C4: corresponds to a nozzle with elliptic inlet of aspect ratio 4 and $CSR = 1$, i.e. the nozzle starts converging from the inlet

3.4.2 Statistical Study

The development of the parametric model is essentially performed using statistical methods. For any given statistical model, there are three parts that make up the model:

- The response variable;
- The mathematical function; and
- Random error.

The relation between these three parts that define the statistical model, is generally given by:

$$y = f(\mathbf{x}\,;\boldsymbol{\beta}) + \varepsilon \tag{3.6}$$

where, y is the response variable; $f(\mathbf{x}\,;\boldsymbol{\beta})$ is the mathematical function; and ε is the random error.

The mathematical function can be further represented by two parts: $x_1, x_2, \ldots$ are the predictor variables, while $\beta_0, \beta_1, \ldots$ are the parameters (NIST (2003)).

Such a mathematical function is then devised from the observed values of the response variable. In this case, the simulations corresponding to the different combinations provide the observed values for the response variable. Using curve-fitting techniques, the relationship between the response for the different combinations may then be worked out. The mathematical function thus obtained can then be used to predict the values of the response variable for the same given combinations. The difference between the observed and the predicted values of the response give us the random errors for each model case.

3.4.2.1 Validation of the Parametric Model

To ensure that the statistical model is able to predict the value of the response variable with confidence:

- The coefficient of determination, R^2, should be almost equal to 1, and
- The residual errors, ε_i should be random for the given model and should generally follow a probability distribution with mean, $\mu = 0$ and an unknown standard deviation, σ

The coefficient of determination and the probability distribution of the residual error for each type of nozzle, i.e. $R-$series and $E-$series, are then calculated using the following steps:

- The residual error, ε_i is calculated as:

$$\varepsilon_i = y_i - f\left(x_i\,;\,\beta_i\right) \tag{3.7}$$

  where, y_i denotes the observed value (from the simulation) and f_i denotes the predicted value (from the model)

- The different 'sum of squares' are then calculated to determine the variability of the data:
  - Total sum of squares,

$$SS_{tot} = \sum_i \left(y_i - \bar{y}\right)^2$$

- Regression sum of squares,

$$SS_{reg} = \sum_i \left(f_i - \bar{f}\right)^2$$

- Sum of squares of residuals,

$$SS_{err} = \sum_i (y_i - f_i)^2$$

- The coefficient of determination is then given by,

$$R^2 = 1 - \frac{SS_{err}}{SS_{tot}}$$

- The scatter plot of predictors vs. residuals is then plotted; if the residuals are randomly distributed, it shows the sufficiency of the functional part of the model. A histogram may also be plotted to estimate the distribution of the error.

- The mean, μ and standard deviation, σ of the residuals are calculated and the corresponding probability distribution is plotted.

- Finally, a normal probability plot is generated for the errors. It is a graphical technique for normality testing, i.e. assessing whether a data set is approximately normally distributed or not. The data are plotted against a theoretical normal distribution such that the points approximately form a straight line. If the errors are normally distributed, the normal probability plot depicts a straight line indicating that the statistical model is valid. If such a straight line cannot be generated, the data are deemed to be departed from normality and the model becomes invalid.

Chapter 4

Experimental Methods

Numerical simulations by themselves cannot provide enough confidence in the results obtained. This is partly because the solution process is limited by the levels of accuracy that one can get from the iterative process of solving a partial differential equation. Inherently, all the *CFD* solvers work on a principle that can be simply put as: "Garbage In, Garbage Out", i.e. if the input for the problem is not specified correctly, it will still produce results, albeit incorrect.

To improve the confidence with which a numerical solution may be accepted, the results produced are usually compared with some 'standard results'. These standard results will have been obtained using techniques that have been reliably set up in the real world. Conventionally, the most widely accepted standard results are in the form of theoretical calculations (generally based on first principles), experimental work which can be successfully repeated for the given setup, or established empirical formulae. Even in the case of using empirical formulae, experimental work serves as either a direct basis for the calculations or to determine the empirical constants or functions appearing in the calculation methods. Consequently, the validation work for the current study is primarily based on experiments carried out using the compressed air facility in the college.

4.1 Experimental Facilities

This section describes the facilities based at Cranfield University, Shrivenham that were used for the experimental work. These include the jet rig used to supply the compressed air, the jet seeder that seeded the flow for *LDA* measurements and the traverse used to mount and position the *LDA* 2-component probe.

4.1.1 Jet Rig

The jet rig was undoubtedly the most important facility necessary for the experiments; no compressible nozzle flow studies could be possible without a continu-

ous supply of air at the required nozzle pressure ratio (*NPR*). The general layout of the jet rig facility is provided in Figure 4.1.

The settling chamber and the nozzle assembly was located in a rectangular room, 7×7.5×3.5 *m* in size, designated the jet impingement room. The settling chamber was supported by a steel frame, 4×3×2.5 *m*, fixed to the floor. The frame had attachments that allowed the settling chamber to be fixed in either a vertical or horizontal position, as required. The settling chamber was connected to the compressed air supply with a flexible hose. This eliminated additional sharp bends in the supply line, thus helping to minimise any substantial changes in temperature or turbulence of the compressed air. There still, however, remained a significant pressure differential along the flow. The computers used for controlling the nozzle pressure, the traverse and the *LDA* data acquisition were placed in an adjacent room, primarily due to Health and Safety requirements. Along with the loud noise emitted when the jet is operated, the seeding introduced in the room presents a health hazard over prolonged working periods in the jet impingement room. Furthermore, this also separated the operator from the laser and thus improved safety from that perspective. Two *CCTV* cameras were placed so that they could transmit back visual information to the operator while the jet impingement room was isolated during the experimental runs. This helped the operator keep a closer eye on the experiment, along with all the instrumentation in the control room that provided information about the different systems.

4.1.1.1 Compressor

The nozzle test rig was supplied with compressed air using a CompAir L110-10A screw-type compressor. This compressor was rated to run at a maximum operating pressure of 10 $bar(g)$. It could supply compressed air at 18.63 m^3/min at 8°*C* above the ambient temperature (CompAir (2008)). The compressed air was stored in a pressure tank rated at 7 $bar(g)$. Although the compressor had its own control system, it could also be externally controlled using appropriate control units. As such, a SmartAir3 control unit was utilised for this purpose. A pressure gauge, in-line with the tank, fed the tank pressure back to the control unit which then established if the compressors were required to be turned on to re-fill the tank. This lower pressure limit was set at 5.5 $bar(g)$.

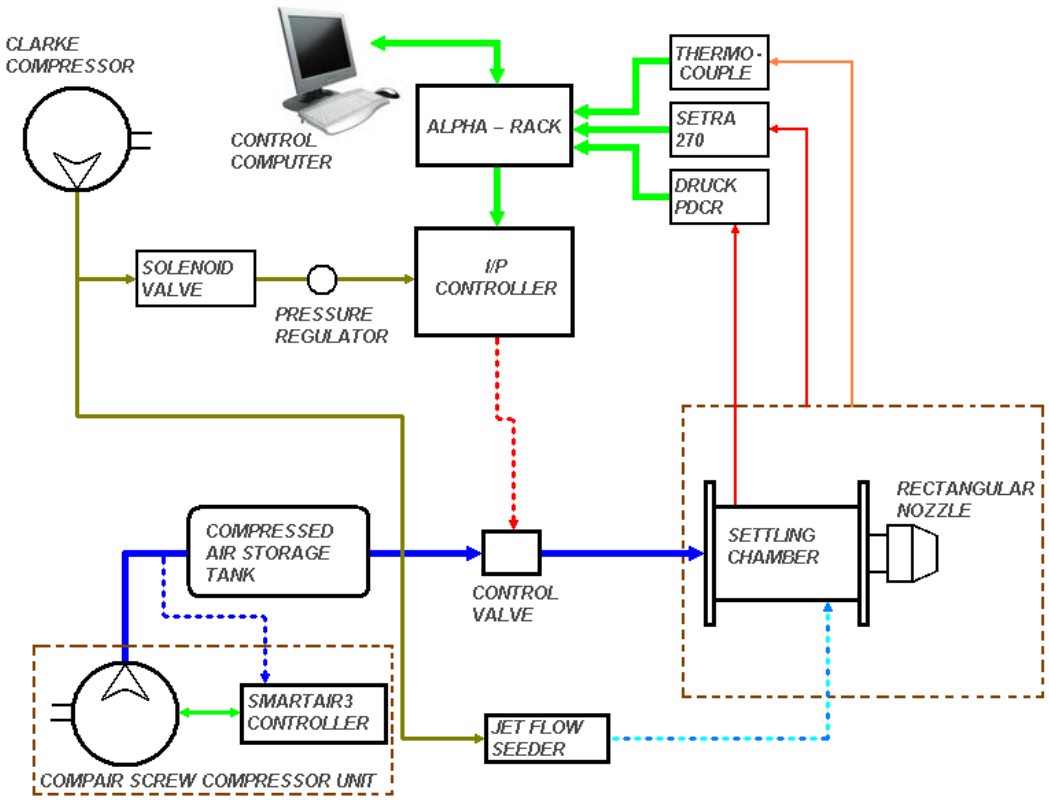

Figure 4.1: Layout of the Nozzle Test Rig facility at the college

The compressed air from the tank passed through two airline filters that partially removed any impurities present. It then passed through a drier/separator unit that separated the air from water and oil droplets suspended in the compressed air received from the compressor. It was further passed through another in-line air filter before being stored in the 34 m^3 reservoir. From here, the compressed air could be supplied to the jet rig, and also the transonic and supersonic wind tunnels and various other test cells, as required.

4.1.1.2 Settling Chamber and *AR*4 Nozzle

The settling chamber comprised six sections, held together between two end plates and connected with each other using eight *M*8 bolts. Each section was interchangeable and could fit into the other section with the help of a locating groove. An 'O-ring' seal was used to ensure air-tight connections. The initial end plate had an inlet of 70 *mm* diameter that was connected to the compressed

air supply using the flexible hose, as mentioned earlier. The first five sections were tubular with an inner diameter of 203 *mm* and a 12.7 *mm* wall thickness. The first section was 110 *mm* long and contained eight equispaced holes, 12.7 *mm* in diameter for injecting seeding into the flow. For the current study, only four alternate holes were connected to the seeder while the other four were connected to each other. The second section, 35 *mm* long, housed a filter material for preventing dirt/rust from damaging the nozzle and other instrumentation that might be used for intrusive measurement techniques. The filter material used, Multivee 99, was easily capable of filtering the compressed air without causing a significant pressure loss. The filter was held in place using a perforated plate with holes 3 *mm* in diameter and porosity of 24%. A circular aluminium disc, attached to the centre of this, acts as a baffle plate to prevent direct discharge of the compressed air to the nozzle. The third section was used to incorporate a honeycomb mesh that acted as flow straightener. This section was 75 *mm* in length. Following this was a 50 *mm* section which accommodated the pressure tappings to measure the chamber static pressure. Four equispaced pressure tappings ensured that the reading sent to the jet rig control was as accurate as possible. The fifth section was identical to the second section except that the perforated plate did not have the aluminium disc as a baffle plate.

The final section of the settling chamber was a 225 *mm* long converging section with an exit diameter of 65 *mm*. The two ends were connected with a spline that ensured minimal flow separation through the settling chamber and thus minimum turbulence at the end of the chamber. The end plate of the settling chamber could accept different circular nozzles screwed on to the $M82 \times 2$ countersunk threads. The *AR*4 nozzle used for the experiments, however, had an internal diameter of 35 *mm* (Figure 3.1(*b*)). An aluminium adapter with an inlet diameter of 65 *mm* and exit diameter of 35 *mm*, served as the connector between the nozzle and the settling chamber. The contour of this adapter was also a spline, created along the same principles as that of the converging section of the settling chamber to ensure minimal flow separation. Additionally, two flange sections were designed (Figure 4.2) so that the nozzle could be rotated though any angle between the major or minor axis positions, with no other change in the setup required. The flanges were held together using two $M6 \times 1$ bolts and sealed using an 'O-ring' placed in the 2 *mm* groove in Flange-SC.

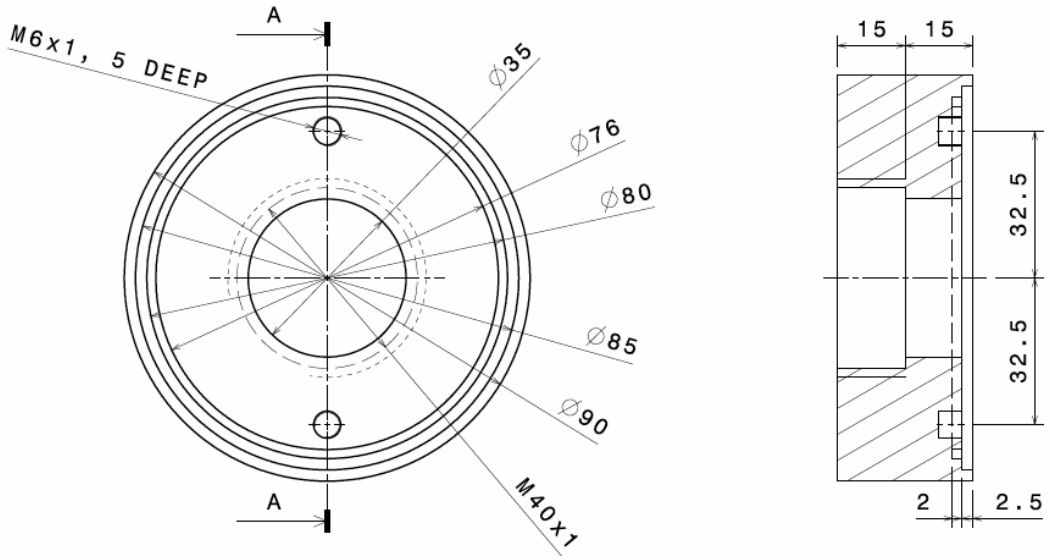

(a) Flange-SC; connects to the adapter

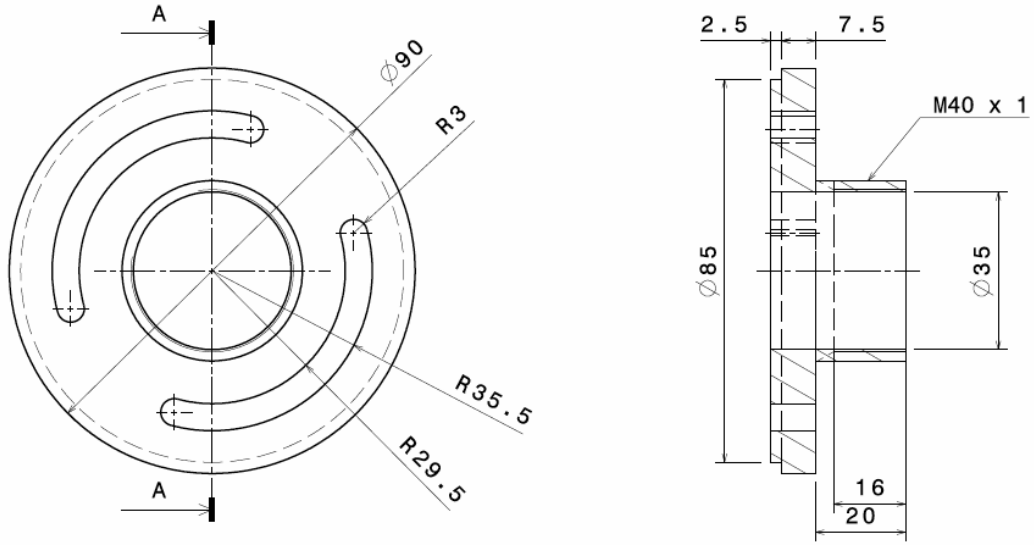

(b) Flange-Nozz; connects to the nozzle

Figure 4.2: Flange sections incorporated to ease the measurement of the AR4 nozzle flow-field through any angle between the major and minor axis positions

4.1.1.3 Jet Rig Pressure Control

The jet rig pressure control was used to adjust the pressure ratio in the settling chamber. The *NPR* was controlled using a computer with an accuracy of 0.5% through FORTRAN-based software written by Dr. Mark Finnis (Cranfield University). The control system essentially comprised of a Pentium processor-based desktop computer running MS-DOS, an Alpha-Rack, a solenoid control valve and a CompAir A119 pneumatic-controlled valve (marked 'Control Valve' in Figure 4.1). The ambient pressure was measured using a SETRA Model 270 pressure transducer while the pressure tappings in the settling chamber were connected to a DRUCK PDCR 10 – 3.5 pressure transducer to measure the static chamber pressure. Each transducer was calibrated using a DRUCK DPI 610 portable pressure calibrator. The ambient temperature was measured using a *K*-type thermocouple. Using the calibration data from the two transducers, a set voltage (and hence a set current) was then sent to the current-pressure converter that controlled the control valve. This opened the valve just enough to let the compressed air through the settling chamber at the required *NPR*. Thus a feedback system was established that helped to maintain the pressure in the settling chamber as necessary. The Clarke compressor (rated at 12 $bar(g)$) was used to regulate the pressure at the control valve. The solenoid valve served as a safety device at the pneumatic control of the control valve. In case of an emergency, the solenoid could be de-energised, thus closing off the control valve and terminating the air supply to the settling chamber.

4.1.2 Jet Flow Seeder

The successful measurement of flow properties using an *LDA*, to a large extent, depends on the quality of the seeding in the flow. The flow seeding must ideally have neutral buoyancy and should not affect the flow development. This requires the seeding particles to be extremely small. At the same time, however, the seeding particles need to be large enough to scatter back the light so that a good signal-to-noise ratio is obtained at the photo detector of the *LDA*.

The jet flow seeder used in the current setup (Figure 4.3) was manufactured and assembled in the laboratory using a mix of standard parts and parts manufactured at the college workshop. The design was prepared several years ago by Mr. Mark

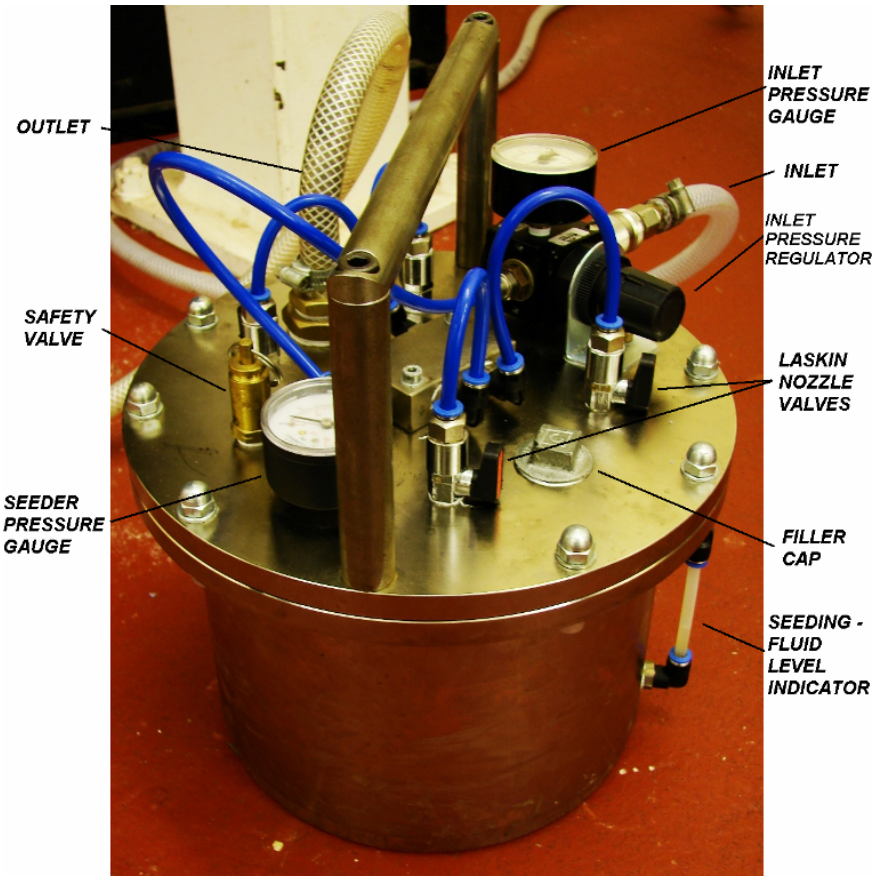

Figure 4.3: Jet Flow Seeder

Eyles (Cranfield University). The seeder comprised a cylindrical pressure vessel of diameter 20 *cm* with a capacity of approximately 5 *litres*. The pressure vessel is rated at a working pressure of 10 $bar(g)$. A pressure regulator controls the inlet pressure into the seeder. Through a manifold block, the compressed air is diverted into four Laskin nozzles which can be opened or closed independently of each other. The seeding fluid was a solution of 15% glycerine in water ($\rho = 1.05\ g/cm^3$). The operating procedure required that at any given time, the seeder should have no more than 2 *litres* and no less than 1 *litre* of the fluid. The pressurised air through the Laskin nozzles passes into the seeder and produces micro-bubbles. These bubbles burst on reaching the surface of the fluid and produce a fine mist of seeding particles. Two baffle plates, placed near the top of the vessel, ensure that the bigger particles do not easily escape through the outlet. The average diameter of the seeding particles produced by this seeder was 1 μm.

4.1.3 Traverse

A lightweight traverse was used so that the measurement of the flow at various points could be taken with ease. The traverse could be moved along all three axes. The column of the traverse had an attachment plate that was used to fix aluminium extrusion sections which, in turn, mounted the *LDA* probes. The traverse could be moved 160 *cm* along its length, 80 *cm* along its width and 160 *cm* in the vertical direction. The motion was controlled using an Isel Automation C116–4 *CNC* controller supplied by Dantec Measurement Technology. This controller could be accessed using the same BSA Flow software that managed the *LDA* control and data acquisition. The controller drove three stepper motors, one for each axis, which converted the rotational motion to translational motion using a square-toothed screw. The least count of the traverse along all the three axes was 0.1 *mm*. The traverse was aligned with the length along the streamwise direction of the flow. The axes orientation for the nozzle and the traverse is shown in Figure 4.4. After the traverse was aligned with respect to the nozzle as required, the *LDA* probe was mounted on to it and the position of the beam intersection point noted. This point was then moved to the centre of the nozzle exit and the traverse coordinates reset so that this became the origin of the experimental setup. It also served as the parking location for the traverse when it was not in use. Parking the traverse ensured that the motors were locked and no slip in movement occurred when the motors were de-energised.

4.2 Experimental Techniques

Through the preliminary work for the current study, different experimental techniques were sought for obtaining data that could be used for validation of the simulations. From various past studies on experiments for nozzle flows, a number of techniques were identified to be of interest. These techniques and their uses, along with a past study that has incorporated the same (indicated using square brackets), are given below:

- *Flow-field probe measurements*: Primarily used for measuring pressure and temperature of the flow-field. The technique can be employed to measure

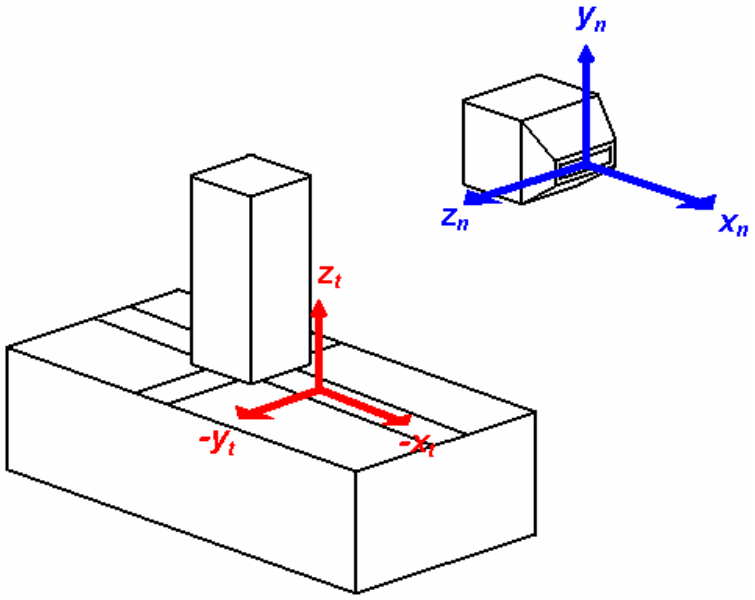

Figure 4.4: Representative figure showing the orientation of the nozzle and the traverse

the static and total pressures as well as the total temperature in the flow-field [e.g. Donaldson & Snedeker (1971)].

- *Hot-wire measurements*: For measuring flow velocities and turbulences [e.g. Sfeir (1976)].

- *Laser Doppler Anemometry (LDA)*: The *LDA* can be employed to measure the flow velocities and turbulences in averaged and instantaneous states. Simultaneous measurements can be made for 2-D or 3-D flow fields using *LDA* [e.g. Lau et al. (1979)].

- *Particle Image Velocimetry (PIV)*: As the name suggests, *PIV* makes use of correlation between the tracer particles in the flow, captured in successive images, to measure the flow velocities. Like the *LDA*, *PIV* may be used in 2-D or 3-D, as required [e.g. Alkislar et al. (2000)].

- *Schlieren Technique*: Schlieren (and shadowgraph) techniques make use of the fluid property that the change in density of a fluid affects the refractive index of the fluid. The schlieren and shadowgraph techniques provide qualitative information about the first and second derivative of density respectively. Although predominantly qualitative or semi-quantitative results are generated, successful attempts have been made to obtain quantitative data from

these techniques (Settles (2001)). A variation of the schlieren technique, Background Oriented Schlieren (*BOS*), combines the basics of schlieren and *PIV* and may be used to obtain quantitative information about the density field (Meier (2002)).

The first two techniques mentioned above are intrusive techniques; the measurement probe is in the flow volume. This disturbs the flow structure at and behind the probe and corrections may need to be applied to get exact values for the measured flow property. The other techniques mentioned are non-intrusive by nature, i.e. the measurement probes do not interfere with the flow-field development. Amongst all the techniques mentioned, it was decided to employ the Laser Doppler Anemometry (*LDA*) for measuring the subsonic flow. Besides the accuracy associated with a properly aligned *LDA* system, it also gives the option of measuring both velocity and turbulences in 2-D or 3-D and steady or unsteady states, as required. Although harder to set up than the *PIV*, which can be used for similar measurements, an accurately set up *LDA* is more reliable. Details regarding the *LDA* and the setup used has been given in Section 4.2.1. For the additional measurements involving supersonic flow, the Background Oriented Schlieren (*BOS*) was used. *BOS* has not been extensively used for studies since it is still in its infancy, having been proposed by Meier in 1999 (Meier (2002)). More explanation regarding this technique and its advantages over conventional schlieren are provided in Section 4.2.2.

4.2.1 Laser Doppler Anemometry

Laser Doppler Anemometry (*LDA*), as the name suggests, involves the use of lasers and the Doppler effect principle to measure the velocity and turbulence of a given flow. It is a non-intrusive measurement technique, i.e. the measurement probe is outside the flow and hence does not disturb the flow or cause a pressure loss. Additionally, it is not affected by the particulate matter in the flow; it may actually be advantageous for the measurement (Durst et al. (1981)). The laser Doppler technique was first demonstrated in 1964 by Yeh and Cummins as a technique for velocity measurement of small tracer particles suspended in a flowing fluid (Yeh & Cummins (1964)). A year later, this technique (then known as Laser Doppler Flowmeter) was employed for measuring velocities of gases in

water (Foreman, Jr. et al. (1965)). A more detailed description about the *LDA* technique is given in Durst et al. (1981).

4.2.1.1 Principles of LDA

The basic principle of *LDA* is the Doppler effect. A single laser beam passing through a seeded flow will cause a frequency shift in the light scattered by the particles in the fluid due to the Doppler effect. If these particles in the fluid move with a velocity V, the frequency shift (also known as the Doppler shift) due to the motion of the seeding particles relative to the incident laser beam is given by:

$$\Delta v_D = \frac{v_0 V}{c} (\cos\ \alpha - \cos\ \theta) \tag{4.1}$$

where, v_0 is the frequency of the incident laser beam, c is the speed of light and α and θ are the incident and scattering angles, respectively.

There are, however, three unknowns in Equation 4.1, namely v_0, V and Δv_D. Even if this equation is solved, the frequency shift Δv_D for known fluid flows is beyond the resolution capabilities of most sophisticated *LDA* hardware systems. This is because it depends on the speed of light which is much larger than the flow velocities encountered in fluid flows. These problems may be overcome by using a modified technique known as 'differential Doppler'.

The differential Doppler technique, developed by Goldstein & Kreid (1967), uses a second incident laser beam which crosses the first beam at a known separation angle α. This is also known as the dual-beam *LDA* system and is the most common optical arrangement for current *LDA* systems. A single coherent beam is split into two parallel beams of equal intensities using optical beam splitters. These beams are then focussed at a point in the flow using a converging lens. The beam diameters decrease continually to a minimum value (called the beam waist) at the focal point where the beams intersect. The intersecting beams thus form a 'measurement volume' in the flow, the dimensions of which are dependent on the optics and the corresponding beam parameters, i.e. beam diameter and separation angle. Since the intersected beams have plane wavefronts, on interfering with each other, they produce parallel planes of light and darkness, i.e. fringes. The fringe spacing (d_f) can be calculated as:

$$d_f = \frac{\lambda}{2\ \sin\left(\alpha/2\right)} \tag{4.2}$$

where, λ is the wavelength of the incident laser light and α is the subtended angle between the beams.

The fluid flow to be measured is seeded with particles that scatter light in all directions when the laser light is incident upon them. As a particle passes through the interference pattern in the measurement volume, the intensity of the scattered light varies. The receiving optics collect a part of this scattered light; this is then passed on to a photodetector which converts it into an analogue electric signal. The rate of rise and fall in this signal is directly proportional to the velocity of the particle in the flow, and thus the flow velocity itself. This electric signal is then analysed by a signal processor that extracts the necessary frequency information. A typical signal received from an *LDA* in burst mode is shown in Figure 4.5(*a*). This signal consists of the actual frequency information, the pedestal signal, i.e. the portion of signal associated with particle transit through the light beams, and noise. The signal is first filtered using a low-pass filter to remove noise. Usually the frequency band of the pedestal signal lies outside the band of the Doppler signal and can therefore be separated by passing it through a high-band filter (Durst et al. (1981)). The resultant clean Doppler signal (Figure 4.5(*b*)) is then digitised and read as instantaneous velocity.

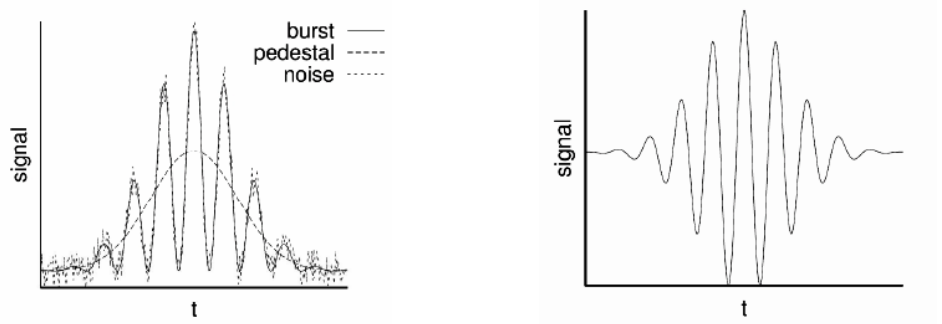

(a) Typical photodetector signal for Doppler burst (b) Clean Doppler signal

Figure 4.5: An example of a typical Doppler signal; (a) Typical photodetector signal; (b) Clean Doppler signal after removal of noise and pedestal (Cabrita (2006))

For very low flow velocities or for flows with high turbulent intensities, however, a high-pass filter may not be very effective. In such cases, light-frequency shifting can increase Doppler frequencies without altering the pedestal-signal frequency, thus rendering the location of the high-pass filter less critical. Additionally, automatic filterbanks may be employed to accommodate the variation in

the ranges of the Doppler and pedestal signals at different locations in the flow. Besides this, the velocity measurements with *LDA* are directionally ambiguous, i.e. the detector is unable to discern if the two particles in the measurement volume move with a velocity of u or $-u$. Light-frequency shifting is also able to solve the problem. This is achieved by introducing an acousto-optic device of known frequency f_s in the path of one of the incident beams after the beam-splitter. One of the most popular acousto-optic devices is a Bragg cell. An electro-mechanical transducer attached to one side of the Bragg cell, which is typically a slab of glass, generates a periodic pattern of high and low density. The opposite side is shaped such that the acoustic wave reflection is minimised. Additionally, it is also attached to an acoustic-absorbing material. The travelling wave fronts act as a thick diffraction grating. The incident beam, on passing through this, undergoes a fixed frequency shift, as compared to the other unaffected beam. The relationship between the Doppler frequency and the particle velocity due to the frequency shift can now be written as:

$$f_{s,1} = f_1 + \frac{\mathbf{U}}{\lambda_1}(\hat{e}_s - \hat{e}_1) \tag{4.3}$$

$$f_{s,2} = f_2 + \frac{\mathbf{U}}{\lambda_2}(\hat{e}_s - \hat{e}_2) \tag{4.4}$$

where, $\hat{e}_1$ and $\hat{e}_2$ are unit vectors in the direction of the incident beams and $\hat{e}_s$ is the unit vector in the direction of the receiver. The Doppler frequency shift f_D is given by the difference in Equations 4.3 and 4.4. Thus,

$$f_D = f_{s,2} - f_{s,1} \tag{4.5}$$

Since both the incident beams originate from the same coherent light source, $f_1 = f_2 = f_I$ where subscript I indicates incident light. Therefore, it follows that:

$$f_D = \frac{2\ \sin\ (\alpha/2)}{\lambda}\ u_x \tag{4.6}$$

where, α is the beam separation angle. Rearranging the terms, we get:

$$u_x = \frac{\lambda}{2\ \sin(\alpha/2)}\ f_D \tag{4.7}$$

The Doppler frequency f_D is much lower than the frequency of light itself and can be measured as the fluctuations in the intensity of light reflected from the seeding particles. Also, for f_s sufficiently larger than f_D corresponding to the smallest

velocity, the value of $|f_D|$ is uniquely related to one velocity value. Consequently, the directional ambiguity is also removed.

A seeding particle scatters light differently in different directions. Studies by Mie (1908)[6] indicate that a particle scattering light will do so approximately 100 times more in the forward direction, i.e. in the direction of the incident beams, than in the direction back towards the source (Figure 4.6). Consequently, initial *LDA* techniques were arranged in 'forward-scatter' mode with the receiving optics aligned opposite to the source to capture maximum information. This technique, however, suffers from a very serious disadvantage; the transmitting and receiving optics need to be aligned extremely precisely for measurement accuracy. It also requires that the setup must have optical access on either side of the flow to position the necessary optics. This liberty is usually not available for most setups and hence the 'back-scatter' technique was developed.

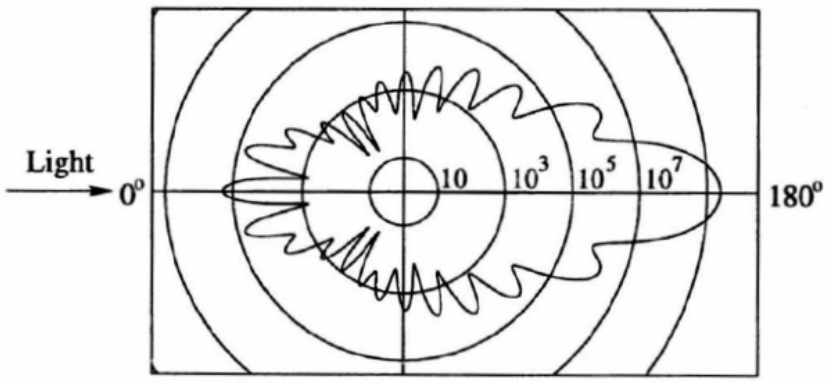

Figure 4.6: Light scattering pattern for a 1μm oil particle in air following the Mie scattering theory (Raffel et al. (1998))

The transmitting and receiving optics in the back-scatter configuration are combined into a single probe. The transmitted beams are scattered back and less intense light is collected by the receiving lens placed in the same probe. This system is advantageous since it is more compact than the 'forward-scatter' technique and requires access to the setup from one side only. The disadvantage in terms of less intensity of light is overcome by using photomultipliers which

[6] As mentioned in Raffel et al. (1998). The original article by Mie (1908) has not been referred to.

amplify the received signal by adding a current gain to it. Also, in case of *LDA*, since the laser beams are focussed at the point of measurement, the intensity of light is quite high. The elements of a typical one-component, dual-beam *LDA* system in back-scatter configuration are shown in Figure 4.7.

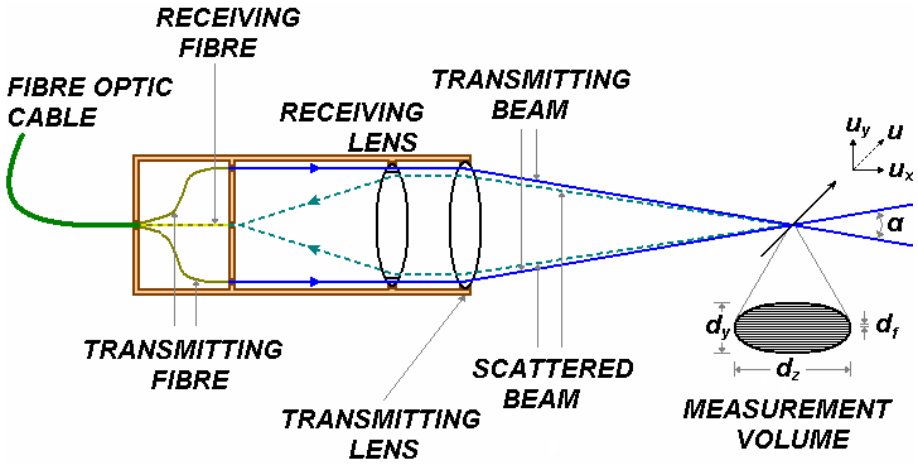

Figure 4.7: Typical components of a one-component, dual-beam, back-scatter LDA arrangement

4.2.1.2 Components of the LDA System

The *LDA* setup used for the current study has been described in this section (Figure 4.8). The coherent light was supplied by a Lexel 95 Argon-Ion laser. This water-cooled, Class 4 laser could be split into three different wavelengths for 3-D flow anemometry. The three beams had wavelengths of 514.5 *nm* (green), 488 *nm* (blue) and 455 *nm* (purple). The laser was focussed into the transmitter end of a Dantec 60X FibreFlow Optic module. This module was independently aligned with the laser beam and was designed to accommodate a beam splitter and a Bragg cell, which introduced a frequency shift of 40 *MHz*. The FibreFlow module also isolated the laser into the three above-mentioned wavelengths. Fibre optic manipulators were used to fine-focus the laser into the transmitting fibre optic that was connected to the probe. For the current work, a 2-D probe was used with wavelengths of 514.5 *nm* and 488 *nm*. The scattered light was collected by the receiving optics and sent to the photomultiplier, where it was amplified and passed into the Burst Spectrum Analyser (*BSA*). These *BSA* Enhanced Processors

then converted the signal as required and after passing it through the low and high-pass filters, obtained the clean Doppler signal. The *BSA* processors are calibrated according to the optical parameters so that they can read the instantaneous velocity directly from the signal. Each velocity component required a separate *BSA* processor. Additionally, these required to be synchronised for measuring time-dependent data. Hence, the first processor clock was set as master and the subsequent processor clocks were set as slaves.

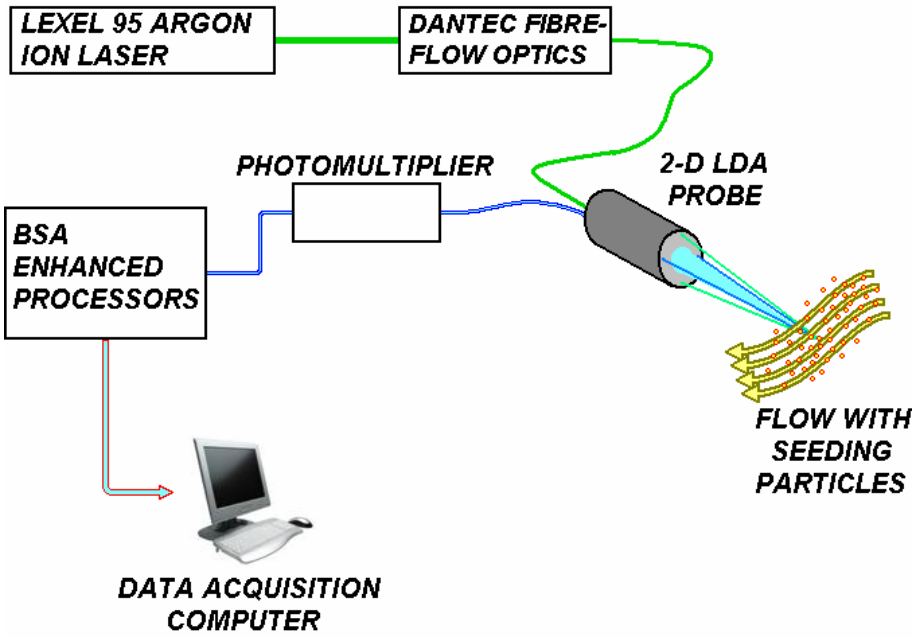

Figure 4.8: Schematic representation of the LDA system available for the current study

The signal processors could be controlled independently from a control panel on the main processor or externally using the BSA Flow Software v1.41 installed on a computer. This software was capable of controlling the processors and acquiring data through them, as well as post-processing the data, as required by the operator. The software could also communicate with the traverse controller, making it convenient to set up the entire experimental run through a single operating unit.

From Figure 4.7, using simple geometry, it can be seen that if the beam separation angle is large, the measurement volume will be large in the $x-$ and $y-$directions. Thus it requires that the focal length of the transmitting lens be as small as possible. Also, in the actual experimental setup, to ensure that the

probe remains outside the flow at all times, a 1000 *mm* lens was used as opposed to a 300 *mm* lens. However, a small separation angle results in the measurement angle being too wide in the $z-$direction. This could introduce a significant error in the measurements. Consequently, a beam expander of ratio 1.98 was attached to the probe. This resulted in a beam spacing of 36.36 *mm* and a beam separation half-angle of 2.062°. The beam diameter was measured to be 2.2 *mm* and the number of fringes in the measurement volume was 21 for both the set of beams. Since the beams of wavelength 514.5 *nm* were stronger, they were used for measuring the spanwise velocity (the weaker flow component), while the other beam of wavelength 488 *nm* was used to measure the streamwise velocity. The resulting measurement volumes, fringe spacing and calibration factor, along with the rest of the setup parameters, are summarised in Table 4.1. It was also necessary to set a correct measurement range for both components of the *LDA*. The maximum streamwise velocity expected for a flow at *NPR* 1.05 is approximately 90 m/s. This decreases rapidly as the measurement volume goes outside the potential core region and velocities here could be very close to zero. Thus the range was set such that the centre was at 54.3 m/s with a span of 217 m/s for the streamwise component. In the spanwise direction, the velocity at most points in the flow is expected to be close to 0 m/s and hence the centre velocity was set as 0 m/s and the range was selected as 28.6 m/s.

A burst mode was used for velocity measurement with a time interval of 5 *sec* or 10000 bursts, whichever was earlier. The measurement was run in coincidence mode allowing instantaneous data to be captured, although for the current study it was averaged.

4.2.1.3 Procedure for Experiments

The initial experimental setup plan intended to make use of the 3-D system for flow measurement. It was, however, deemed to be extremely cumbersome from the experience of previous operators and was abandoned in favour of taking 2-D measurements. The measurements of velocity in the spanwise direction for any plane parallel to the nozzle exit could be taken by moving the traverse accordingly. This method though had a serious shortcoming; as mentioned earlier, the measurement volume in the $z-$direction is large for small beam separation angles. The measurement volume dimension in this direction, i.e. in the direction of the

Table 4.1: Values for different parameters in the LDA setup

Beam System	**U1 (Streamwise)**	**U2 (Spanwise)**
Wavelength (*nm*)	488	514.5
Focal Length (*mm*)	1000	1000
Beam Diameter (*mm*)	2.20	2.20
Expander Ratio	1.98	1.98
Beam Spacing (*mm*)	36.36	36.36
Number of Fringes	21	21
Fringe spacing (μm)	6.783	7.151
Beam Half-Angle	2.062°	2.062°
d_x (*mm*)	0.143	0.150
d_y (*mm*)	0.143	0.150
d_z (*mm*)	3.965	4.181
Range: Centre (m/s)	54.3	0
Range: Span (m/s)	217	28.6
Calibration Factor ($m/s/MHz$)	6.78	7.15

beam incidence, was 3.965 *mm* and 4.181 *mm* for the two beam systems. Consequently, the accuracy of the measurement was compromised in that direction since, e.g. at the shear layer near the exit, half the volume would still be seeded and provide velocity data while the other half would register zero velocity due to lack of seeding. To enable the measurement of the entire flow field in 3-D it was decided to make use of a dual-flange arrangement (Figure 4.2) so that the nozzle could be easily turned through any angle between 0° and 90°. The streamwise component would serve as the reference component for each measurement in a given plane parallel to the nozzle exit. Depending on the rotation angle of the nozzle, the spanwise component was resolved into its resultant velocities along the nozzle axis system. This still meant that the component of velocity in the direction parallel to the $z-$direction of the measurement volume was not accounted for. Thus, the values of the spanwise component were only valid for the setup at positions corresponding to 0° and 90° under an assumption that the velocity in $z-$direction did not contribute to it.

Although this system also made use of an approximation, all the measurements were taken in the same state; the centreline plane in the vertical direction. This was expected to generate the results for the streamwise component as realistically as possible for the given measurement point in the flow-field. The angles and the traversing positions are shown in Figure 4.9.

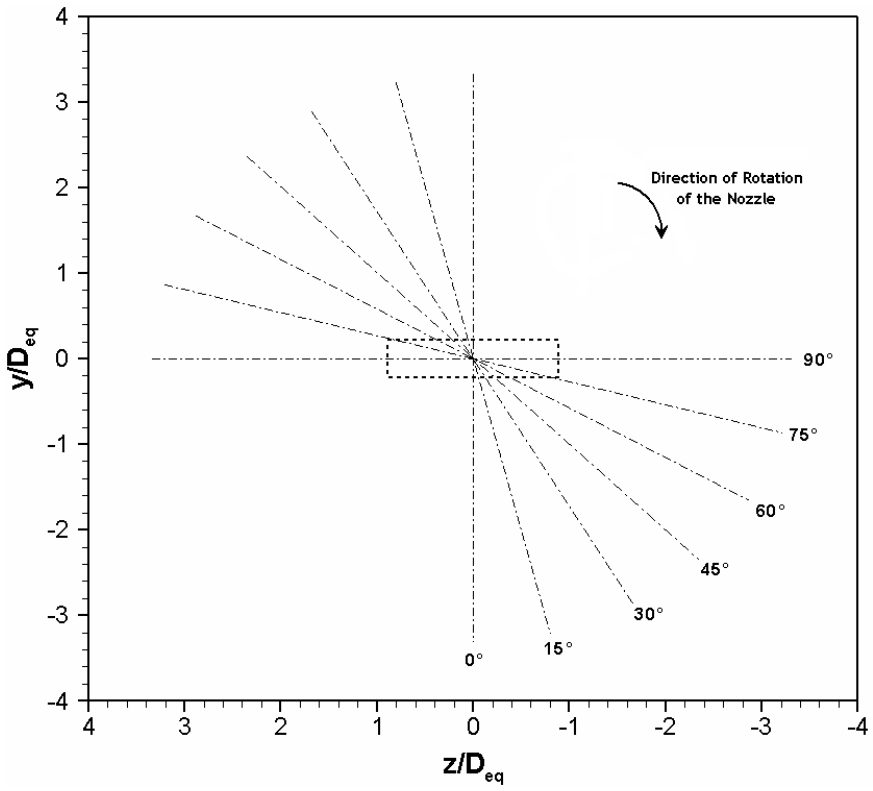

Figure 4.9: The angles and the traversing positions for the LDA; distances shown correspond to the plane 16 D_{eq} downstream of the exit; the dotted outline indicates the nozzle exit in the base configuration with the major axis oriented horizontally

The measurements were taken by rotating the nozzle by 15° between each run to give a total of seven runs. The data was obtained over three independent runs, partly ensuring that any error due to repetitive movement of the traverse (e.g. backlash) was averaged out. The mean data, thus obtained, was exported into Tecplot. The details of the measurement procedure, the results obtained and their subsequent analysis have been provided in Appendix A and the discussion in Chapter 5 (Section 5.1.2). Figure 4.10 shows the *LDA* probes at a ready position at the origin of the setup, i.e. at the centre of the nozzle exit.

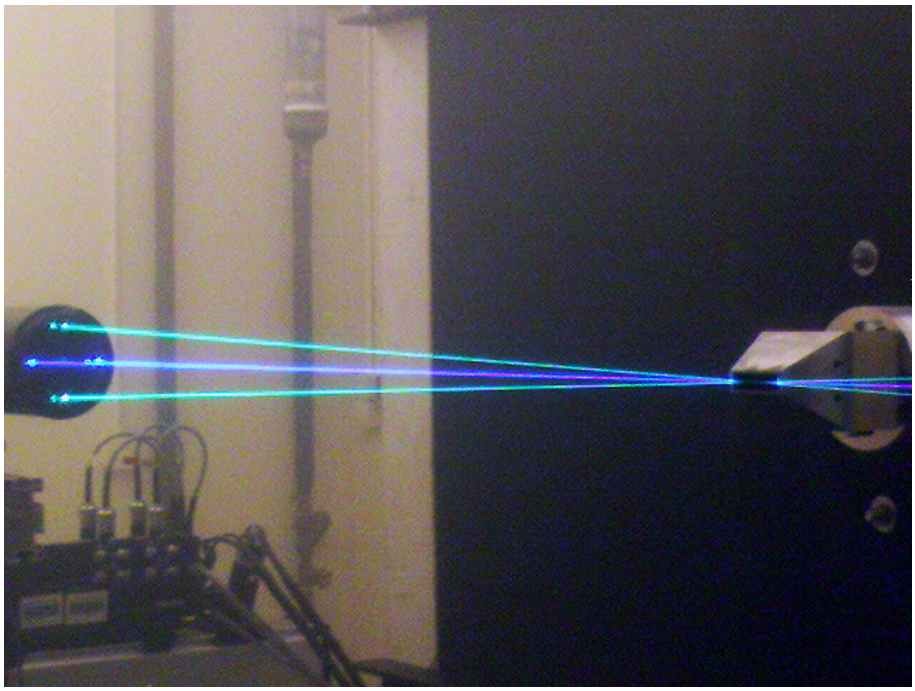

Figure 4.10: LDA setup with the origin set at the centre of the nozzle exit

4.2.2 Background Oriented Schlieren

Meier defines Background Oriented Schlieren as "a schlieren measurement technique based on computer evaluation of image variations due to refractive index variations in the propagation medium" (Meier (2002)). He first proposed this method in his patent application (DE 199 42 856 A1) in the year 1999. In principle, the distorted image of a specific background is numerically compared with an undistorted one to determine the gradients of density. The *BOS* method offers a possibility of determination of the density fields by the integration of the measured gradient fields.

4.2.2.1 Schlieren Technique

Schlieren and shadowgraph techniques are said to lie between microscopy and telescopy. Although a schlieren or shadowgraph setup cannot be directly used as an aid to view objects based on size or distance, it assists in looking at optical inhomogeneities in a transparent medium in considerably more detail than by a naked eye (Settles (2001)). The volume under observation is known as *schliere*, i.e.

schlieren object. The schlieren technique was first developed by Robert Hooke using an in-line single lens arrangement with two candles. It has evolved quite considerably since then; it is now possible to get coloured schlieren images depicting the variations in the observed medium.

The first practical apparatus for viewing schlieren images was developed by August Toepler (1836–1912). It consisted of an adjustable knife-edge cutoff, a lantern as the light source and a telescope which enabled the image to be viewed directly. His test results established that temperature differences of 1°C were visible, which correspond to a change in refractive index of about one part per million. Ernst Mach (1838–1916) and Peter Salcher (1848–1928) observed the first schlieren photograph of a supersonic jet emanating from a converging jet. Based on Toepler's design principles and techniques, there are two basic types of schlieren systems: *lens-type* and *mirror-type*. Usually, lens-type systems are in-line whereas mirror-type systems are folded, i.e. the path of light in the setup is not along a single axis. The typical setups for a dual-lens in-line and a dual-mirror Z-type schlieren arrangement are shown in Figure 4.11.

Both the arrangements make use of some common components, namely, a slit-source and a knife-edge. A slit-source is easily obtained by introducing a slit in front of the light source and condenser lens setup so that the slit is placed at the focal point of the first schlieren optic (lens or mirror depending on the setup). The knife-edge is placed at the focal point of the second optic and can be adjusted to determine the amount of cut-off which helps to observe the required schlieren image with the necessary detail. As with any technique requiring an optical setup, extreme care has to be taken to ensure that the optics are perfectly aligned. Additional care has to be taken when setting up the Z-type schlieren arrangement. Figure 4.12 shows the typical Z-type arrangement with the angles at which the optics are usually placed with respect to the axis. For the setup to produce an image with minimum aberrations, the angle made by the incident beam on the first parabolic mirror ($2\theta_1$) has to be made as small as possible. Consequently, it means that the angle at which the mirror is tilted with respect to the axis (θ_1) is also at a minimum. This applies to the second mirror as well, where the angle between the axis and the reflected beam towards the knife-edge ($2\theta_2$) is maintained a small as possible. In the most ideal situation, for best results, these angles should be equal.

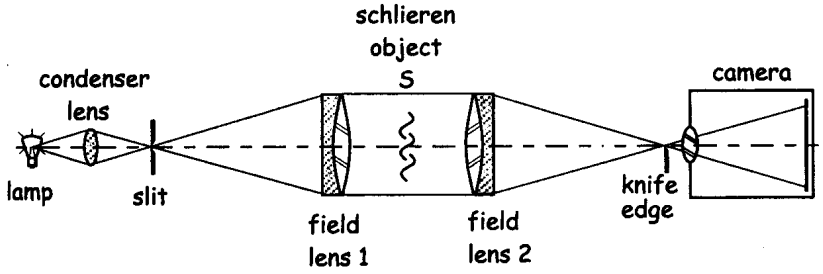

(a) Dual-lens in-line arrangement

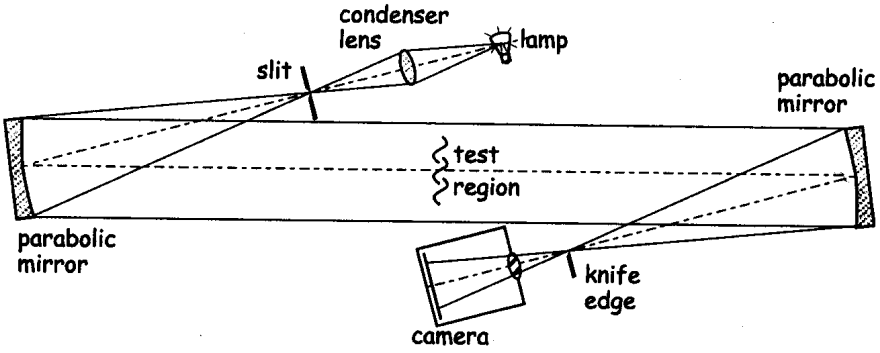

(b) Dual-mirror Z-type arrangement

Figure 4.11: Typical setups for employing the Schlieren technique (Settles (2001))

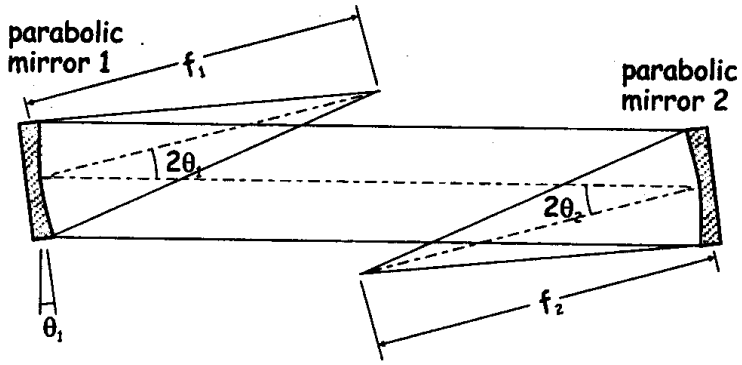

Figure 4.12: Z-type schlieren optics with typical angles (Settles (2001))

Another factor to be considered is the alignment of the knife-edge. The knife-edge can affect only those ray refractions that are perpendicular to its edge. This means that, for observing the density gradients in the axial direction of a horizontally aligned jet, the knife-edge must be positioned vertically. An example is shown in Figure 4.13 where the different effects of a circular cut-off, a vertical knife-edge and a horizontal knife-edge on the schlieren image of an oxy-acetylene flame can be seen. A typical schlieren image for a choked axisymmetric jet at *NPR* 2.5 is shown in Figure 4.14.

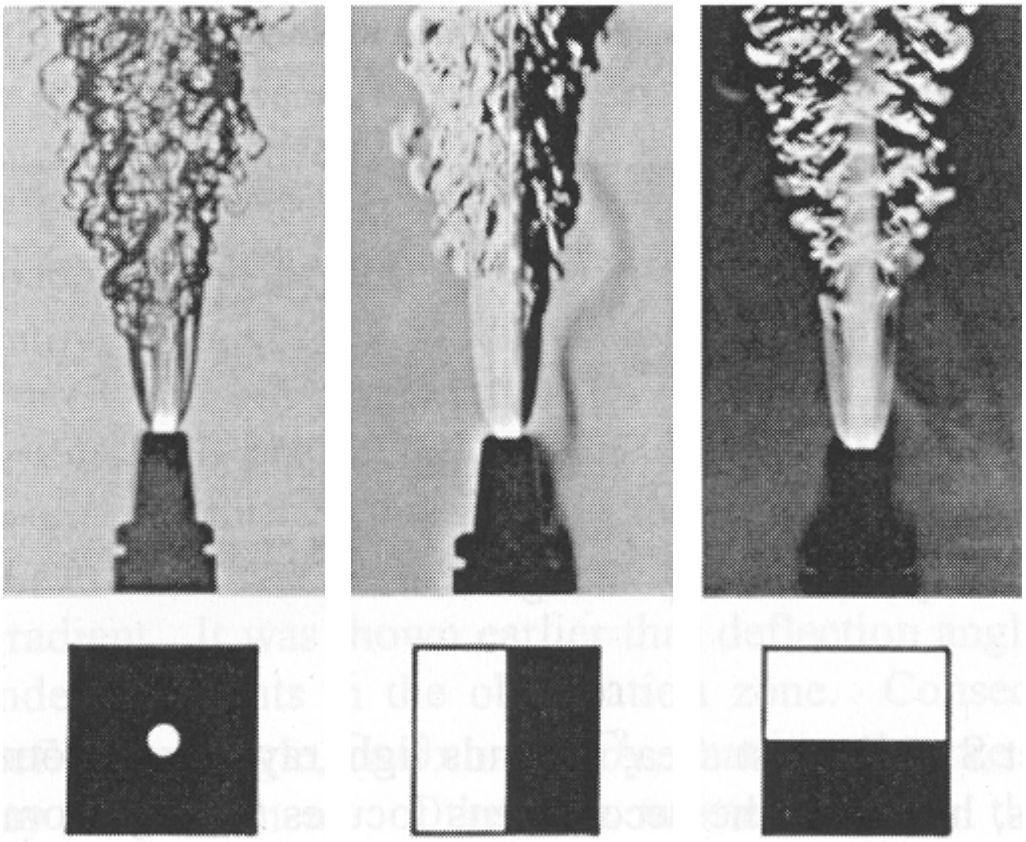

(a) Circular cut-off (b) Vertical knife-edge (c) Horizontal knife-edge

Figure 4.13: Schlieren photograph of an oxy-acetylene flame showing effects of different cut-offs (Settles (2001))

4.2.2.2 The BOS Technique

The Background Oriented Schlieren derives its basic principles from the schlieren technique. It differs, however, in that it does not require the use of the extensive

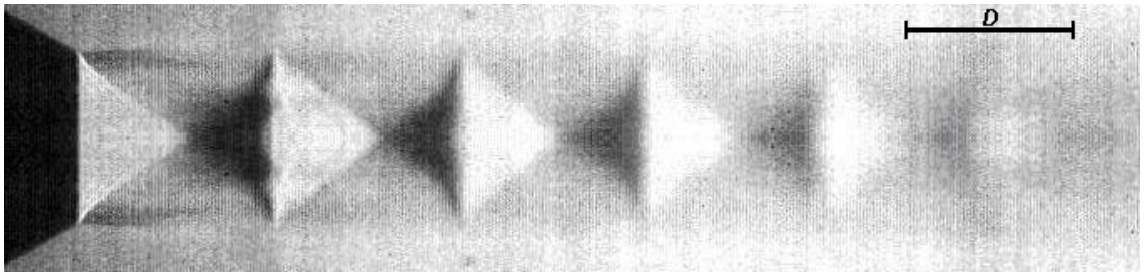

Figure 4.14: Typical schlieren image; choked axisymmetric jet at NPR 2.5, flow from left to right

setup that is typical of a schlieren arrangement. A specific illuminated background pattern and a digital camera are the only instruments required for this setup. Consequently, it is easier to set up than the conventional schlieren. Different backgrounds provide different results for correlation, depending on the contrast of the captured image and the flow direction. Consequently, the best results are usually generated using a random dot background since it has a high contrast and unique features which are ideal for image correlation algorithms to determine pixel shift (Hargather & Settles (2010)).

The variation in the density of the transparent medium affects the refractive index. This is the principle on which the *BOS* technique is based. The relation between the density gradients and the refractive index variation can be represented by the Gladstone-Dale equation (Equation 4.8):

$$\frac{n-1}{\rho} = G(\lambda) \tag{4.8}$$

where, n is the refractive index; ρ is the density of the medium (kg/m^3); and $G(\lambda)$ is the Gladstone-Dale constant. The Gladstone-Dale constant is dependent on certain characteristics of the medium and weakly on the frequency of light used. The reader is directed to Merzkirch (1987) for more details.

Typically, as a first step, an image is taken of the random dot pattern with the medium (air) at rest, i.e. no-flow condition. The second image is then taken with the nozzle running at required *NPR*. This image contains the necessary density gradients that distort the background image. A cross-correlation algorithm is employed to generate the displacements of the dots between the two images in

x and y directions. In the current setup, $+x$ is along the centreline of the jet downstream of the exit with the origin at the centre of the exit. The vertical axis is denoted by y while z is in the line-of-sight direction. Now, the deflection of a single beam contains information about the spatial gradient of the refractive index integrated along the axial path (Venkatakrishnan & Meier (2004)). Thus, the image deflection β may be defined as:

$$\beta = \frac{1}{n_0} \int_{a-\Delta a}^{a+\Delta a} \frac{\delta n}{\delta y} dz \tag{4.9}$$

This classical *BOS* situation for calculation of the different parameters is represented in Figure 4.15. The background pattern is positioned at B, the schlieren is positioned at S, the camera lens is at L and the image plane is positioned at I. The solid line indicates one undistorted image ray $R1$ while one distorted image ray, $R2$, is shown by a dashed line.

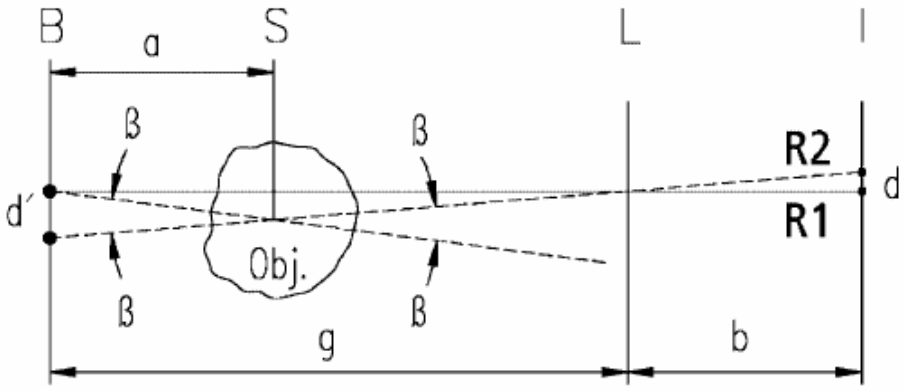

Figure 4.15: A representative diagram for typical BOS setup (Meier (2002))

From the figure, using simple geometrical reasoning, we can see that the virtual displacement d' is related to the image displacement d by the distance of the background from the lens g and the distance of the image plane from the lens b. For large g, this may be replaced by the focal length of the camera f. Thus we have,

$$\frac{d'}{g} = \frac{d}{b} = \frac{d}{f} \tag{4.10}$$

Also, if the deflection angle β is considered very small, it may be approximated as d'/a, where a is the distance of the *schliere* from the background. Using this approximation, the proportionality relation $\beta \sim \nabla n$ and Equation 4.10, the sensitivity for a given setup is given as:

$$\left(\frac{d}{\nabla n}\right) \sim \left(\frac{af}{g}\right) \tag{4.11}$$

Thus, the shift of the background and the sensitivity increases with increasing the distance of the density gradient from the background. For a constant image field, this implies that the increased distance between the background and the lens g may then be compensated by increasing the focal length of the camera f.

The obtained displacements are thus the density gradients at each point in the field. The derivatives of these gradients in the x and y direction can be together represented in the form of an elliptic partial differential equation called the Poisson Equation (Equation 4.12):

$$\frac{\partial^2}{\partial x^2}\rho(x,y) + \frac{\partial^2}{\partial y^2}\rho(x,y) = S(x,y) \tag{4.12}$$

where, $S(x, y)$ is the source term. The displacements at each mesh point, obtained through correlation, are used for calculating this source term (Venkatakrishnan & Meier (2004)). The solution of this equation yields the line-of-sight integrated density field, i.e. the three-dimensional density field as projected when viewing from one direction. The projected density fields, obtained from observing the phase object along different directions, can then be simultaneously deconvoluted using optical tomography techniques (for e.g. filtered backprojection technique). This enables the density distribution to be obtained for any given plane. More details on the filtered backprojection technique may be obtained from Venkatakrishnan & Meier (2004). In particular, for details about various tomographic techniques available, the reader is referred to Kak & Slaney (1988).

The *BOS* process of determining the density field can thus be laid out in three steps (Venkatakrishnan (2005)):

- The displacements of the background, imaged through the phase object (Figures 4.16 (*a*) and (*b*)), are calculated using cross-correlation algorithms (similar to the ones used for *PIV*). These displacements are essentially the vectors indicative of the density gradient at each point (Figure 4.16 (*c*)).

- These displacement vectors in x and y directions can be represented in the form of a Poisson equation which is then solved to get the line-of-sight integrated density field (Figure 4.16 (*d*)).
- Optical tomography (using filtered backprojection technique) may then be employed to get the density field in the required plane of interest (Figure 4.16 (*e*)).

Background Oriented Schlieren is advantageous over the conventional schlieren system as it is easier and cheaper to set up. It does not suffer from the cumbersome alignment process experienced when using optics. Besides this, the methodology of generating quantitative data from *BOS* is simpler; conventional schlieren is still pre-dominantly used for obtaining qualitative and semi-quantitative results.

4.2.2.3 Current BOS Setup

The light source, converging lens, slit, mirrors/lenses to produce the collimated beam and the knife-edge of the conventional schlieren setup is replaced by a background pattern for the background oriented schlieren. As previously mentioned, a random dot pattern is an ideal background for most of the cases. The best results are observed when the background is backlit using a diffusive source of light so that the whole pattern is evenly illuminated.

For the current setup, a Matlab™program[7] was used to produce the random dot pattern on A3 paper. The LED and diffuser assembly from an LCD monitor, along with the frame, was used as the back-illumination source. This was able to provide an even level of illumination for the pattern. The images were captured using a Casio Exilim EX-F1 digital camera. The camera offered a resolution of 6 *Megapixel*, storage of the files in RAW format and the option of taking images using an external trigger. The RAW format files could be converted into TIF format, ensuring that the images were not distorted by compression if stored in JPG format. The external trigger was especially useful since even the slightest movement

[7]The author would like to acknowledge Dr. Frédéric Moisy, Assistant Professor, University Paris-Sud, the originator of a Matlab program for creating a background pattern for A4 paper size (http://www.fast.u-psud.fr/ moisy/ml/).

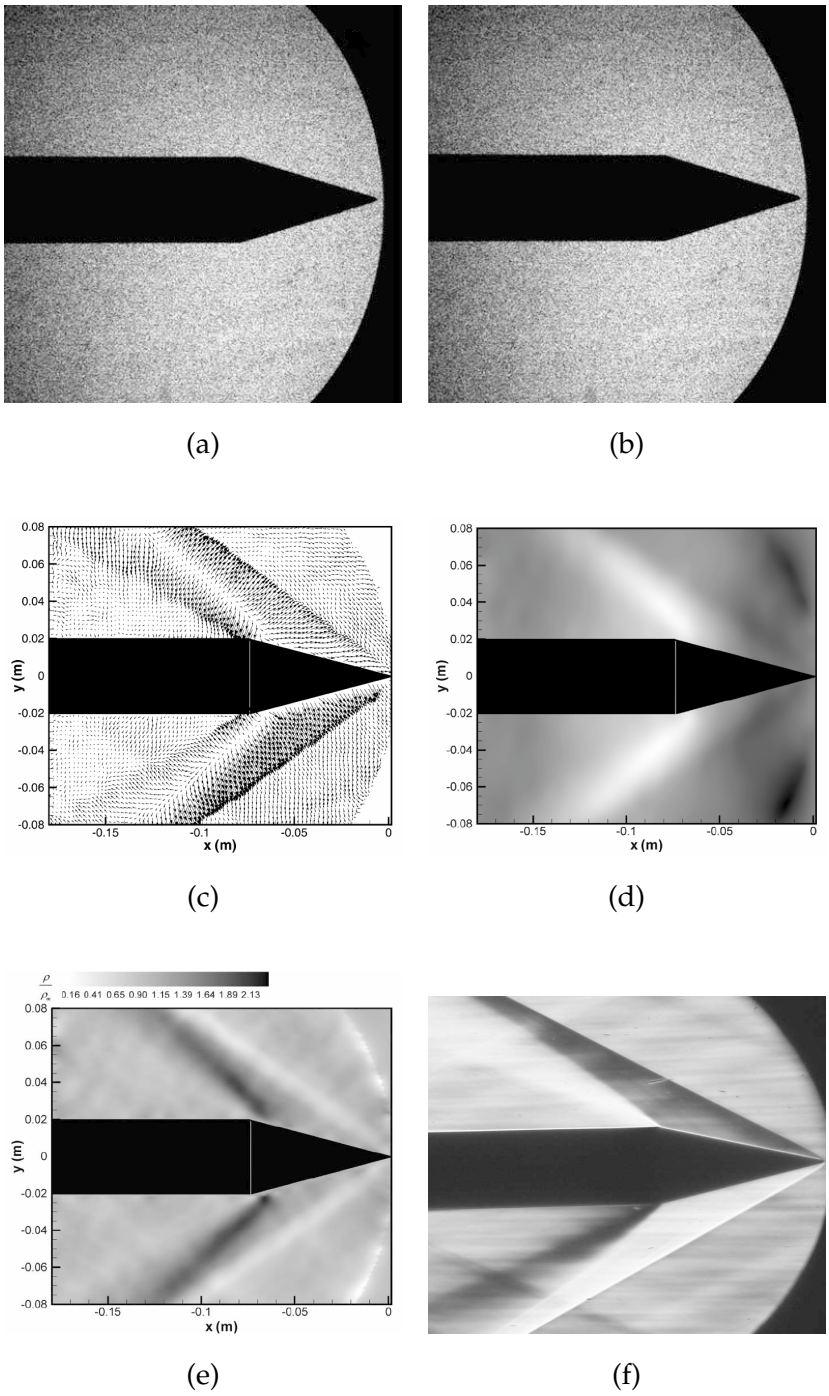

Figure 4.16: The process of obtaining the density field for a required plane of interest—setup for flow over a 15° cone-cylinder at Mach 2.0 (Venkatakrishnan & Meier (2004)); (a) Background pattern without flow; (b) Background pattern with flow; (c) Vectors of density gradients; (d) Projected density field as computed from the Poisson equation; (e) Backprojected normalised density field; (f) Conventional schlieren (horizontal knife-edge)

of the camera would have registered as a substantial pixel displacement in the correlation. The experimental setup is shown in Figure 4.17. For the rectangular nozzle setup, the distance between the *schliere* and the background (a) was 156 *cm* while that between the camera (lens) and the background (g) was 213 *cm*. The focal length of the camera lens was set at 22.2 *cm*.

The post-processing of the images to calculate the vector displacements and the integration of the resulting Poisson equation was done using a FORTRAN-based code written by Dr. Mark Finnis (Cranfield University). The program was able to take multiple images for averaging the results. The individual images of the integrated density field thus generated were then analysed using Matlab™. The image processing toolbox in Matlab has a built-in Inverse Radon Transform function. A simple program was written to incorporate this function for convolution of the entire density field. The input was the integrated density field images and the angles at which the images were taken. Using only this data, the whole-field density was calculated and stored in the form of pixel values in a cell array, each cell containing a 2-D matrix with the image information for each cross-plane in the volume. The density was then normalised using the free-stream density value. The data from the cell array could then be used, such that density information at any required plane in the volume was obtainable. It can be clearly inferred that the resolution of the processed images could be improved by increasing the number of integrated density field images used as input.

Before the *BOS* technique could be used for the rectangular nozzle, both the FORTRAN and Matlab codes were required to be tested. Additionally, it was also necessary to ensure that the images captured are able to resolve the necessary flow structures as required. This all formed the validation process for the *BOS* technique, the details of which are given in Appendix E.

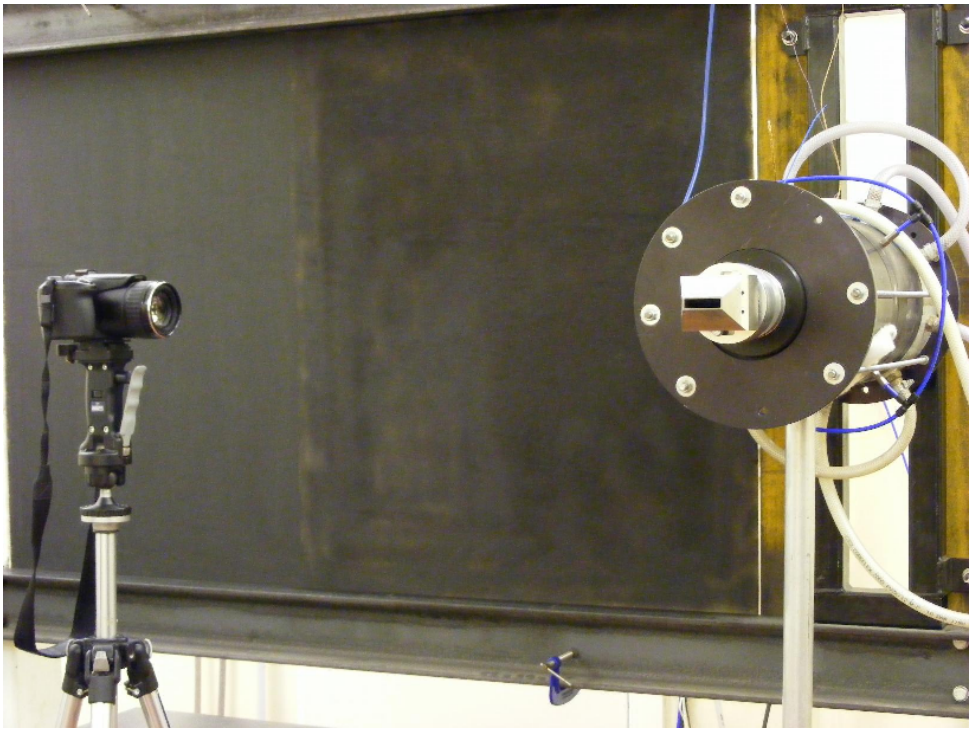

(a) The camera position with respect to the nozzle

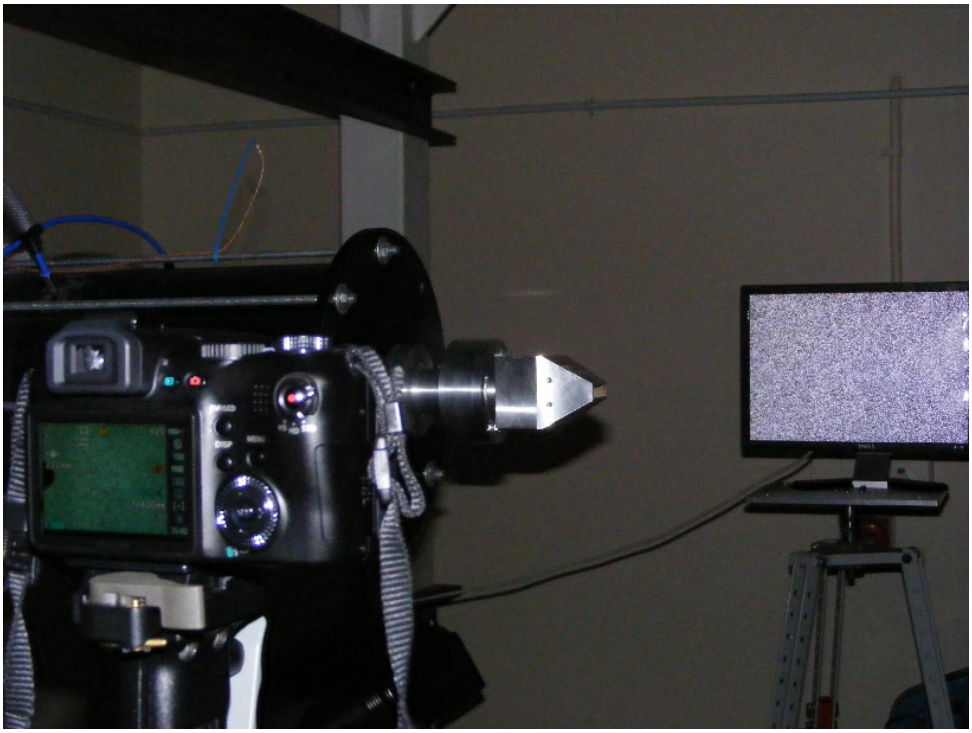

(b) The *BOS* setup showing the camera, nozzle and the background pattern alignment

Figure 4.17: BOS arrangement for the rectangular nozzle setup

4.3 Error Estimation

Experimental measurements, although, significantly reliable within limits, are prone to errors. These errors could be due to wrong calibration, instrumentation fault, losses in information propagation as well as operator errors. Assuming that the operator is able to set up everything as necessary, ensuring no errors are introduced into the system due to wrong setup, calibration or method, the equipment will still have some limitations that need to be taken into consideration.

The errors for the current *LDA* setup are mainly due to seeding response variation, velocity bias, sampling and jet rig control system. All these errors are discussed in details in Appendix B. The total velocity error due to the *LDA* components, i.e. seeding response, velocity bias and sampling variation, is 0.25%. In addition to this, the pressure control system also introduces some error into the velocity of the flow-field. The error due to this was found to be 5.57%, the details of the estimation for this are also provided in Appendix B. The total error in the *LDA* measurements can therefore be calculated as:

$$\left(\frac{\partial U}{U}\right)_{total} = \sqrt{\left(\frac{\partial U}{U}\right)^2_{LDA} + \left(\frac{\partial U}{U}\right)^2_{PCS}} \tag{4.13}$$

Thus, for the current *LDA* experiments, the total uncertainty in velocity measurements was 5.576%.

Chapter 5

Results and Discussions

This chapter deals with the main results obtained during the course of the current study. The grid independence and validation of the simulations are presented, followed by the results generated by the simulations and their analysis. The parametric models proposed to combine the effects of the inlet aspect ratio (AR_i) and the length of the converging section of the nozzle are detailed, explaining their formulation and validation.

The Laser Doppler Anemometry (*LDA*) data were first obtained for a circular nozzle subsonic case to gain confidence in the setup and measurement technique. The corresponding results showing the validation of the methodology have been provided in Appendix C. Following this, the *LDA* was employed for obtaining the flow-field velocity measurements for the *AR*4 nozzle running at subsonic conditions. The primary aim behind this exercise was to generate data that could be used for validation of the simulation, as explained in Section 5.1. The *CFD* simulations were then set up using Fluent^{TM}with appropriate variations in the AR_i and *CSR* parameters for both the rectangular and elliptic inlets. The results pertaining to the locations of cross-over points and spreading of the jet were then incorporated into respective parametric models using statistical methods.

The additional results covered in Section 5.5 were intended to compare the effect of changing the nozzle pressure ratio (*NPR*) on the flow development of the free jet issuing from the *AR*4 nozzle. This aspect of the *NPR* variation was deemed to be a separate research area and could probably be considered as a part of future work. Consequently, it was meant to serve primarily as a confidence test in application of the Background Oriented Schlieren (*BOS*) method for determining the density flow-field. The *BOS* technique has been validated in Appendix E using data from the Stratford nozzle schlieren measurements. The subsequent comparison with the corresponding *CFD* has also been given. After validation of the *BOS* technique, it has been employed to measure the density flow-field for the *AR*4 nozzle running at *NPR* 2.50. Data obtained from *AR*4 simulations at *NPR* 2.50 and 3.50 are also provided for comparison with conventional schlieren. The results obtained from these simulations were then further analysed.

5.1 Grid Independence and Validation

5.1.1 Grid Independence

One of the most important aspects of *CFD* simulations is to ensure that the grid does not affect the results produced. A coarse mesh may not be able to resolve all the flow structures that could be seen for a fine mesh. At the same time, using a fine mesh increases the computing expenses for the simulation; as an estimate, from personal experience, roughly one million cells can be processed with 1 GB of available RAM. Besides this, the time required for solution convergence also increases substantially. For any simulation, a high number of cells near regions of importance is highly desirable so that maximum details about the flow can be obtained. Since the focus of the current study is on the development of the free jet and its effect on axis-switching, the regions of importance are the regions inside the nozzle and near the exit of the nozzle. The correct resolution of the flow structures through these regions is required for the development of the flow through the rest of the domain. Higher cell densities are maintained in these regions of importance compared to the rest of the domain.

This, however, does not completely solve the problem of dependence of the solution on the grid. The definition of a coarse or fine mesh varies from one simulation problem to another. To eliminate this issue, grid independence tests are carried out on a sample simulation before the entire set is run. The grid independence for the current problem was tackled in two steps:

- The grid inside the nozzle was resolved to ensure that the wall y^+ values along the inner wall of the nozzle were maintained between 1 and 5 as far as possible (Figure 5.1). This was done during the preliminary tests; the nozzle was meshed and tested without the exterior domain, i.e. the exit was set as a pressure outlet at required conditions.
- The resolved grid of the nozzle was then incorporated with the rest of the domain and the mesh density close to the nozzle exit in the streamwise direction was varied. This variation formed the basis of the grid independence tests. Four different cases were considered and based on mesh density, classified as: coarse, medium, medium-fine and fine meshes.

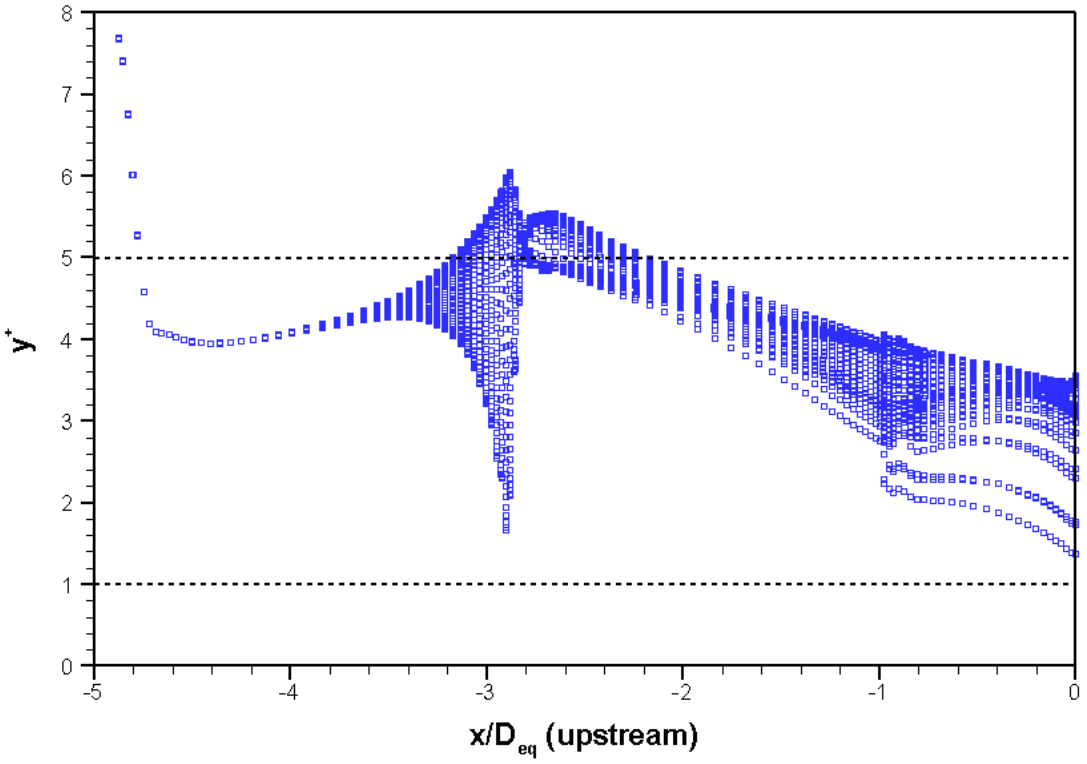

Figure 5.1: y^+ values along the inner wall of the nozzle; the dashed lines indicate the recommended upper and lower bounds for the y^+ values

The mesh density in all the four cases was varied in the streamwise direction. The details of the variation are given in Table 5.1. Figure 5.2 shows the mesh distribution for a medium grid. Along the spanwise directions, y and z, the mesh distribution was kept the same for all the cases. This variation of mesh density was not in the classical sense, where generally a coarse mesh has half the number of cells along one dimension than the finer mesh (implying that the finer mesh has 8 times more cells in a three-dimensional domain), while the finest mesh would have 8 times more cells than the medium (finer) mesh. Since the streamwise dimension of the first cell of the domain was dependent upon the dimension of the cell inside the nozzle at the exit, this was fixed for all the grid independence test domains. Also, the domain outside the nozzle, upstream of the exit (Figure 5.3), was unaltered for all the domains under consideration. Consideration also had to be given to the number of cells in the domain since too many cells would mean that the simulation would be computationally very expensive and time-consuming.

Table 5.1: Mesh density variation for grid independence tests

Type	**Downstream Mesh Points**	**Mesh Distribution**	**Number of Cells**
Coarse	100	0.05 *mm* at exit; 50 *mm* at outlet	462,600
Medium	150	0.05 *mm* at exit; 50 *mm* at outlet	642,600
Medium-fine	120; 80	0.05 *mm* at exit; 0.5 *mm* at 2 D_{eq}; 50 *mm* at outlet	822,600
Fine	250	0.05 *mm* at exit; 55 *mm* at outlet	1,002,600

The centreline velocity decay results obtained for each simulation, run at *NPR* 1.05 is given in Figure 5.4. It has to be noted here that the simulations had not yet been validated. The ideal conditions of ambient pressure set at 1013.25 *mbar* and ambient temperature set at 300 *K*, that the *AR*4 simulations were expected to run at, were used with these simulations. It can be seen from Figure 5.4 that the medium grid was able to resolve the centreline velocity almost as well as the finest mesh. Consequently, all further simulations were done using this mesh density for the exterior domain.

In addition to this, care was also taken to ensure that the grid matching at the interface inside the nozzle (see Figure 3.9) did not introduce any errors into the simulation. This was accomplished by keeping the same minimum cell height of the cells closest to the wall, along the symmetry boundaries, on both sides of the interface. Figure 5.5 shows the velocity profiles at two locations, 0.5 *mm* on either side of the interface, along the width and height at the symmetry planes. The velocity profiles along both axes show an extremely close match, indicating that the velocity development through the nozzle is unaffected by the grid interface.

5.1.2 Validation

The validation of the *CFD* simulation was based on various criteria such as exit velocity profile, centreline velocity decay and spreading of the jet ascertained on the development of streamwise velocity contours downstream of the nozzle exit.

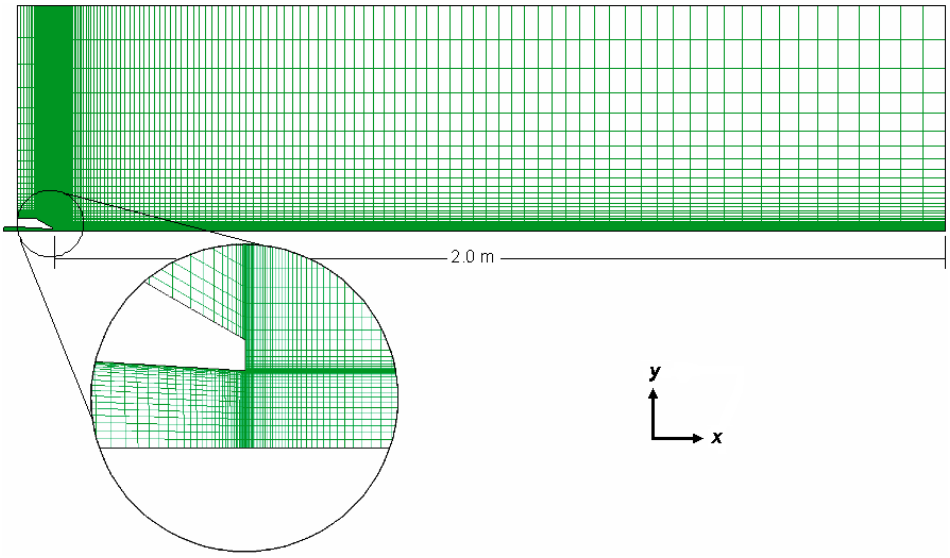

(a) Along the *xy* symmetry plane

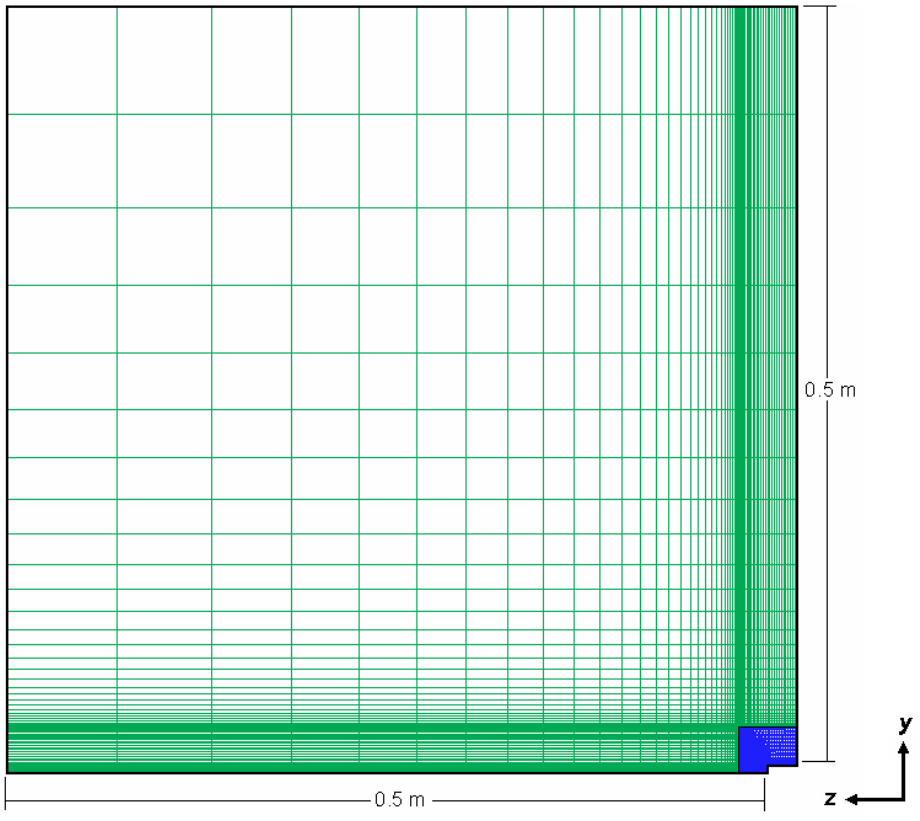

(b) Along the spanwise direction, at the free inlet boundary

Figure 5.2: Mesh distribution and extents of the AR4 simulation domain (medium grid)

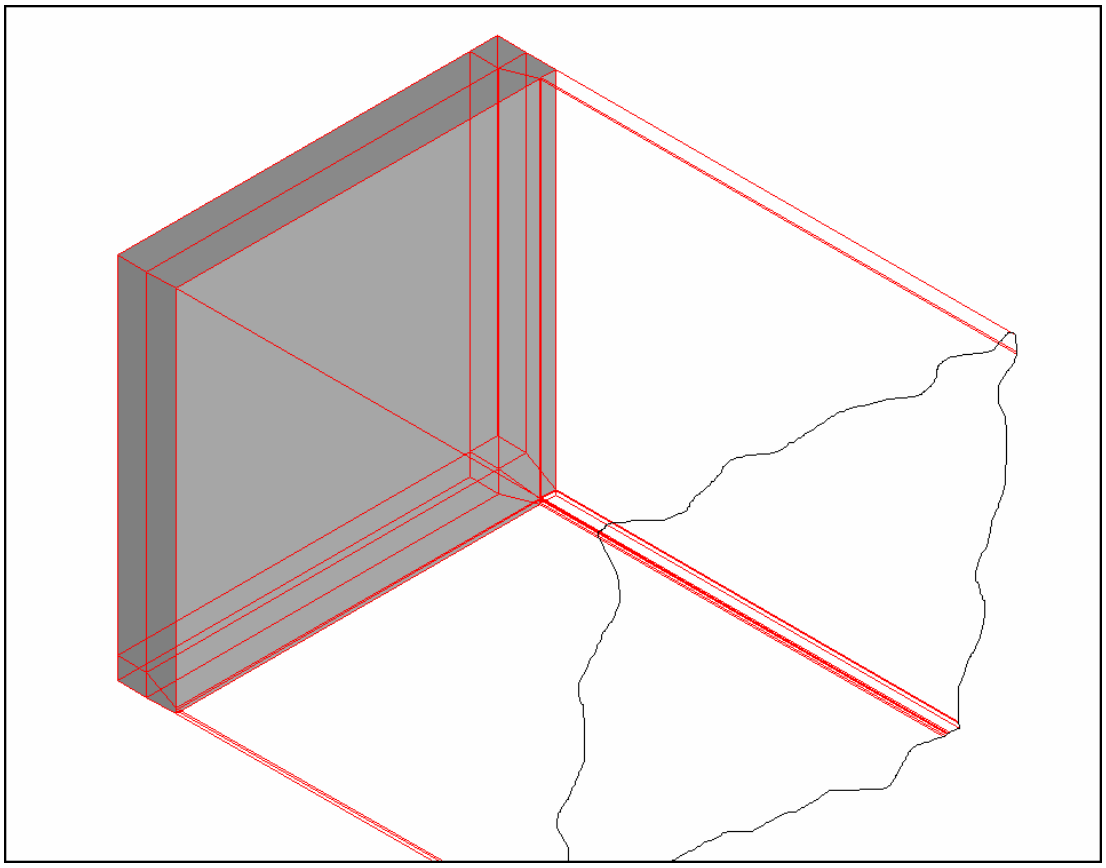

Figure 5.3: AR4 simulation domain (partial) showing the region outside the nozzle, upstream of the exit (shaded in grey colour)

The medium mesh selected on the basis of grid independence study was used for validation purposes. The procedure used for carrying out the experiments was partially explained in Section 4.2.1.3. As mentioned in that section, a detailed explanation about the measurements, results and their analyses has been provided in Appendix A with the relevant analyses presented here for the validation of the *CFD* simulations. For all the analyses provided henceforth in this section, averaged data from the experiments have been used for validation.

Figure 5.6 shows the normalised velocity profile at the nozzle exit. The simulation results match extremely well with the experimental data, within the limitations of the experiments. The same, however, cannot be said convincingly about the centreline velocity decay (Figure 5.7). The experimental data used for the centreline velocity decay comparison corresponds to the measurements done at 0° nozzle orientation (i.e. major axis horizontal). This was considered to be the

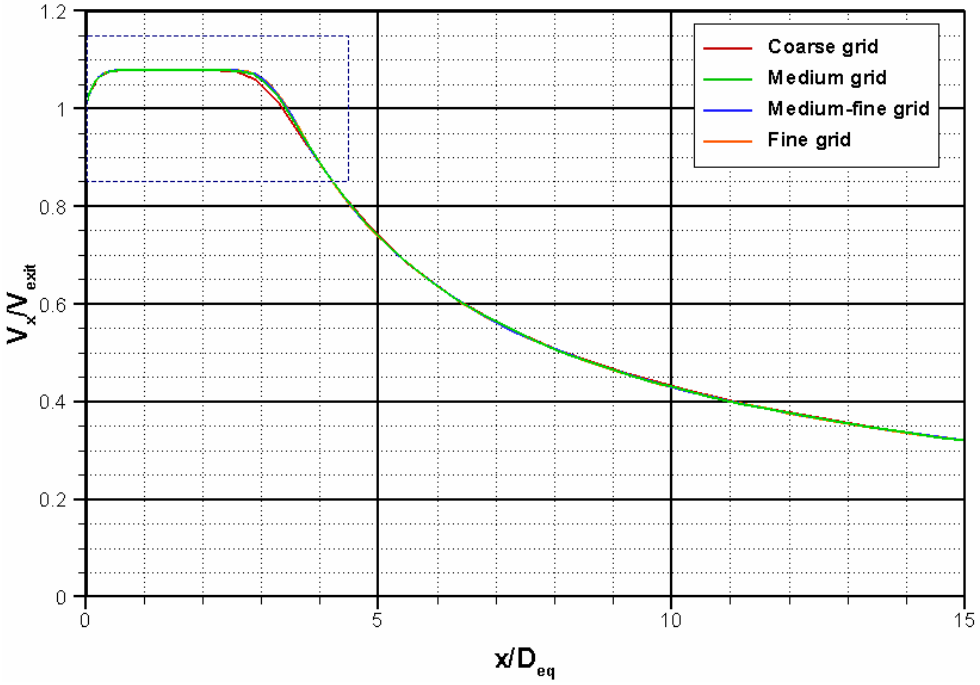

(a) Up to 15 D_{eq} downstream of the exit

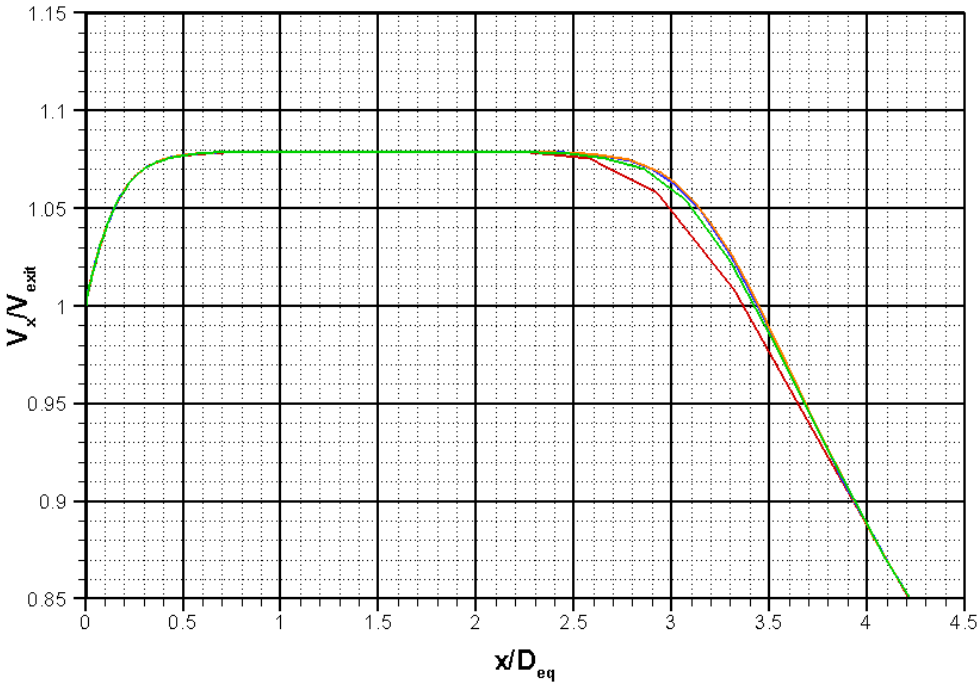

(b) Zoomed-in view of the region marked in (*a*)

Figure 5.4: Centreline velocity decay comparison for grid independence study of domains with different mesh densities

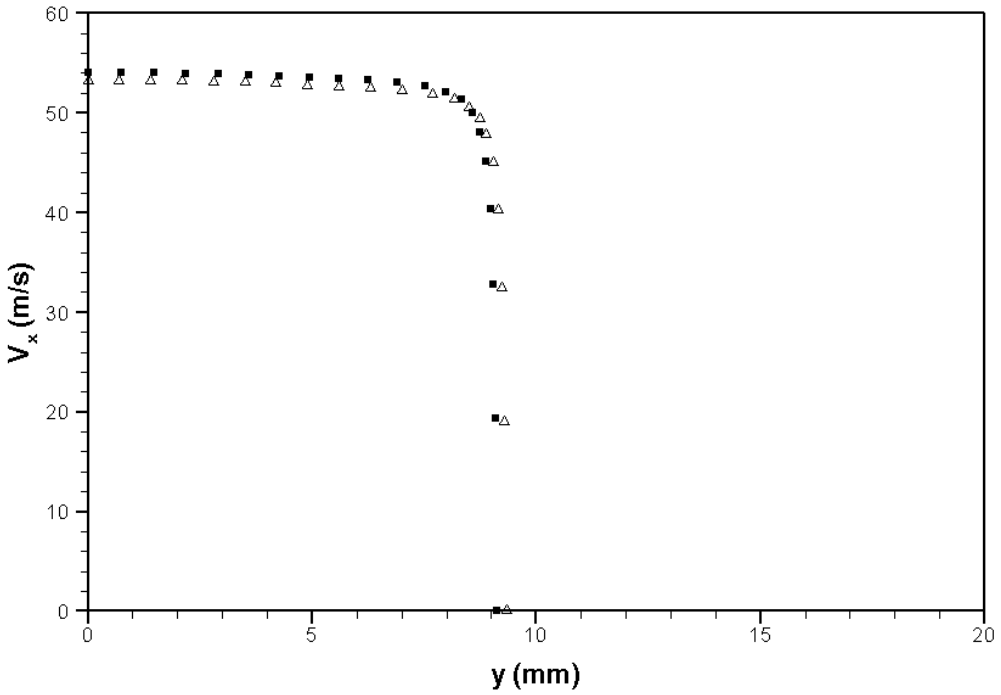

(a) Along the direction of $y-$axis

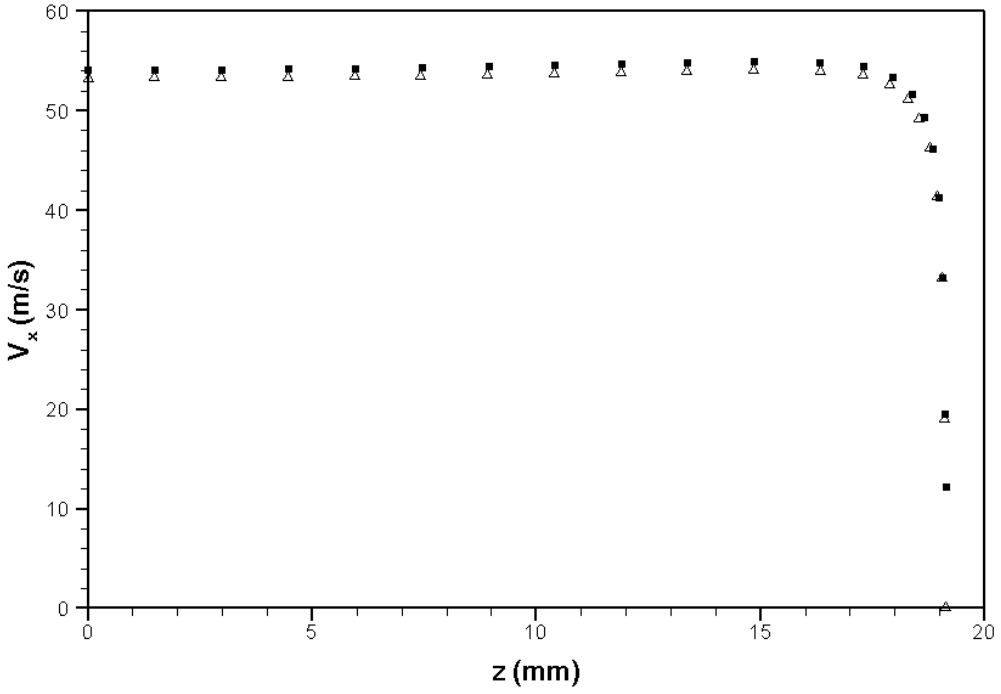

(b) Along the direction of $z-$axis

Figure 5.5: Velocity profile matching at the grid interface, 0.5 mm on either side of the interface; △, upstream of the interface; ■, downstream of the interface

basic configuration, with the whole setup being aligned with respect to this. It can clearly be seen that the simulation data initially show a very good match with the *LDA* data, capturing the flow acceleration at the exit. The potential core region, however, is significantly longer in case of the simulations (≈3.5 D_{eq}) compared to the *LDA* results (≈2.5 D_{eq}). Further downstream (after about $6D_{eq}$), the velocity decay seems to match the experiments well.

The individual points in the flow-field at which the measurements were taken by the *LDA* are shown in Figure 5.8, along with the measured normalised streamwise velocity at the respective points. It can clearly be seen that, for corresponding points on either side of the centreline, the velocity magnitudes are greater on the negative side (lower side of the centreline). These measurements were then averaged and imported into Tecplot. Rectangular regions were created with a grid density of 80 cells per equivalent diameter so that the data from the individual planes could then be interpolated for comparison with the data obtained using *CFD* (details in Appendix A). This comparison is provided in Figure 5.9. The two data sets show a very close match, especially along the major and minor axes where the spread of the jet is similar for both the *CFD* and *LDA* results[8].

The comparison of the results presented in the current section indicate a very good match between the *LDA* experiment and the *CFD* simulation. The only exception to this was the length of the potential core. From the detailed discussion of the experimental procedure and results, presented in Appendix A, we can conclude that the geometric centreline of the nozzle (which was used to align the traverse and hence the *LDA* probe) and the aerodynamic centreline of the jet issuing from it, were not coincident. Indeed, the velocity profiles obtained at the various planes downstream of the exit indicate that the maximum velocity was observed at a position vertically lower than the centreline. This observation was noticed for all seven configurations (due to rotation) of the nozzle, the reasons for which are discussed in Appendix A. It can, therefore, be inferred that the experiment used for validation by itself was not completely ideal. However, the results pertaining to velocity profiles and boundary layer development at the exit, flow acceleration after the exit and the far-field velocity decay are able to provide reasonable data for comparing the overall jet development.

[8]It is to be noted that the experimental data are most reliable at these positions because of the relative orientations of the *LDA* measurement volume and the jet shear layer.

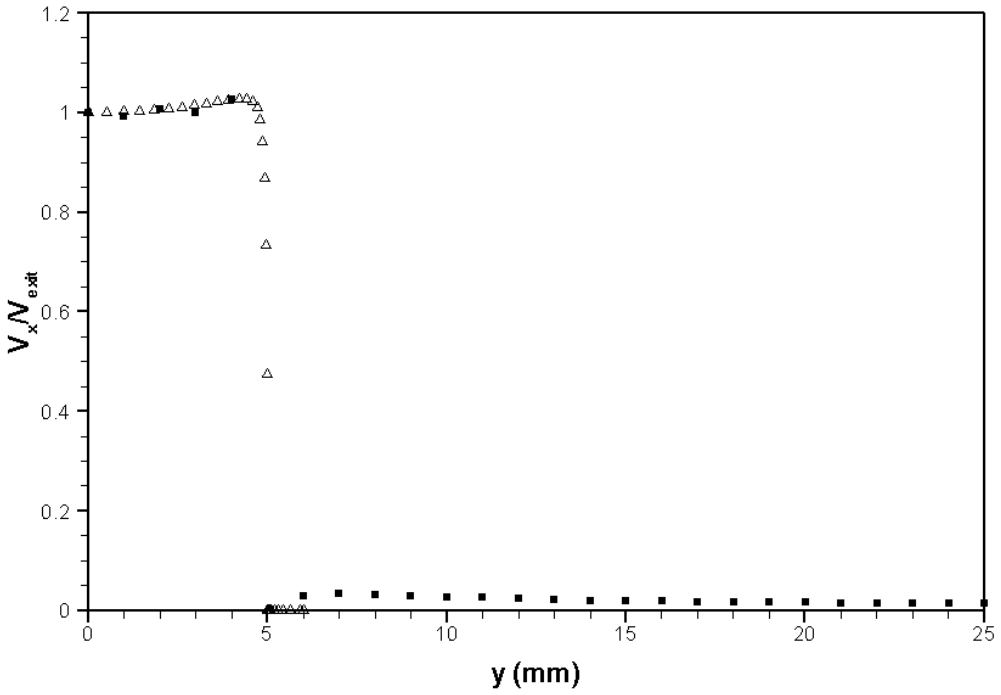

(a) Along the minor axis

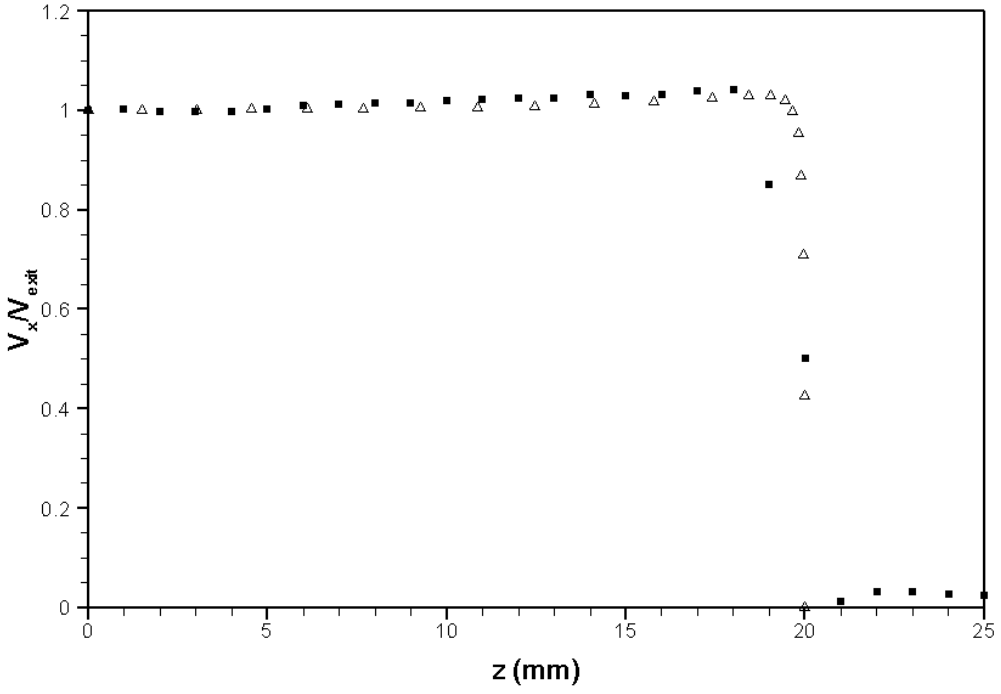

(b) Along the major axis

Figure 5.6: Normalised velocity profile at the AR4 nozzle exit; ■, experimental results using LDA; △, CFD simulation results

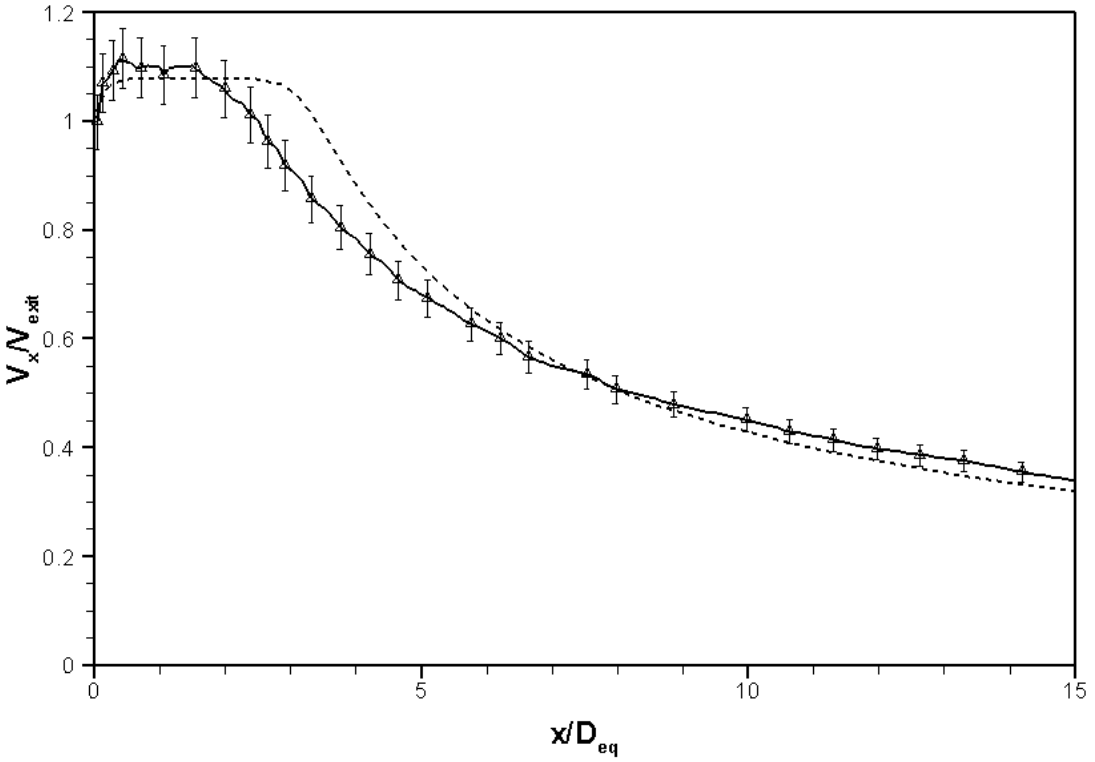

Figure 5.7: Centreline velocity decay comparison for validation of CFD; − − −, simulation results; —△—, experimental results; the error bars are set at 5% representing the uncertainty of LDA measurements

Consequently, all the tests done with regards to domain meshing, turbulence model selection, grid independence and validation were considered to be successfully completed. The *CFD* simulations could now be carried out for the various AR_i and *CSR* configurations and the results, thus obtained, could now be accepted with confidence to provide an indication towards the actual behaviour of the flow issuing from these nozzle configurations.

5.2 Rectangular Nozzle CFD Results

Following the validation of the *AR*4 simulation (*EA*1*C*2 configuration), the other simulations were initialised and iterated with the required variation of AR_i and *CSR* incorporated. The results and discussions pertaining to each of the *E*− and *R*−series are given in the following sections.

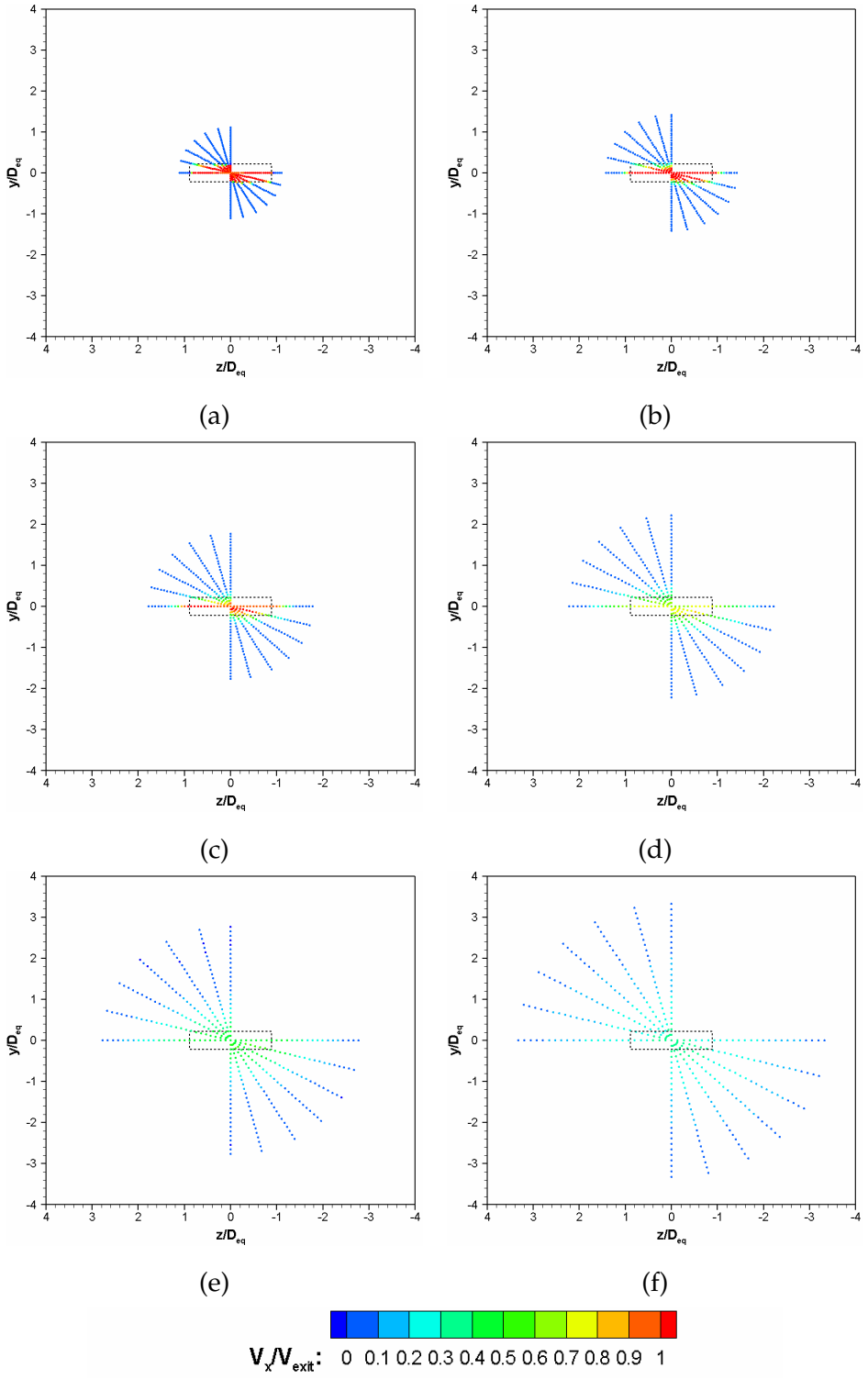

Figure 5.8: Scatter plots indicating measurement points in the flow-field for nozzle exit and five planes parallel to the exit: (a) At nozzle exit; (b) At 1 D_{eq}; (c) At 2 D_{eq}; (d) At 4 D_{eq}; (e) At 8 D_{eq}; (f) At 16 D_{eq}

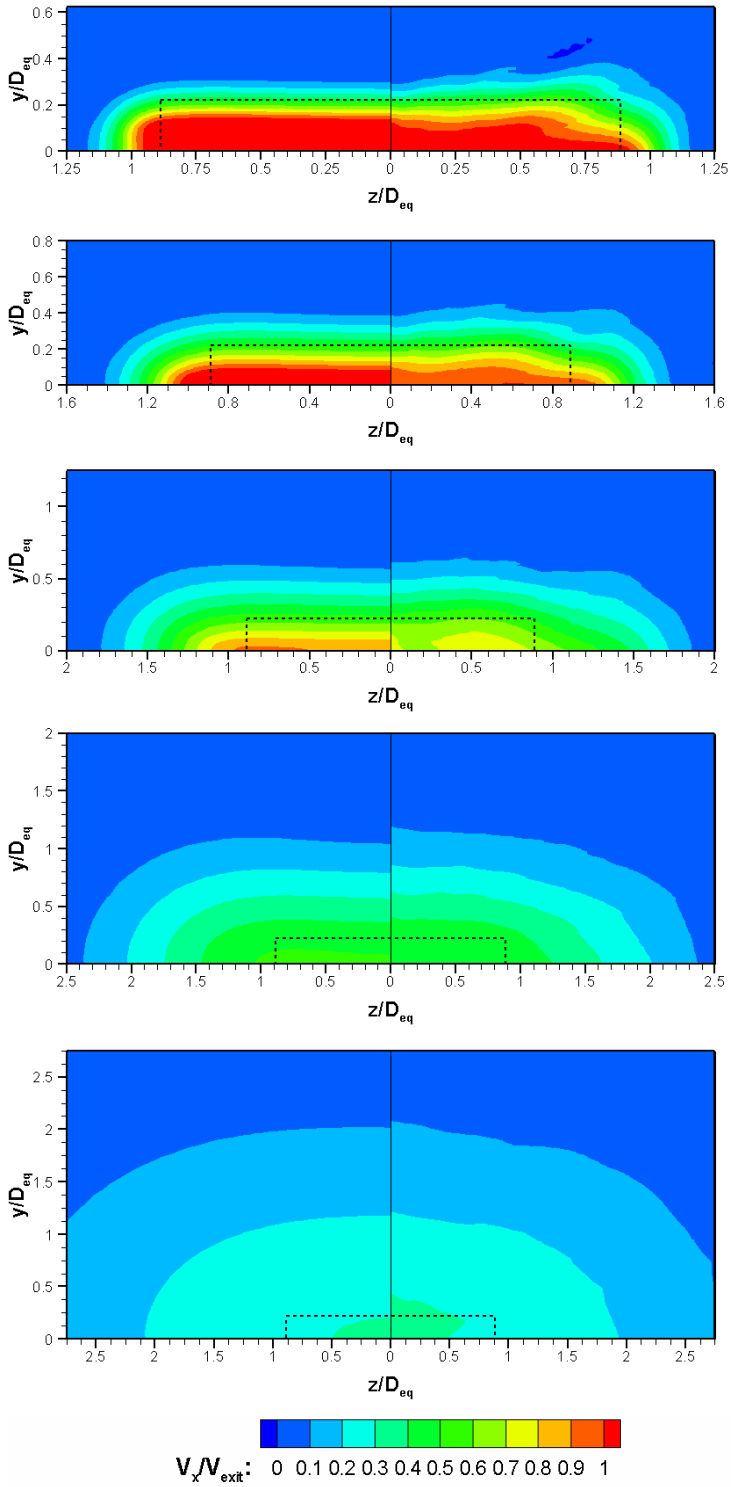

Figure 5.9: Comparison of normalised streamwise velocity contours (V_x/V_{exit}) at planes downstream of the exit; from top to bottom*, at 1, 2, 4, 8 and 16 D_{eq}; (left), CFD simulation results; (right), LDA experiment results; the dotted outline indicates the dimensions of the nozzle exit*

5.2.1 Exit velocity (V_{exit})

Since all the simulations were run at identical initial conditions, the maximum velocity achieved by the jet at the centreline was ≈91.130 m/s, corresponding to $M_j = 0.265$. Due to flow acceleration after the nozzle exit, however, the centreline velocity at the exit of the nozzle (V_{exit}) was different for each configuration.

The $E-$series nozzles correspond to the configurations with elliptic inlets of aspect ratios ranging from 1 to 4 in steps of one. However, the variation in the inlet aspect ratio (AR_i) and the length of the converging section (CSR) affect the exit velocity of the jet. This variation is shown in Figure 5.10. Clearly, from the figure, it can be seen that this particular variation of V_{exit} is not linear with respect to either AR_i or CSR; the exit velocity increases with an increase in the inlet aspect ratio and the converging section length.

The $R-$series nozzles are similar to the $E-$series for their variations with the obvious change being that the inlets are rectangular. Again, the maximum jet velocity at the centreline was ≈91.112 m/s, with the exit velocity of the jet varying for different configurations of AR_i and CSR. Although the exit velocities were higher for the corresponding configuration of the $R-$series compared to the $E-$series, the general trends were very similar (Figure 5.11).

5.2.2 Half-velocity-widths

One of the primary ideas behind study and comparison of the various configurations was to understand if the given configuration indicates axis-switching, or not. In the case of axis-switching, it was important to find the location of the cross-over point—the downstream location where the spread of the jet along the spanwise axes is equal. For configurations that do not exhibit axis-switching, the approximate location of the point where the jet indicates transition to a round cross-section or where the spreading rates along the spanwise axes become roughly equal, had to be determined. One indicator that is popularly used for this purpose is the jet half-velocity-width (B). This is defined as twice the distance from the centreline of the jet to where the local streamwise velocity is equal to half of the local centreline streamwise velocity. It is generally normalised using the equivalent exit diameter of the nozzle (D_{eq}).

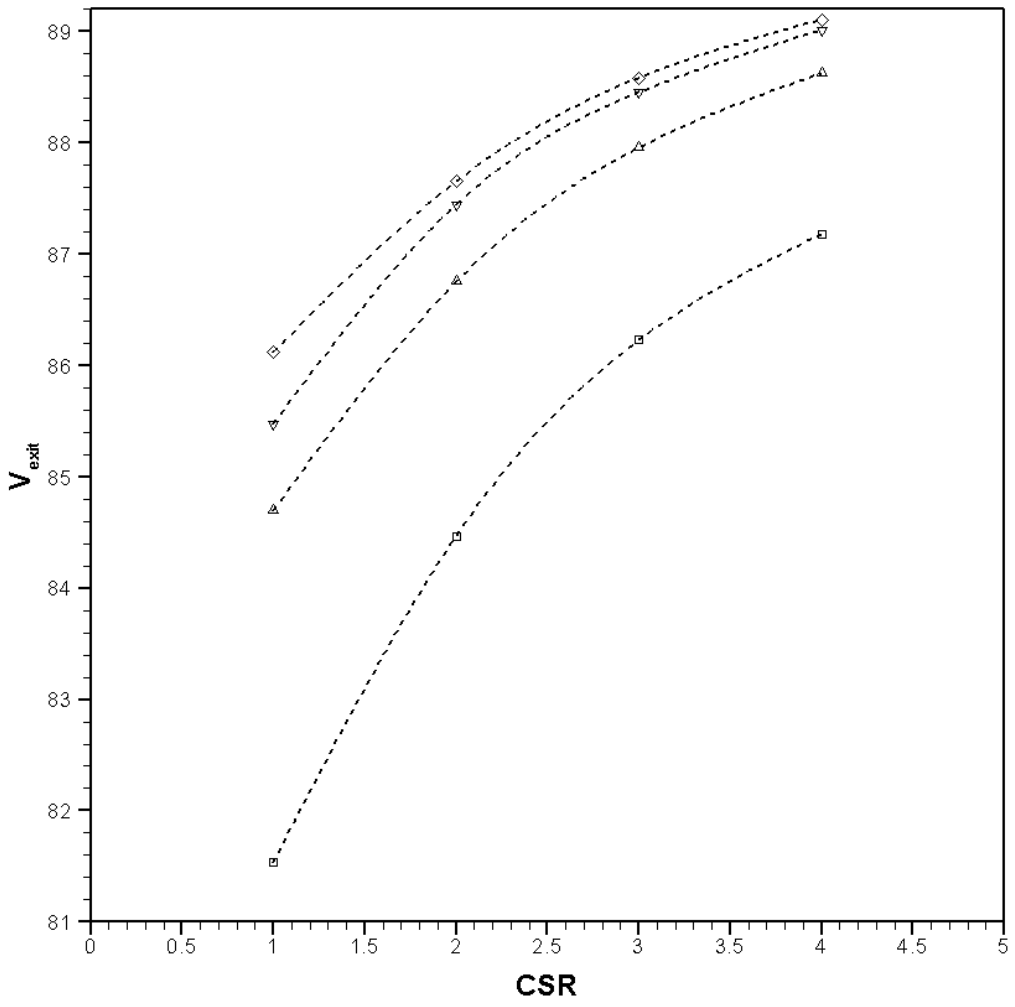

Figure 5.10: V_{exit} variation with respect to the converging section length (CSR) for the E−series nozzles; the individual lines indicate variation for different inlet aspect ratios (AR_i); − − □ − −, AR_i = 1; − − △ − −, AR_i = 2; − − ▽ − −, AR_i = 3; − − ◇ − −, AR_i = 4

Since the concept of the project was inspired by potential issues with the roll-post ducts of the *F-35 Lightning II (JSF)*, the extent of region of interest was considered to be up to 30 equivalent diameters downstream of the nozzle exit. Consequently, the half-velocity-width plots for the current study are generated up to 30 D_{eq} from the exit. The half-velocity-width plots corresponding to the *E*− and *R*−series are provided in Figures 5.12 and 5.13, respectively.

It is clear from the jet half-velocity-width variations for both the *E*− and *R*−series that the axes do not switch within 30 D_{eq} from the nozzle exit for simu-

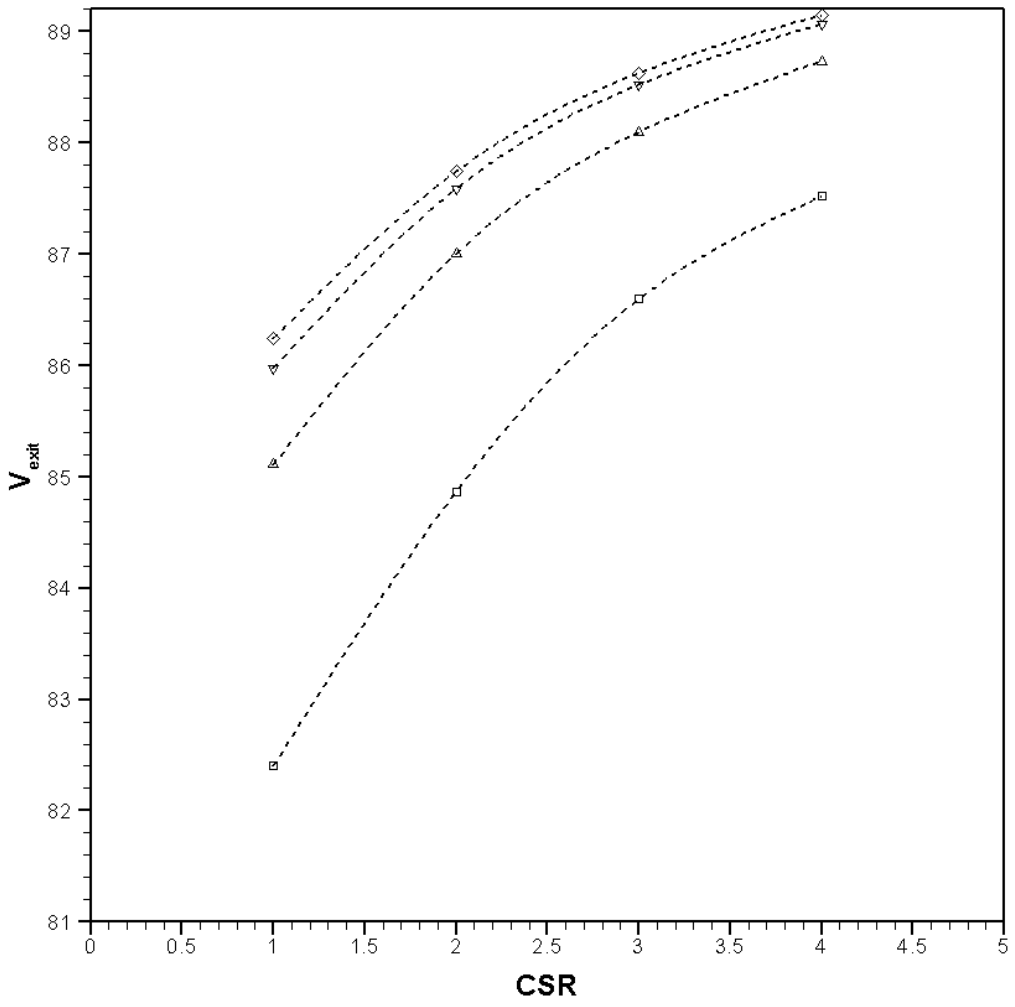

Figure 5.11: V_{exit} variation with respect to the converging section length (CSR) for the R−series nozzles; the individual lines indicate variation for different inlet aspect ratios (AR_i); – – □ – –, AR_i = 1; – – △ – –, AR_i = 2; – – ▽ – –, AR_i = 3; – – ◇ – –, AR_i = 4

lations with $AR_i = 1$. These simulations were therefore analysed further downstream to determine the location where the jet spreading assumes axisymmetry or where the spreading rates become approximately equal in the spanwise directions. These results are shown in Figures 5.14 and 5.15. The jet half-velocity-widths are shown in the left column of these figures. The blue vertical line indicates the approximate downstream location where the jet assumes axisymmetry or equal spreading rates. The corresponding velocity contours are obtained by normalising the local streamwise velocity with the local centreline streamwise velocity. These are displayed in the right column of the corresponding figures.

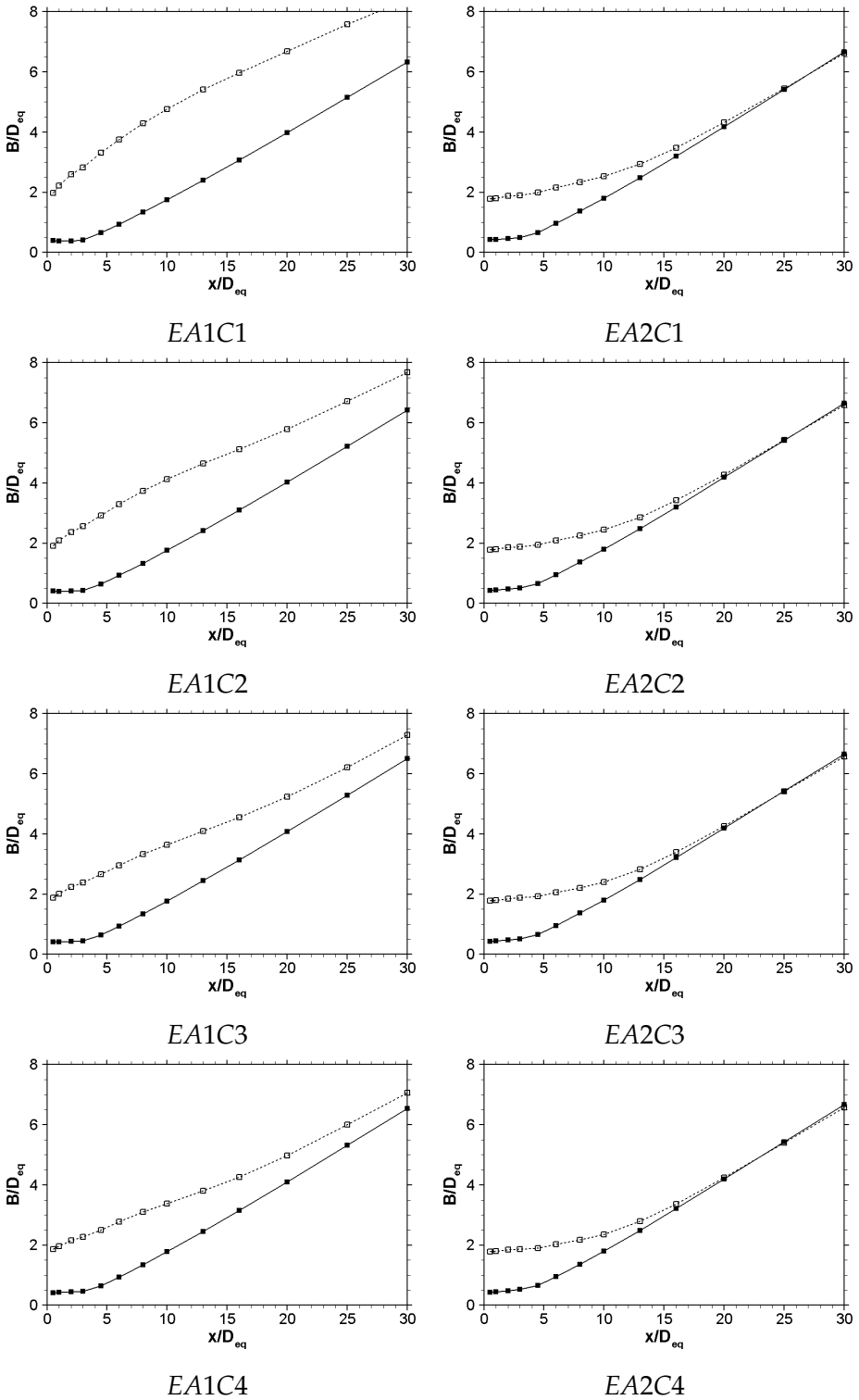

Figure 5.12: Streamwise variation of jet half-velocity-width for E−series: —■—, B_y/D_{eq}; – – □ – –, B_z/D_{eq}

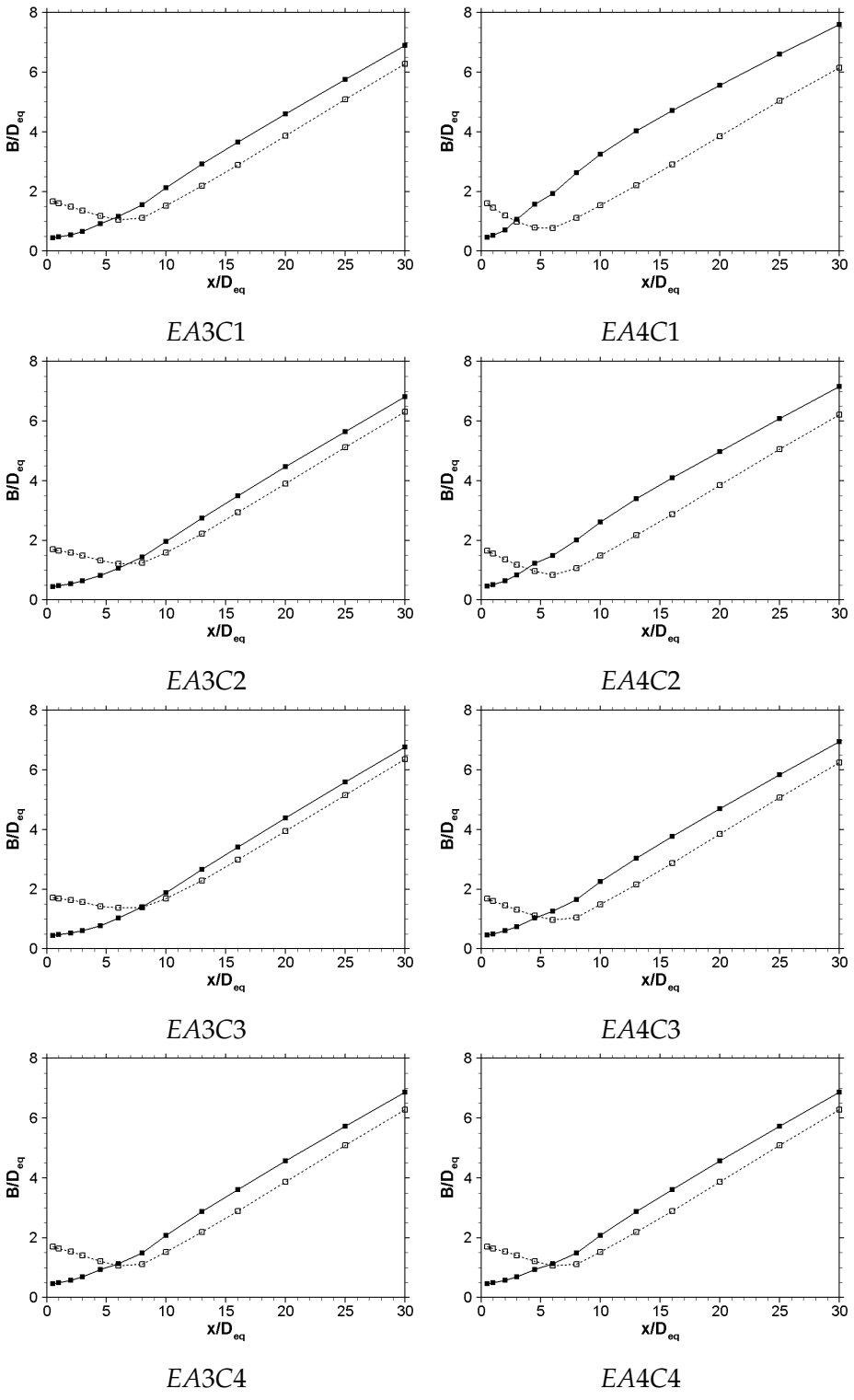

Figure 5.12: Continued

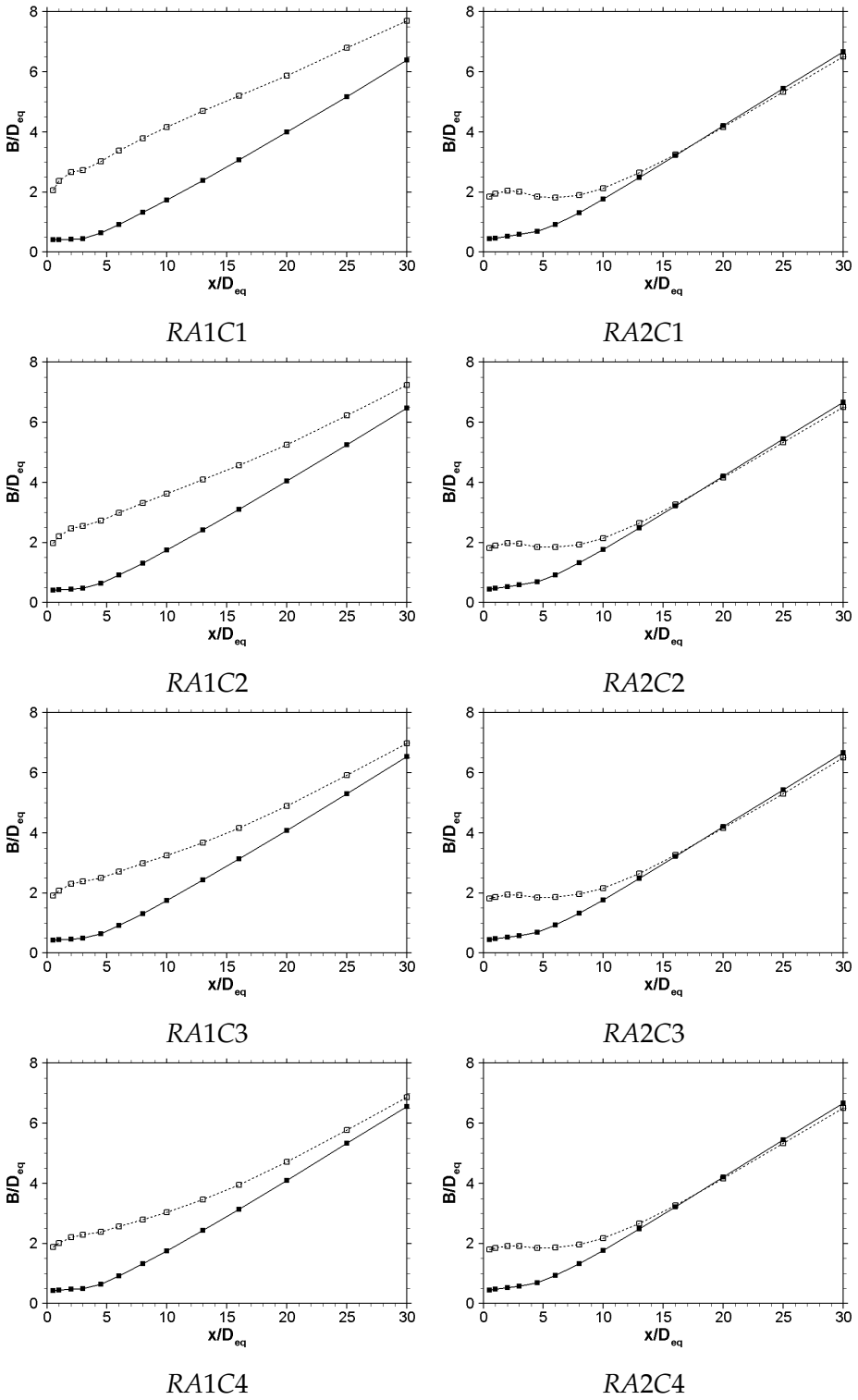

Figure 5.13: Streamwise variation of jet half-velocity-width for E−series: —■—, B_y/D_{eq}; − − □ − −, B_z/D_{eq}

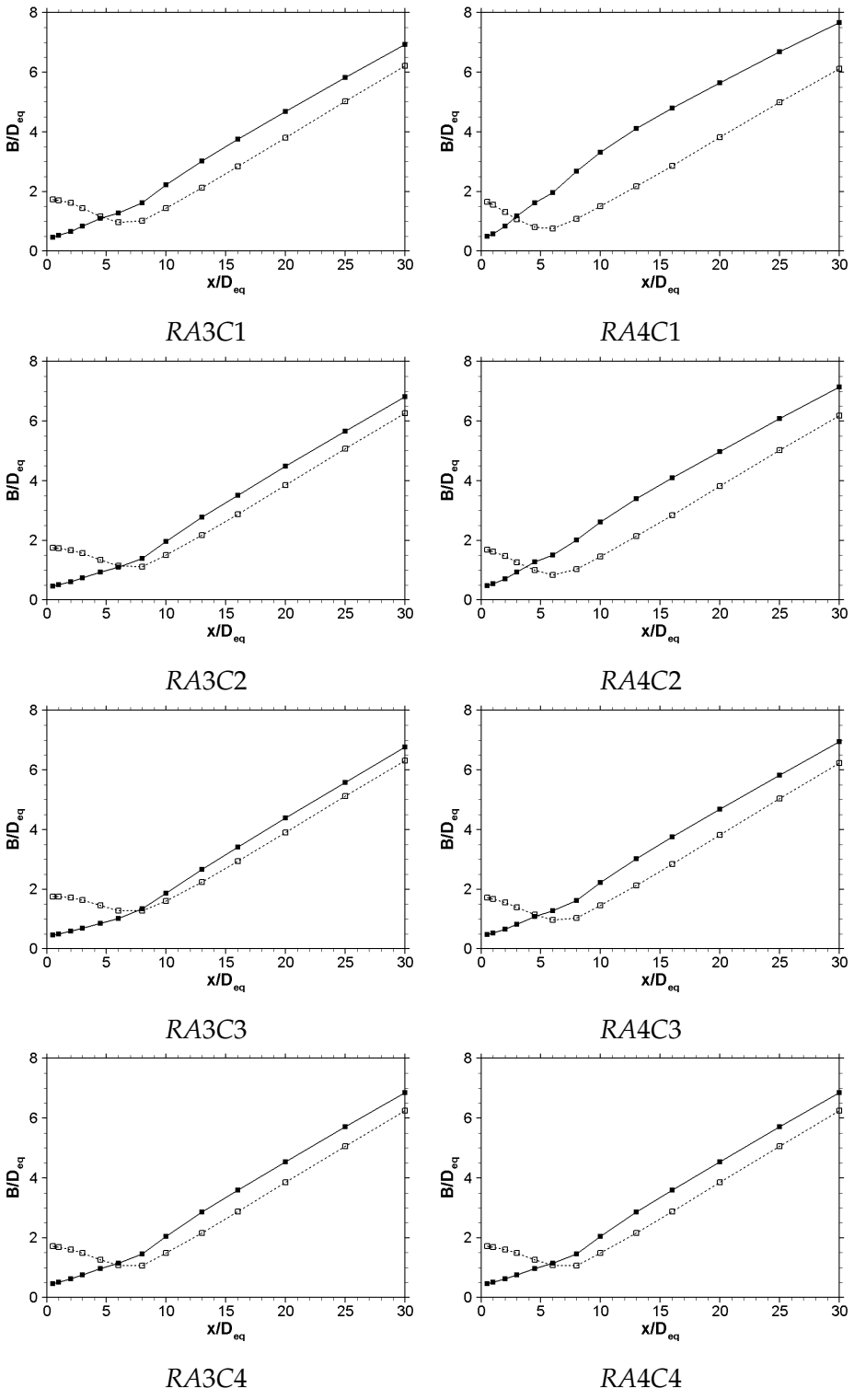

Figure 5.13: Continued

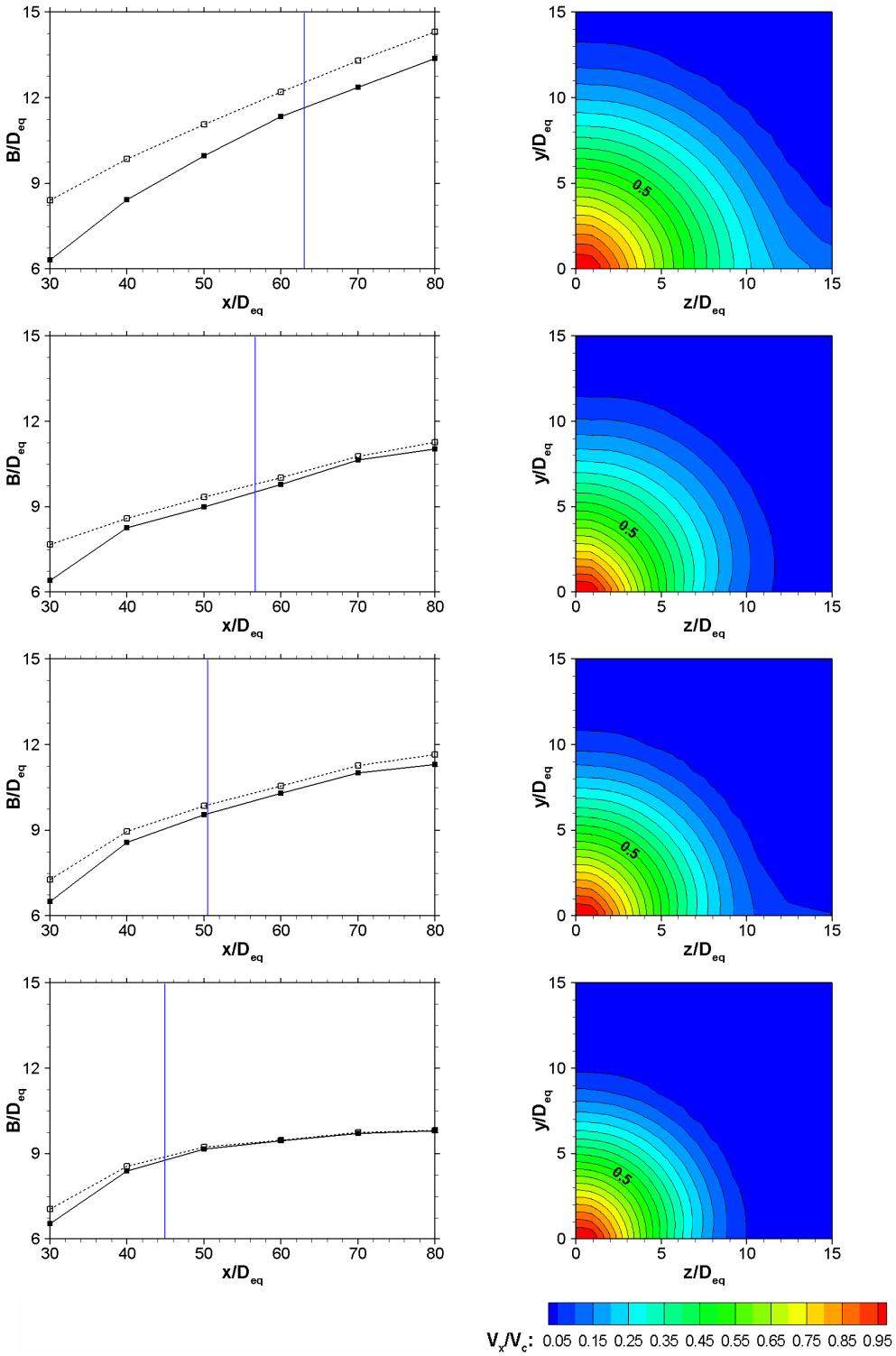

Figure 5.14: Extended plots for streamwise variation of jet half-velocity-width for E−series (left): —■—, B_y/D_{eq}; − − □ − −, B_z/D_{eq}; normalised velocity contours at the location indicated by the vertical blue line on the extended plots (right); from top to bottom, EA1C1, EA1C2, EA1C3, EA1C4

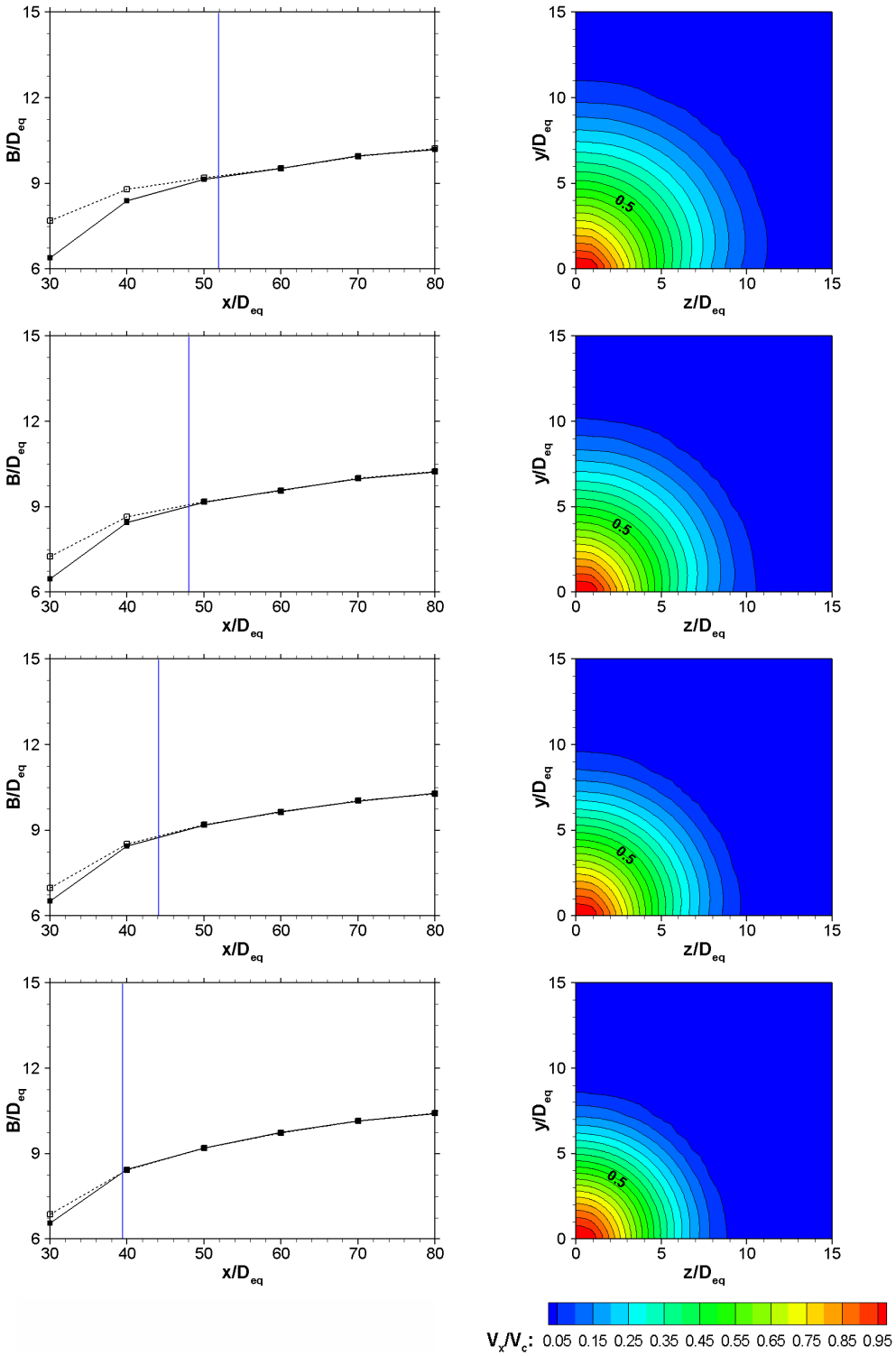

Figure 5.15: Extended plots for streamwise variation of jet half-velocity-width for R−series (left): —■—, B_y/D_{eq}; − − □ − −, B_z/D_{eq}; normalised velocity contours at the location indicated by the vertical blue line on the extended plots (right); from top to bottom, RA1C1, RA1C2, RA1C3, RA1C4

The jets with circular inlets show transition to an elliptic jet spreading with approximately equal rate of spreading along the major and minor axes; the eccentricity of the elliptic spreading reducing with an increase in the length of the converging section. For the jets with square inlets, on the other hand, the jet assumes an axisymmetric cross-section at some downstream location and continues further without undergoing any additional axis-switching.

The locations of the cross-over (or transition, in case of the $A1$ configurations) points were noted for both series. In the case of the configurations with inlet aspect ratio of 1, the information corresponded to the location where the jet exhibits approximately equal spreading rates. These data are presented in Tables 5.2 and 5.3. Additionally, the difference between the jet-widths along the major and minor axes, at a distance of 30 D_{eq} downstream of the exit (ΔB_{30}) was also recorded and used as the other parameter to identify axis-switching. The data for these are presented in Tables 5.4 and 5.5.

Table 5.2: Location of cross-over point (X_c) for $E-$series, normalised using D_{eq}

$C \backslash A$	**1**	**2**	**3**	**4**
1	62.8851	27.4395	5.5478	2.8705
2	56.6425	25.5563	6.8772	3.8284
3	50.6883	24.0450	7.9894	4.8271
4	45.1857	22.1871	9.0704	5.7174

Table 5.3: Location of cross-over point (X_c) for $R-$series, normalised using D_{eq}

$C \backslash A$	**1**	**2**	**3**	**4**
1	51.8169	17.5091	4.7780	2.7942
2	48.0521	17.7100	6.2531	3.7933
3	44.1317	17.9032	7.5502	4.7911
4	39.6184	18.0566	8.4929	5.6953

Table 5.4: Difference between the jet-widths along the major and minor axes at 30 D_{eq} downstream of the exit (ΔB_{30}) for E−series, normalised using D_{eq}

$C \backslash A$	1	2	3	4
1	2.0823	-0.0454	-0.6188	-1.4391
2	1.2544	-0.0655	-0.5047	-0.9467
3	0.7820	-0.0773	-0.4114	-0.7098
4	0.5174	-0.0863	-0.3582	-0.5899

Table 5.5: Difference between the jet-widths along the major and minor axes at 30 D_{eq} downstream of the exit (ΔB_{30}) for R−series, normalised using D_{eq}

$C \backslash A$	1	2	3	4
1	1.3127	-0.1642	-0.7251	-1.5479
2	0.7759	-0.1657	-0.5526	-0.9684
3	0.4496	-0.1674	-0.4613	-0.7165
4	0.3080	-0.1692	-0.3949	-0.5893

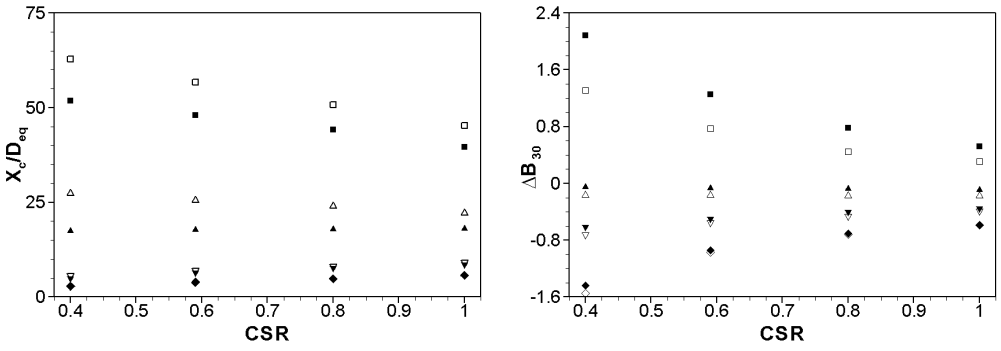

(a) X_c variation (b) ΔB_{30} variation

Figure 5.16: Graphical representation of the CFD results: − − □ − −, AR_i = 1; − − △ − −, AR_i = 2; − − ▽ − −, AR_i = 3; − − ◇ − −, AR_i = 4; open symbols indicate E−series, while closed symbols indicate R−series

The *CFD* data for X_c and ΔB_{30} variation from the Tables 5.2–5.5 are represented in Figure 5.16. The following observations are made from this figure:

- The variation of the cross-over point is within the range as expected for a nozzle with aspect ratio 4. This is based on the published data from Figure 2.7; if the region indicating variation of cross-over point is extrapolated back towards the lower aspect ratios, the values obtained from the *CFD* simulations lie within the extended region, as seen in Figure 5.17.
- For a given inlet aspect ratio, the variation of the location of the cross-over point (X_c) is roughly linear with respect to the converging section ratio; higher *CSR*, corresponds to higher X_c. The exceptions to these are the *EA*1, *EA*2 and *RA*1 configurations where higher *CSR* corresponds to lower X_c values.
- The converging section ratio remaining constant, the X_c varies inversely with respect to the inlet aspect ratio (AR_i); lower AR_i values correspond to higher X_c values.
- For any given configuration, the $R-$series indicates lower values for X_c compared to the corresponding configuration of the $E-$series.
- The variation of ΔB_{30} is non-linear with respect to both AR_i and *CSR*. Positive values of ΔB_{30} indicate that the jet has not undergone axis-switching while a negative value indicates the occurrence of axis-switching by 30 D_{eq} downstream of the exit.

These results are analysed and discussed in further detail under Sections 5.3 and 5.4, and form the basis of the current study. The following section (5.2.3 attempts to provide an understanding of the mechanisms and also to provide a sound reasoning for the unequal jet spreading observed for the nozzle configurations in this study.

5.2.3 Effects of Nozzle Geometry Variation

From the previous section (5.2.2), it can clearly be established that a change in nozzle geometry affects the development of the free jet, especially the unequal

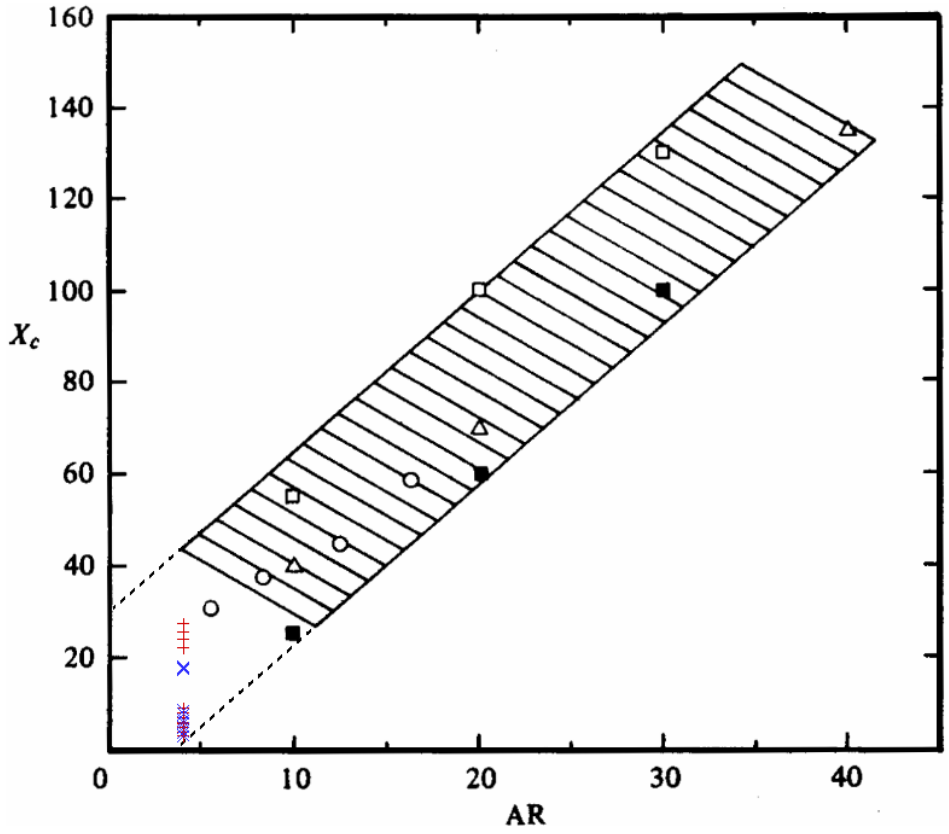

Figure 5.17: Validation of cross-over point locations obtained using CFD data; the data from Figure 2.7 is extrapolated back towards the lower aspect ratios; +: E−series; ×: R−series

spreading rates that may or may not result in axis-switching. The unequal spreading rates may be due to the presence of secondary flows through the nozzle, which arise due to the change in the geometry. An explanation is provided in this section for understanding the development of the secondary flows. The trends observed for variation in either the AR_i or CSR, keeping the other parameter constant, are described here using the $A3$ and $C2$ sets for both the series. Similar plots for all the other configurations are provided in Appendix D.

5.2.3.1 Pressure and Velocity Distribution

The normalised static pressure distribution (P_s/P_a) and the resultant vectors of spanwise velocities (V_y/V_{exit} and V_z/V_{exit}) at the nozzle exit are shown in Figures 5.18 and 5.19.

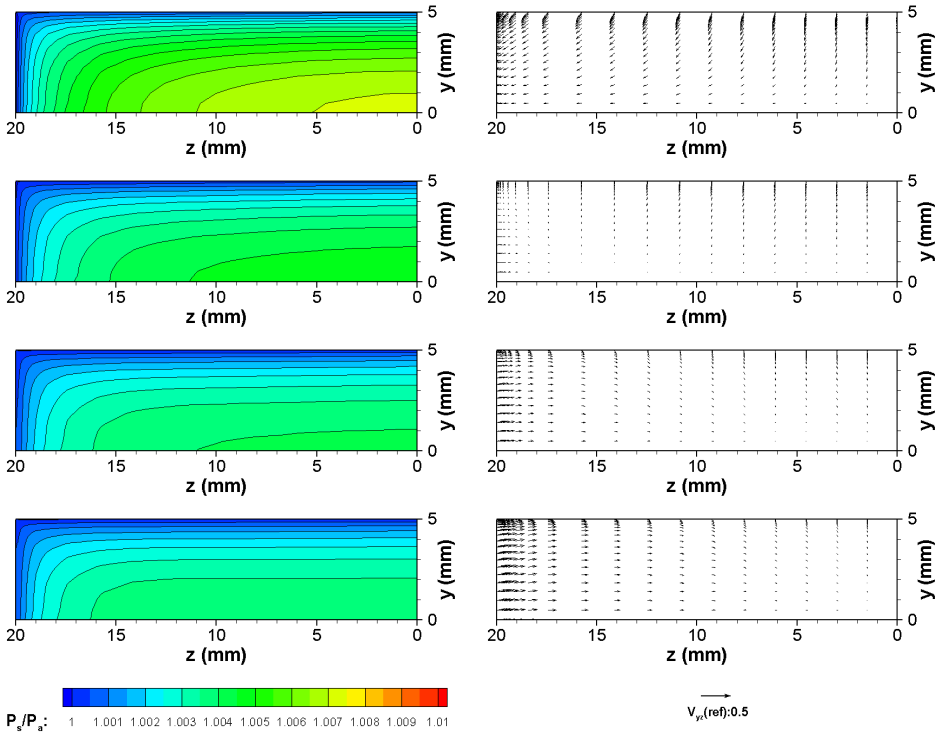

(a) CSR constant; from top to bottom, AR_i = 1, 2, 3, 4

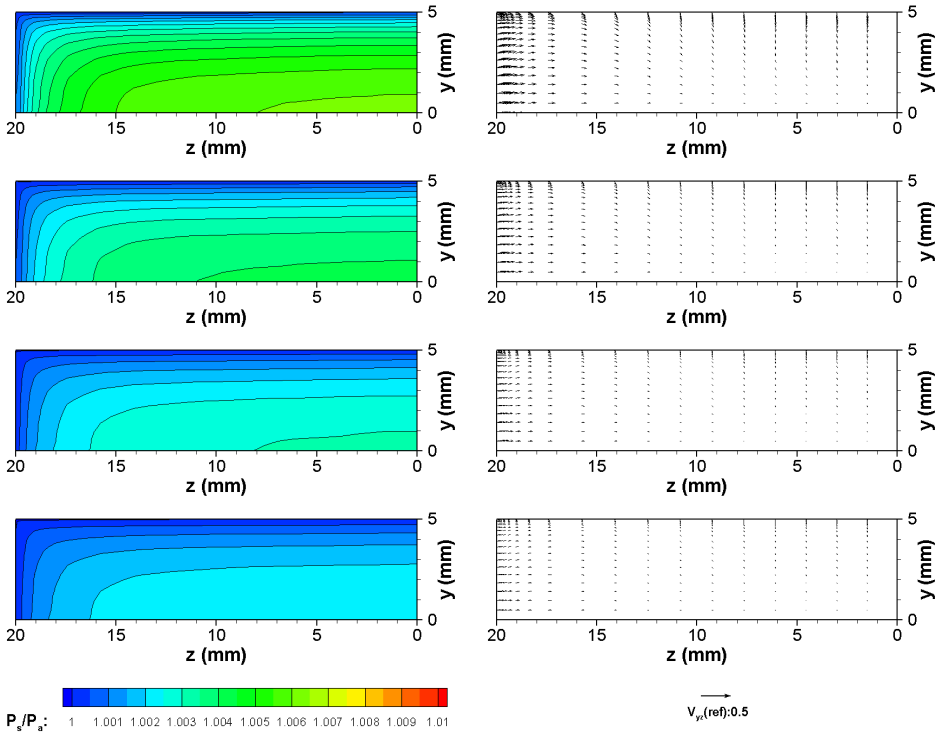

(b) AR_i constant; from top to bottom, CSR = 1, 2, 3, 4

Figure 5.18: Contours of normalised static pressure, P_s/P_a (left) and resultant vectors of normalised spanwise velocities, V_y/V_{exit} and V_z/V_{exit} (right) at the nozzle exit (E−series)

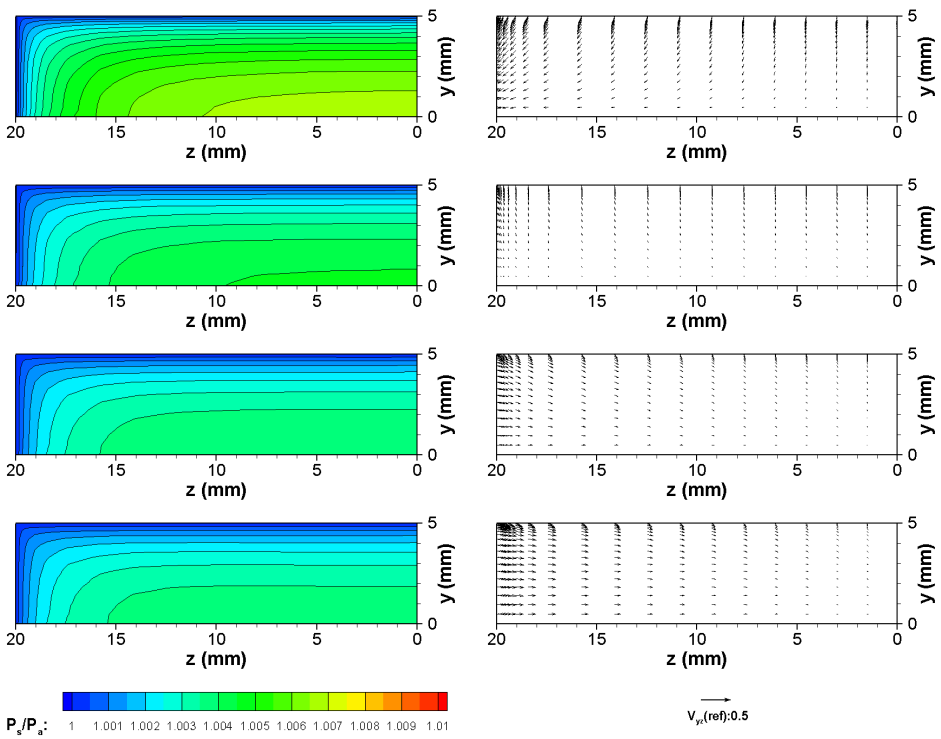

(a) *CSR* constant; from top to bottom, AR_i = 1, 2, 3, 4

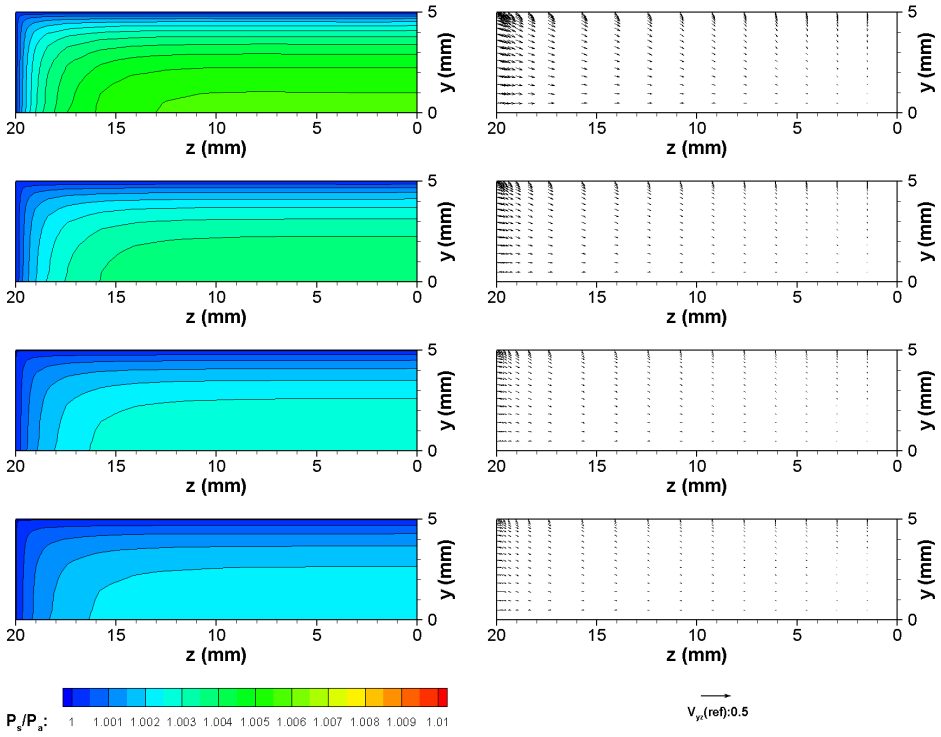

(b) AR_i constant; from top to bottom, *CSR* = 1, 2, 3, 4

Figure 5.19: Contours of normalised static pressure, P_s/P_a (left) and resultant vectors of normalised spanwise velocities, V_y/V_{exit} and V_z/V_{exit} (right) at the nozzle exit (R−series)

The most visible difference seen from Figures 5.18 and 5.19 is the maximum pressure at the centre of the nozzle exit; the configurations with $CSR = 1$ have a higher magnitude and this decreases with an increase in the CSR value. Clearly, the length of the contraction section determines the magnitude of the pressure. The AR_i variation, on the other hand, affects the pressure distribution. The shorter sides show lower pressure compared to the longer sides for $AR_i = 1$ and 2, the difference being less in case of the latter. As the AR_i increases, the pressure on the shorter side increases while along the longer sides decreases; $AR_i = 3$ and 4 show higher pressure along the shorter side compared to the longer side. This is to be expected under consideration of streamline curvature; the direction of the velocity vectors shown in Figures 5.18 and 5.19 are also influenced by this. Since the flow direction is essentially governed by the associated nozzle wall shape, the resultant of the spanwise velocities indicate the directions of the streamlines generated by the flow through the nozzle. Figure 5.20 shows the nozzle configurations as seen from the front, based on their inlet aspect ratios. For cases involving the $AR_i = 1$ configurations, the short walls diverge from the initial geometry during transition. Consequently, the flow direction along the major axis is away from the centre towards the short walls. For the other AR_i configurations, the nozzle converges along all the sides. Thus the velocity vectors indicate flow in the plane towards the centre of the nozzle. Again, the length of the converging section determines the magnitude of the velocity vectors; the magnitude of the vectors is higher for a shorter length of the contraction section.

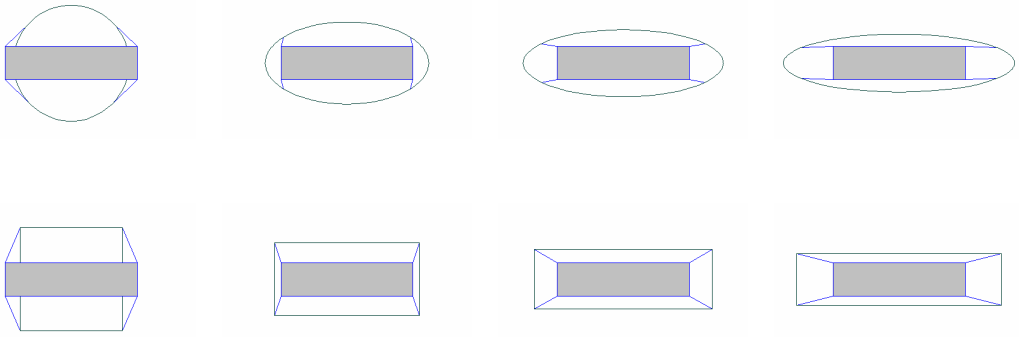

Figure 5.20: Front view of the configurations based on different inlet aspect ratios: Elliptic inlets (top), and Rectangular inlets (bottom); from left to right, AR_i =1, 2, 3, 4; the shaded area indicates nozzle exit

5.2.3.2 Streamwise Vorticity Distribution

This change in the nozzle cross-sectional geometry is responsible for the generation of the secondary flows. These secondary flows essentially affect the vorticity distribution inside the nozzle. The development of the vorticities inside the nozzle, indicating the origins of vorticity structures, are shown in Figure 5.21. Two normalised streamwise vorticity ($\omega_x D_{eq}/V_{exit}$) iso-surfaces of magnitudes +0.1 and −0.1 are created. The positive vorticity iso-surfaces are shown in red colour while the negative vorticity iso-surfaces are shown in blue. The inner and outer walls of the nozzle are also shown. Since the iso-surfaces were created for the entire domain, the origins and development of these outside the nozzle are also seen. These vorticity structures outside the nozzle can be seen as a constant feature for all the internal geometry variations. As such, these cannot be neglected, but for the current study, the focus is maintained on the development of streamwise vorticity inside the nozzle.

The location and extent of the $\omega_x D_{eq}/V_{exit}$ iso-surfaces are indicative of their origins and the strength of the vortex structures in each case; clearly, for all the cases, the iso-surfaces generally extend less in the downstream direction with an increase in the *CSR* value. Primary vortex structures, both positive and negative, that can be seen at the nozzle exit, start developing near the start of the converging section for all the cases. Generally, as the length of the converging section increases, these structures also start developing further upstream of the exit and thus lose their strength earlier. There are, however, differences in the development of these structures, depending on the AR_i of the nozzle.

While the circular inlet (*EA*1) does not show the presence of any vorticity structures near the inlet, the other elliptic AR_i configurations indicate the development of a positive vorticity structure near the inlet. This is possibly formed due to the non-uniform pressure distribution along the nozzle inlet. As the flow develops downstream, the pressure gets distributed more evenly and the flow follows the contour of the nozzle.

The rectangular series, on the other hand, shows the presence of positive vorticity structure near the top wall of the inlet and negative vorticity structure near the side wall. Again, depending on the AR_i of the nozzle, these particular structures may be isolated or may combine with the structures developing due

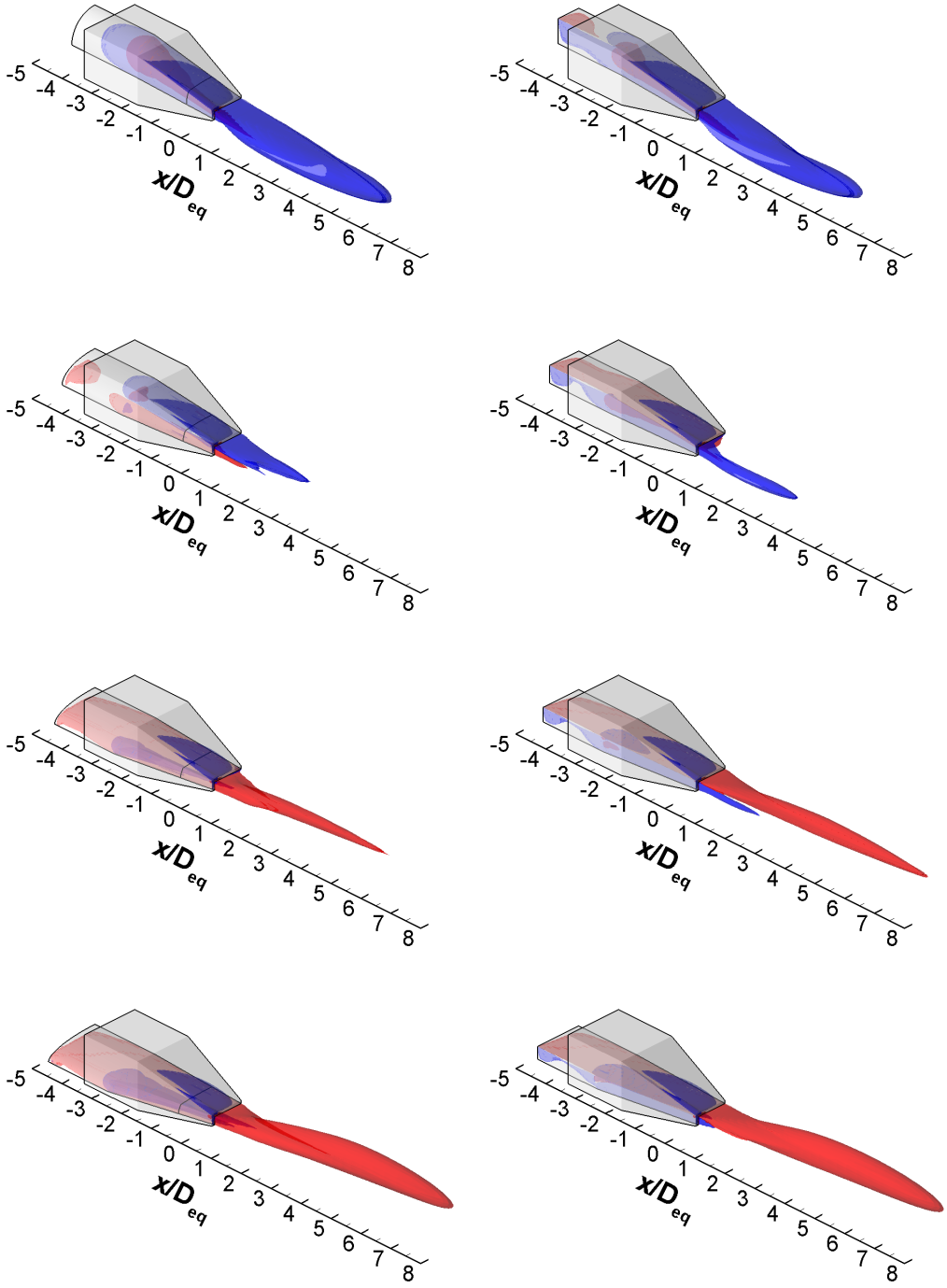

E−series *R*−series

(a) *CSR* constant; from top to bottom, AR_i = 1, 2, 3, 4

Figure 5.21: Development of normalised streamwise vorticity ($\omega_x D_{eq}/V_{exit}$) inside the nozzle for the E−series; iso-surface of +0.1 are shown in red and that of −0.1 are shown in blue (Note: only one quadrant is shown for all cases)

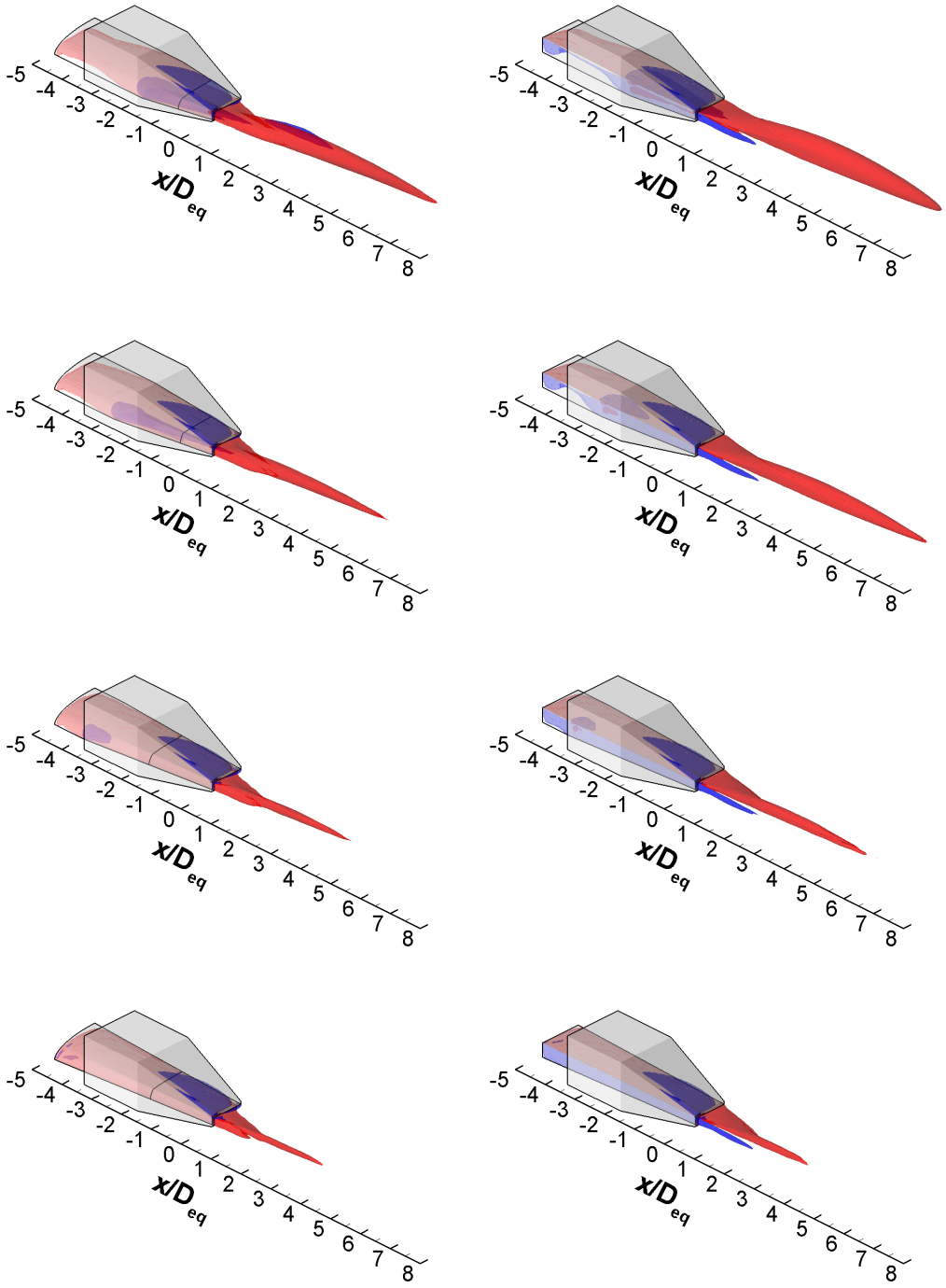

E−series *R*−series

(b) AR_i constant; from top to bottom, CSR = 1, 2, 3, 4

Figure 5.21: Continued

to the converging of the nozzle. While the $A3$ and $A4$ sets in case of elliptic series show a presence of positive vorticity along the inner walls of the nozzle, the rectangular series shows a distinct presence of positive and negative vorticity structures along the top and side walls, respectively. This is expected due to the presence of corners causing secondary flows of the second kind (discussed in more detail later). Consequently, we see a difference in the vorticity development for rectangular $AR_i \neq 1$ configurations as compared to the elliptic series. This also serves to explain why the $RA2$ configurations show cross-over point variation similar to the other $AR_i = 3$ and $AR_i = 4$ configurations while $EA2$ configurations show a variation similar to the $AR_i = 1$ configurations.

From Figure 5.21, it is thus clear that the vorticities observed at the nozzle exit essentially develop at the start of the contraction section. The strength of these structures is also primarily dependent on the CSR of the nozzle.

5.2.3.3 Jet Flow Development

The secondary flows inside the nozzle are generated by two mechanisms: the distortion and change in the cross-section, and the presence of corners. Both the mechanisms affect the magnitude and direction of the streamwise vorticity and are, thus, closely dependent on the AR_i and CSR. The secondary flows due to distortion and change in the cross-section result in Prandtl's secondary flows of the first kind which are of a higher magnitude compared to the secondary flows due to corners which result in Prandtl's secondary flows of the second kind.

The development of the secondary flows of the first kind can be explained on the basis of velocity development through the nozzle. Normalised streamwise velocity (V_x/V_{exit}) contours at three locations in the nozzle: 4.5 D_{eq} from the exit, 3 D_{eq} from the exit and at the nozzle exit, are shown in Figure 5.22. These provide an understanding of the velocity development as the flow accelerates through the nozzle. The change in the cross-section induces a difference in the acceleration of the flow along the shorter and the longer sides. The flow along the sides, which have a higher slope during the transition from the inlet to the exit geometry, tends to accelerate faster. The higher inertial forces generated along this side imply that the boundary layer thickness is smaller since, along any given plane inside the nozzle, the viscous forces along the nozzle wall are uniform. The flow, therefore,

leads to the production of secondary flows in the plane such that the fluid is pushed inwards from the side which exhibits faster flow towards the centreline of the nozzle and then outwards to the side exhibiting slower flow and back along the walls of the nozzle. Such a secondary motion is thus conducive to the formation of streamwise vorticities.

Indeed, for the $AR_i = 1$ configurations, the flow accelerates faster along the ends of the minor axis compared to the major axis. This induces a secondary flow that pushes the fluid towards the centre of the nozzle from the minor axis ends and outwards towards the major axis end, i.e. in a clockwise sense. Such a flow tends to produce streamwise vorticity pairs ('out-flow' pairs) such that they push the fluid outwards from the ends of the major axis and inwards from the ends of the minor axis. This would resist the axis-switching process. The difference in the flow accelerations along the major and minor axes is very small for the $AR_i = 2$ configurations; this can explain the delayed axis-switching encountered for these configurations. The $AR_i = 3$ and 4 configurations, however, show a distinctly higher sloping of the nozzle walls along the major axis compared to the minor axis. Consequently, the flow acceleration is higher along the walls at the ends of the major axis and it induces a secondary flow in the counter-clockwise sense, i.e. from the ends of the major axis towards the centre, on to the ends of the minor axis and back along the nozzle wall. This type of flow produces the 'in-flow' pairs which tend to assist axis-switching.

The change in the *CSR* of the nozzle affects the slope of the nozzle walls along the transition section from the inlet to the exit geometry. Although this does not influence the sense of the streamwise vorticity, it affects the strength of the vorticities developed. Clearly, for lower *CSR* values, the slope of the nozzle walls is higher than that for higher *CSR* values. The flow developing along the walls, therefore, tends to accelerate faster and thus induces secondary flows of higher magnitude. This is confirmed by the location of the cross-over point; the configurations with lower *CSR* switch axes earlier. In case of the *A*1 set (and the *EA*2 set) of nozzle configurations as well, where a lower *CSR* corresponds to a delay in transition or axis-switching, the observations can be explained due to the strength of the vortices generated; since the vortex pairs for these configurations tend to resist axis-switching, the stronger vortices generated for lower *CSR* configurations delay the transition or axis-switching. As the strength of the vortex field

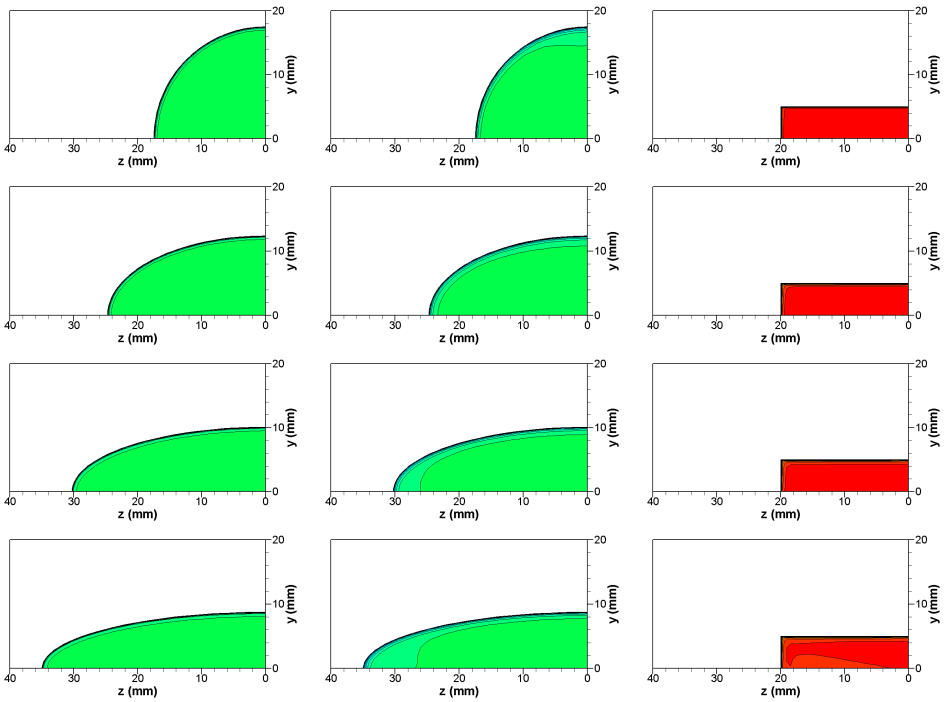

(a) $E-$series, CSR constant; from top to bottom, AR_i = 1, 2, 3, 4

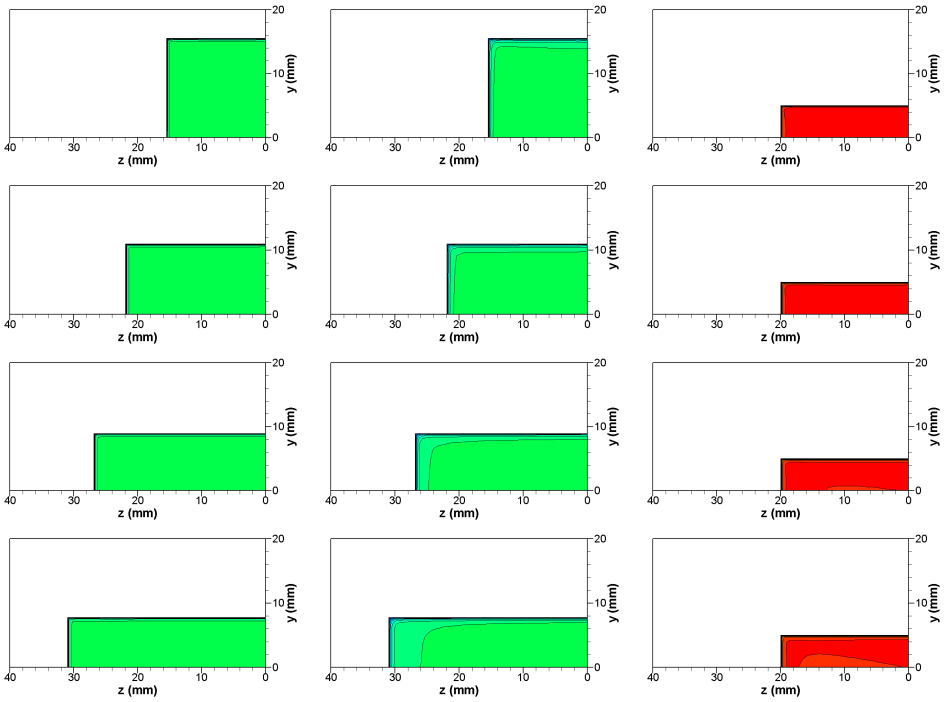

(b) $R-$series, CSR constant; from top to bottom, AR_i = 1, 2, 3, 4

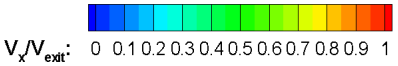

Figure 5.22: Contours of normalised streamwise velocity (V_x/V_{exit}) at planes 4.5 D_{eq} upstream (left), 3 D_{eq} upstream (centre) and at the nozzle exit (right)

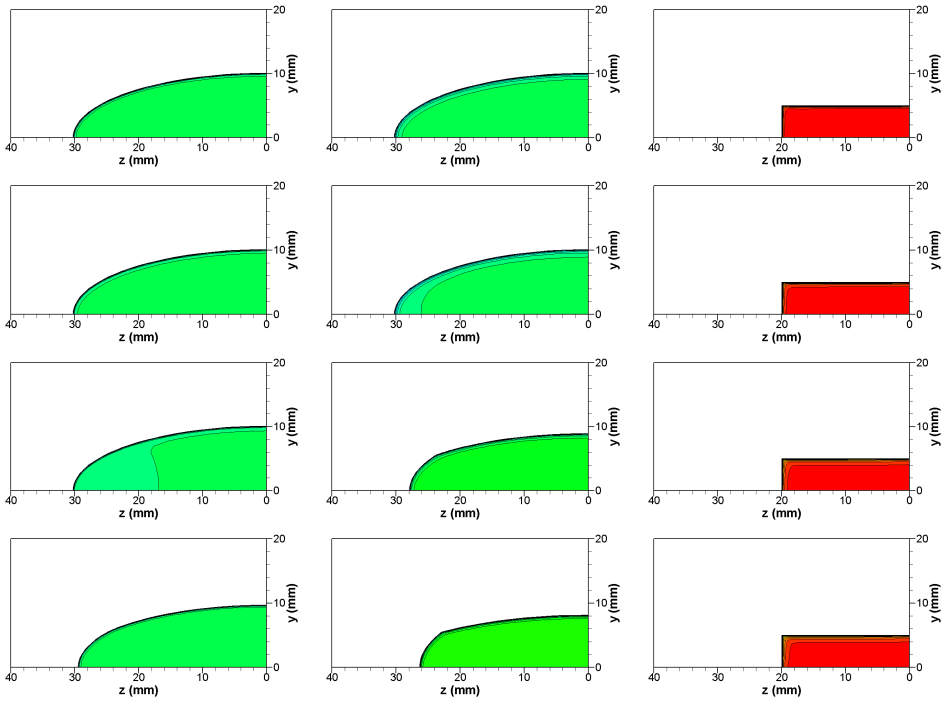

(c) $E-$series, AR_i constant; from top to bottom, CSR = 1, 2, 3, 4

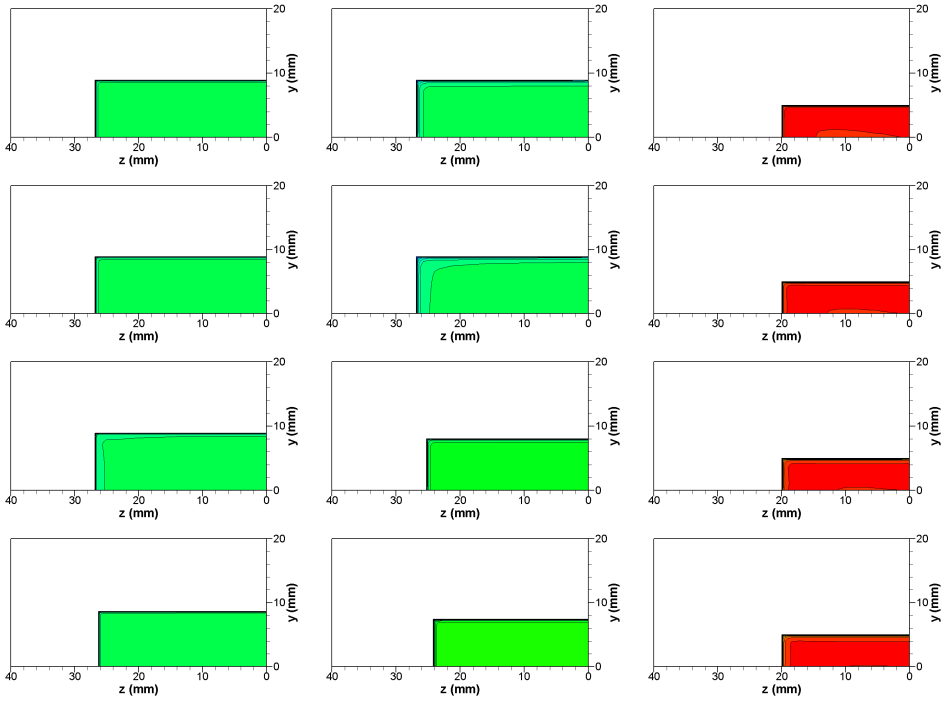

(d) $R-$series, AR_i constant; from top to bottom, CSR = 1, 2, 3, 4

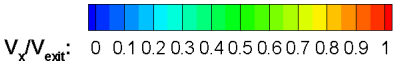

Figure 5.22: Continued

decreases with an increase in the *CSR* value, the location at which the transition to an elliptic/round jet cross-section with equal spreading rates occurs moves closer to the nozzle exit with increasing *CSR*.

From the above discussion, two important observations may be established:

- The difference in the flow acceleration along the side walls of the nozzle induces secondary flows in the flow which are responsible for the generation of streamwise vorticity.
- The sense, or direction, of the streamwise vorticity is mainly dependent on the AR_i of the nozzle, while the magnitude of the vortex core, on the other hand, is mainly dependent on the *CSR* of the nozzle.

The effects of the induced secondary flows on the generated streamwise vorticities can be seen from Figures 5.23 and 5.24. Figure 5.23 presents the normalised vorticity and velocity contour plots for the $E-$series at planes $D_{eq} = 2$ and 8 downstream of the nozzle exit. Similar plots concerned with the $R-$series are provided in Figure 5.24.

The streamwise vorticity for all the plots in Figures 5.23 and 5.24 was normalised using the nozzle equivalent diameter and centreline velocity at the nozzle exit. In the case of all these plots, a negative vorticity structure indicates that the flow induced by it is in the clockwise direction while that due to a positive vorticity structure is in the counter-clockwise direction. Clearly, a higher magnitude of the vorticity implies that a greater force is exerted by the vortex field on the fluid.

The $A1$ configurations (Figures 5.23(a) and 5.24(a)) indicate the presence of 'out-flow' pairs of vortices which tend to resist axis-switching (rotating to induce flow into the jet on the long sides and out on the short sides); the strength of the vortex field decreasing with an increase in the *CSR* value. A similar trend can be seen for the $A2$ configurations but the vorticity magnitudes are very low and it is difficult to get a clear indication about the magnitude and sense of the vortex fields. On changing the contour scales, however, a better explanation for the observed jet development (Figure 5.25(a)) may be determined. The $EA2$ configurations now resemble the $EA1$ configurations in terms of the sense of the vortex fields. The lower magnitudes might be responsible for the delay in the axis-switching before attaining similar spreading rates along the spanwise axes. This probably

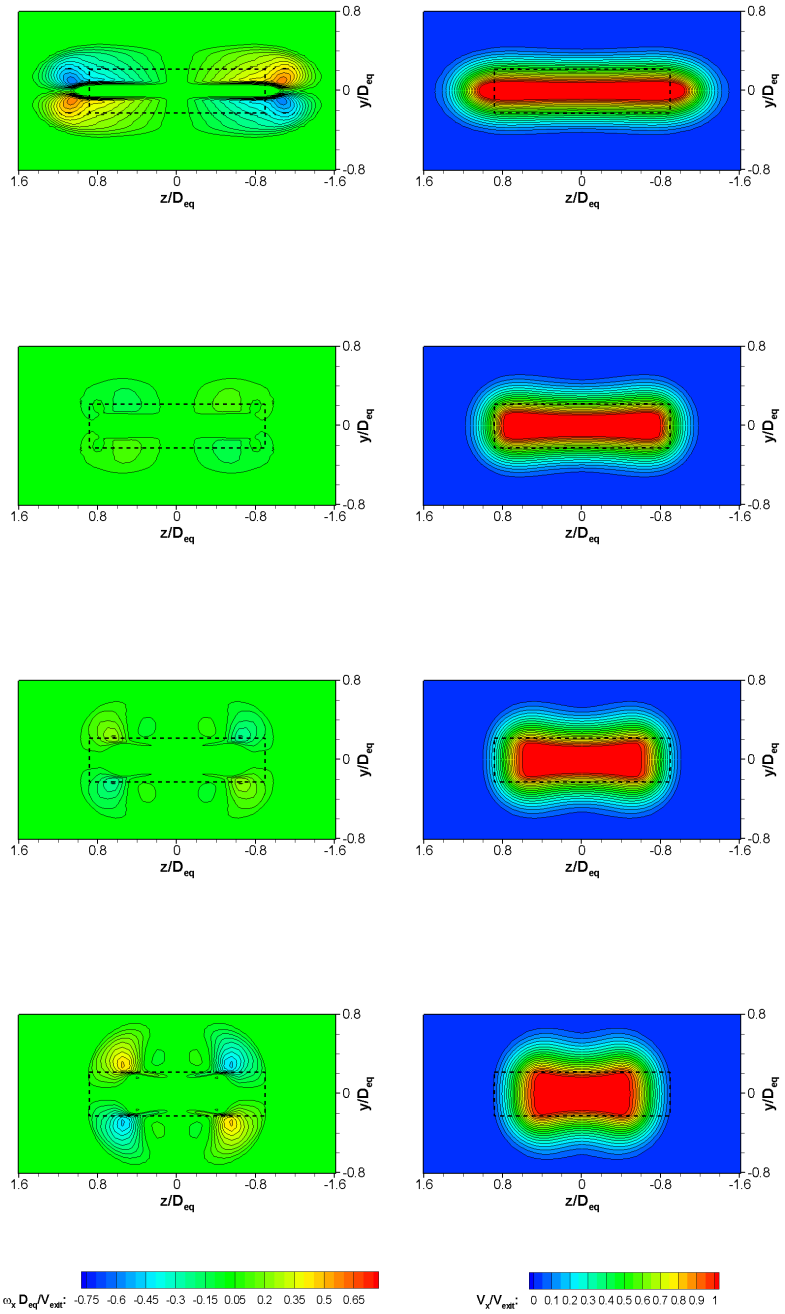

(a) *CSR* constant, 2 D_{eq}; from top to bottom, AR_i = 1, 2, 3, 4

Figure 5.23: Contours of normalised streamwise vorticity ($\omega_x D_{eq}/V_{exit}$) (left) and normalised streamwise velocity (V_x/V_{exit}) (right) for the E−series configurations at planes 2 D_{eq} and 8 D_{eq} downstream of the exit; the dashed outline represents the nozzle exit

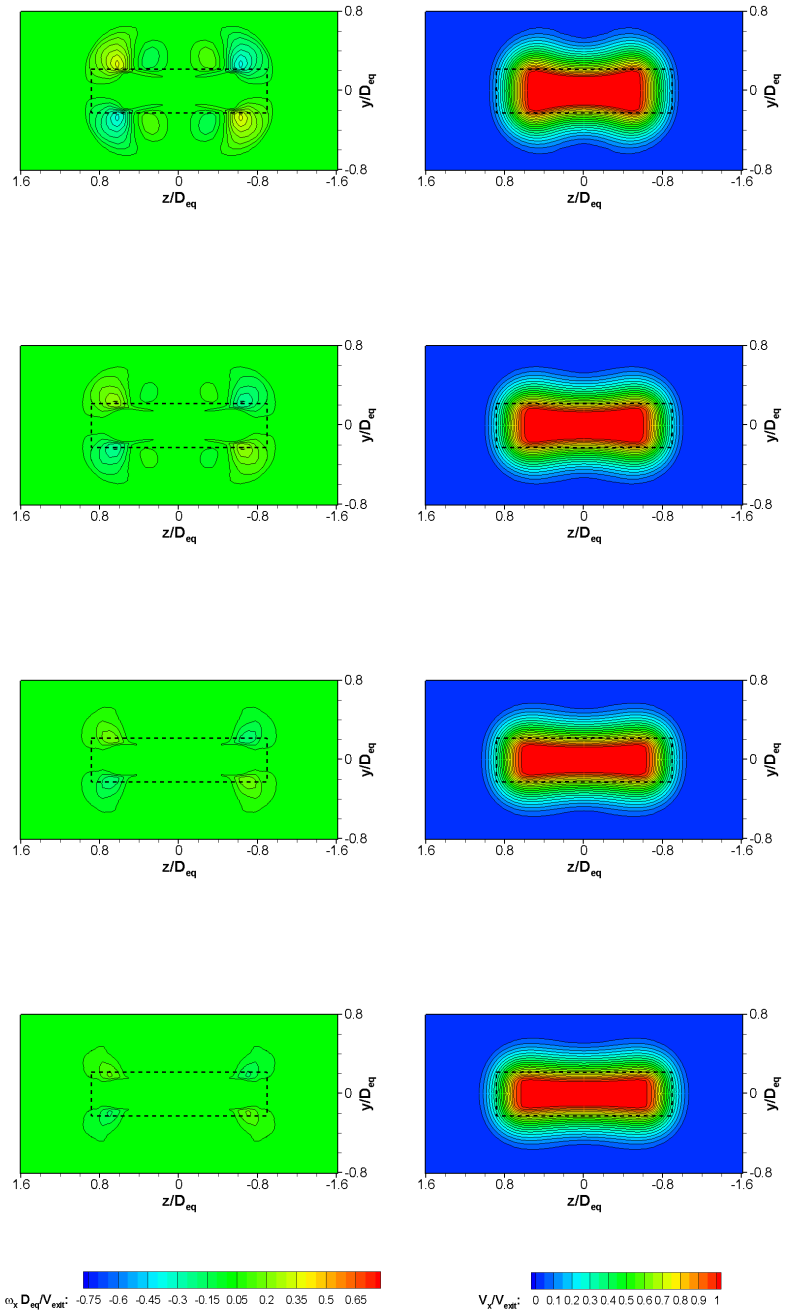

(b) AR_i constant, 2 D_{eq}; from top to bottom, CSR = 1, 2, 3, 4

Figure 5.23: Continued

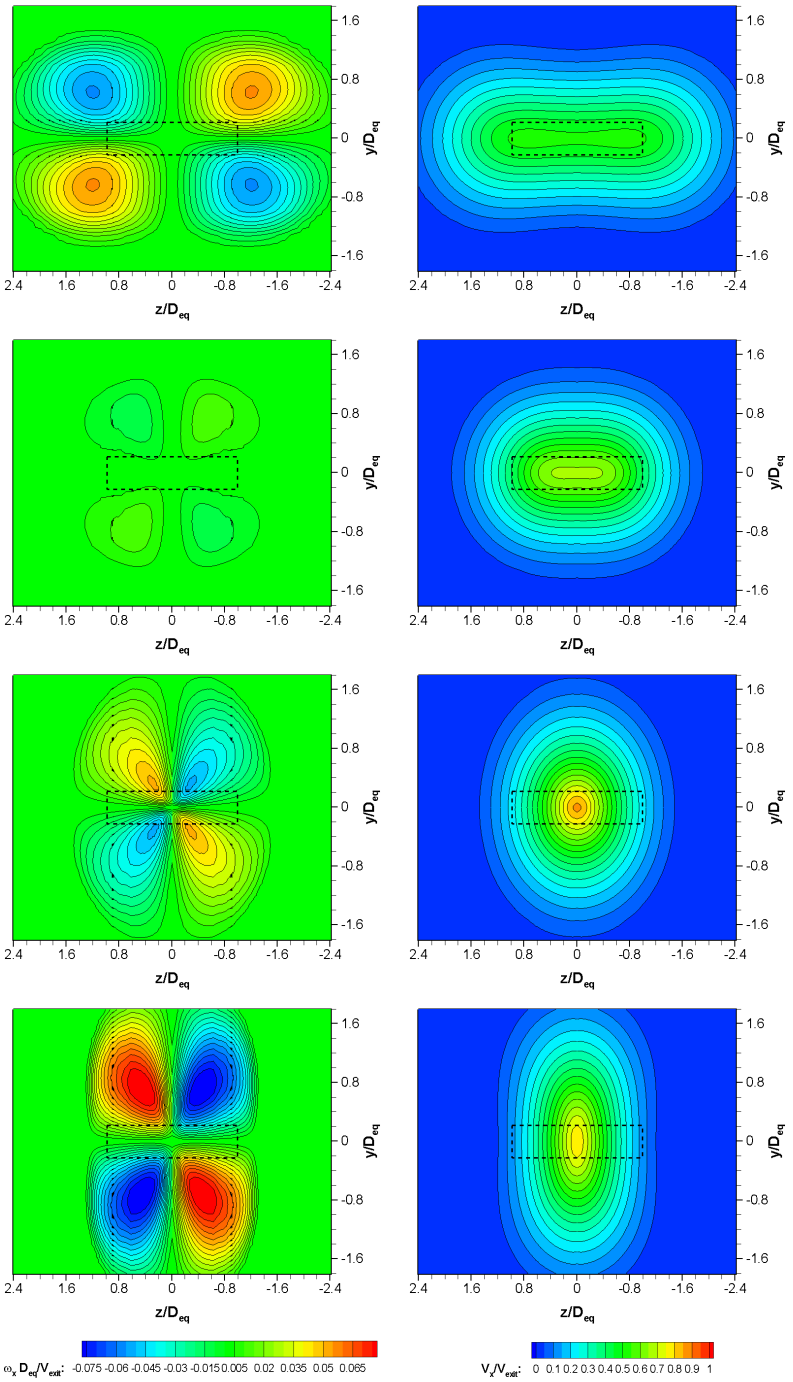

(c) *CSR* constant, 8 D_{eq}; from top to bottom, AR_i = 1, 2, 3, 4

Figure 5.23: Continued

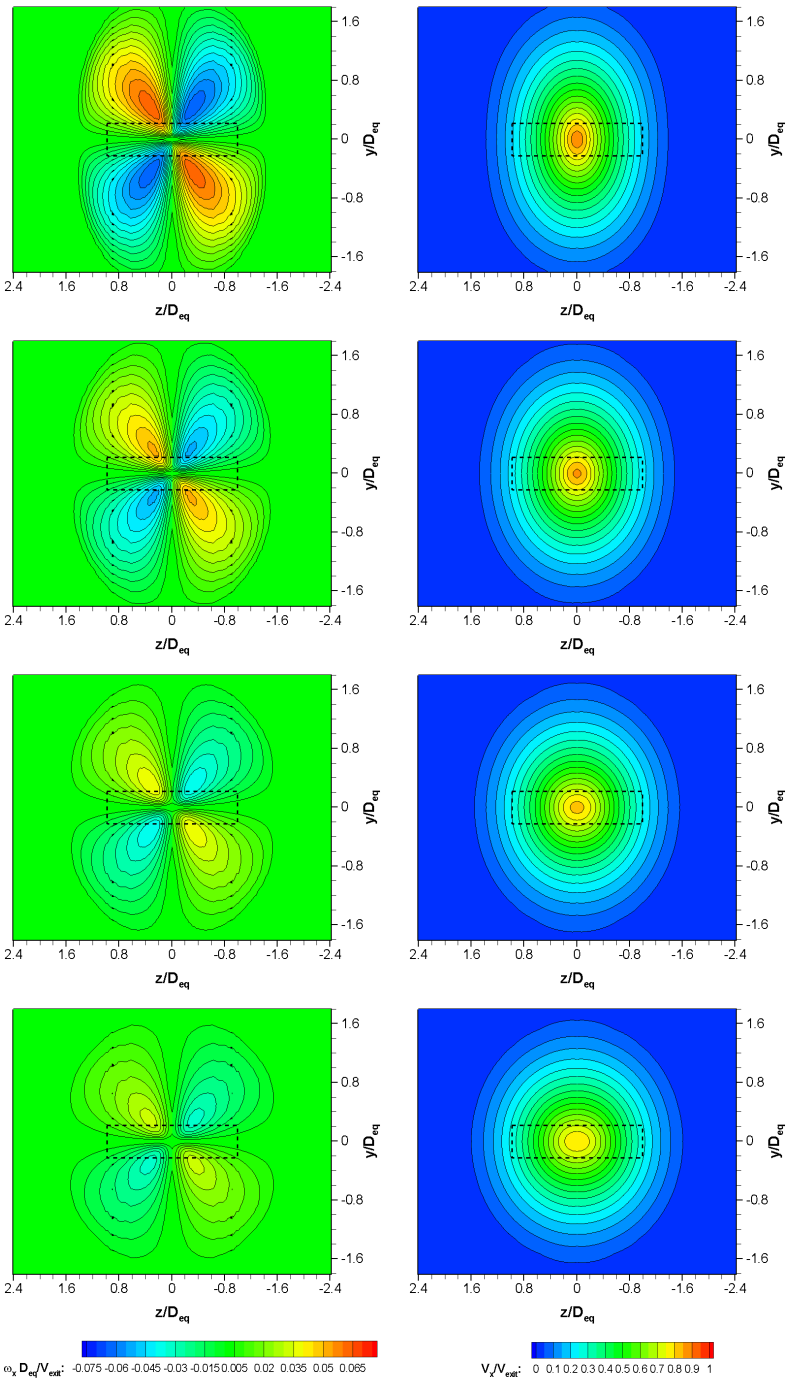

(d) AR_i constant, 8 D_{eq}; from top to bottom, CSR = 1, 2, 3, 4

Figure 5.23: Continued

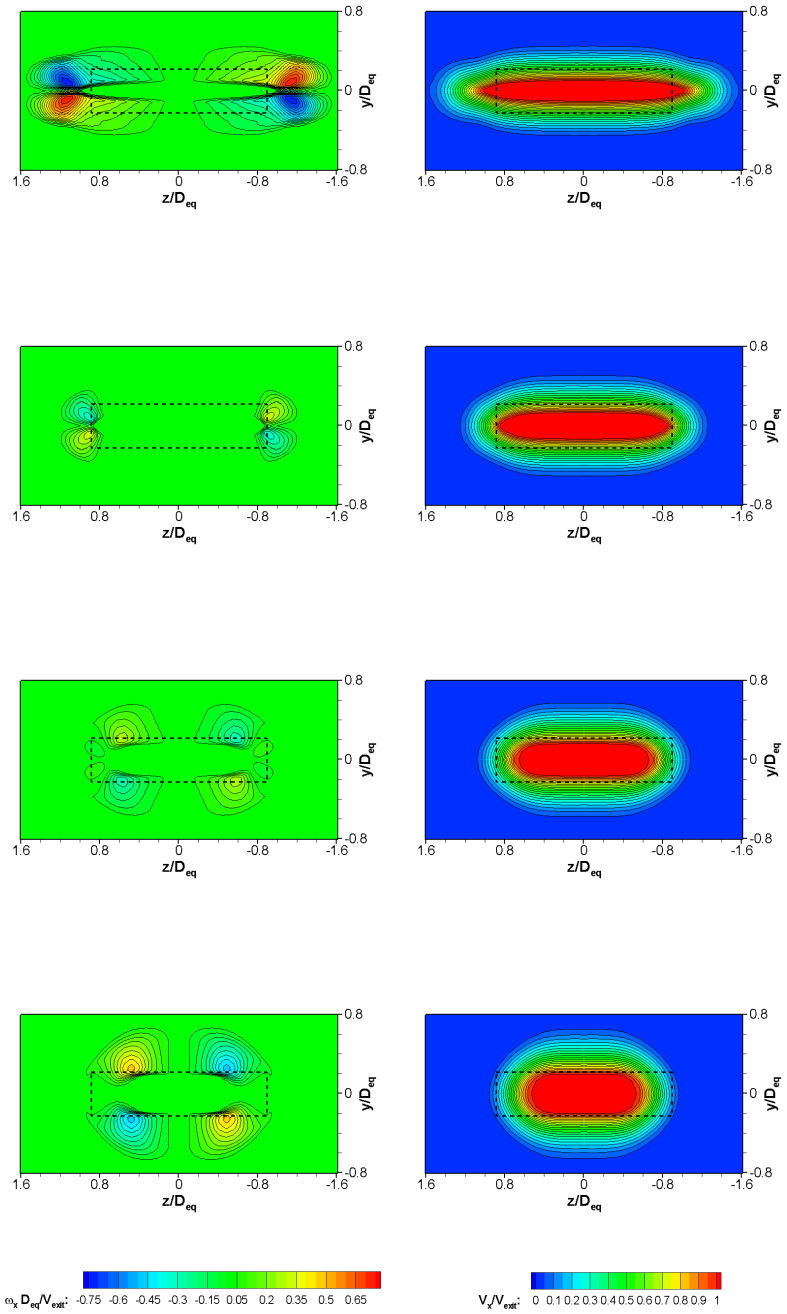

(a) *CSR* constant, 2 D_{eq}; from top to bottom, AR_i = 1, 2, 3, 4

Figure 5.24: Contours of normalised streamwise vorticity ($\omega_x D_{eq}/V_{exit}$) (left) and normalised streamwise velocity (V_x/V_{exit}) (right) for the R−series configurations at planes 2 D_{eq} and 8 D_{eq} downstream of the exit; the dashed outline represents the nozzle exit

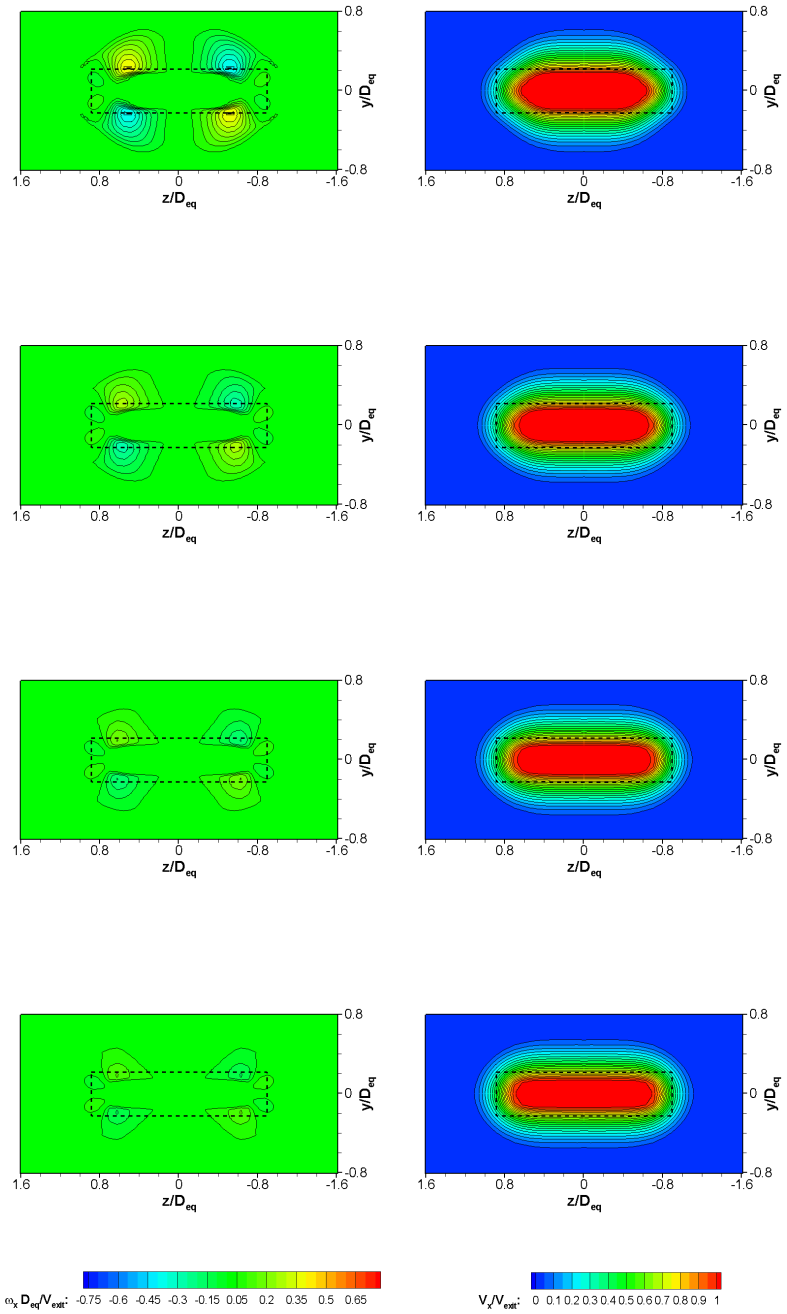

(b) AR_i constant, 2 D_{eq}; from top to bottom, CSR = 1, 2, 3, 4

Figure 5.24: Continued

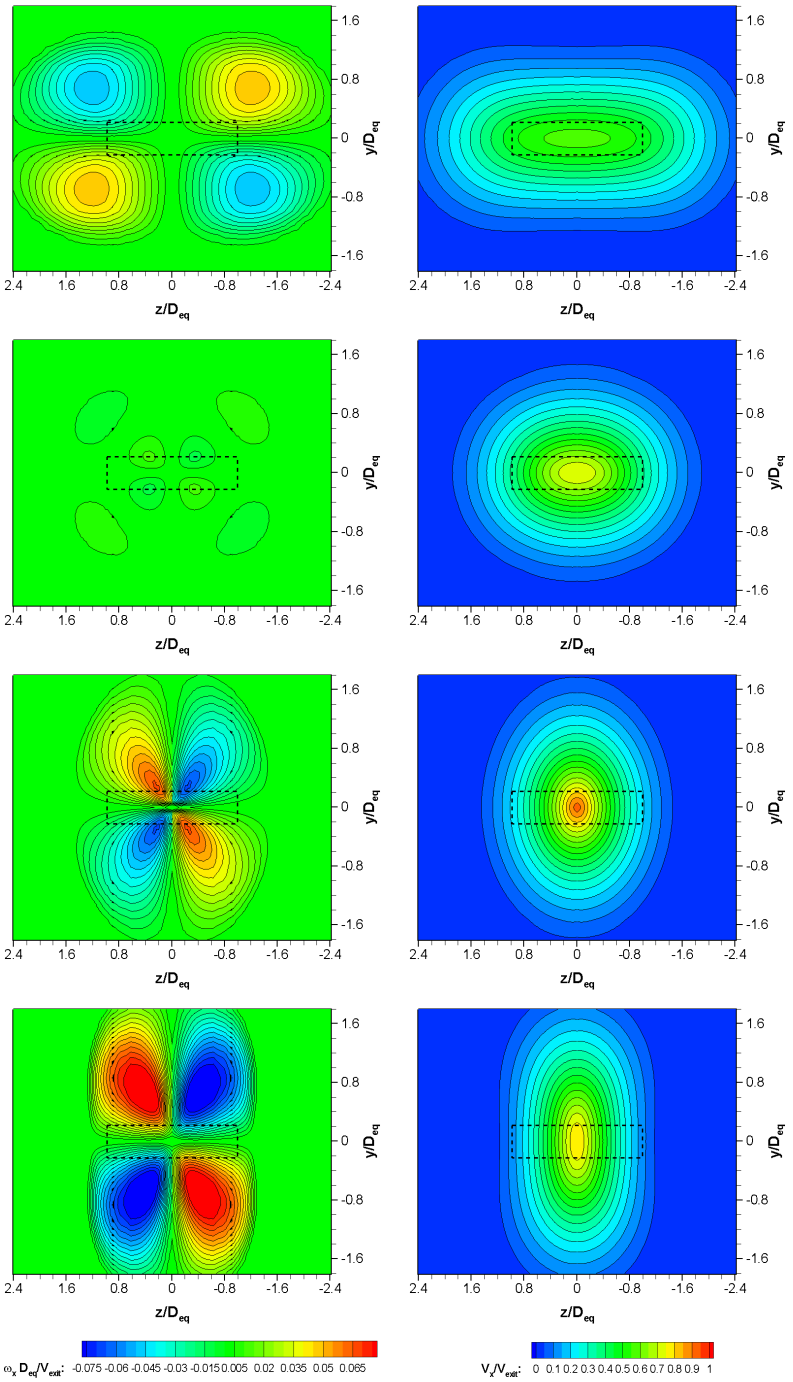

(c) *CSR* constant, 8 D_{eq}; from top to bottom, AR_i = 1, 2, 3, 4

Figure 5.24: Continued

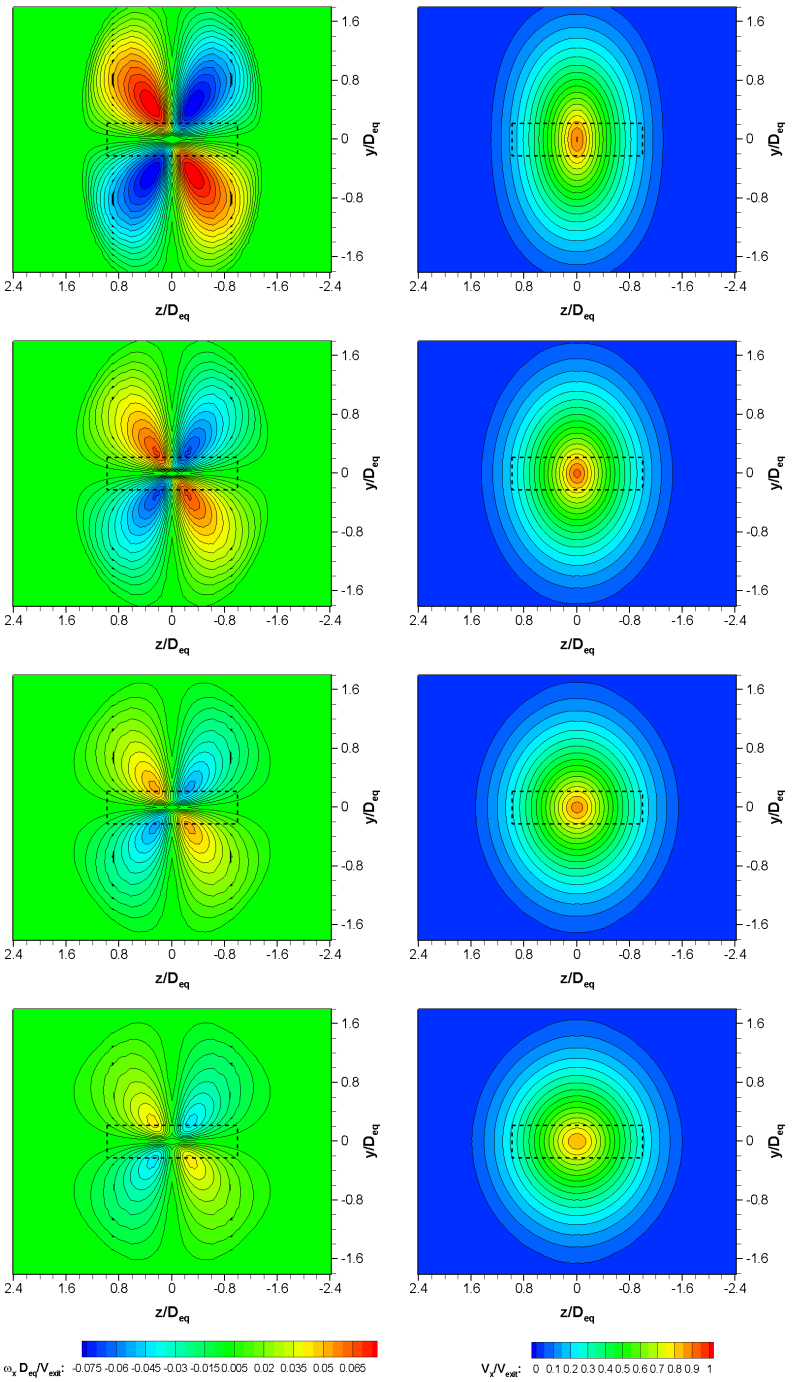

(d) AR_i constant, 8 D_{eq}; from top to bottom, CSR = 1, 2, 3, 4

Figure 5.24: Continued

also accounts for the trend, that with an increase in the *CSR*, the location of the cross-over point moves closer to the nozzle exit. The *RA*2 configurations, on the other hand, reveal an interesting feature in the flow-field. The stronger vortex fields, resisting the axis-switching process, seem to be on the outside of smaller vortex fields which promote axis-switching. The strength of all these vorticity structures is lower for higher *CSR* values, indicating delayed axis-switching. The *A*3 and *A*4 configurations show similar trends (Figures 5.23(c), (d) and 5.24(c), (d)) indicating the presence of 'in-flow' pairs and thus axis-switching; the magnitude of the vortex fields reduces with increase in the *CSR* value, implying a delay in axis-switching for configurations with higher *CSR* values. The *A*4 configurations also show higher magnitudes compared to their corresponding *A*3 configurations. Indeed, the jets issuing from *A*4 configurations switch axes earlier than the *A*3 configurations.

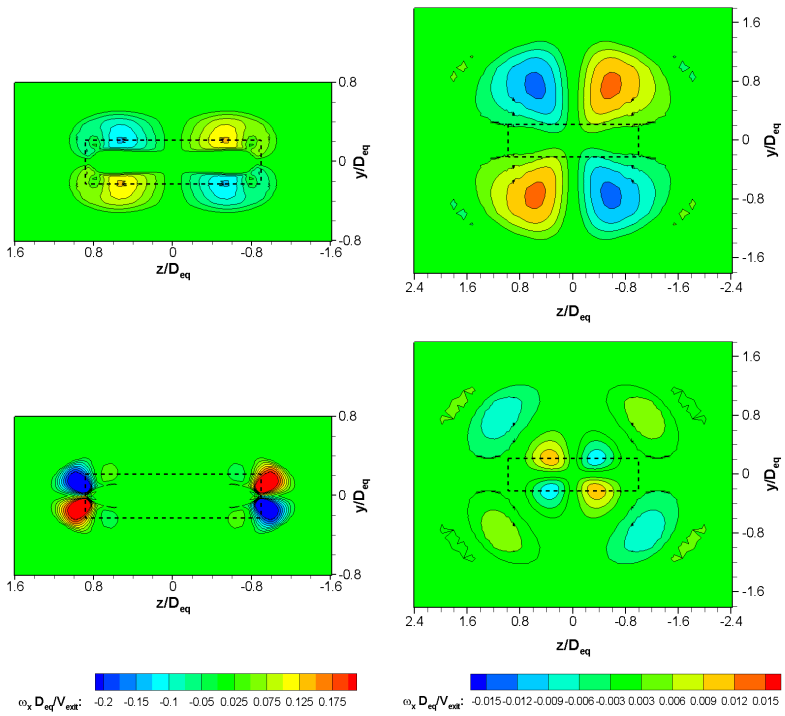

(a) 2 D_{eq} (b) 8 D_{eq}

Figure 5.25: Contours of normalised streamwise vorticity ($\omega_x D_{eq}/V_{exit}$) for E− series (top) and R−series (bottom) configurations at planes 2 D_{eq} (left) and 8 D_{eq} (right) downstream of the exit presented in a different scale; the dashed outline represents the nozzle exit

The velocity contour plots, normalised using the centreline velocity at the nozzle exit, show a similar effect of the streamwise vorticity on the flow-field development and the spreading of the jet along the spanwise axes for both the series. The spread of the jet along the major axis reduces, while along the minor axis it increases, with an increase in the *CSR* value for the *A*1 set of simulations. The variation in jet spread is not very clear in the case of the *A*2 configurations for either series. A slight increase in the jet spread along the major axis is observed for the *A*3 configurations; the jet spread decreases along the minor axis with increase in the *CSR*. A similar trend is seen for the *A*4 configurations with the variation along the major axis being quite distinct.

The vorticity distribution and the jet spreads in terms of velocity distribution, at a distance of 8 D_{eq} downstream of the exit are given in Figures 5.23 and 5.24 for the *E*− and *R*−series, respectively. Both the figures exhibit the development of the jet as expected from the previous observations.

The streamwise vorticity contours show a pattern similar to that observed at the plane 2 D_{eq} downstream of the exit. It is to be noted here that the magnitude of the vortex fields in Figures 5.23(c), (d) and 5.24(c), (d), is represented on a scale which is one-tenth of the scale used for representing the vortex fields at 2 D_{eq}; the velocity plots are on the same scale for both the planes at 2 and 8 D_{eq}. The strength of the vortex field reduces for all the configurations with an increase in the *CSR*. The *A*1 configurations show the presence of an 'out-flow' pair resisting axis-switching whilst the *A*3 and *A*4 show the presence of an 'in-flow' pair assisting axis-switching. The strength of the vortex fields are higher for the *EA*1 set compared to the *RA*1 set, implying delayed transition to equal spreading rates along the spanwise axes for the elliptic series compared to the rectangular series. Similarly, higher magnitudes for the *RA*3 and *RA*4 configurations compared to their elliptic counterparts mean that the jets from these configurations switch axes faster. The *A*2 configurations for both the series also presented results representative of that seen for the 2 D_{eq} plane. On changing the scale to lower values (Figure 5.25(b)), it can be seen that the elliptic series shows an 'out-flow' pair resisting axis-switching; the strength reducing with increasing *CSR* and thus the delay in axis-switching for *EA*2*C*4 is the least amongst the *EA*2 set (refer to figures in Appendix D). The *RA*2 set shows the existence of an 'in-flow' pair closer to the jet centre which assists axis-switching. However, there also exists the 'out-flow' pair

outside this which resists axis-switching; the result being delayed axis-switching, although the location of X_c is closer to the exit compared to the elliptic series. Also, since the magnitude of the vortex field reduces with increasing *CSR*, this affects the effect of *CSR* on the location of X_c with higher *CSR* corresponding to a higher X_c.

The *A*4 configurations switch axes before 8 D_{eq} and this can be seen from the velocity contour plots. With an increase in the *CSR*, the spreading along the major axis increases while that along the minor axis decreases. The *A*3 configurations, except for the *C*4 set, also switch axes before 8 D_{eq} and show a trend similar to the *A*4 configuration. Although, all the plots show distinct axis-switching in terms of the total jet spread, since the location of the cross-over point is determined on the basis of equal half-velocity-widths along the major and minor axes, closer examination of the *EA*3*C*4 and *RA*3*C*4 velocity contour plots confirms that the half-velocity-width is slightly greater at the major axis than the minor axis.

An interesting point to note here is the difference in the strengths of the streamwise vorticities between the corresponding configurations of the *E*− and the *R*−series. For any given configuration from the *A*3 or *A*4 set, the *R*−series nozzles show a higher vorticity magnitude, while it shows lower magnitude for the *A*1 set. In case of the *A*2 set, the two series show a distinct difference in the distribution of the vortices. This may be attributed to the existence of additional secondary flows in the nozzles of the *R*−series due to the presence of sharp corners. The streamwise vorticities due to these flows tend to assist axis-switching. For the *A*1 set, this therefore reduces the total magnitude of the 'out-flow' pairs of vortices. For the *A*3 and *A*4 sets, however, the total magnitude of the 'in-flow' pairs of vortices increases. The strength of these vortices due to the presence of corners is generally about a tenth of the magnitude of vortices produced due to skewness. Indeed, in this case, their effect is more pronounced for the *A*2 set wherein the vortices produced due to skewness are not very strong (Figure 5.25). Thus, while the *EA*2 configuration tends to show the presence of 'out-flow' pairs, the *RA*2 configuration shows the presence of additional 'in-flow' pairs and hence tends to switch axes earlier than its elliptic counterpart.

5.3 Parametric Study Results: Location of Cross-over Point

The data recorded in Tables 5.2 and 5.3 are now used for creating a parametric model of axis-switching behaviour, based on location of the cross-over point, using statistical methods. The definitions and the formulae for calculation of the various statistical terms involved have already been discussed in Section 3.4.2. The process of creating a parametric model each for the $E-$ and the $R-$ series is carried out in the following steps:

- The data are plotted for both the $E-$ and the $R-$series such that comparisons may be made with variations with respect to the inlet aspect ratio (AR_i) keeping the converging section ratio (CSR) constant, and vice-versa. The statistical fits obtained such are then compared, based on the coefficient of determination, R^2, and the residual errors, ε_i;
- The best-fit curves, based either on constant AR_i or constant CSR, are then selected for creating the model based on two predictor variables, AR_i and CSR.
- The parametric model is then again checked in terms of coefficient of determination and residual errors. It is then validated by generating a normal probability plot for the errors and tested for normality.

5.3.1 One-predictor-variable Models

The one-predictor-variable models were the first step in creating a complete parametric model for understanding the combined effects of changing the inlet aspect ratio (AR_i) and the length of the converging section (CSR). It is emphasised that these models are specific to the nozzle under consideration and its variation of the inlet aspect ratio and the converging section length. Also, the values used for the location of the cross-over point in the case of the $A1$ configurations are, in fact, the locations where the spreading rates along the spanwise axes are approximately equal (these are referred as 'transition points'). All of the variables are non-dimensional. The location of the cross-over point, X_c is normalised using

the equivalent diameter, D_{eq}; for convenience, however, the normalised value is referred to only as X_c.

5.3.1.1 Model creation

The variation in the location of the cross-over point was considered to be the dependent variable. Keeping one of AR_i or CSR constant and considering the other parameter as the predictor variable, two statistical models were created each for the $E-$ and the $R-$series.

The X_c variation based on constant AR_i, as observed from the simulation results, for both the series is presented in Figure 5.26. Using statistical curve-fitting, it is established that the best fit is observed with a linear correlation. This confirms the initial observation mentioned in Section 5.2.2. These linear equations, for each AR_i configuration in both series, are given below:

$E-$**series:**

***A1*:** $X_c = -29.3612\,CSR + 74.3298$
***A2*:** $X_c = -8.5827\,CSR + 30.7934$
***A3*:** $X_c = 5.8045\,CSR + 3.3226$
***A4*:** $X_c = 4.7446\,CSR + 1.0015$

$R-$**series:**

***A1*:** $X_c = -20.1562\,CSR + 59.9637$
***A2*:** $X_c = 0.9126\,CSR + 17.1582$
***A3*:** $X_c = 6.1825\,CSR + 2.4562$
***A4*:** $X_c = 4.8243\,CSR + 0.9036$

A similar exercise is carried out for understanding the X_c variation based on constant CSR. The results of these are given in Figure 5.27. Again, on the basis of statistical curve-fitting, it is concluded that the best-fit results are obtained using a quadratic equation for each set of constant CSR. The equations that govern these curve-fits are:

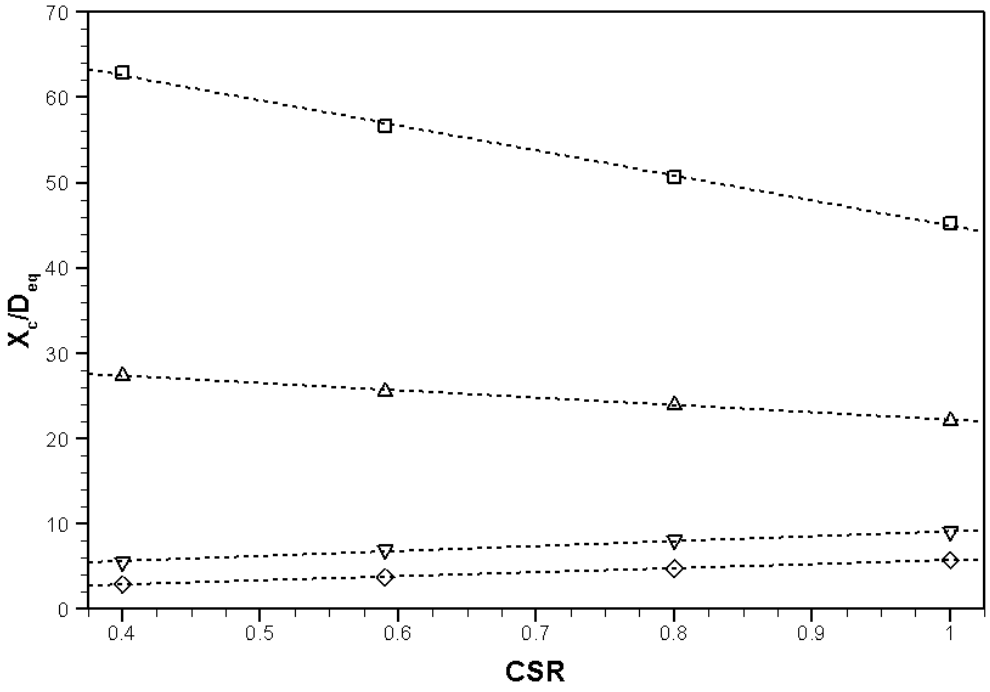

(a) $E-$series

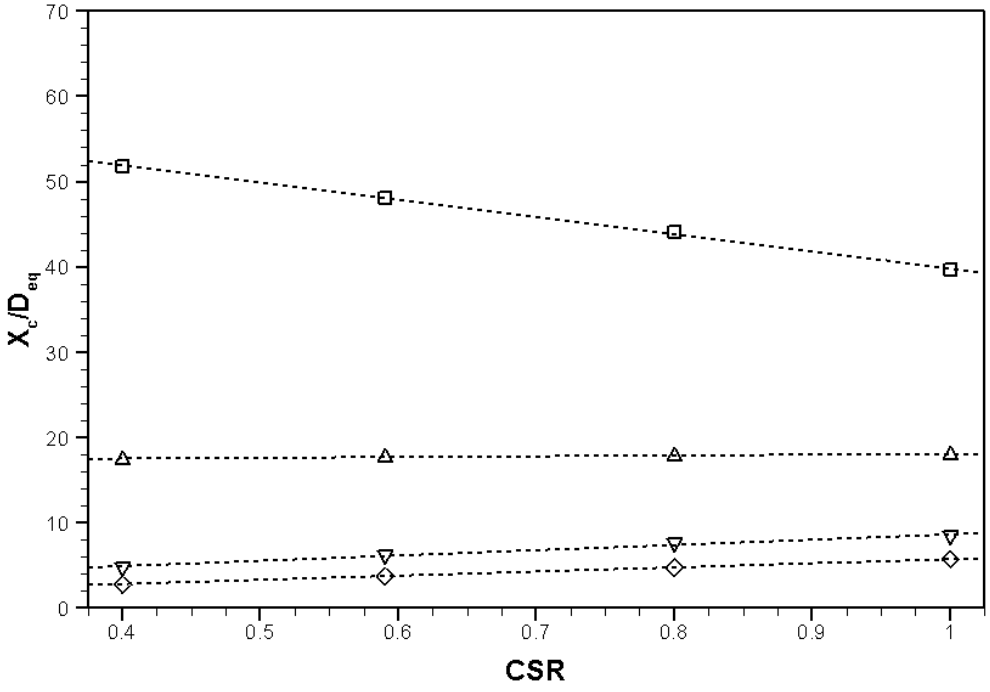

(b) $R-$series

Figure 5.26: X_c variation with respect to CSR, based on constant AR_i; $--\square--$, $AR_i = 1$; $--\triangle--$, $AR_i = 2$; $--\triangledown--$, $AR_i = 3$; $--\diamond--$, $AR_i = 4$

$E-$**series:**

***C1*:** $X_c = 8.3942\,AR^2 - 62.2456\,AR + 117.3834$
***C2*:** $X_c = 7.1245\,AR^2 - 53.3805\,AR + 103.2669$
***C3*:** $X_c = 5.9526\,AR^2 - 45.1598\,AR + 90.1590$
***C4*:** $X_c = 4.9072\,AR^2 - 37.6863\,AR + 77.9514$

$R-$**series:**

***C1*:** $X_c = 7.6942\,AR^2 - 54.2964\,AR + 97.1814$
***C2*:** $X_c = 6.6174\,AR^2 - 47.3692\,AR + 87.6738$
***C3*:** $X_c = 5.5716\,AR^2 - 40.5771\,AR + 78.1907$
***C4*:** $X_c = 4.5042\,AR^2 - 33.5795\,AR + 68.0958$

Following the process of obtaining the curve equations that depict the variation of X_c with respect to either the AR_i or CSR, it is now possible to select the equation set that best represents the observed values. This is done by undertaking a statistical error analysis based on finding the coefficients of determination (R^2) using the sum of squares.

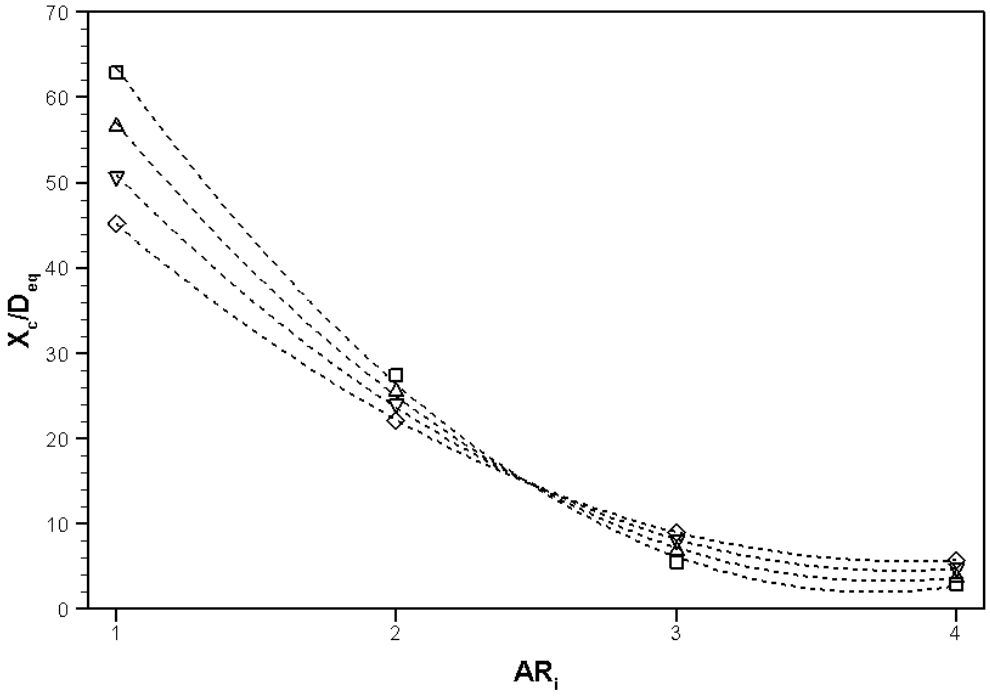

(a) *E*−series

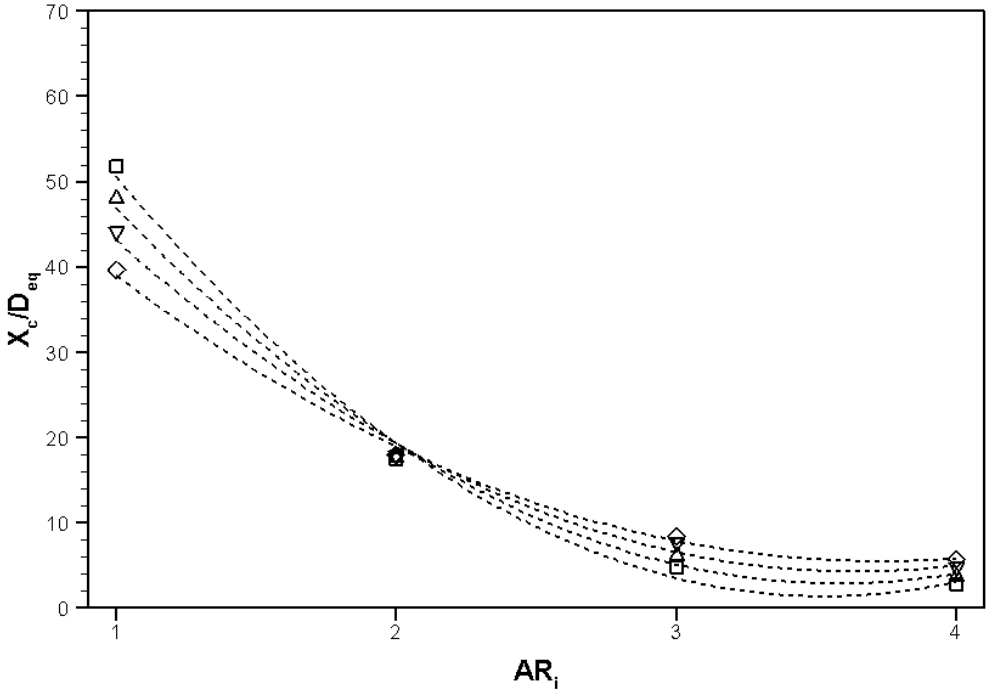

(b) *R*−series

Figure 5.27: X_c variation with respect to AR_i, based on constant CSR; − −□− −, CSR = 0.40; − − △ − −, CSR = 0.59; − − ▽ − −, CSR = 0.80; − − ◇ − −, CSR = 1.00

5.3.1.2 Model Selection

The results obtained by using the predictor model (f_i) as compared with the observed results from the simulations (y_i) are shown in Tables 5.6 to 5.9. The sum of squares are calculated for the individual sets, as required; the calculation process has been explained in Section 3.4.2. The values of the coefficients of determination are provided separately in Table 5.10. It is clear that the linear statistical models based on constant AR_i are able to predict the value of X_c more consistently across both the series. Although the model based on constant CSR shows a very good match for the elliptic series, it is not able to predict as accurately for the rectangular series. Consequently, the parametric model to predict the influence of both the parameters, AR_i and CSR, simultaneously on the location of the cross-over point, is developed from the linear one-predictor-variable model based on constant AR_i.

5.3.2 Two-predictor-variable Models

The linear-fit, one-predictor-variable models for constant AR_i give the variation of the X_c with respect to CSR. The slope and the $y-$intercept of this linear-fit model is different for the different AR_i values. Thus, to understand the combined effect of CSR and AR_i, we try to establish the variation of two factors, the coefficient (i.e. slope) and the constant (i.e. $y-$intercept), with respect to AR_i variation is established. Once again, statistical curve-fitting techniques are employed to find a curve that fits the data. Figure 5.28 shows the results of the curve-fitting. Both the series exhibit similar trends for the coefficients and the constants; the best-fit curves that pass through the data can be represented by cubic equations. The parametric models can now be constructed from Equations 5.1 and 5.2 for the $E-$ and the $R-$series, respectively. Henceforth in this study, the two-predictor-variable models are referred to as 'XOP-models' for simplicity.

$$\begin{aligned} X_{c,E} = &\left(-1.5093\,AR^3 + 5.8602\,AR^2 + 13.7631\,AR - 47.4752\right)\,CSR \\ &+ \left(1.5140\,AR^3 - 1.0513\,AR^2 - 50.9806\,AR + 124.8477\right) \end{aligned} \tag{5.1}$$

$$\begin{aligned} X_{c,R} = &\left(1.5285\,AR^3 - 17.0702\,AR^2 + 61.5803\,AR - 66.1947\right)\,CSR \\ &+ \left(-2.4923\,AR^3 + 29.0058\,AR^2 - 112.3766\,AR + 145.8268\right) \end{aligned} \tag{5.2}$$

Table 5.6: Error Analysis of one-predictor-variable model for the E−series based on constant AR_i

	CSR	y_i	f_i	$(y_i-\bar{y})^2$	$(f_i-\bar{f})^2$	$(y_i-f_i)^2$
	0.40	62.8851	62.5853	1624.1061	1600.0320	0.0899
	0.59	56.6425	57.0067	1159.9201	1184.8603	0.1326
EA1	***0.80***	50.6883	50.8408	789.8011	798.3959	0.0233
	1.00	45.1857	44.9686	510.7962	501.0300	0.0471
	SS			**4084.6235**	**4084.3182**	**0.2929**
	0.40	27.4395	27.3603	23.5671	22.8044	0.0063
	0.59	25.5563	25.7296	8.8292	9.8891	0.0300
EA2	***0.80***	24.0450	23.9272	2.1319	1.8018	0.0139
	1.00	22.1871	22.2107	0.1582	0.1400	0.0006
	SS			**34.6865**	**34.6354**	**0.0507**
	0.40	5.5478	5.6444	290.2628	286.9805	0.0093
	0.59	6.8772	6.7473	246.7318	250.8296	0.0169
EA3	***0.80***	7.9894	7.9662	213.0286	213.7064	0.0005
	1.00	9.0704	9.1271	182.6417	181.1124	0.0032
	SS			**932.6649**	**932.6289**	**0.0300**
	0.40	2.8705	2.8993	388.6576	387.5228	0.0008
	0.59	3.8284	3.8008	351.8063	352.8424	0.0008
EA4	***0.80***	4.8271	4.7972	315.3395	316.4023	0.0009
	1.00	5.7174	5.7461	284.5126	283.5452	0.0008
	SS			**1340.3159**	**1340.3127**	**0.0033**

Table 5.7: Error Analysis of one-predictor-variable model for the R−series based on constant AR_i

	CSR	y_i	f_i	$(y_i-\bar{y})^2$	$(f_i-\bar{f})^2$	$(y_i-f_i)^2$
	0.40	51.8169	51.9012	1097.0801	1103.3757	0.0071
	0.59	48.0521	48.0715	861.8569	863.6193	0.0004
RA1	***0.80***	44.1317	43.8387	647.0410	632.7539	0.0858
	1.00	39.6184	39.8075	437.8012	446.1980	0.0358
	SS			**3043.7793**	**3045.9469**	**0.1291**
	0.40	17.5091	17.5232	1.4056	1.3477	0.0002
	0.59	17.7100	17.6966	0.9696	0.9752	0.0002
RA2	***0.80***	17.9032	17.8883	0.6265	0.6333	0.0002
	1.00	18.0566	18.0708	0.4072	0.3761	0.0002
	SS			**3.4089**	**3.3323**	**0.0008**
	0.40	4.7780	4.9292	193.6745	189.1973	0.0229
	0.59	6.2531	6.1039	154.7934	158.2614	0.0223
RA3	***0.80***	7.5502	7.4022	124.1999	127.2813	0.0219
	1.00	8.4929	8.6387	104.0767	100.9101	0.0213
	SS			**576.7446**	**575.6500**	**0.0883**
	0.40	2.8705	2.8333	250.4053	251.2479	0.0014
	0.59	3.8284	3.7499	221.0069	223.0303	0.0062
RA4	***0.80***	4.8271	4.7630	192.3103	193.7970	0.0041
	1.00	5.7174	5.7279	168.4103	167.8631	0.0001
	SS			**832.1328**	**835.9383**	**0.0118**

Table 5.8: Error Analysis of one-predictor-variable model for the E−series based on constant CSR

	AR_i	y_i	f_i	$(y_i-\bar{y})^2$	$(f_i-\bar{f})^2$	$(y_i-f_i)^2$
	1	62.8851	63.5320	1624.1061	1675.0439	0.4185
	2	27.4395	26.4690	23.5671	14.9328	0.9419
EC1	***3***	5.5478	6.1944	290.2628	269.2979	0.4181
	4	2.8705	2.7082	388.6576	395.8707	0.0263
	SS			**2326.5936**	**2355.1454**	**1.8048**
	1	56.6425	57.0109	1159.9201	1183.7866	0.1357
	2	25.5563	25.0039	8.8292	5.7562	0.3051
EC2	***3***	6.8772	7.2459	246.7318	235.8927	0.1359
	4	3.8284	3.7369	351.8063	355.9939	0.0084
	SS			**1767.2875**	**1781.4294**	**0.58.52**
	1	50.6883	50.9518	789.8011	803.5581	0.0694
	2	24.0450	23.6498	2.1319	1.0922	0.1562
EC3	***3***	7.9894	8.2530	213.0286	205.9713	0.0695
	4	4.8271	4.7614	315.3395	318.3834	0.0043
	SS			**1320.3011**	**1329.0050**	**0.2994**
	1	45.1857	45.1723	510.7962	509.2966	0.0002
	2	22.1871	22.2076	0.1582	0.1577	0.0004
EC4	***3***	9.0704	9.0573	182.6417	183.5320	0.0002
	4	5.7174	5.7214	284.5126	285.0458	0.0000
	SS			**978.1087**	**978.0321**	**0.0008**

Table 5.9: Error Analysis of one-predictor-variable model for the R−series based on constant CSR

	AR_i	y_i	f_i	$(y_i-\bar{y})^2$	$(f_i-\bar{f})^2$	$(y_i-f_i)^2$
	1	51.8169	50.5792	1097.0801	1021.2051	1.5319
	2	17.5091	19.3654	1.4056	0.5513	3.4458
RC1	***3***	4.7780	3.5400	193.6745	227.4939	1.5326
	4	2.8705	3.1030	250.4053	240.8673	0.0541
	SS			**1542.5656**	**1490.1176**	**6.5645**
	1	48.0521	46.9220	861.8569	800.8391	1.2771
	2	17.7100	19.4050	0.9696	0.6117	2.8730
RC2	***3***	6.2531	5.1228	154.7934	182.2527	1.2776
	4	3.8284	4.0754	221.0069	211.6298	0.0610
	SS			**1238.6269**	**1195.3332**	**5.4887**
	1	44.1317	43.1852	647.0410	603.3066	0.8959
	2	17.9032	19.3229	0.6265	0.4900	2.0155
RC3	***3***	7.5502	6.6038	124.1999	144.4588	0.8957
	4	4.8271	5.0279	192.3103	184.8240	0.0403
	SS			**964.1777**	**933.0794**	**3.8474**
	1	39.6184	39.0205	437.8012	416.0621	0.3575
	2	18.0566	18.9536	0.4072	0.1094	0.8046
RC4	***3***	8.4929	7.8951	104.0767	115.0857	0.3574
	4	5.7174	5.8450	168.4103	163.2747	0.0163
	SS			**710.6954**	**694.5319**	**1.5357**

Table 5.10: Coefficient of Determination, R^2, as calculated for the different one-predictor-variable models

***E*:, constant AR_i**	***R*:, constant AR_i**	***E*:, constant *CSR***	***R*:, constant *CSR***
0.9999	1.0000	0.9992	0.9957
0.9985	0.9998	0.9997	0.9956
1.0000	0.9998	0.9998	0.9960
1.0000	1.0000	1.0000	0.9978

The two equations are now used to create surfaces corresponding to the values of X_c as calculated by the two parametric models. The range of AR_i and *CSR* is split into 60 equal steps each, the divisions being 0.05 and 0.01 for AR_i and *CSR*, respectively. These surfaces are shown in Figure 5.29.

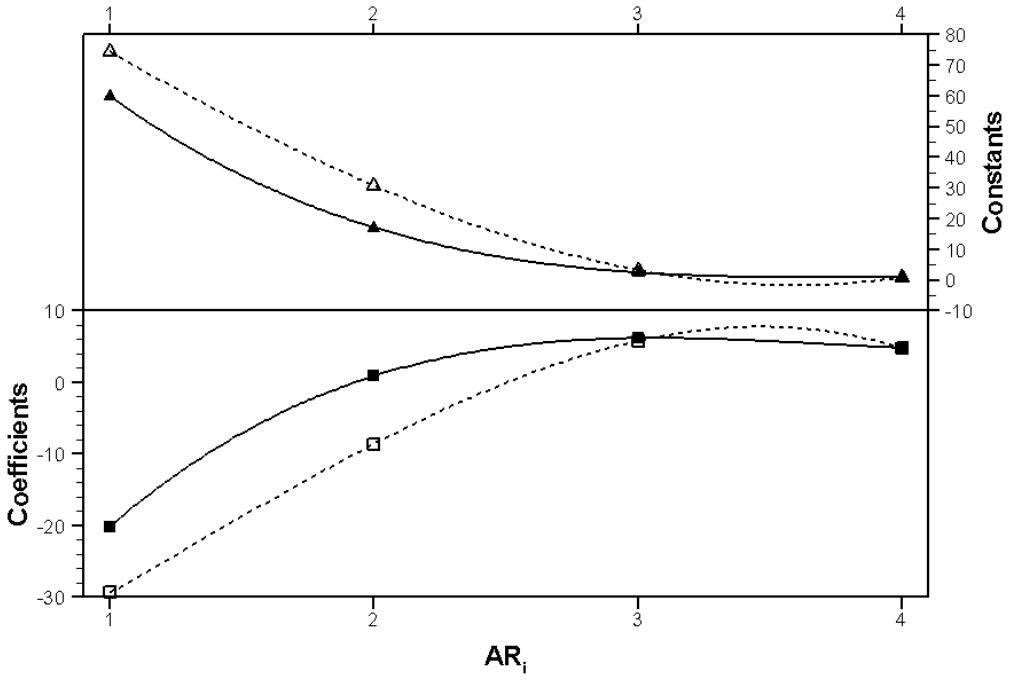

Figure 5.28: XOP-models developed from linear one-predictor-variable model; – – □ – –, coefficient, E–series; —,■,—, coefficient, R–series; – – △ – –, constant, E–series; —,▲,—, constant, R–series

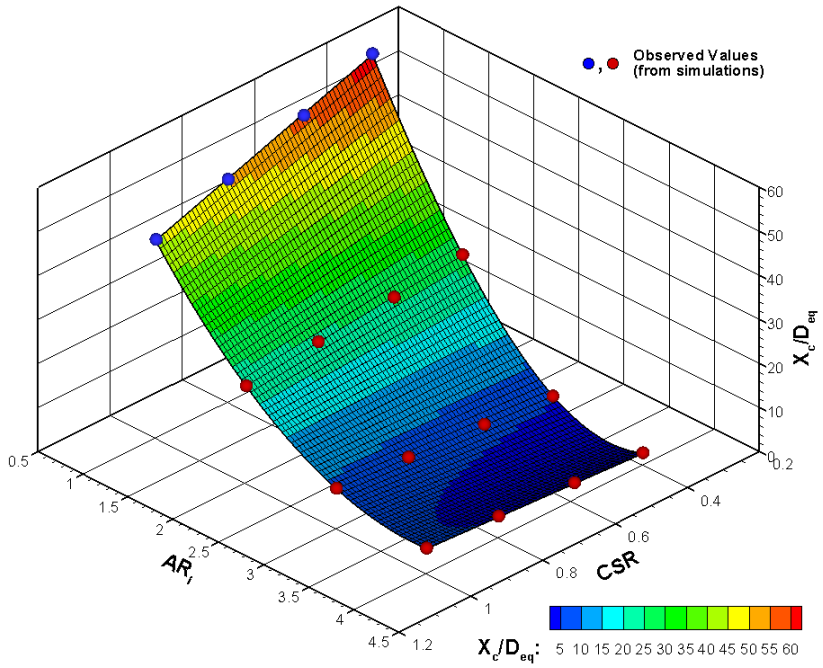

(a) $E-$series

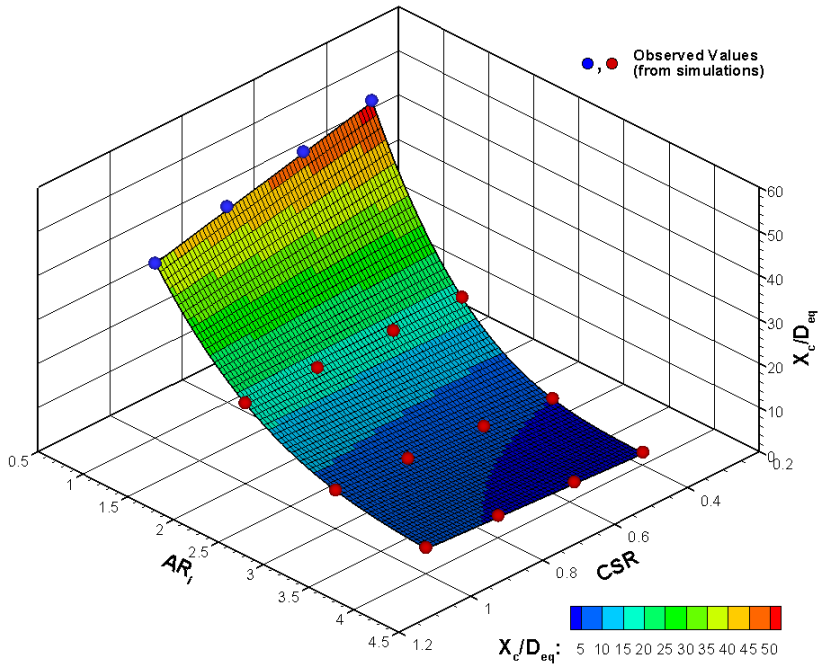

(b) $R-$series

Figure 5.29: Surfaces created using the X_c values calculated from the two XOP-models; the observed values from the CFD simulations are indicated by red circles for cross-over points and by blue circles for transition points

5.3.2.1 Analysis of the XOP-Models

The XOP-models were then tested for error analysis and validation. The error analysis carried out was similar to that for the one-predictor-variable model. The observed and predicted values, along with the sum of squares, for the $E-$ and the $R-$series are given in Tables 5.11 and 5.12, respectively. Based on these calculations, the coefficient of determination (R^2) for both the series comes to 0.9999.

Further analyses were carried out to ensure that the results observed were not biased in any way. These analyses formed part of the validation of the parametric model and are given in the next section.

Table 5.11: Error Analysis of parametric XOP-model for the E−series

	CSR	y_i	f_i	$(y_i\text{-}\bar{y})^2$	$(f_i\text{-}\bar{f})^2$	$(y_i\text{-}f_i)^2$	ε_i
EA1	***0.40***	62.8851	62.5853	1624.1061	1600.0496	0.0899	0.2998
	0.59	56.6425	57.0067	1159.9201	1184.8735	0.1326	-0.3642
	0.80	50.6883	50.8408	789.8011	798.4094	0.0233	-0.1525
	1.00	45.1857	44.9686	510.7962	501.0390	0.0471	0.2171
EA2	***0.40***	27.4395	27.3603	23.5671	22.8060	0.0063	0.0792
	0.59	25.5563	25.7296	8.8292	9.8902	0.0300	-0.1733
	0.80	24.0450	23.9272	2.1319	1.8024	0.0139	0.1178
	1.00	22.1871	22.2107	0.1582	0.1399	0.0006	-0.0236
EA3	***0.40***	5.5478	5.6641	290.2628	286.9833	0.0093	-0.0936
	0.59	6.8772	6.7470	246.7318	250.8317	0.0169	0.1302
	0.80	7.9894	7.9660	213.0286	213.7052	0.0005	0.0234
	1.00	9.0704	9.1270	182.6417	181.1097	0.0032	-0.0566
EA4	***0.40***	2.8705	2.8986	388.6576	387.5433	0.0008	-0.0281
	0.59	3.8284	3.8002	351.8063	352.8586	0.0008	0.0282
	0.80	4.8271	4.7967	315.3395	316.4144	0.0009	0.0304
	1.00	5.7174	5.7457	284.5126	283.5519	0.0008	-0.0283
	SS			**6392.2908**	**6392.0081**	**0.3769**	

Table 5.12: Error Analysis of parametric XOP-model for the R−series

	CSR	y_i	f_i	$(y_i\text{-}\bar{y})^2$	$(f_i\text{-}\bar{f})^2$	$(y_i\text{-}f_i)^2$	ε_i
RA1	***0.40***	51.8169	51.9013	1097.0801	1103.2601	0.0071	-0.0844
	0.59	48.0521	48.0716	861.8569	863.5194	0.0004	-0.0195
	0.80	44.1317	43.8388	647.0410	632.6694	0.0858	0.2929
	1.00	39.6184	39.8076	437.8012	446.1262	0.0358	-0.1892
RA2	***0.40***	17.5091	17.5236	1.4056	1.3508	0.0002	-0.0145
	0.59	17.7100	17.6971	0.9696	0.9777	0.0002	0.0129
	0.80	17.9032	17.8889	0.6265	0.6352	0.0002	0.0143
	1.00	18.0566	18.0715	0.4072	0.3775	0.0002	-0.0149
RA3	***0.40***	4.7780	4.9307	193.6745	189.2066	0.0233	-0.1527
	0.59	6.2531	6.1056	154.7934	158.2639	0.0218	0.1475
	0.80	7.5502	7.4042	124.1999	127.2763	0.0213	0.1460
	1.00	8.4929	8.6410	104.0767	100.9000	0.0219	-0.1481
RA4	***0.40***	2.8705	2.8369	250.4053	251.1902	0.0011	0.0336
	0.59	3.8284	3.7541	221.0069	222.9584	0.0055	0.0743
	0.80	4.8271	4.7678	192.3103	193.7124	0.0035	0.0593
	1.00	5.7174	5.7333	168.4103	167.7698	0.0003	-0.0159
	SS			**4456.0656**	**4460.1941**	**0.2286**	

5.3.2.2 XOP-Model Validation

The residuals (ε_i) between the observed and the predicted values (shown in the last columns in Tables 5.11 and 5.12) are shown in Figure 5.30. The scatter can be seen to exhibit a fairly random pattern. A good fit for a model ensures that these residual errors are normally distributed with a mean (μ) of approximately zero and an unknown standard deviation (σ), which is calculated later. These residual errors are further analysed to determine if they represent a normal distribution. Figure 5.31 shows the histogram of the errors and the corresponding normal distribution curve that fits the current data for both the series. The means of the normal distribution in both the cases are fairly close to zero; although the lower value observed for the elliptic series indicates a better fit of the model.

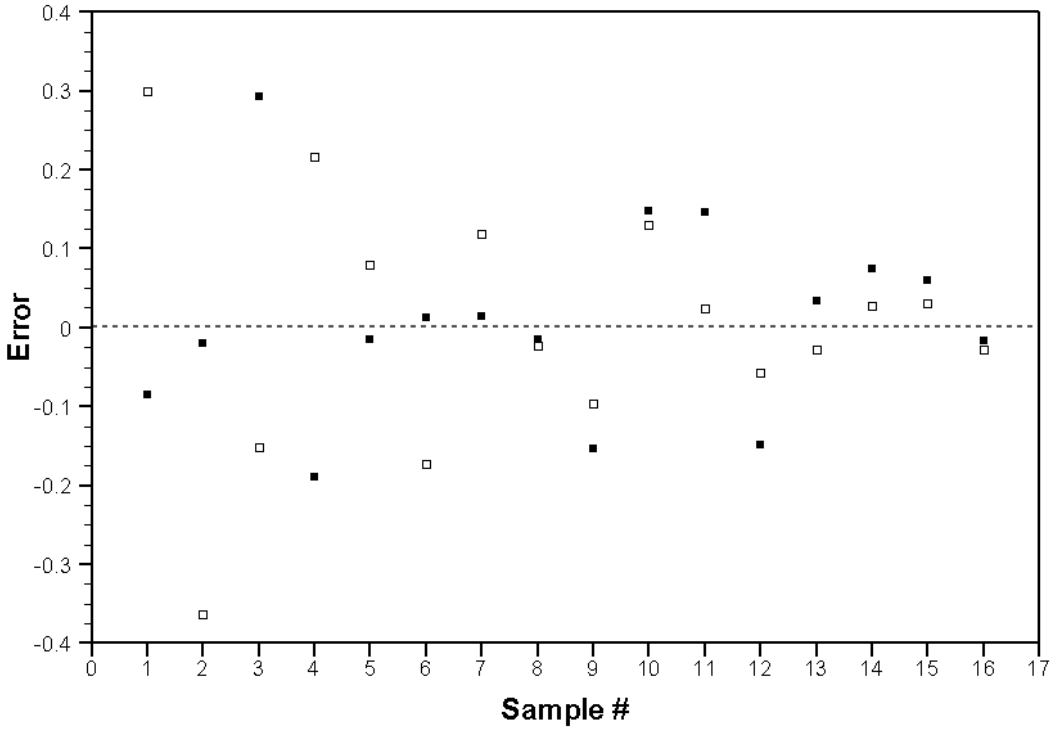

Figure 5.30: Residual error scatter for the parametric XOP-models; □, E−series; ■, R−series

A normal probability plot is generally used as a graphical method for normality testing. This is helpful in assessing if the given data are normally-distributed or not. Since it has already been established that a good fit for any particular model is justified by the presence of unbiased, normally-distributed residual errors, the error data for the current parametric model are checked for normality. The error analyses based on normality testing were done using a built-in function in MATLAB. There are three main elements to these normal probability plots:

- The empirical probability vs. data values for each point are plotted, represented on the figures with a '+' sign. It is to be noted that the scales for probability ($y-$axis) are not linear.
- The thick dashed line, indicating a robust linear-fit, is generated by connecting the 25^{th} and the 75^{th} percentiles of the data. This line is insensitive to the extremities of the sample.
- The thin dashed line is simply an extension of the robust linear-fit and helps in establishing if the data deviated from normality.

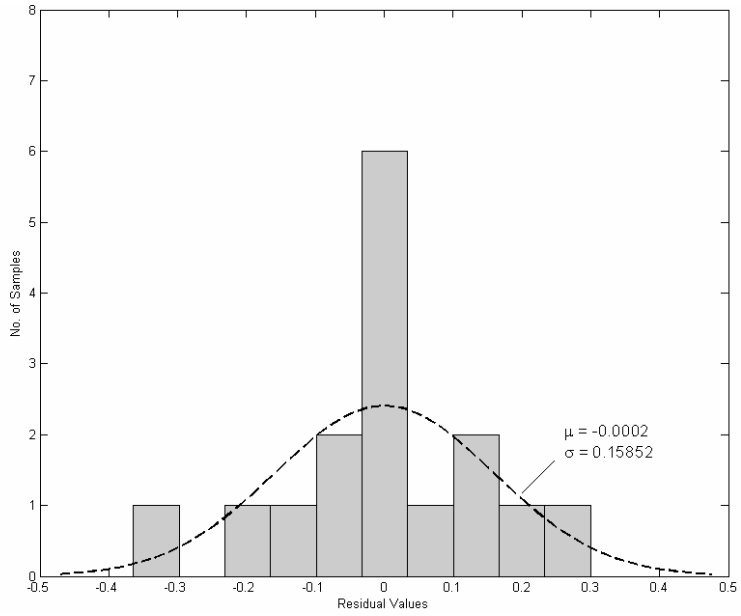

(a) $E-$series

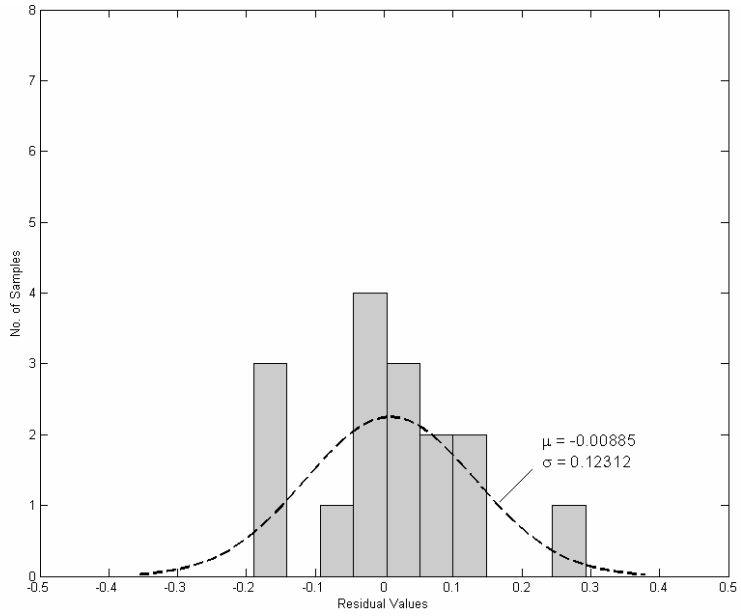

(b) $R-$series

Figure 5.31: Histogram for the residual error and the normal distribution curve for the residuals of XOP-models; the mean (μ) and standard deviation (σ) for each series are specified in the figure

If the data are normally distributed, most of the data points lie close to the linear fit generated by the function. The normal probability plots for the elliptic and the rectangular series are given in Figure 5.32.

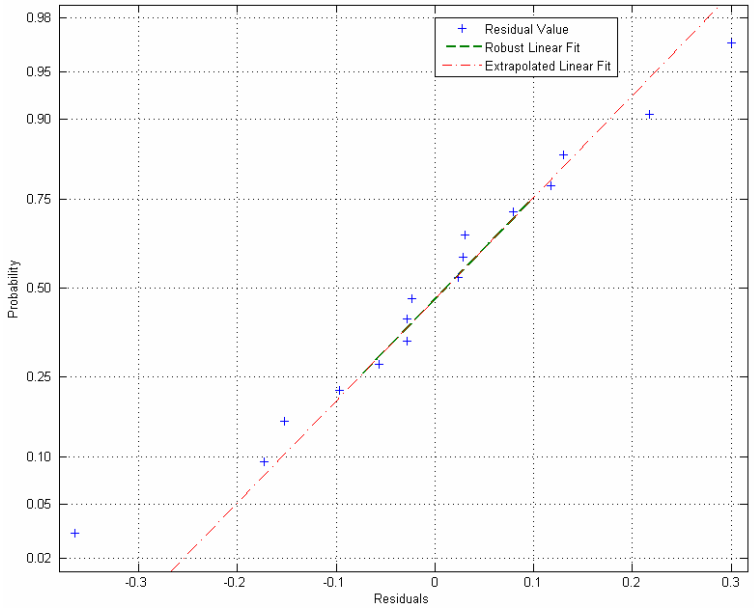

(a) $E-$series

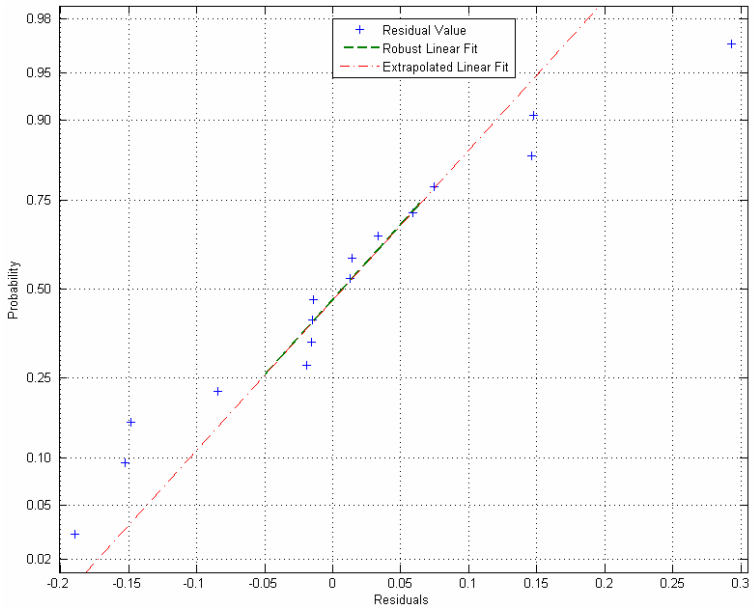

(b) $R-$series

Figure 5.32: Normal probability plots for testing normality of the residual errors of XOP-models

It is clear from both the normal probability plots that the data are normally distributed. A single outlier is observed deviated in case of the $R-$series, indicative that the parametric model in the case of the elliptic series shows a better fit than its rectangular series counterpart.

5.4 Parametric Study Results: Jet Spread

Although the XOP-models are useful in understanding the effect of varying the AR_i and CSR on the location of the cross-over point, the dependence of axis-switching on these variations cannot be fully determined. Since the transition point in case of the $AR_i = 1$ cases is used for determining these models, it is not possible to estimate the possible configurations that might actually show axis-switching within 30 D_{eq} downstream of the exit. Thus, another parametric model is created, based on the difference of jet half-velocity-widths along the major and minor axes at the location 30 D_{eq} from the exit, each for the $E-$ and the $R-$series. This model is referred to as the 'DB30-model'. For the response variable in case of this particular model:

$$\Delta B_{30} = \frac{\left(B_z - B_y\right)}{D_{eq}} \tag{5.3}$$

The ΔB_{30} values obtained from the simulation results are given in Tables 5.4 and 5.5. Depending on the value of ΔB_{30}, it can be estimated if axis-switching has occurred, or not. A positive value indicates that the spread along the major axis is greater than that along the minor axis and hence the jet has not undergone axis-switching. It is therefore clear that a negative ΔB_{30} indicates that axis-switching has occurred. As with the XOP-models, the *CFD* simulation results were identified as the observed values (y_i) and the calculated results from the model were termed as the predicted values (f_i). The equations for the models were developed on similar lines to the earlier parametric models. One-predictor-variable models were proposed based on constant AR_i and constant CSR for each series. All the models were essentially cubic in nature as shown below:

***E*-series, AR_i constant:**

***A1*:** $\Delta B_{30} = -5.0163\,CSR^3 + 14.2488\,CSR^2 - 14.7311\,CSR + 6.0160$

***A2*:** $\Delta B_{30} = -0.1612\,CSR^3 + 0.4125\,CSR^2 - 0.3942\,CSR + 0.0566$

***A3*:** $\Delta B_{30} = -0.0737\,CSR^3 - 0.2586\,CSR^2 + 0.9114\,CSR - 0.9373$

***A4*:** $\Delta B_{30} = 3.9491\,CSR^3 - 10.7276\,CSR^2 + 10.2734\,CSR - 4.0848$

***R*-series, AR_i constant:**

***A1*:** $\Delta B_{30} = -1.8595\,CSR^3 + 6.5071\,CSR^2 - 7.8836\,CSR + 3.5440$
***A2*:** $\Delta B_{30} = -0.0028\,CSR^3 + 0.0046\,CSR^2 - 0.0103\,CSR - 0.1606$
***A3*:** $\Delta B_{30} = 1.5537\,CSR^3 - 3.9639\,CSR^2 + 3.6761\,CSR - 1.6607$
***A4*:** $\Delta B_{30} = 5.4196\,CSR^3 - 14.3272\,CSR^2 + 13.2012\,CSR - 4.8829$

***E*-series, *CSR* constant:**

***C1*:** $\Delta B_{30} = -0.3002\,AR^3 + 2.5783\,AR^2 - 7.7613\,AR + 7.5655$
***C2*:** $\Delta B_{30} = -0.1472\,AR^3 + 1.3238\,AR^2 - 4.2607\,AR + 4.3385$
***C3*:** $\Delta B_{30} = -0.0816\,AR^3 + 0.7521\,AR^2 - 2.5445\,AR + 2.6560$
***C4*:** $\Delta B_{30} = -0.0486\,AR^3 + 0.4575\,AR^2 - 1.6360\,AR + 1.7445$

***R*-series, *CSR* constant:**

***C1*:** $\Delta B_{30} = -0.1963\,AR^3 + 1.6539\,AR^2 - 5.0104\,AR + 4.8835$
***C2*:** $\Delta B_{30} = -0.0973\,AR^3 + 0.8609\,AR^2 - 2.8436\,AR + 2.8558$
***C3*:** $\Delta B_{30} = -0.0474\,AR^3 + 0.4459\,AR^2 - 1.6230\,AR + 1.6741$
***C4*:** $\Delta B_{30} = -0.0367\,AR^3 + 0.3459\,AR^2 - 1.2581\,AR + 1.2569$

An exhaustive analyses similar to that seen in Section 5.3.1 was carried out (not shown here) to determine the best equation set for developing the DB30-model. The constant *CSR* models exhibited a better match to the simulated values. The coefficients of these constant *CSR* models were then analysed and compared with the corresponding *CSR* values for developing the DB30-models. A power-law based correlation was seen for the coefficients with respect to the *CSR* values (Figure 5.33). The resulting equations for determining ΔB_{30} for the two series are given as:

$$\begin{aligned}\Delta B_{30,E} = &-\left(0.0506\ CSR^{-1.9705}\right)\ AR_i^3 + \left(0.4772\ CSR^{-1.8716}\right)\ AR_i^2 \\ &-\left(1.6952\ CSR^{-1.6878}\right)\ AR_i + \left(1.8096\ CSR^{-1.5909}\right)\end{aligned} \tag{5.4}$$

$$\Delta B_{30,R} = -\left(0.0345\ CSR^{-1.8947}\right)\ AR_i^3 + \left(0.3291\ CSR^{-1.7507}\right)\ AR_i^2 - \left(1.2192\ CSR^{-1.5463}\right)\ AR_i + \left(1.2414\ CSR^{-1.5084}\right) \tag{5.5}$$

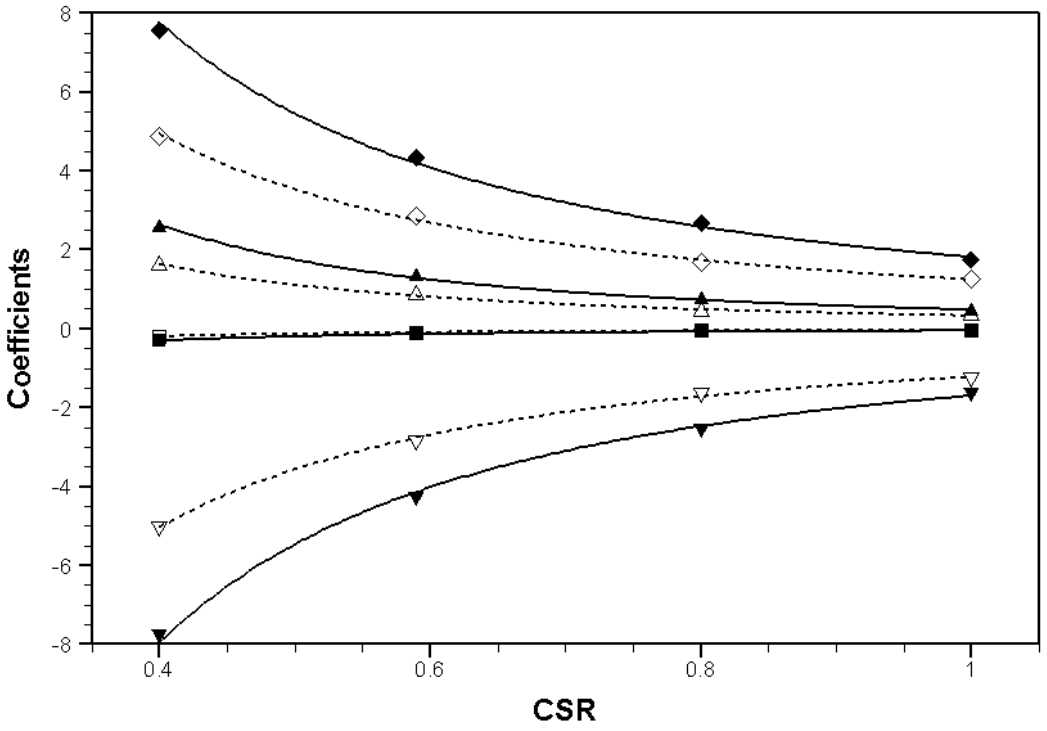

Figure 5.33: Determination of AR_i variation for the DB30-Model developed from the constant CSR model for ΔB_{30}; □, coefficient of the cubic term; △, coefficient of the quadratic term; ▽, coefficient of the linear term; ◇, constant; filled symbols indicate E−series, open symbols indicate R−series

5.4.1 Error Analysis and Validation

5.4.1.1 DB30-Model Error Analysis

These two equations, 5.4 and 5.5, were then used to generate the calculated values (f_i) for the statistical study. The resulting error analyses are given in Tables 5.13 and 5.14 for the $E-$ and the $R-$series, respectively. The sum of squares thus calculated were used to determine the coefficient of determination (R^2). The values of R^2 as calculated for the $E-$ and the $R-$series were 0.9972 and 0.9982, respectively.

Table 5.13: Error Analysis of parametric DB30-model for the E−series

	CSR	y_i	f_i	$(y_i\text{-}\bar{y})^2$	$(f_i\text{-}\bar{f})^2$	$(y_i\text{-}f_i)^2$	ε_i
EA1	***0.40***	2.0823	2.1589	4.9952	4.9662	0.0059	-0.0766
	0.59	1.2544	1.1969	1.6205	1.6040	0.0033	0.0575
	0.80	0.7820	0.7563	0.6929	0.6821	0.0007	0.0257
	1.00	0.5174	0.5410	0.3808	0.3728	0.0006	-0.0236
EA2	***0.40***	-0.0454	-0.0005	0.0057	0.0048	0.0020	-0.0449
	0.59	-0.0655	-0.0919	0.0002	0.0005	0.0007	0.0264
	0.80	-0.0773	-0.0903	0.0002	0.0004	0.0002	0.0130
	1.00	-0.0863	-0.0768	0.0000	0.0001	0.0001	-0.0095
EA3	***0.40***	-0.6188	-0.5508	0.2253	0.2316	0.0046	-0.0680
	0.59	-0.5047	-0.5360	0.2115	0.2175	0.0010	0.0313
	0.80	-0.4114	-0.4303	0.1255	0.1301	0.0004	0.0189
	1.00	-0.3582	-0.3474	0.0736	0.0772	0.0001	-0.0108
EA4	***0.40***	-1.4391	-1.3389	1.5947	1.6111	0.0100	-0.1002
	0.59	-0.9467	-0.9940	0.8425	0.8545	0.0022	0.0473
	0.80	-0.7098	-0.7350	0.4341	0.4428	0.0006	0.0252
	1.00	-0.5899	-0.5744	0.2483	0.2548	0.0002	-0.0155
	SS			**11.4512**	**11.4505**	**0.0326**	

5.4.1.2 DB30-Model Validation

Since the coefficient of determination values for the DB30-models were almost equal to one, it can be said that they show a very good likeness to the actual trend of the observed values. The next step was validation of the model based on the residual error analysis. The scatter plots for the two DB30-models are shown in Figure 5.34. The randomness in the scatter can be seen quite clearly. The histogram of the residual values and the corresponding normal distribution curve fit to the data are given in Figure 5.35. As with the XOP-models, it is evident that the number of samples in the current study for individual series is low. Consequently, although the histograms do not reveal a perfect normal

Table 5.14: Error Analysis of parametric DB30-model for the R−series

	CSR	y_i	f_i	$(y_i\text{-}\bar{y})^2$	$(f_i\text{-}\bar{f})^2$	$(y_i\text{-}f_i)^2$	ε_i
RA1	***0.40***	1.3127	1.3578	2.3985	2.5424	0.0020	-0.0451
	0.59	0.7759	0.7298	1.0239	0.9341	0.0021	0.0461
	0.80	0.4496	0.4503	0.4700	0.4720	0.0000	-0.0007
	1.00	0.3080	0.3168	0.2959	0.3064	0.0001	-0.0088
RA2	***0.40***	-0.1642	-0.1304	0.0052	0.0113	0.0011	-0.0338
	0.59	-0.1657	-0.1967	0.0049	0.0016	0.0010	0.0310
	0.80	-0.1674	-0.1807	0.0047	0.0031	0.0002	0.0133
	1.00	-0.1692	-0.1566	0.0045	0.0064	0.0002	-0.0126
RA3	***0.40***	-0.7251	-0.6945	0.2392	0.2096	0.0009	-0.0306
	0.59	-0.5526	-0.5903	0.1002	0.1250	0.0014	0.0377
	0.80	-0.4613	-0.4707	0.0508	0.0548	0.0001	0.0094
	1.00	-0.3949	-0.3858	0.0252	0.0222	0.0001	-0.0091
RA4	***0.40***	-1.5479	-1.5093	1.7211	1.6195	0.0015	-0.0386
	0.59	-0.9684	-1.0137	0.5364	0.6037	0.0021	0.0453
	0.80	-0.7165	-0.7357	0.2309	0.2490	0.0004	0.0192
	1.00	-0.5893	-0.5778	0.1248	0.1163	0.0001	-0.0115
	SS			**7.2363**	**7.2775**	**0.0132**	

distribution in terms of the bin counts, the data are still normally distributed with mean (μ) and sigma (σ) of -0.0065 and 0.0461 for the $E-$series, and 0.0007 and 0.0297, correspondingly for the $R-$series. The normality of the residual errors was then tested using a normal probability plot (Figure 5.36) for each series. The data show a very good fit across most of the points; the presence of two extreme outliers may be seen for both the cases that do not show a good match with respect to the extrapolated robust linear fit. In general, however, the residual error data were acceptable as normally distributed and the model exhibited a reasonable match with the observed values.

Following the validation of the model, it could now be implemented to de-

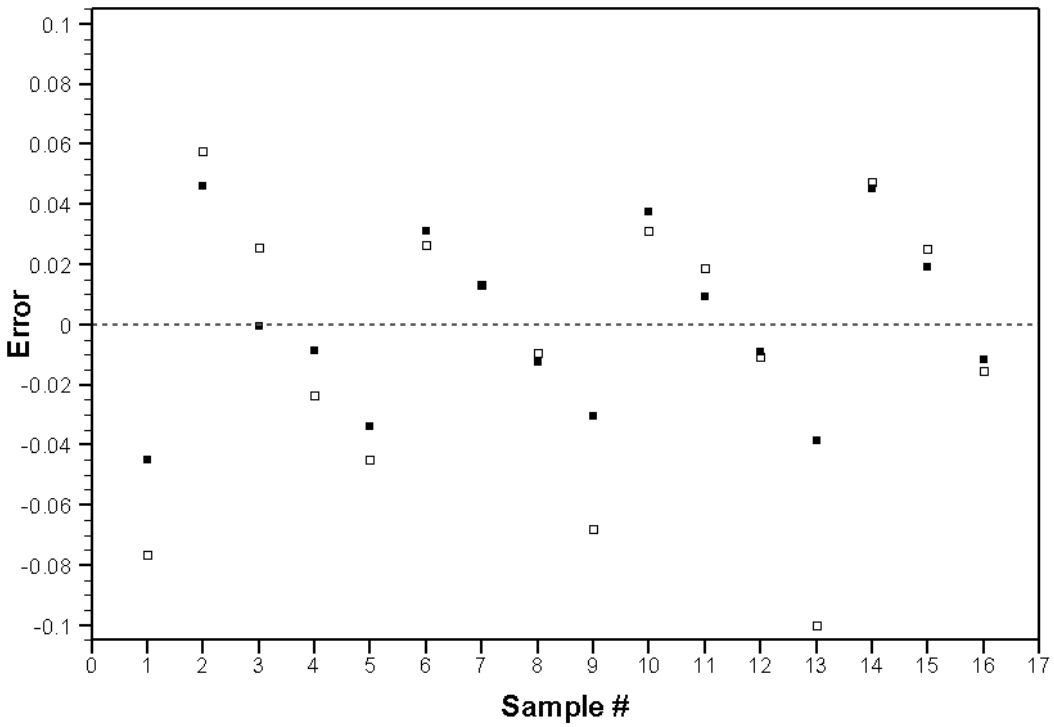

Figure 5.34: Residual error scatter for the parametric DB30-models; □, E−series; ■, R−series

termine the different possible configurations of the nozzle based on AR_i and CSR variation that exhibit axis-switching. A grid was created with increments of 0.1 each in case of both the parameters (Figure 5.37). The models were then used to predict the corresponding values of ΔB_{30}. All positive values indicate absence of axis-switching; these were shown using light-coloured squares in the grid. On the other hand, all negative values of ΔB_{30} indicate that the jet spread along the minor axis to be greater than that along the major axis, thus indicating the occurrence of axis-switching (dark-coloured squares in the grid).

The XOP and DB30 models could now be used for the AR_e = 4 nozzles in the current study to determine if they switch axes and, if so, the location of the cross-over point downstream of the exit (Figures 5.29 and 5.37). In cases where the model indicates that a particular configuration does not switch axes, the location of the cross-over point corresponds to the point where the jet spreading along the spanwise axes becomes almost equal.

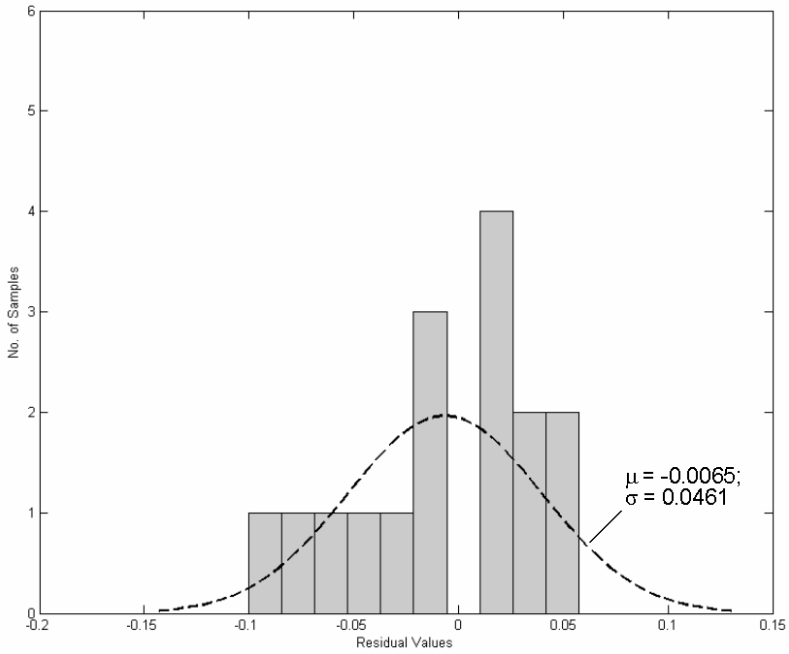

(a) $E-$series

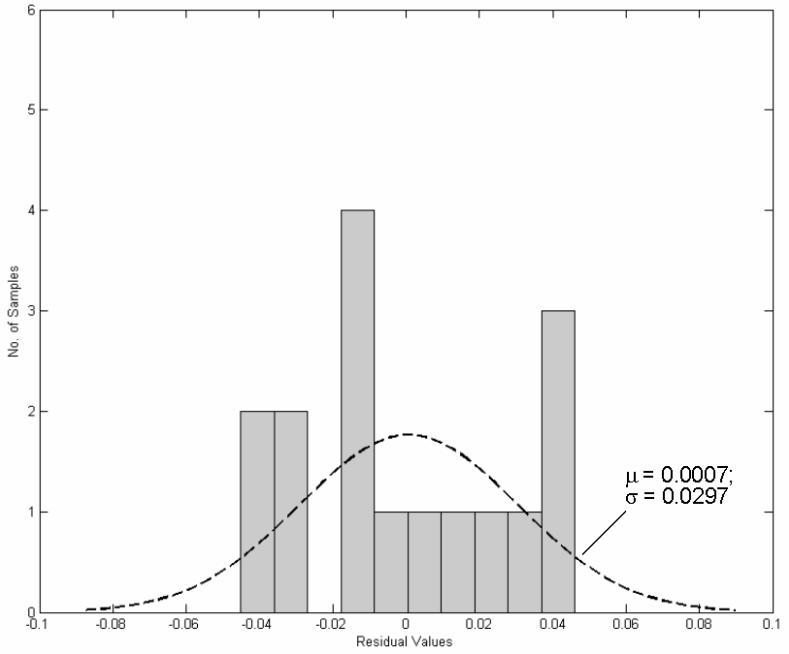

(b) $R-$series

Figure 5.35: Histogram for the residual error and the normal distribution curve for the residuals of DB30-models; the mean (μ) and standard deviation (σ) for each series are specified in the figure

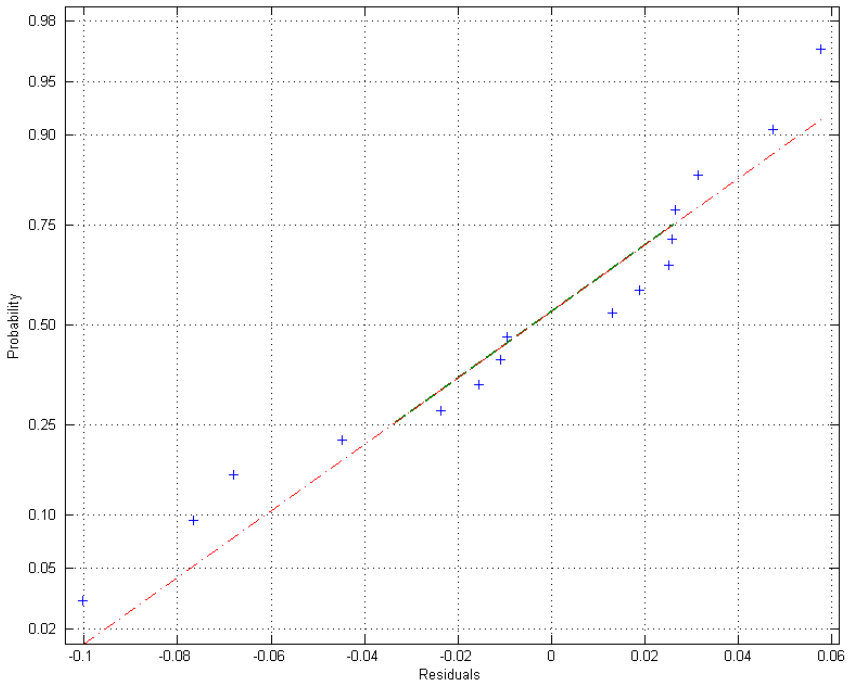

(a) $E-$series

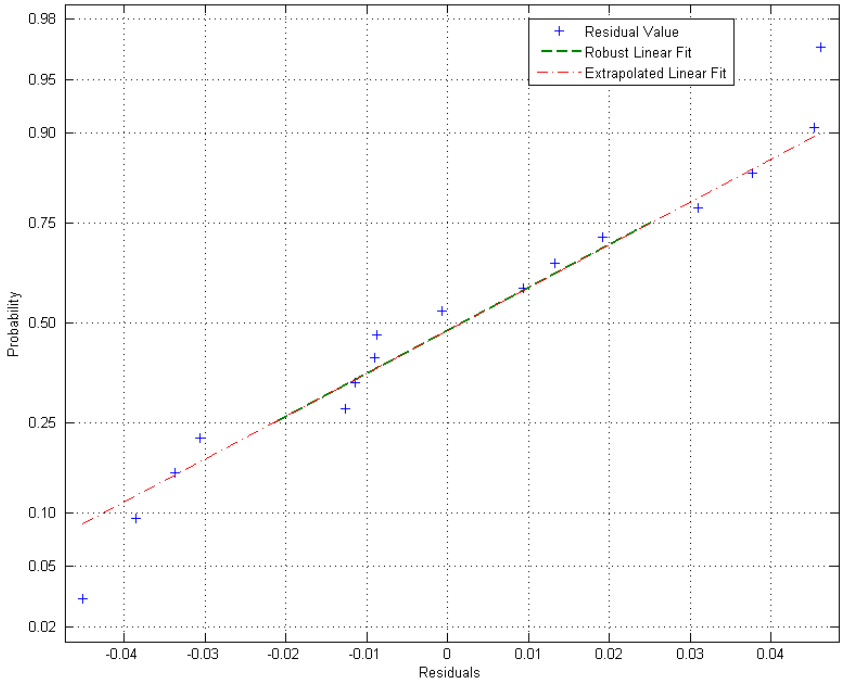

(b) $R-$series

Figure 5.36: Normal probability plots for testing normality of the residual errors of DB30-models

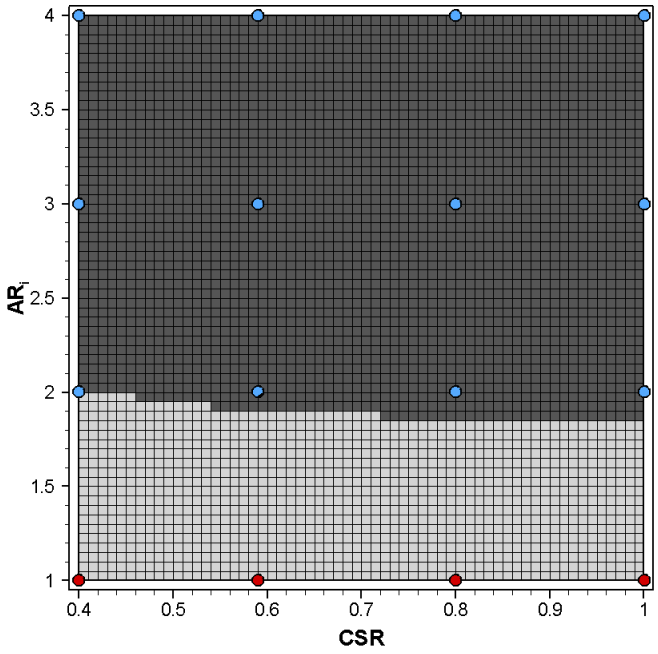

(a) $E-$series

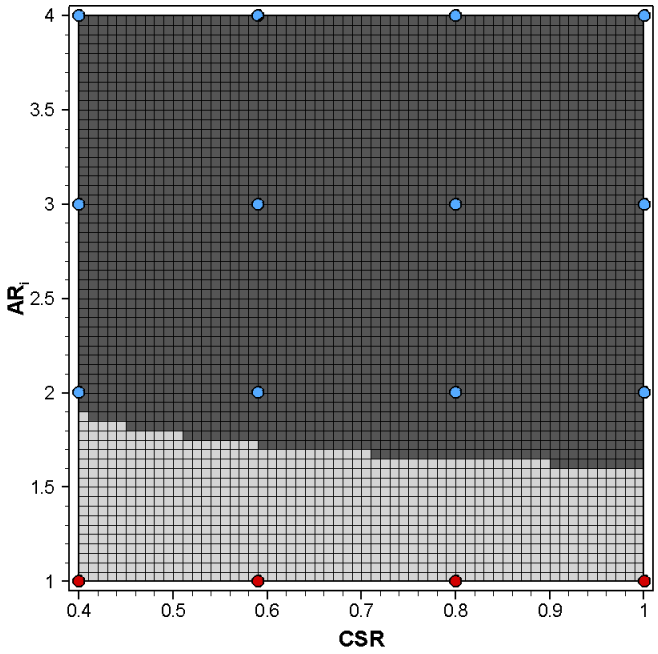

(b) $R-$series

Figure 5.37: Estimation of axis-switching based on the geometric criteria, AR_i and CSR; dark squares indicate occurrence of axis-switching before 30 D_{eq} downstream of the exit, light squares indicate otherwise; CFD results are shown for the respective configurations, blue circles indicate switching cases, whilst red circles indicate non-switching cases

5.5 Additional Results

Following the study to understand the combined effects of inlet aspect ratio and converging section length variation, another parameter that was considered for variation was the nozzle pressure ratio (*NPR*). As mentioned earlier, it is known that a convergent nozzle, when non-ideally expanded, produces a shock-cell structure that might assist axis-switching. This is due to the presence of screech; the discrete tones associated with shock-noise, caused due to unsteady structures in the jet interacting with the shock-cells. This, however, is a complete comprehensive study in itself. Since the numerical part of the current study involved steady state behaviour of the jet, it would have been impossible to capture the effects of screech on the jet development using the *CFD* simulations. As a result, the understanding of *NPR* effects combined with the variation of AR_i and *CSR* is recommended for future work.

Some preliminary work, however, was carried out related to supersonic jet flow from the *AR*4 nozzle. Experiments based on background-oriented schlieren (*BOS*) and conventional schlieren were performed for the jet running at *NPR* 2.5 and 3.5. Steady-state *CFD* simulations were also run for these cases with the *AR*4 nozzle. Some data related to this study are presented in Appendix E. The validation of background-oriented schlieren, based on the circular, Stratford nozzle results, is also given in the same appendix. The data from these simulations and experiments are, though, not very different from those of the subsonic jet study, their relevance to this part of the work is limited. All the results and discussions related to the supersonic jet study are considered beyond the scope of the main study and are therefore contained in Appendix E.

Chapter 6

Conclusions and Future Work

Experiments and simulations were performed to understand the effects of changing the internal geometry of an aspect ratio 4 rectangular, converging nozzle on the development of the free jet issuing from it. The study was carried out for subsonic flow at nozzle pressure ratio of 1.05. Changes in the internal geometry were achieved by varying two parameters: inlet aspect ratio (AR_i) and length of the converging section (expressed as a ratio to the total length of the nozzle; CSR). The external geometry of the nozzle was based on an existing nozzle (called $AR4$ nozzle) that was employed for experiments to generate validation data for the simulations. Consequently, the variation in AR_i was limited from 1 to 4 while that in CSR was limited from 0.4 to 1.0, due to the physical dimensions of the $AR4$ nozzle. The inlet area was unaltered, thus maintaining the converging ratio of the nozzle in all the cases.

Two variations were considered for the inlet geometry: elliptic and rectangular. The geometry of the exit was maintained constant through the whole study. The variation in the jet development was observed on the basis of axis-switching; the location of the cross-over point (X_c) and the difference in the jet-half-velocity-widths along the major and minor axes at 30 D_{eq} from the exit (ΔB_{30}) were considered as the parameters to determine if axis-switching occurred for a given combination of AR_i and CSR, and if yes, the corresponding location of X_c. The conclusions of the current study are provided in Section 6.1. Additional work recommended as an extension to the current study has been given in Section 6.2.

6.1 Conclusions

Based on the work carried out in the current study, the following conclusions can be drawn:

- The internal geometry of the nozzle affects the centreline velocity at the exit (V_{exit}). This variation in V_{exit} is non-linear with respect to both AR_i and CSR;

it increases with an increase in either parameter. The flow, however, accelerates after exiting the nozzle and reaches the expected jet Mach number, $M_j \approx 0.265$, corresponding to $NPR = 1.05$.

- The jet-half-velocity-widths are studied up to 30 D_{eq} from the exit. These give us information about the two parameters, X_c and ΔB_{30}, for ascertaining the variation of axis-switching with respect to AR_i and CSR.
  - For a constant AR_i, the X_c variation is roughly linear to variation in CSR with a higher CSR implying a higher X_c value. Exceptions to this trend were the $EA1$, $EA2$ and $RA1$ configurations where although a linear variation was observed, a higher CSR corresponded to lower X_c values.
  - The X_c values vary inversely and non-linearly with respect to the inlet aspect ratio variation, the CSR being kept constant.
  - For any combination of AR_i and CSR, the X_c values are lower for the rectangular series compared to their elliptic counterparts.
  - The variation in ΔB_{30} is non-linear with respect to both AR_i and CSR; a positive ΔB_{30} indicates that the jet has resisted axis-switching by 30 D_{eq} from the nozzle exit.
- From the analyses of the flow features at the nozzle exit, we observe that the sense of the streamwise vorticity is primarily dependent on the AR_i whilst the magnitude of the vorticity is dependent mainly on the CSR of the nozzle. This is further confirmed from the observations noted for the development of vorticities inside the nozzle. These 'ω_x-induced' vortices affect the flow development; either assisting or resisting the initial axis-switching, depending on their sense and strength. The 'out-flow' pairs, rotating to induce flow into the jet on the long sides and out on the short sides, resist axis-switching. The 'in-flow' pairs work in the opposite sense and, thus, promote axis-switching.
- Based on the results obtained from the simulations for the elliptic and the rectangular series, two parametric models, XOP and $DB30$, are created to predict the occurrence of axis-switching. The XOP models can estimate the location of the cross-over/transition point for the given configuration.

The *DB*30 models, on the other hand, are useful for establishing if axis-switching has occurred for that configuration. The equations governing these two models for each series are given as:

– ***E*-series:**

$$X_{c,E} = \left(-1.5093\,AR^3 + 5.8602\,AR^2 + 13.7631\,AR - 47.4752\right)\,CSR + \left(1.5140\,AR^3 - 1.0513\,AR^2 - 50.9806\,AR + 124.8477\right) \tag{6.1}$$

$$\Delta B_{30,E} = -\left(0.0506\,CSR^{-1.9705}\right)\,AR_i^3 + \left(0.4772\,CSR^{-1.8716}\right)\,AR_i^2 - \left(1.6952\,CSR^{-1.6878}\right)\,AR_i + \left(1.8096\,CSR^{-1.5909}\right) \tag{6.2}$$

– ***R*-series:**

$$X_{c,R} = \left(1.5285\,AR^3 - 17.0702\,AR^2 + 61.5803\,AR - 66.1947\right)\,CSR + \left(-2.4923\,AR^3 + 29.0058\,AR^2 - 112.3766\,AR + 145.8268\right) \tag{6.3}$$

$$\Delta B_{30,R} = -\left(0.0345\,CSR^{-1.8947}\right)\,AR_i^3 + \left(0.3291\,CSR^{-1.7507}\right)\,AR_i^2 - \left(1.2192\,CSR^{-1.5463}\right)\,AR_i + \left(1.2414\,CSR^{-1.5084}\right) \tag{6.4}$$

Within the scope of this study, these two models are useful for determining if a nozzle of any combination of AR_i and CSR switches axes, or not; and if yes, the location of the cross-over point.

6.2 Proposed Future Work

Within the scope of this study, the two parametric models proposed each for the elliptic and rectangular series, are able to predict the location of the cross-over/transition point and the occurrence of axis-switching accurately; ≈ 95% lie within ±3% for the XOP-model and ≈ 75% lie within ±7.5% for the DB30-model, when compared to the *CFD* simulation results. It was felt that there are, however, some areas that might need more investigation and understanding. These form the part of proposed future work as given below:

- *Understanding the effects of NPR variation*: A brief description is provided in Appendix E regarding the effects of changing the *NPR* on the development of the free jet issuing from the *AR*4 nozzle. That particular exercise was,

however, aimed more towards development of the background-oriented schlieren technique for future supersonic flow experiments. The study based on *NPR* variation could be carried out in two stages:

  - Experimental data using *LDA* and *BOS*; the *LDA* can provide both steady and time-dependent velocity and turbulence data while the *BOS* can provide steady state density data for the flow-field.
  - Data from *CFD* simulations for unsteady state to incorporate the effects of screech on axis-switching.

- *Expanding the variation*: The variation in AR_i and *CSR* for the current study is limited from 1 to 4 and 0.4 to 1.0, respectively, due to the dimensions of the exterior geometry. With appropriate changes to the exterior nozzle geometry, we can include a greater variation in the two parameters; for AR_i from 0 to $+\infty$, and for *CSR* from 0 (i.e. slot nozzle) to 1. All the while, we maintain the nozzle exit geometry constant.

- *Understanding the subsonic flow-field*: The experiment for the current study was not particularly ideal. One of the reasons was the absence of complete flow-field data for the in situ configuration with major axis horizontal. A possible way to overcome this is by use of a three-dimensional *LDA* system or using stereoscopic particle image velocimetry (*PIV*) to capture the entire flow-field, as necessary.

References

References

Abramovich, G. N. (1982). On the deformation of the rectangular turbulent jet cross-section. *International Journal of Heat Mass Transfer*, *25*(12), 1885–1894.

AIAA (1998). *AIAA Guide for Verification and Validation of Computational Fluid Dynamics Simulations*. AIAA. AIAA G-077-1998.

Alkislar, M. B., Lourenco, L. M., & Krothapalli, A. (2000). Stereoscopic piv measurements of a screeching supersonic jet. *Journal of Visualization*, *3*(2), 135–143.

Anufriev, V. M., Komarov, V. V., Kuptsov, V. M., Mel'nikov, D. A., & Sergienko, A. A. (1969). Discrete component in the noise spectrum of supersonic jets. *Izv. AN SSSR. Mekhanika Zhidkosti i Gaza*, *4*, 162–165.

Arms, R. J. & Hama, F. R. (1965). Localized-induction concept on a curved vortex and motion of an elliptic vortex ring. *Physics of Fluids*, *8*(4), 553–559.

Bradshaw, P. (1987). Turbulent secondary flows. *Annual Review of Fluid Mechanics*, *19*, 53–74.

Brown, G. L. & Roshko, A. (1974). On density effects and large structure in turbulent mixing layers. *Journal of Fluid Mechanics*, *64*, 775–816.

Cabrita, P. M. (2006). *Steady and Unsteady Features of Twin-Jet STOVL Ground Effects*. Phd thesis, Cranfield University, Shrivenham, Defence Academy, UK.

CompAir (2008). *User Manual: Screw Air Compressor: L90 - L132, L110 - L132SR*. CompAir.

Crow, S. C. & Champagne, F. H. (1971). Orderly structure in jet turbulence. *Journal of Fluid Mechanics*, *48*, 547–591.

Curtis, P. (1987). Investigation into the behaviour of a single jet in free air and impinging perpendicularly on the ground. Technical Report BAe-KAD-R-RES-3349, British Aerospace.

Dantec (2000). *BSA/FVA Flow Software: Installation and User's Guide* (4^{th} ed.). Denmark: Dantec Measurement Technology.

Demuren, A. O. (1991). Calculation of turbulence-driven secondary motion in ducts with arbitrary cross section. *AIAA Journal*, *29*(4), 531–537.

Demuren, A. O. (1993). On the generation of secondary motion in circular to rectangular transition ducts. Number 1993–0681 in AIAA, Reno, NV. 31st Aerospace Science Meeting and Exhibit.

Dhanak, M. R. & Bernardinis, B. (1981). The evolution of an elliptic vortex ring. *Journal of Fluid Mechanics*, *109*, 189–216.

Donaldson, C. D. & Snedeker, R. S. (1971). A study of free jet impingement. part 1. mean properties of free and impinging jets. *Journal of Fluid Mechanics*, *45*(2), 281–319.

Dring, R. P. (1982). Sizing criteria for laser anemometry particles. *Journal of Fluids Engineering*, *104*, 15–17.

Durst, F., Melling, A., & Whitelaw, J. H. (1981). *Principles and Practice of Laser-Doppler Anemometry* (2nd ed.). London: Academic Press.

Foreman, Jr., J. W., George, E. W., & Lewis, R. D. (1965). Measurement of localized flow velocities in gases with a laser doppler flowmeter. *Applied Physics Letters*, *7*, 77–78.

George, Jr., W. K., Beuther, P. D., & Lumley, J. L. (1979). Processing of random signals. Dynamic measurements in unsteady flows; Proceedings of the Dynamic Flow Conference 1978, (pp. 757–800)., Denmark.

Glass, D. R. (1968). Effects of acoustic feedback on the spread and decay of supersonic jets. *AIAA Journal*, *6*(10), 1890–1897.

Goldstein, R. J. & Kreid, D. K. (1967). Measurement of laminar flow development in a square duct using a laser-doppler flowmeter. *Journal of Applied Mechanics*, *34*, 813–818.

Grinstein, F. F. (1993). Vorticity dynamics in spatially developing rectangular jets. Number 1993–2286 in AIAA, Orlando, Florida. Shear Flow Conference.

Grinstein, F. F. (1997). Entrainment, axis switching, and aspect-ratio effects in rectangular free jets. Number 1997–1875 in AIAA, Snowmass Village, CO, USA. 4th Shear Flow Control Conference.

Gutmark, E. & Ho, C.-M. (1983). Preferred modes and the spreading rates of jets. *Physics of Fluids*, *26*(10), 2932–2938.

Gutmark, E., Schadow, K. C., Parr, T. P., Hanson-Parr, D. M., & Wilson, K. J. (1989). Noncircular jets in combustion systems. *Experiments in Fluids*, *7*(4), 248–258.

Gutmark, E. J. & Grinstein, F. F. (1999). Flow control with noncircular jets. *Annual Review of Fluid Mechanics*, *31*, 239–272.

Hammond, A. D. (1966). Thrust losses in hovering for jet vtol aircraft. Technical Report SP-116, NASA.

Hargather, M. J. & Settles, G. (2010). Natural-background-oriented schlieren imaging. *Experiments in Fluids*, *48*(1), 59–68.

Hertzberg, J. R. & Ho, C.-M. (1992). Time-averaged, three-dimensional flow in a rectangular sudden expansion. *AIAA Journal*, *30*(10), 2420–2425.

Ho, C.-M. & Gutmark, E. (1987). Vortex induction and mass entrainment in a small-aspect-ratio elliptic jet. *Journal of Fluid Mechanics*, *179*, 383–405.

Husain, H. S. & Hussain, F. (1983). Control excitation of elliptic jet. *Physics of Fluids*, *26*, 2763–2766.

Hussain, A. K. M. F. (1986). Coherent structures and turbulence. *Journal of Fluid Mechanics*, *173*, 303–356.

Hussain, F. & Husain, H. S. (1989). Elliptic jets. part 1. characteristics of unexcited and excited jets. *Journal of Fluid Mechanics*, *208*, 257–320.

Kader, B. (1981). Temperature and concentration profiles in fully turbulent boundary layers. *International Journal of Heat Mass Transfer*, *24*(9), 1541–1544.

Kak, A. C. & Slaney, M. (1988). *Principles of Computerized Tomographic Imaging*. New York: IEEE Press.

Kassab, S. Z., Bakry, A. E., & Warda, H. A. (1996). Laser doppler anemometry measurements in an axisymmetric turbulent jet. *Review of Scientific Instruments*, *67*(5), 1842–1849.

Kleinstein, G. (1964). Mixing in turbulent axially symmetric free jets. *Journal of Spacecraft*, *1*(4), 403–408.

Knowles, K. & Saddington, A. J. (2002). Modelling and experiments on under-expanded turbulent jet mixing. In *5th Engineering Turbulence Modelling and Measurements*, Mallorca, Spain.

Knowles, K. & Saddington, A. J. (2006). A review of jet mixing enhancement for aircraft propulsion applications. *Proceedings of the Institution of Mechanical Engineers, Part G: Journal of Aerospace Engineering*, *220*(2), 103–127.

Krothapalli, A., Baganoff, D., & Karamcheti, K. (1981). On the mixing of a rectangular jet. *Journal of Fluid Mechanics*, *107*, 201–220.

Lau, J. C. (1981). Effects of exit mach number and temperature on mean-flow and turbulence characteristics in round jets. *Journal of Fluid Mechanics*, *105*, 193–218.

Lau, J. C., Morris, P. J., & Fisher, M. J. (1979). Measurements in subsonic and supersonic free jets using a laser velocimeter. *Journal of Fluid Mechanics*, *93*(1), 1–27.

Launder, B. E. & Spalding, D. B. (1972). *Lectures in Mathematical Models of Turbulence*. London, England: Academic Press.

Launder, B. E. & Spalding, D. B. (1974). The numerical computation of turbulent flows. *Computer Methods in Applied Mechanics and Engineering*, *3*(2), 269–289.

Lepicovsky, J. (1990). Total temperature effects on centerline mach number characteristics of freejets. *AIAA Journal*, *28*(3), 478–482.

Liepmann, D. & Gharib, M. (1992). The role of streamwise vorticity in the near-field entrainment of round jets. *Journal of Fluid Mechanics*, *245*, 643–668.

Mathieu, J. & Charnay, G. (1981). Stucture and development of turbulent jets. Number CP 308 in AGARD, (pp. 9–1–9–23). Fluid Dynamics of Jets with Applications to V/STOL.

Meier, G. E. A. (2002). Computerized background-oriented schlieren. *Experiments in Fluids*, *33*, 181–187.

Menter, F. R. (1994). Two-equation eddy-viscosity turbulence models for engineering applications. *AIAA Journal*, *32*(8), 1598–1605.

Merzkirch, W. (1987). *Flow Visualization* (2nd ed.). Academic Press.

Mie, G. (1908). Beiträge zur optik trüber medien, speziell kolloidaler metallösungen. *Annalen der Physik*, *330*(3), 377–445.

Moustafa, G. H. (1993). Further study of high speed single free jets. *Aeronautical Journal*, *97*, 171–176.

Neemeh, R., AlGattus, S., & Neemeh, L. (1999). Experimental investigation of noise reduction in supersonic jets due to jet rotation. *Journal of Sound and Vibration*, *221*(3), 505–524.

NIST (2003). *NIST/SEMATECH e-Handbook of Statistical Methods* (Updated 06/02/2010 ed.). http://www.itl.nist.gov/div898/handbook/.

Papamoschou, D. & Roshko, A. (1988). The compressible turbulent shear layer: an experimental study. *Journal of Fluid Mechanics*, *197*, 453–477.

Perkins, H. J. (1970). The formation of streamwise vorticity in turbulent flow. *Journal of Fluid Mechanics*, *44*(4), 721–740.

Powell, A. (1953). On the mechanism of choked jet noise. *Proceedings of the Physical Society Section*, *66*(12B), 1039–1056.

Prandtl, L. (1952). *Essentials of Fluid Dynamics* (1st ed.). London and Glasgow: Blackie and Son Limited.

Quinn, W. R. (1992). Streamwise evolution of a square jet cross section. *AIAA Journal*, *30*(12), 2852–2857.

Raffel, M., Willert, C. E., & Kompenhans, J. (1998). *Particle Image Velocimetry: A Practical Guide* (1st ed.). Experimental Fluid Mechanics. Springer-Verlag.

Raman, G. (1997). Cessation of screech in underexpanded jets. *Journal of Fluid Mechanics*, *336*, 69–90.

Raman, G. (1998). Advances in understanding supersonic jet screech: Review and perspective. *Progress in Aerospace Sciences*, *34*, 45–106.

Ribeiro, M. M. & Whitelaw, J. H. (1980). The structure of turbulent jets. *Proceedings of the Royal Society of London. Series A. Mathematical and Physical Sciences*, *370*, 281–301.

Rodi, W. (1984). *Turbulence Models and their Application in Hydraulics - A State of the Art Review* (2^{nd} ed.). Delft, The Netherlands: International Association for Hydraulic Research.

Schadow, K. C., Gutmark, E. J., Parr, D. M., & Wilson, K. J. (1988). Selective control of flow coherence in triangular jets. *Experiments in Fluids*, *8*(2), 129–135.

Settles, G. S. (2001). *Schlieren and Shadowgraph Techniques* (1^{st} ed.). Experimental Fluid Mechanics. Springer-Verlag.

Sfeir, A. A. (1976). The velocity and temperature fields of rectangular jets. *International Journal of Heat Mass Transfer*, *19*, 1289–1297.

Sforza, P. M. (1969). A quasi-axisymmetric approximation for turbulent three-dimensional jets and wakes. *AIAA Journal*, *7*(7), 1380–1383.

Sforza, P. M., Steiger, M. H., & Trentacoste, N. (1966). Studies on three-dimensional viscous jets. *AIAA Journal*, *4*(5), 800–806.

Spalart, P. & Allmaras, S. (1992). A one-equation turbulence model for aerodynamic flows. Technical Report AIAA-92-0439, American Institute of Aeronautics and Astronautics.

Spalart, P. R. (2003). A versatile implementation of acoustic analogy based noise prediction method in a general purpose cfd code. *International Journal of Heat and Fluid Flow*, *21*, 252–263.

Tam, C. K. W. (1998). Influence of nozzle geometry on the noise of high-speed jets. *AIAA Journal*, *36*(8), 1396–1400.

Trentacoste, N. & Sforza, P. M. (1967). Further experimental results for three-dimensional free jets. *AIAA Journal*, *5*(5), 885–891.

Tsuchiya, Y. & Horikoshi, C. (1986). On the spread of rectangular jets. *Experiments in Fluids*, *4*(4), 197–204.

Van Doormaal, J. P. & Raithby, G. D. (1984). Enhancements of the simple method for predicting incompressible fluid flows. *Numerical Heat Transfer, Part A: Applications*, *7*(2), 147–163.

Vandsburger, U. & Ding, C. (1995). The spatial modulation of a forced triangular jet. *Experiments in Fluids*, *18*(4), 239–248.

Venkatakrishnan, L. (2005). Density measurements in an axisymmetric underexpanded jet by background-oriented schlieren technique. *AIAA Journal*, *43*(7), 1574–1579.

Venkatakrishnan, L. & Meier, G. E. A. (2004). Density measurements using the background oriented schlieren technique. *Experiments in Fluids*, *37*, 237–247.

Viets, H. & Sforza, P. M. (1972). Dynamics of bilaterally symmetric vortex rings. *Physics of Fluids*, *15*(2), 230.

Wilcox, D. C. (1998). *Turbulence Modeling for CFD*. La Canada, California: DCW Industries, Inc.

Witze, P. O. (1974). Centerline velocity decay of compressible free jets. *AIAA Journal*, *12*(4), 417–418.

Wygnanski, I. & Fiedler, H. (1969). Some measurements in the self-preserving jet. *Journal of Fluid Mechanics*, *38*(3), 577–612.

Yakhot, V. & Orszag, S. A. (1986). Renormalization group analysis of turbulence: I. basic theory. *Journal of Scientific Computing*, *1*(1), 1–51.

Yeh, Y. & Cummins, H. Z. (1964). Localized fluid flow measurements with an he-ne laser spectrometer. *Applied Physics Letters*, *4*, 176–178.

Zaman, K. B. M. Q. (1996a). Axis switching and spreading of an asymmetric jet: the role of coherent structure dynamics. *Journal of Fluid Mechanics*, *316*, 1–27.

Zaman, K. B. M. Q. (1996b). Spreading characteristics and thrust of jets from asymmetric nozzles. Number 1996–0200 in AIAA, Reno, NV. 34^{th} Aerospace Sciences Meeting and Exhibit.

Zaman, K. B. M. Q. (1999). Spreading characteristics of compressible jets from nozzles of various geometries. *Journal of Fluid Mechanics*, *383*, 197–228.

Zaman, K. B. M. Q., Steffen, C. J., & Reddy, D. R. (1997). Entrainment and spreading characteristics of jets from asymmetric nozzles. Number 1997–1878 in AIAA, Snowmass village, CO. 4^{th} Shear Flow Conference.

Zhang, Z. (2002). Velocity bias in lda measurements and its dependence on the flow turbulence. *Flow Measurement and Instrumentation*, *13*, 63–68.

Appendices

Appendix A

Experimental Procedure

A very brief description was provided in Chapter 4 regarding the experimental procedure and the reader was directed to this particular appendix for additional details, along with the results and their subsequent analyses.

A technique employing the use of 2-D *LDA* measurements of a rectangular flow-field along all three axes was devised, based on rotation of the nozzle with respect to the settling chamber with the orientation of the traverse and the *LDA* probe remaining unchanged. The *AR*4 nozzle was affixed to the settling chamber using the dual-flange arrangement and aligned with the major axis along the horizontal plane. This was taken as the base configuration of the setup and was used to align the rest of the components. The traverse was oriented with the longer span parallel to the geometric centreline of the nozzle-settling chamber assembly. The four legs of the traverse were then adjusted so that the base plane of the traverse was aligned horizontally. The 2-D *LDA* probe was mounted centrally on to an aluminium extrusion of length 30 *mm* using the probe mounts so that there was minimal overhang. The probe mounts could then be adjusted using a micrometer to align the beams such that the pair measuring streamwise velocity is horizontally oriented and the pair measuring the spanwise velocity is parallel to the nozzle exit plane. The internal alignment of the beams to ensure coincidence is done independently of the experimental setup, the details of which are beyond the scope of the current work. The centre of the major axis, i.e. width of the nozzle exit, is marked on the nozzle face and used for calibrating the zero position of the traverse and the subsequent measurements. Once the traverse home position was located, the nozzle was rotated using the dual-flange arrangement and the centre of the exit was re-checked. This was done to ensure that the geometric centreline of the setup was not altered by the rotation. However, since the marking of the major axis centre and subsequent alignment was done using a scale-rule, it would be reasonable to assign a tolerance of ±0.5 *mm* on the same.

After completing the alignment of the *LDA* probe with respect to the base configuration, the technique to measure the 3-D velocity flow-field was devised. The main assumption in employing this technique was that the flow issuing

from the rectangular nozzle, for subsonic velocities and steady state, would be symmetrical about its major and minor axis planes. Thus, measuring the flow along the radial direction would have resulted in a symmetrical velocity profile about the centreline for any given plane parallel to the nozzle exit. An additional assumption was made about the absence of swirl in the flow. This was based on the presence of flow-straightening sections inside the settling chamber. In the absence of the swirl velocity, the spanwise velocity measured by the 2-D probe (in the vertical direction) could then be resolved into two components, along the major and minor axes of the nozzle exit. Thus, a 2-D *LDA* measurement could be transformed for measuring the 3-D velocity flow-field. Subsequently, it was decided to accomplish the measurements along the radial directions as shown in Figure 4.9 (page 69).

For every angular configuration, three separate runs were assigned. Each run was independent, i.e. in between each run, the nozzle was turned off. As mentioned in Section 4.2.1.3, the independent runs also averaged out the error due to repetition, if any. The initial conditions of ambient temperature and pressure as recorded by the pressure control software were noted down. The ambient temperature was especially important to calculate the corresponding velocity of sound and hence the jet Mach number (M_j). At the start of every run, after the software recorded a steady static pressure in the settling chamber, a measurement was taken at the zero location of the *LDA* traverse, i.e. corresponding to the centreline measurement at the nozzle exit. Since the nozzle was rotated through 15° between the major and minor axes, this gave a total of 21 independent runs. Based on the centreline measurements for the streamwise velocity, the flow properties pertaining to the 21 runs of the *LDA* experiment are summarised in Table A.1.

It can be seen from Table A.1 that the *NPR* recorded using the isentropic flow equations for the runs was lower than the set *NPR* of 1.05. This loss of *NPR* could be attributed to two things. The average total pressure recorded in the settling chamber for feeding the software is, in fact, static pressure averaged at four locations inside the settling chamber. Also, the section of the settling chamber which houses the pressure taps is followed by a section with filter material held in place using perforated plates. This may account for a further pressure loss, although by itself, this is not very significant. This, however, does induce a change in the expected M_j by approximately 5% (lower; mean M_j observed compared to

Table A.1: Flow properties for all the 21 runs during the LDA experiment; ratio of specific heats, γ = 1.4; specific gas constant for air, R_{air} = 286.9 $J/kg-K$; Angle indicates rotation of the nozzle with respect to the base configuration (major axis aligned horizontally)

Angle	V_{exit} **(*m/s*)**	**Avg** V_{core} **(*m/s*)**	T_{amb} **(°*C*)**	M_j **(exit)**	**Avg** M_j **(core)**	***NPR* (calculated)**	T_i **(%) (exit)**
	82.23	88.30	19.46	0.2359	0.2533	1.046	1.77
0°	81.45	87.07	19.07	0.2338	0.2499	1.044	1.83
	77.38	85.66	17.49	0.2227	0.2465	1.043	1.85
	81.67	86.50	19.73	0.2342	0.2480	1.044	2.33
15°	81.25	87.75	19.96	0.2329	0.2515	1.045	1.95
	80.58	86.07	16.62	0.2322	0.2481	1.044	2.06
	79.80	84.81	18.07	0.2294	0.2438	1.042	2.52
30°	80.07	86.34	17.40	0.2305	0.2485	1.044	2.09
	80.51	86.26	18.89	0.2311	0.2476	1.044	2.40
	80.70	85.99	17.86	0.2321	0.2473	1.043	2.58
45°	81.64	87.37	17.84	0.2348	0.2513	1.045	2.24
	81.05	86.11	19.12	0.2326	0.2471	1.043	2.46
	81.15	85.82	20.07	0.2325	0.2459	1.043	2.40
60°	80.32	86.45	20.42	0.2300	0.2476	1.044	2.48
	81.36	85.65	18.38	0.2338	0.2461	1.043	1.80
	80.75	85.55	18.92	0.2318	0.2456	1.043	1.93
75°	79.28	84.73	18.18	0.2279	0.2435	1.042	1.85
	82.74	89.07	20.79	0.2368	0.2549	1.046	1.99
	80.33	85.06	16.58	0.2315	0.2451	1.043	2.44
90°	79.55	85.29	17.41	0.2290	0.2455	1.043	2.03
	80.08	85.76	20.22	0.2294	0.2457	1.043	2.09

expected value of M_j = 0.265). The standard deviation on the observed M_j is about 1.2% indicating that the data are fairly consistent between the runs. The *LDA* measurements also provide information about the turbulence intensity at the nozzle exit which is used for initial setup of the simulations. This value comes to about 2.15% (±0.4%) at the centreline of the exit. Since each individual run was essentially independent, the streamwise velocities (V_x) were normalised using the streamwise velocities at the centreline of the exit (V_{exit}). The data over the three runs for each angular configuration were first normalised using the respective V_{exit} values and then averaged.

The normalised streamwise velocity profiles at each measured plane for the different angular configurations are given in Figure A.3. In all cases, the velocity profiles show higher values on the negative side of the span compared to the corresponding location on the positive side. Additionally, the profiles show a distinct shift from the centreline in the peak velocities at downstream planes, primarily for configurations other than the minor and major axes. This indicated that the flow coming out of the nozzle was not horizontal but, in fact, tends to dip from the centreline. This particular artefact would be captured for every angular configuration of the nozzle. A possible explanation for this discrepancy could be due to pressure differential of the flow upstream of the settling chamber. Although the settling chamber is fitted with flow straightening sections, the flexible pipe section that connects the settling chamber to the compressed air outlet in the jet impingement room comes in from a higher height and is at an angle to the flow exiting from the nozzle. This may possibly create a pressure differential within the settling chamber and the nozzle resulting in the flow to deviate from the streamwise axis of the nozzle. It also introduces the possibility of encountering swirl in the flow.

Consequently, the data by itself could not be used under symmetry conditions about either axes. Also, since the existence of the swirl velocity component could not be ruled out, the proposed 2-D measurements would be inadequate for calculating the spanwise velocities; the swirl velocity would also need to be measured, resolved in a similar manner to the measured spanwise velocity and added to it. The only acceptable measurements, thus, were those along the streamwise direction. In this case too, however, careful consideration had to be given to the data obtained for all the planes and the centreline. Regarding the

centreline, it was observed that the different configurations result in different potential core lengths (Figure A.1). It is clear from Figures A.3 and A.1 that as the jet was allowed to spread more in the vertical direction, the effect of the pressure differential was more prominent; the base configuration (0°) showed maximum length of the potential core compared to 90°. The swirl in the flow might also have had an effect on the length of the potential core, although with the current measurements, it is not possible to confirm this. The averaged data from the three runs using the base configuration were used for velocity decay comparison for validation purposes (Figure 5.7) since the setup was aligned with respect to this configuration. A possibility, at this time though, could not be ruled out that the alignment of the traverse with respect to the geometric centreline of the nozzle setup was incorrect. To check this, the exit turbulence intensity at the nozzle exit along the major and minor axes was plotted (Figure A.2). The spread of the measured values, as seen from Figure A.2, indicated that the alignment of the traverse was acceptable. The values also seem to show a good match with the centreline turbulence intensity at the exit observed for the different configurations (Table A.1).

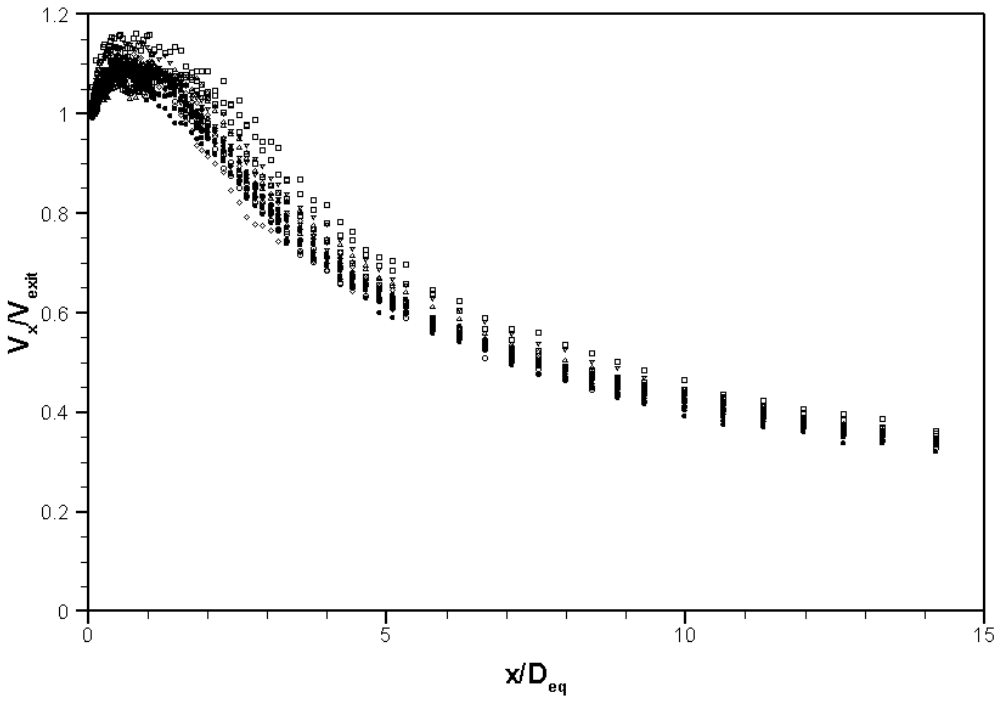

Figure A.1: Centreline velocity decay comparison for all angular configurations; □, 0°; △, 15°; ▽, 30°; ◇, 45°; ○, 60°; ■, 75°; ●, 90°

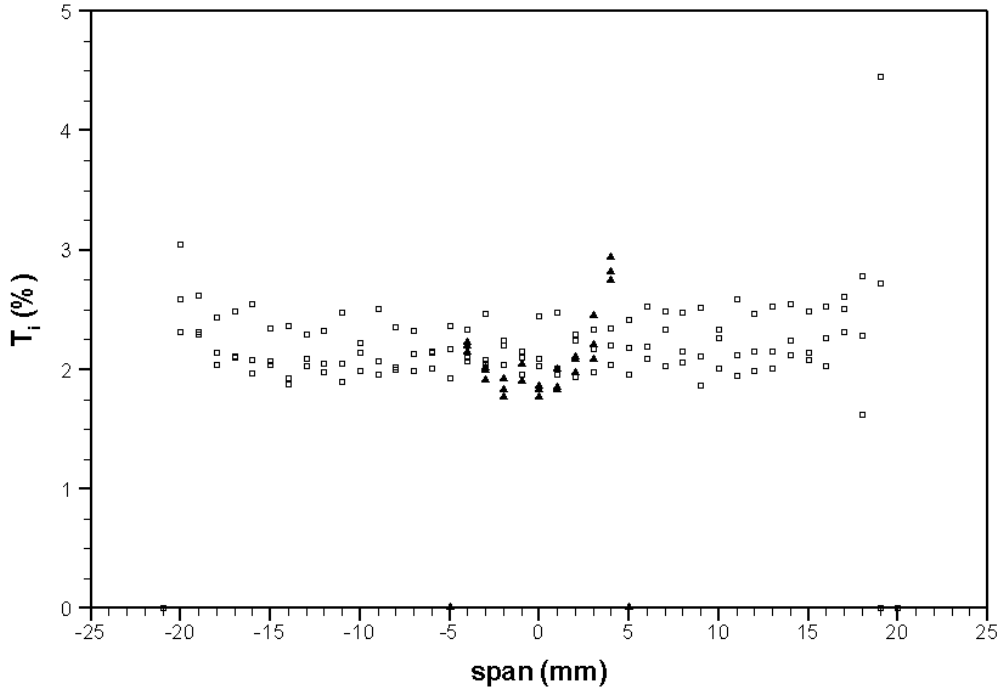

Figure A.2: Exit turbulence intensity at the major and minor axis of the nozzle; □, along the major axis; ▲, along the minor axis

The settling chamber-nozzle configurations by themselves would produce the velocity profiles as shown in Figure A.3 but these values would be meaningless if used to generate a full-field velocity contour map. As a result, the values were averaged over both sides of the centreline and presented in a single quadrant. This data was imported into Tecplot (Figure A.4) for comparing with the data obtained from the simulation. The radial data was interpolated on to rectangular regions of dimensions similar to the rectangular planes exported from Fluent. This interpolation technique was able to highlight a shortcoming though; the number of configurations was inadequate. The flow on the shorter side was measured only at the centre and at the corner (75° and 90°) while at the longer side it was measured in more detail. It, however, does not alter the actual measurements taken along the radial directions and the overall comparison between the velocity contours in this case is acceptable, as can be seen in Figure 5.9.

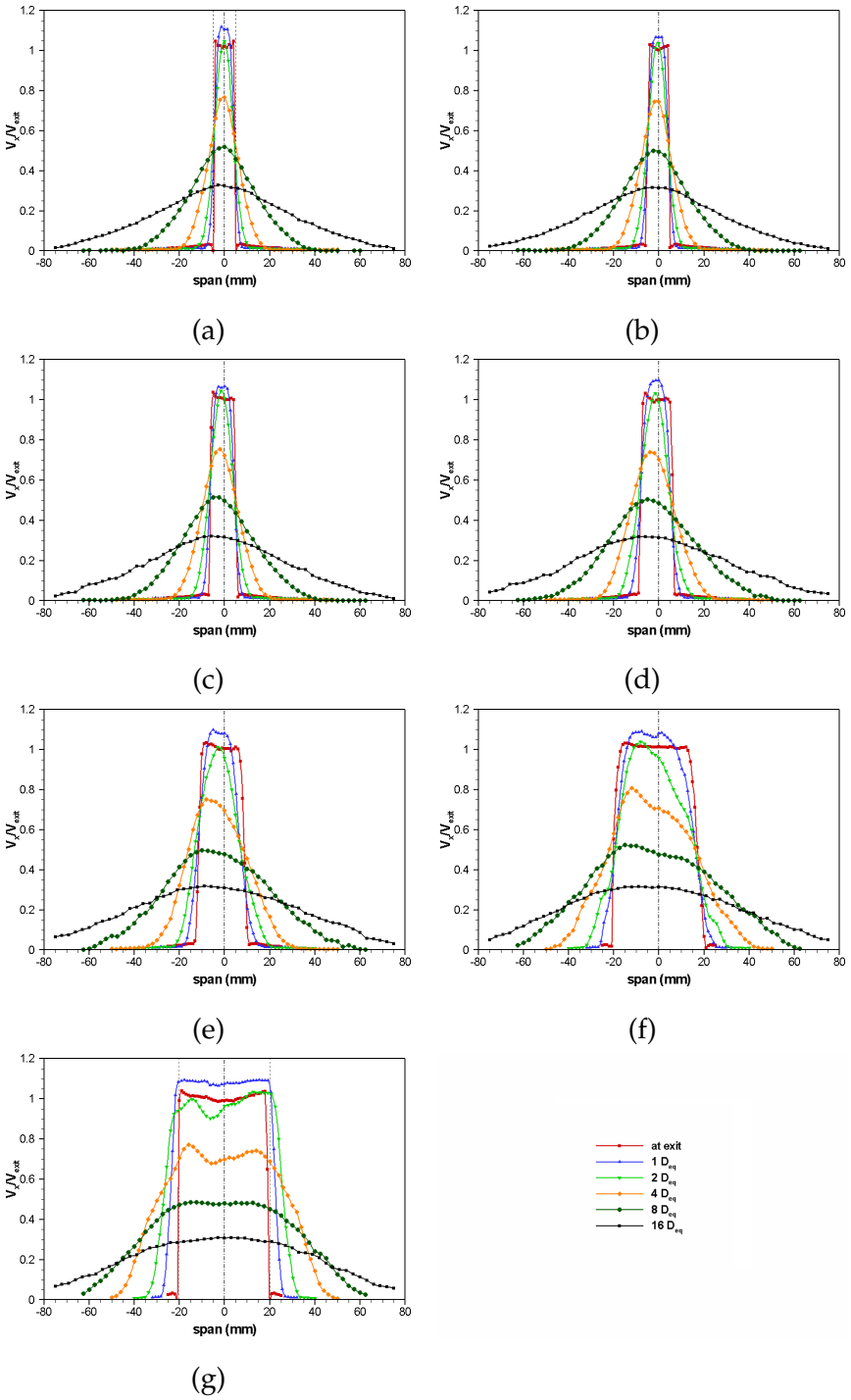

Figure A.3: Normalised streamwise velocity (V_x/V_{exit}) profiles at each measured plane for the different angular configurations: (a) 0° (minor axis); (b) 15°; (c) 30°; (d) 45°; (e) 60°; (f) 75°; (g) 90° (major axis); the dashed lines in (a) and (g) correspond to the span of the nozzle

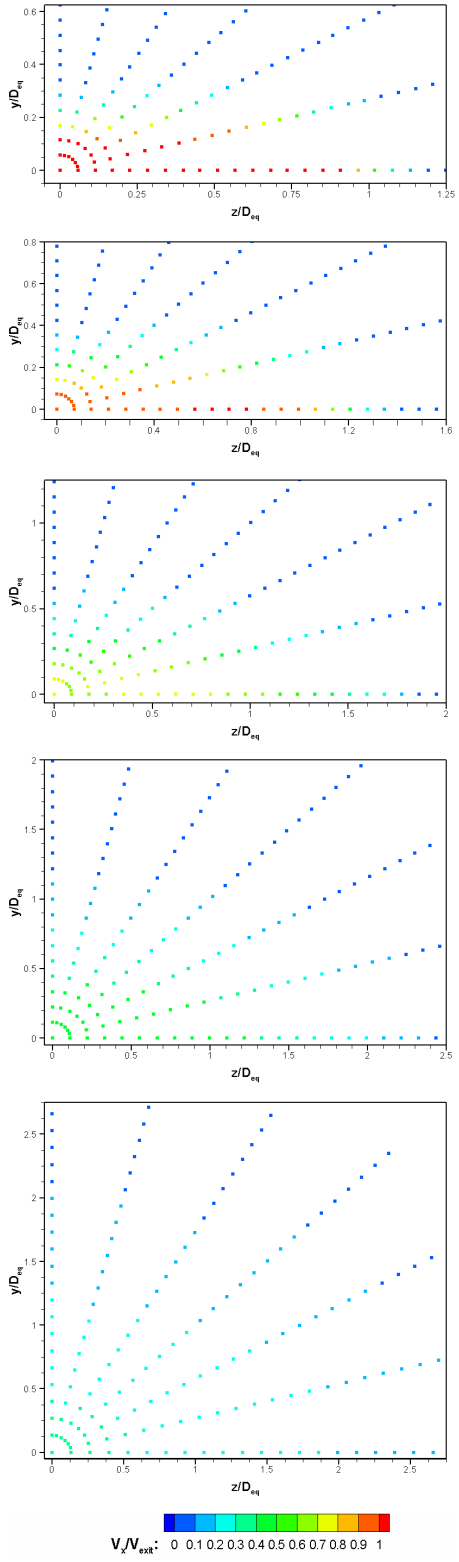

Figure A.4: Scatter plots for individual planes showing averaged normalised streamwise velocity measured using LDA; from top to bottom*, at 1, 2, 4, 8 and 16* D_{eq}

Appendix B

Error Estimation and Analyses

As mentioned in Section 4.3, the errors involved with the use of current *LDA* setup are primarily due to seeding response variation, velocity bias, sampling and jet rig control system. The description and calculations involved for the errors is provided in this Appendix.

B.1 Seeding Response Variation

Dring (1982) provides a comprehensive analysis for determining the seeding particle size and the inherent tracking error associated with it. Assuming the validity of Stokes' theory for the seeding particles, he was able to estimate the error in the velocity based on the Stokes' number of the particles. A nozzle flow problem may be treated as an exponentially accelerating flow-field. The Stokes' number, S_t, is given by,

$$S_t = \frac{\rho_p D_p^2}{18 \mu T_c} \tag{B.1}$$

where, ρ_p is the seeding particle density, D_p is the average seeding particle diameter, μ is the fluid viscosity, and T_c is the rise time, estimated by dividing the nozzle length with the nozzle exit velocity (Cabrita (2006)).

For the current experimental setup, ρ_p is 800 kg/m^3, D_p is 1 μm and μ is 1.78×10^{-4} $kg/m-s$. For a nozzle length of 110 mm and an exit velocity of $\approx$90.28 m/s (based of *NPR* of 1.05), the rise time, T_c comes to 1.218×10^{-3} s. Substituting these values in Equation B.1, we get a Stokes' number of $\approx$0.002, resulting in a maximum error of 0.2%.

B.2 Velocity Bias

For all *LDA* systems operating in 'burst' mode, we get a velocity bias; assuming that each particle triggers a measurement. The likelihood of a particle passing

through the measurement volume is proportional to the fluid velocity if we assume that the particles are uniformly distributed in the fluid. This is because a faster particle will sweep out more volume than a slower particle in a given time. Consequently, the velocity histogram would be biased towards the higher velocities, resulting in erroneous statistical quantities based on arithmetic mean computations.

The BSA Flow Software Installation and User's Guide (Dantec (2000)) provides information about the different weighting factors that may be employed to overcome the velocity bias. Some of the moments associated with the velocity components, as estimated by the software are shown below:

Mean:

$$\bar{u} = \sum_{i=0}^{N-1} \eta_i \, u_i$$

Variance:

$$\sigma^2 = \sum_{i=0}^{N-1} \eta_i \, (u_i - \bar{u})^2$$

RMS:

$$\sigma = \sqrt{\sigma^2}$$

Turbulence:

$$Tu = \frac{\sigma}{\bar{u}}$$

The weighting factor used in the current study is transit-time weighting calculated as:

$$\eta_i = \frac{t_i}{\sum_{j=0}^{N-1} t_j} \tag{B.2}$$

where, t_i is the transit time of the i'th particle crossing the measuring volume. Although the velocity bias is eliminated during processing, a method described

by Zhang (2002) may be used to calculate the estimated error. Based on the maximum turbulence intensity at the nozzle exit, this can be calculated for either one-, two- or three-dimensional flow fluctuations. For real flows with a turbulence intensity less than 30%, the ratio of the biased velocity, $\bar{u}_b$, to the true velocity, $\bar{u}$ is simplified as $\bar{u}_b - \bar{u} = 1 + Tu^2$. The nozzle flow in the current case has an exit turbulence intensity of 2.001%. From Zhang (2002), the error due to velocity bias may be estimated as ≈0.04%.

B.3 Sampling Error

Statistically-independent samples are a necessity for obtaining the population mean and variance of the measurement of a flow-field. Two consecutive samples are considered to be statistically-independent if they are separated by less than one integral time scale (T_u). The sampling error can be estimated for randomly sampled data (such as *LDA* in burst-mode) if the integral time scale (T_u), sampling period (T_s), sampling rate (ν) and the ratio of the standard deviation to the mean ($\sigma/\bar{u}$ are known (George, Jr. et al. (1979)). Thus,

$$\varepsilon_s^2 = \frac{2\,T_u}{T_s}\left(1 + \frac{1}{2\,\nu\,T_u}\right)\left(\frac{\sigma}{\bar{u}}\right)^2 \tag{B.3}$$

The integral time scale may also be defined as the measure of time over which the signal is correlated. The record interval time of the *LDA* is found to be 1.333 μs, while the number of bursts per measurement is set at 10000. This gives a T_u value of 0.0133 s. The sampling period is 5 s, sampling rate is 10000 and the turbulence intensity (i.e. the ratio of standard deviation to mean) is 0.02. Using these values in Equation B.3, the sampling error, ε_s is calculated to be 0.15%.

B.4 Total *LDA* Error

The total error in the *LDA* velocity measurement is given by:

$$\left(\frac{\delta U}{U}\right)_{LDA} = \sqrt{\varepsilon_{sr}^2 + \varepsilon_{vb}^2 + \varepsilon_s^2} \tag{B.4}$$

where, ε_{sr} is the seeding response error, ε_{vb} is the velocity bias error and ε_s is the sampling error. The current *LDA* setup can measure flow-field velocities at *NPR* 1.05 with an uncertainty of 0.25%.

B.5 Pressure Control System Error

A variation between the expected and actual jet velocities may be observed due to an error in the various components of the pressure control system, such as the pressure transducers and also by the precision of the controlling software. The uncertainty in measurement of the ambient pressure using the SETRA Model 270 pressure transducer was 0.03% (ε_{P_∞}), while the DRUCK PDCR 10 – 3.5 measured the settling chamber pressure with an uncertainty of 0.1% (ε_{P_0}). The control software could maintain the nozzle pressure ratio to within 0.5% of the desired value ($\varepsilon_{P_0/P_\infty}$). Assuming isentropic flow conditions and ideal expansion, the jet axial velocity, denoted by U, can be given as:

$$U = \sqrt{\gamma R T}\ \sqrt{\left(\frac{2}{\gamma - 1}\right)\left[\left(\frac{P_0}{P_\infty}\right)^{\frac{\gamma-1}{\gamma}} - 1\right]} \tag{B.5}$$

The contribution of each of the three components, ε_{P_0}, ε_{P_∞} and $\varepsilon_{P_0/P_\infty}$, towards the uncertainty in the velocity due to the pressure control system can now be described by Equation B.6 below:

$$\left(\frac{\partial U}{U}\right)_{PCS} = \sqrt{\left(\frac{\partial U}{\partial P_0}\,\varepsilon_{P_0}\right)^2 + \left(\frac{\partial U}{\partial P_\infty}\,\varepsilon_{P\infty}\right)^2 + \left(\frac{\partial U}{\partial\,(P_0/P_\infty)}\,\varepsilon_{P_0/P_\infty}\right)^2} \tag{B.6}$$

For the current nozzle experiments, running at NPR of 1.05, this error comes to 5.57%.

Appendix C

Validation of LDA Measurements

The validation of the Laser Doppler Anemometry (*LDA*) results for the subsonic case of Stratford nozzle was essential to gain confidence in the setup and measurement technique. The other reason for carrying out *LDA* measurements for the Stratford nozzle was to ensure that all systems in the setup were working satisfactorily before performing the experiments to get data for the *AR*4 nozzle.

Witze (1974) presents an empirical formula for calculating the velocity decay of a compressible free jet by expanding on Kleinstein's theory (Kleinstein (1964)). This formula, valid for $x > x_{core}$ can be expressed as:

$$\bar{u}_c = 1 - \exp\left(\frac{-1}{\kappa\bar{x}(\bar{\rho}_e)^{0.5} - X_{core}}\right) \tag{C.1}$$

where, $\bar{u}_c$ is the normalised jet centreline velocity, $\bar{x} = x/r$ with x being the axial distance from the nozzle exit and r, the diameter of the nozzle, and X_{core} in this case being the non-dimensional correlation parameter core length. Kleinstein determined the value of X_{core} to be 0.70. Consequently, the length of the potential core can be given by:

$$\bar{x}_{core} = \frac{0.70}{\kappa(\bar{\rho}_e)^{0.5}} \tag{C.2}$$

where, $\bar{\rho}_e = \rho_\infty/\rho_j = 1.00$ for ambient air, and κ is a proportionality constant dependent on the jet Mach number and $\bar{\rho}_e$. From a number of experimental results at hand, Witze (1974) determined that κ could be represented as:

$$\kappa = 0.08\left(1 - 0.16\,M_j\right)(\bar{\rho}_e)^{-0.22} \tag{C.3}$$

Since we have $M_j = 0.265$ for the current setup, we get $\kappa = 0.0766$. Using this value in Equation C.2, we have $\bar{x}_{core} = 9.1384$ which results in x_{core} approximately equal to 4.57 times the nozzle diameter for the given jet Mach number.

The experimental results are plotted for $1/ln(1-u/u_j)$ against x/D to determine the potential core length using the formula proposed by Witze (1974). It can be clearly seen that for, $u \geq u_j$, the expression $1/ln(1-u/u_j)$ is meaningless. Figure

C.1 shows the centreline velocity decay and the corresponding $1/ln(1-u/u_j)$ against x/D for the Stratford nozzle at *NPR* 1.05. The corresponding equation of the linear fit that passes through these points gives the potential core length (in nozzle diameters) and the non-dimensional correlation parameter core length for the current experiment.

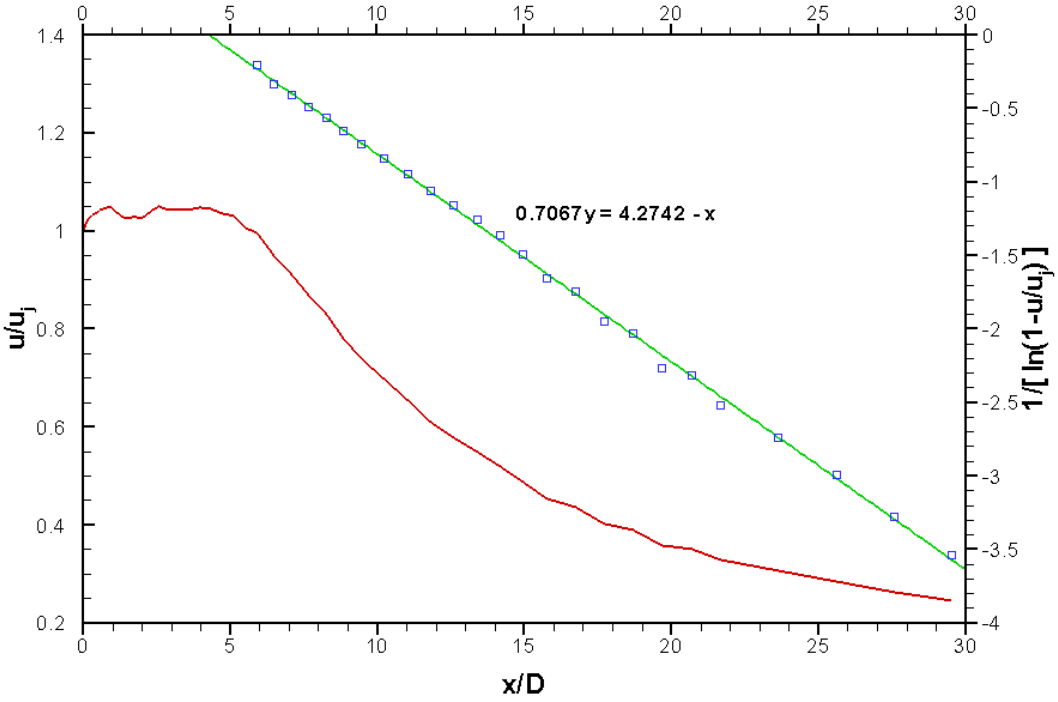

Figure C.1: Centreline velocity decay and plot of $[1/ln(1-u/u_j)]$ *against* x/D *for Stratford nozzle at NPR 1.05*

The results match very closely for those predicted using the Kleinstein-Witze formula. The potential core length is obtained as 4.2742 nozzle diameters while the non-dimensional correlation parameter core length is 0.7067. Lau et al. (1979) propose that when the axial distance from the nozzle exit is normalised using the potential core length, the centreline velocity data for a compressible circular jet, expanded ideally, can be collapsed to a generalised equation of the form:

$$\frac{u}{u_j} = 1 - \exp\left(\frac{1.35}{1 - x/x_{core}}\right) \tag{C.4}$$

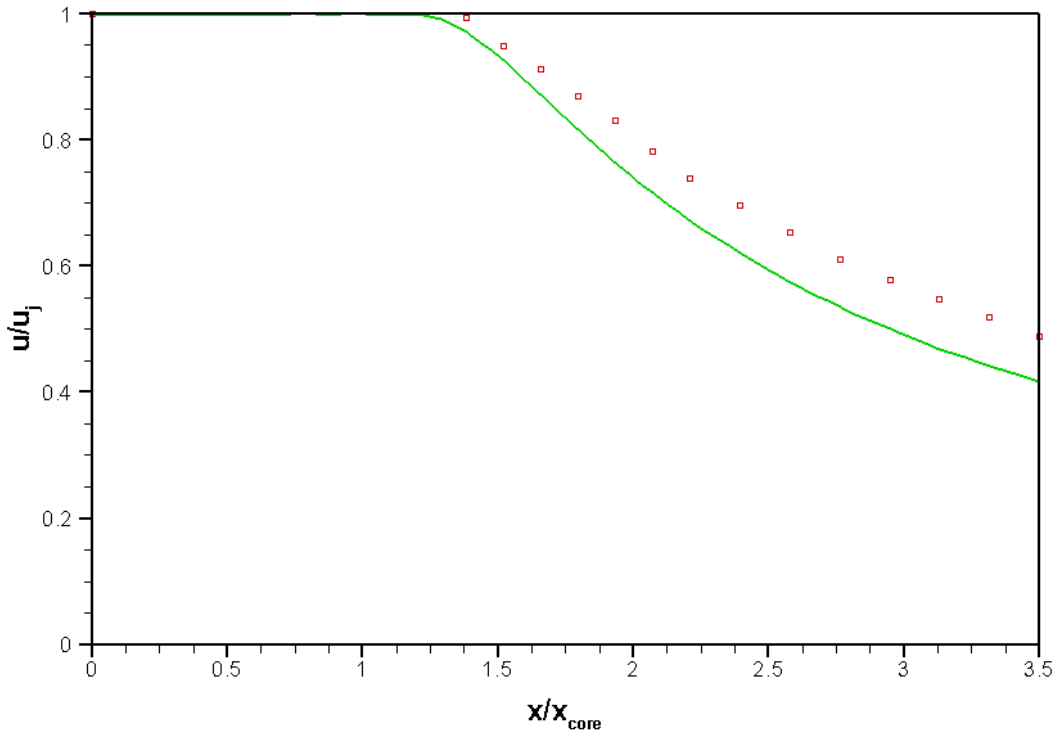

Figure C.2: u/u_j vs. x/x_{core}; symbols indicate experimental value and solid line indicates values produced by equation proposed by Lau et al. (1979)

The data obtained for the current experiment is compared with values from Equation C.4 in Figure C.2. It can be seen that the two show a similar trend.

Appendix D

Data for Nozzle Geometry Variation Effects

The effects of nozzle geometry variation were explained in Chapter 5 (Section 5.2.3) indicating the observed trends. This appendix includes all the plots generated for the various configurations used in the study. The following plots are provided here:

- Contours of normalised static pressure (P_s/P_a) at the nozzle exit (Figure D.1);
- Resultant vectors of normalised spanwise velocities (V_y/V_{exit} and V_z/V_{exit}) at the nozzle exit (Figure D.2);
- Development of normalised streamwise vorticity ($\omega_x D_{eq}/V_{exit}$) inside the nozzle using iso-surfaces of +0.1 and −0.1 (Figures D.3 and D.4);
- Contours of normalised streamwise velocity (V_x/V_{exit}) at 4.5 D_{eq} upstream, 3 D_{eq} upstream and at the nozzle exit (Figures D.5 and D.6);
- Contours of normalised streamwise vorticity ($\omega_x D_{eq}/V_{exit}$) and normalised streamwise velocity (V_x/V_{exit}) at 2 D_{eq} downstream of the exit (Figures D.7–D.9); and
- Contours of normalised streamwise vorticity ($\omega_x D_{eq}/V_{exit}$) and normalised streamwise velocity (V_x/V_{exit}) at 8 D_{eq} downstream of the exit (Figures D.10–D.12).

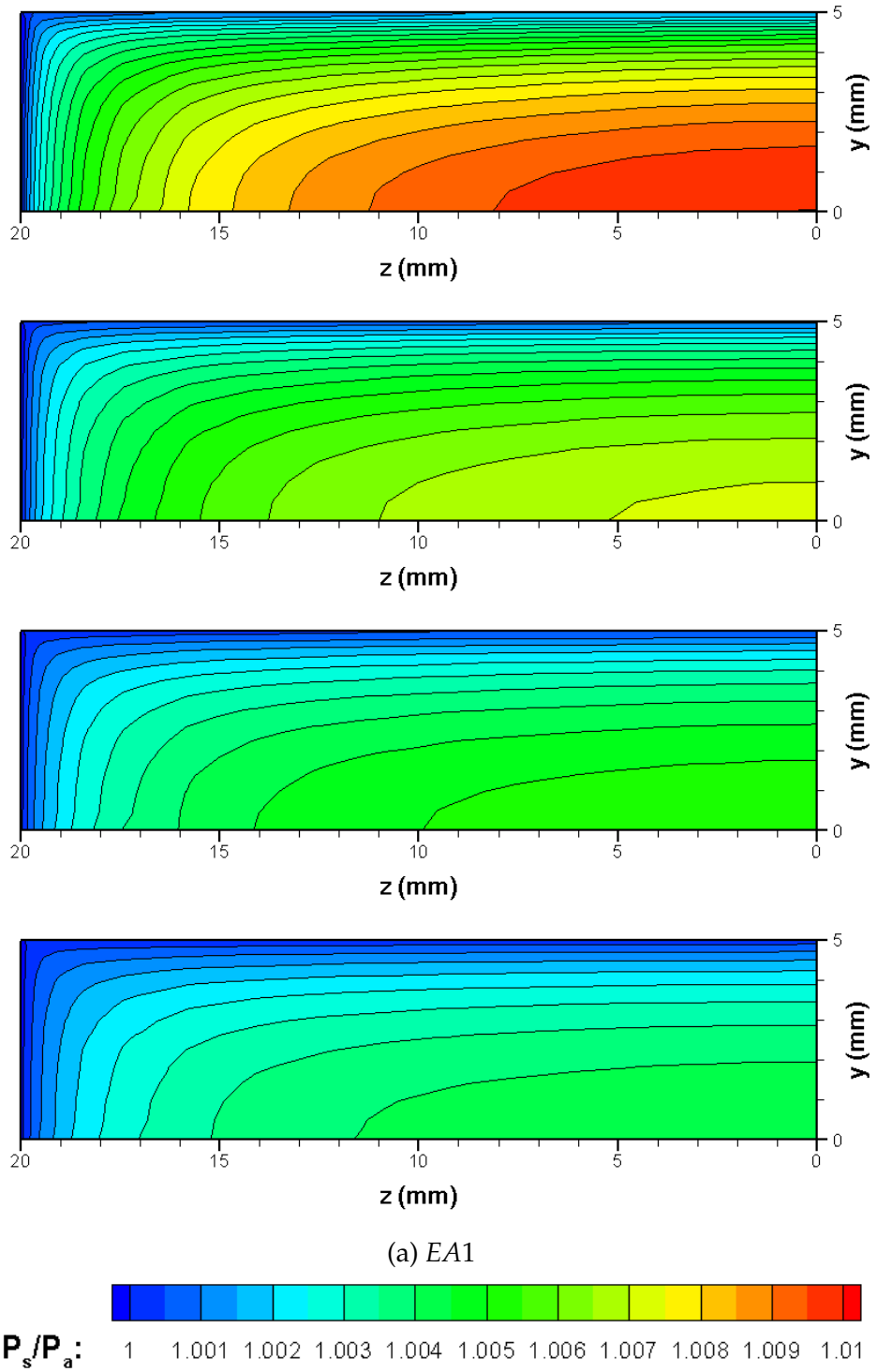

(a) *EA*1

Figure D.1: Contours of normalised static pressure (P_s/P_a) at the nozzle exit; from top to bottom in each configuration, C1, C2, C3, C4; ambient pressure (P_a) is 101.325 kPa

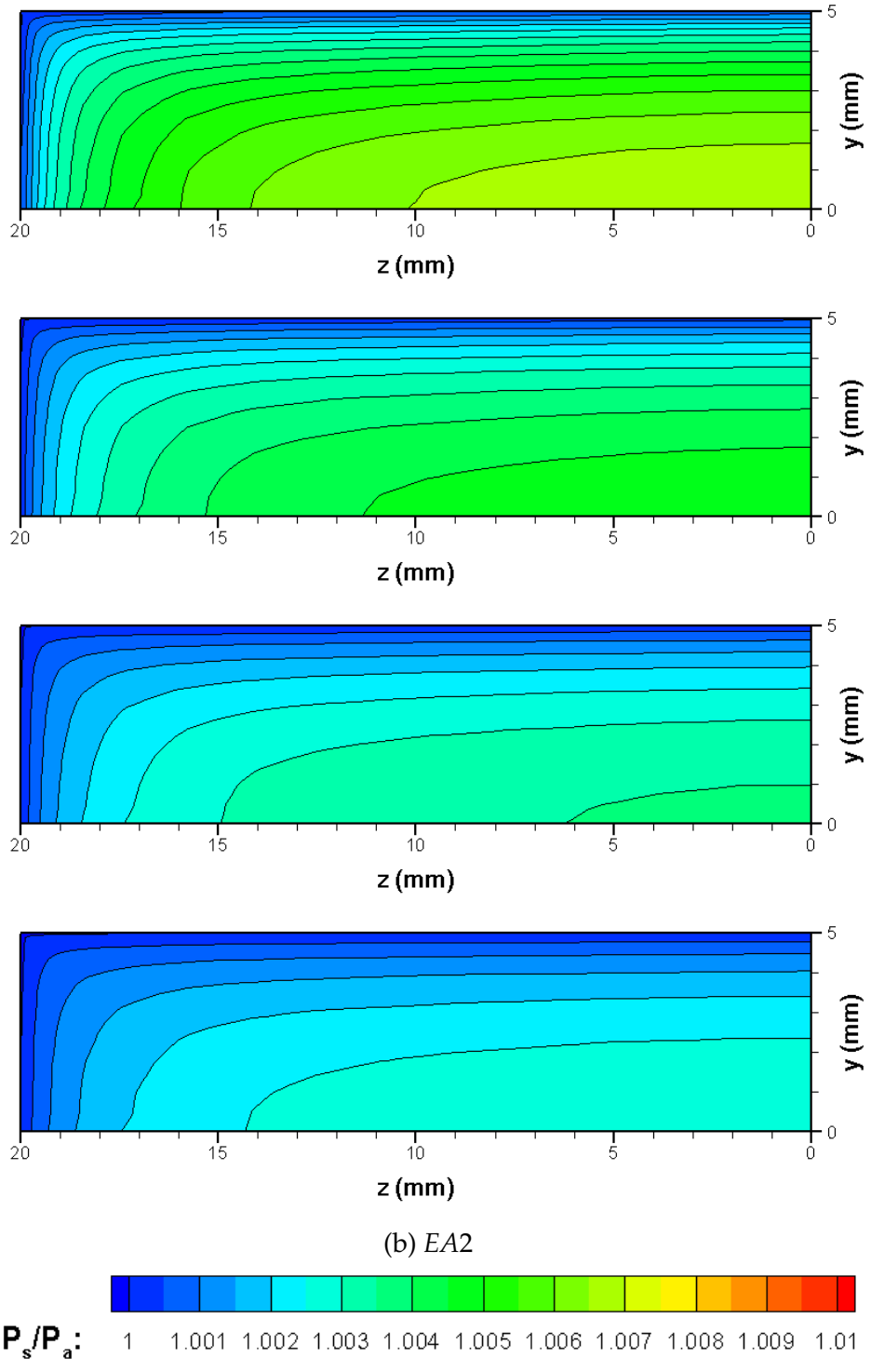

(b) *EA2*

Figure D.1: Continued

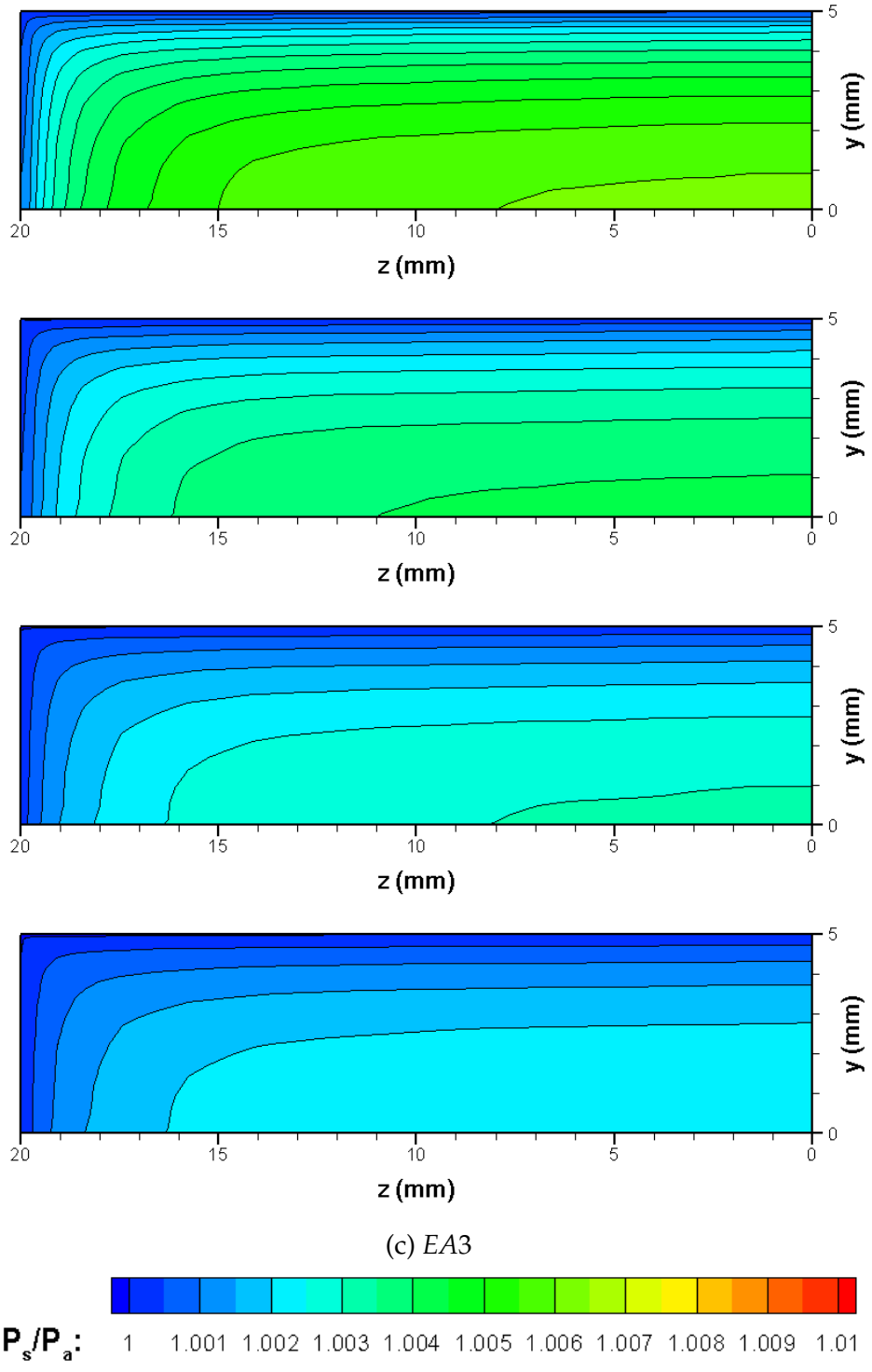

(c) *EA3*

Figure D.1: Continued

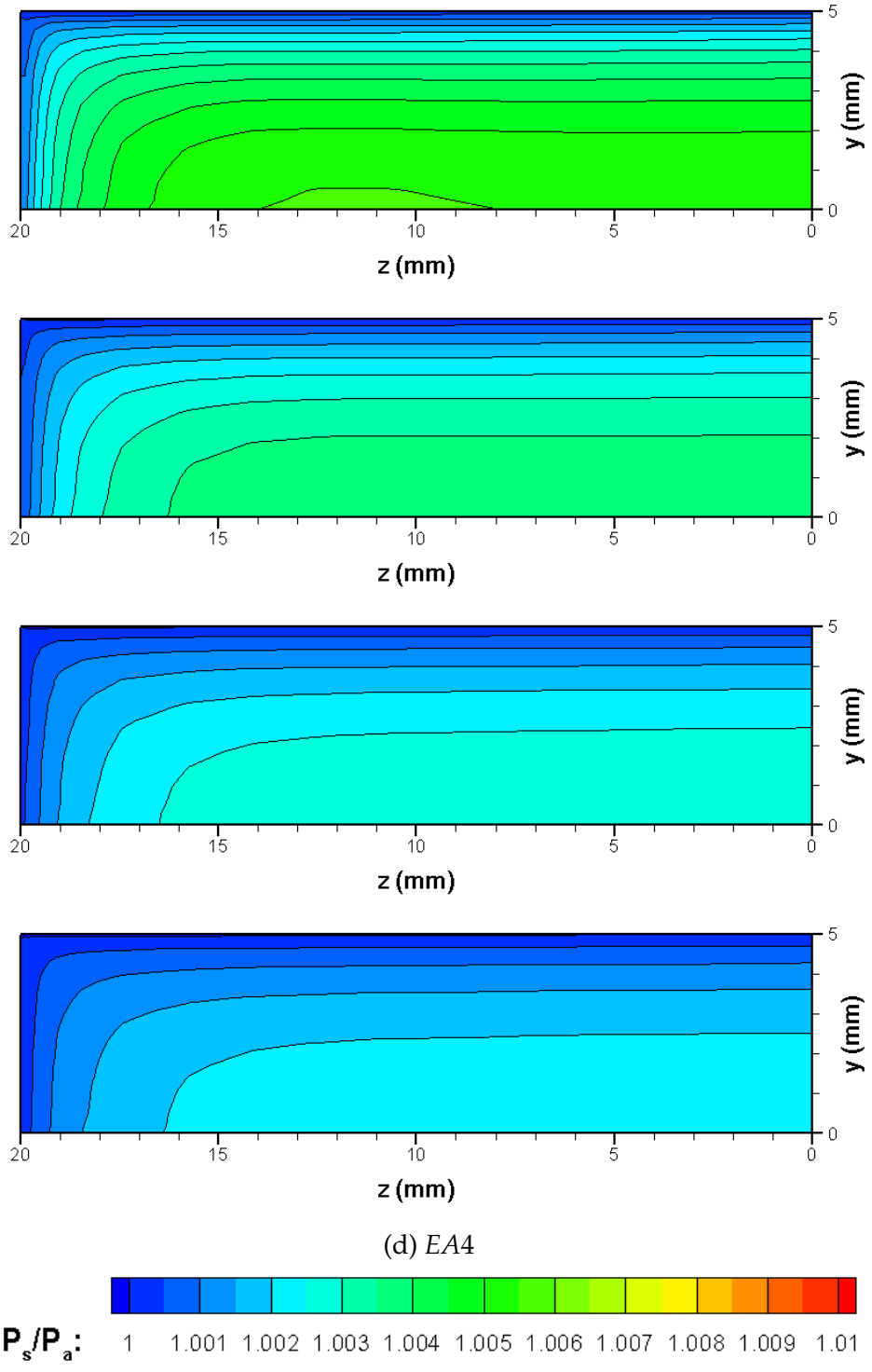

(d) *EA*4

Figure D.1: Continued

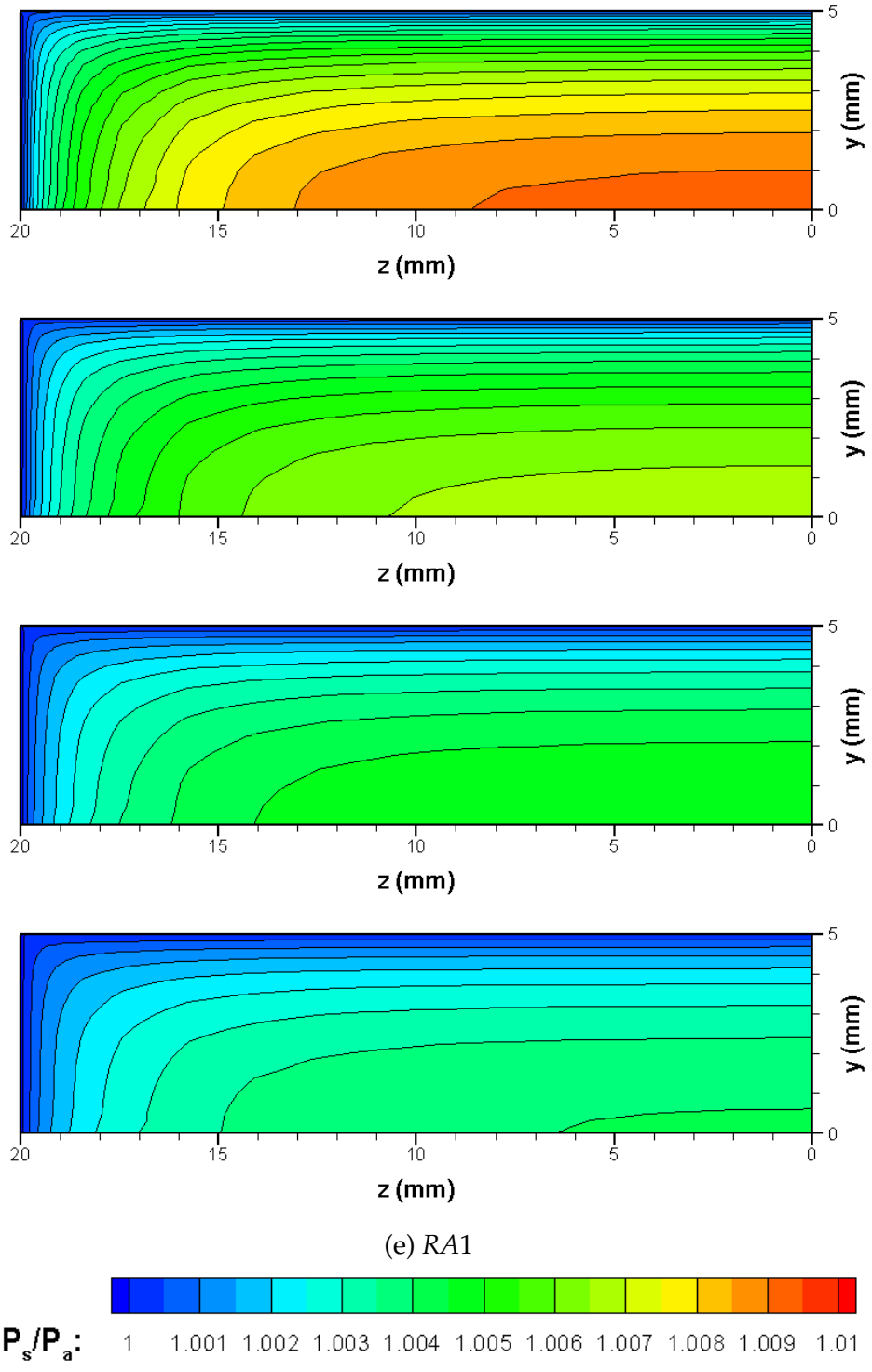

(e) *RA*1

Figure D.1: Continued

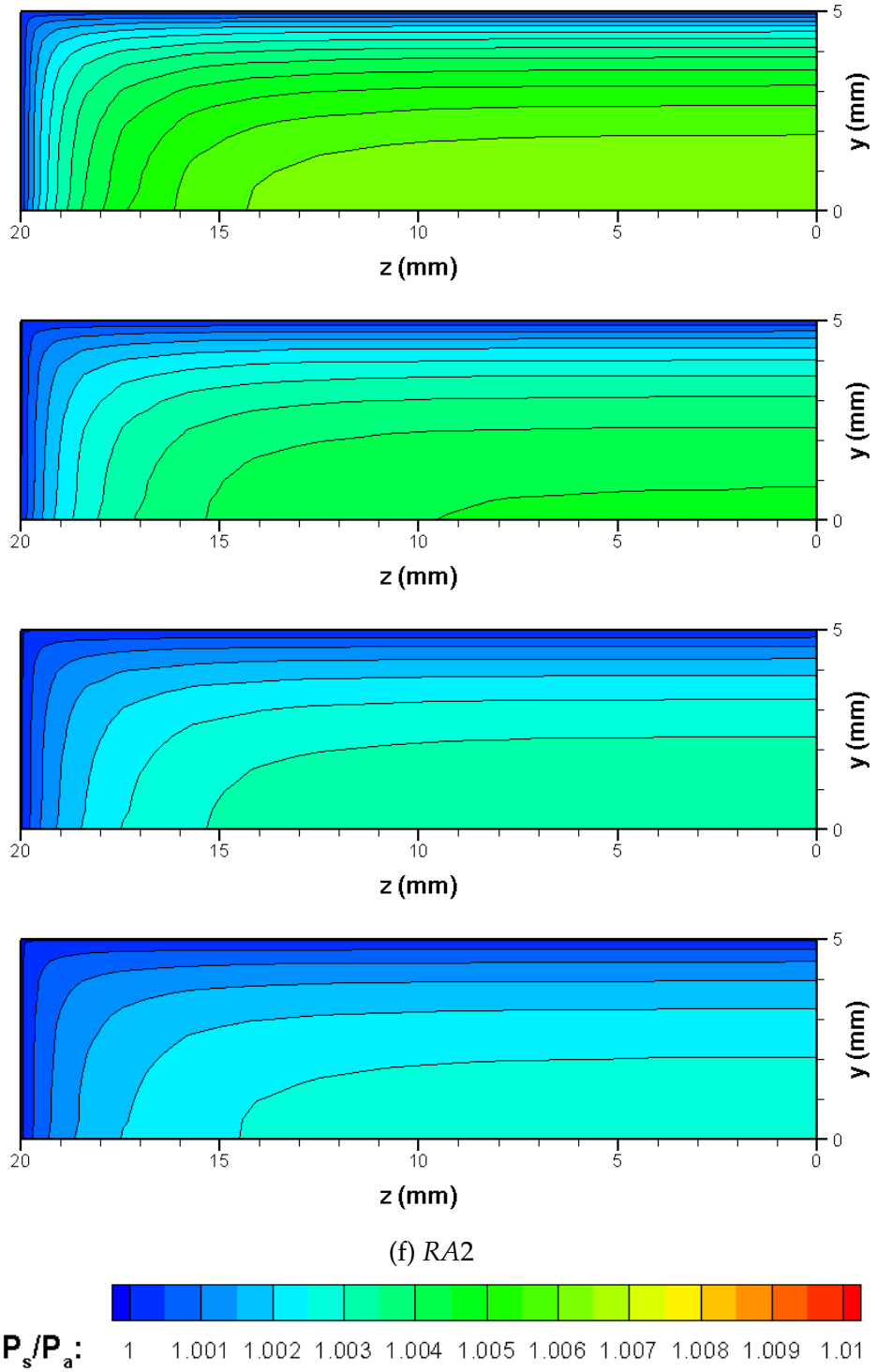

(f) *RA*2

Figure D.1: Continued

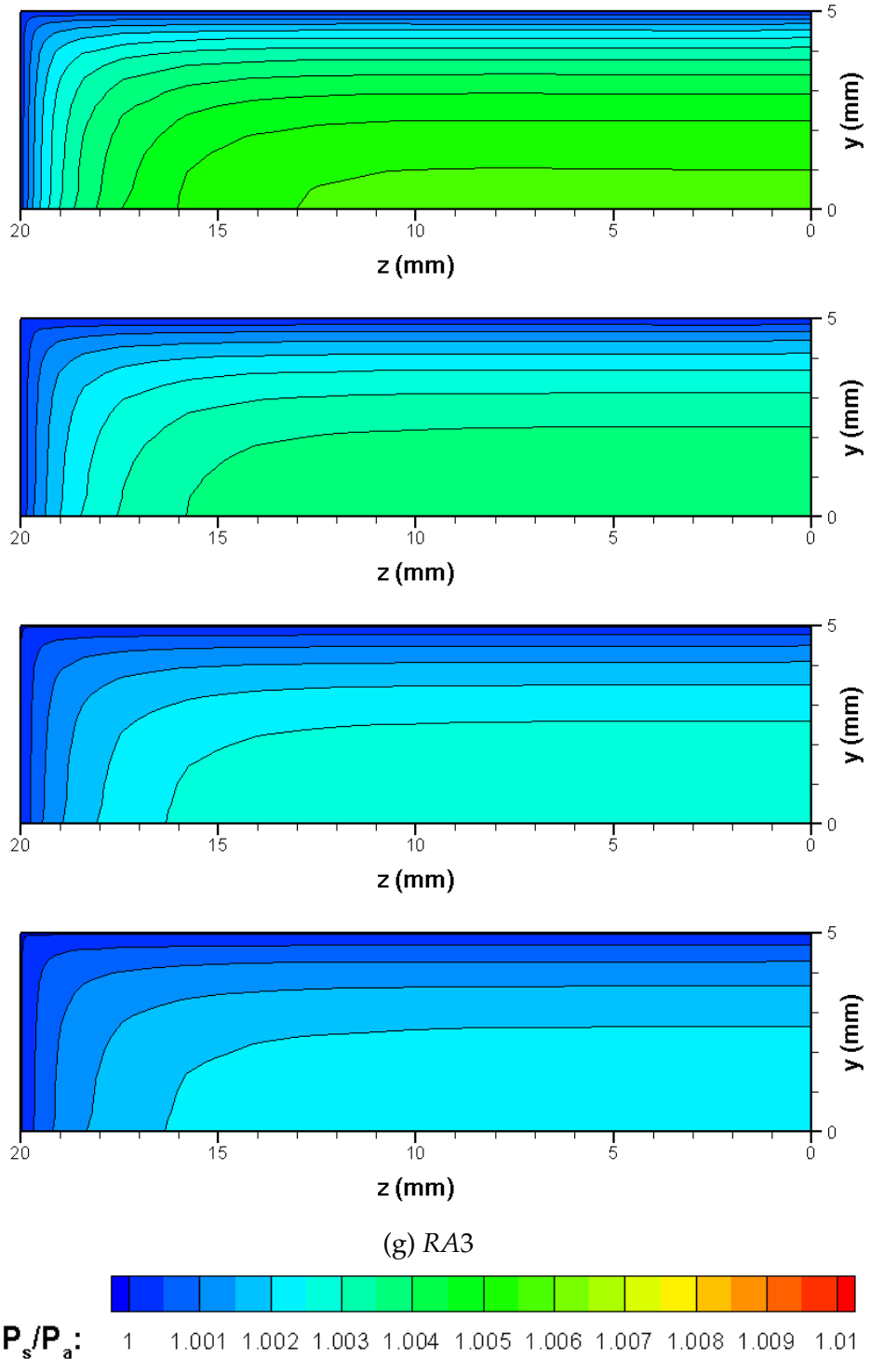

(g) *RA*3

Figure D.1: Continued

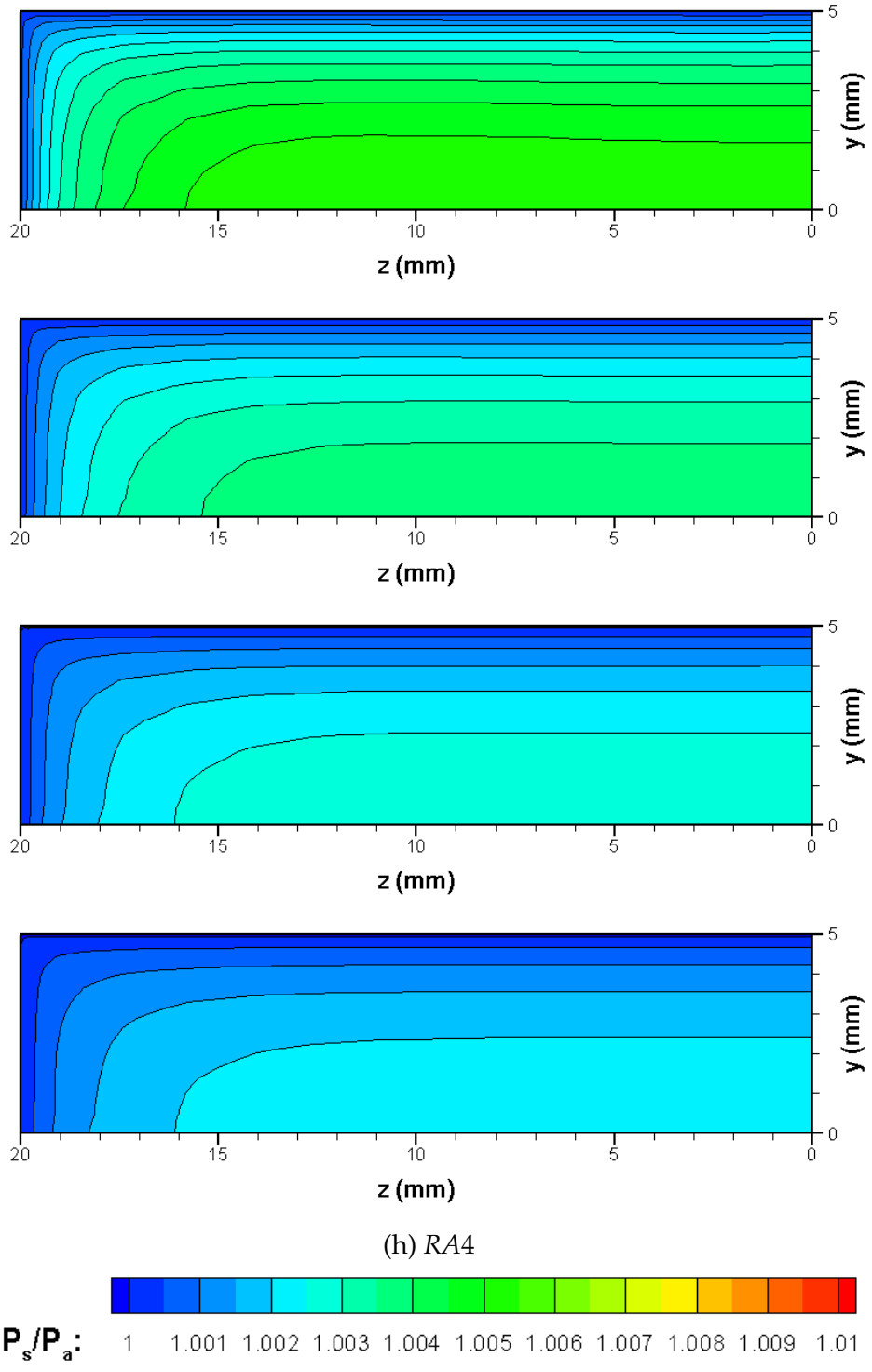

(h) *RA*4

Figure D.1: Continued

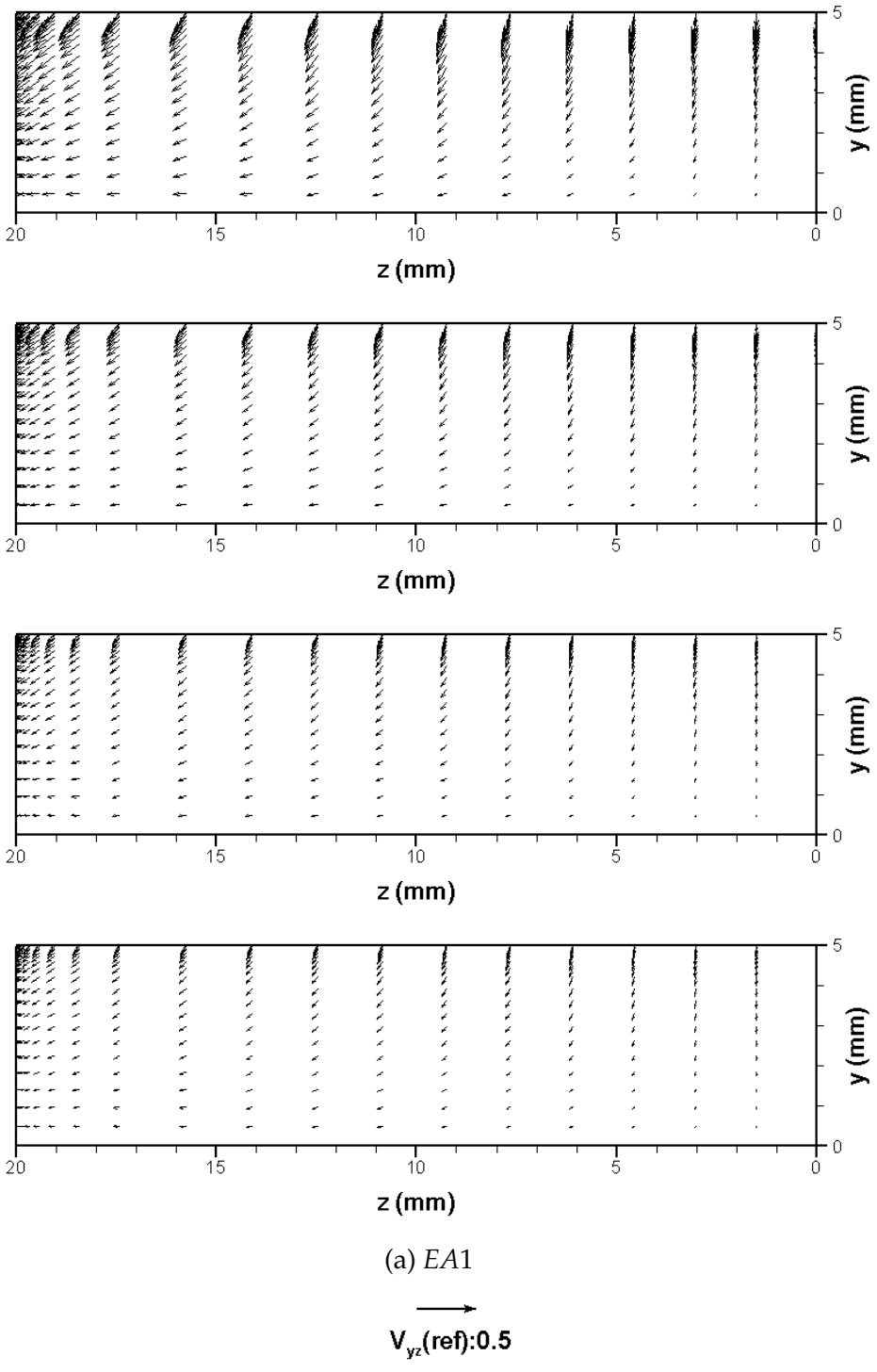

(a) *EA*1

Figure D.2: Resultant vectors of normalised spanwise velocities, V_y/V_{exit} and V_z/V_{exit}, at the nozzle exit; from top to bottom in each configuration, C1, C2, C3, C4

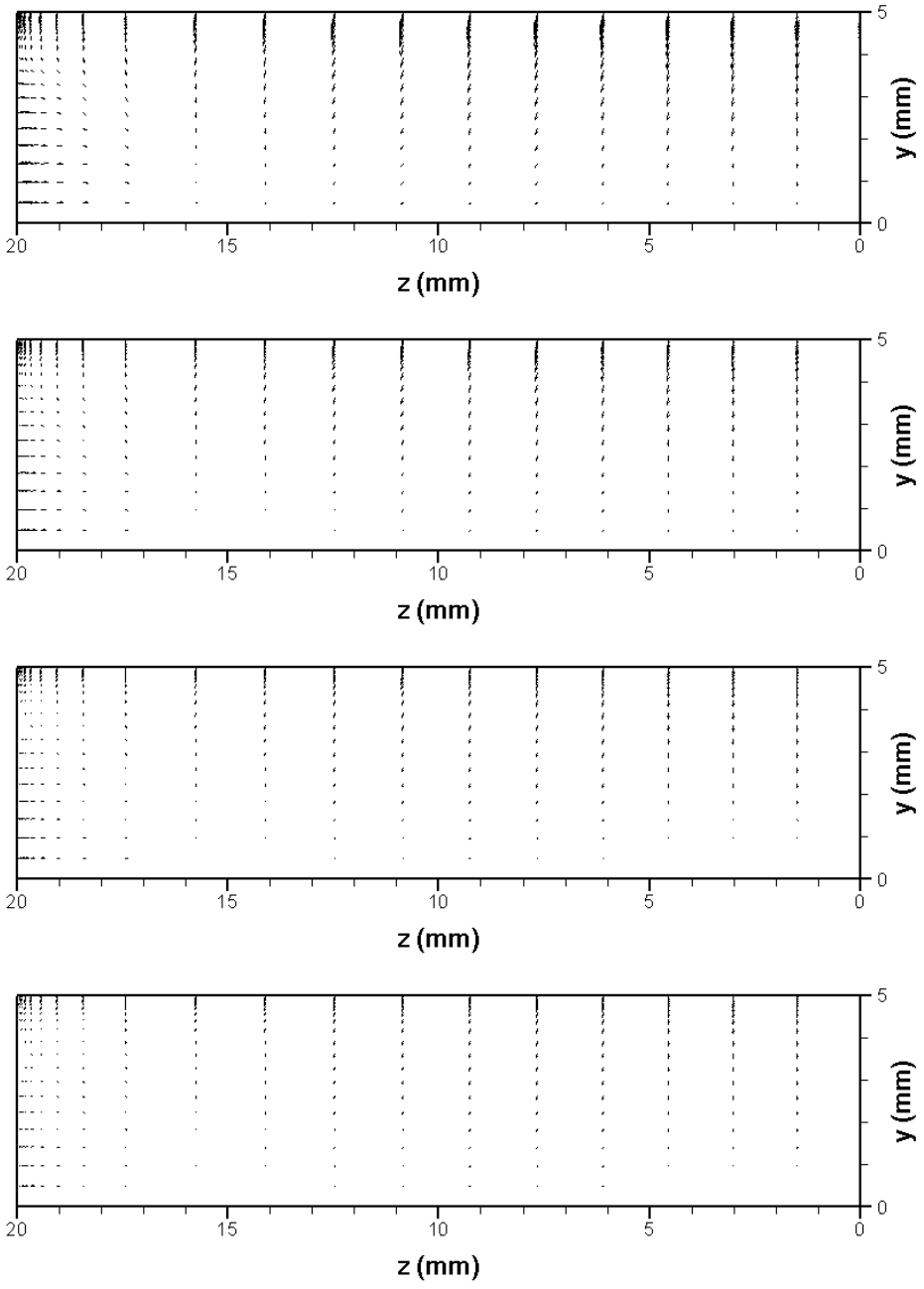

(b) *EA*2

Figure D.2: Continued

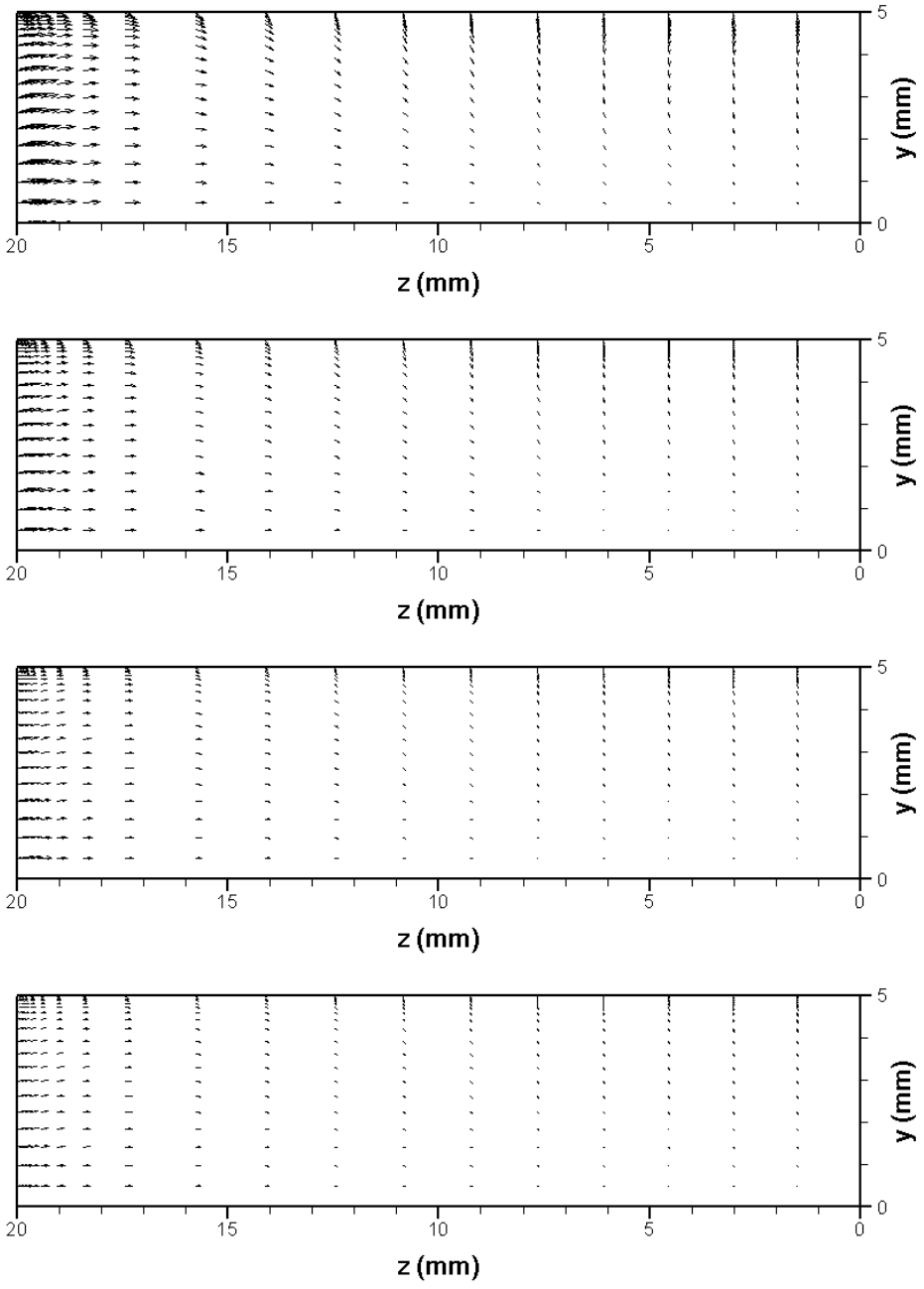

(c) *EA3*

Figure D.2: Continued

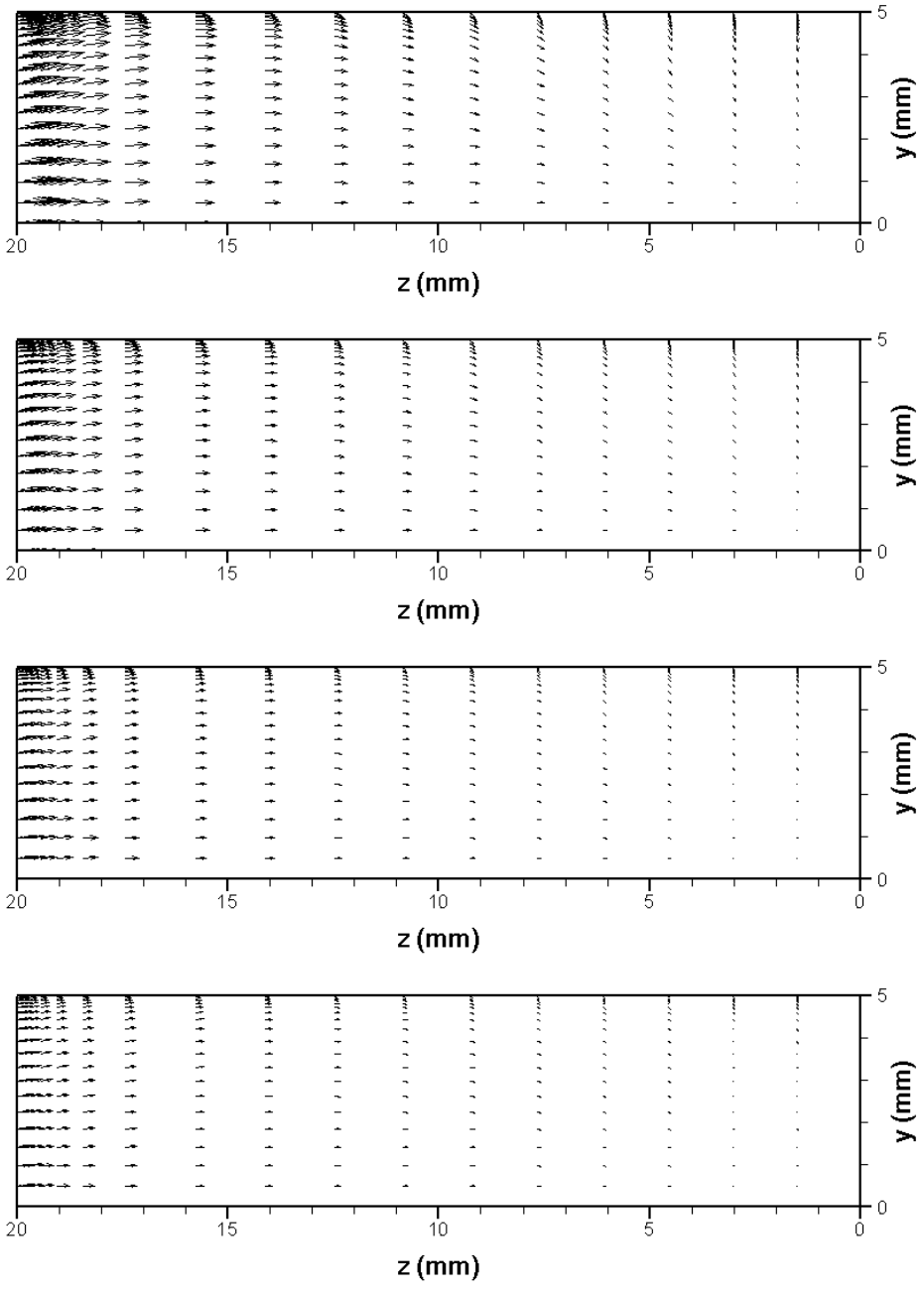

(d) *EA*4

Figure D.2: Continued

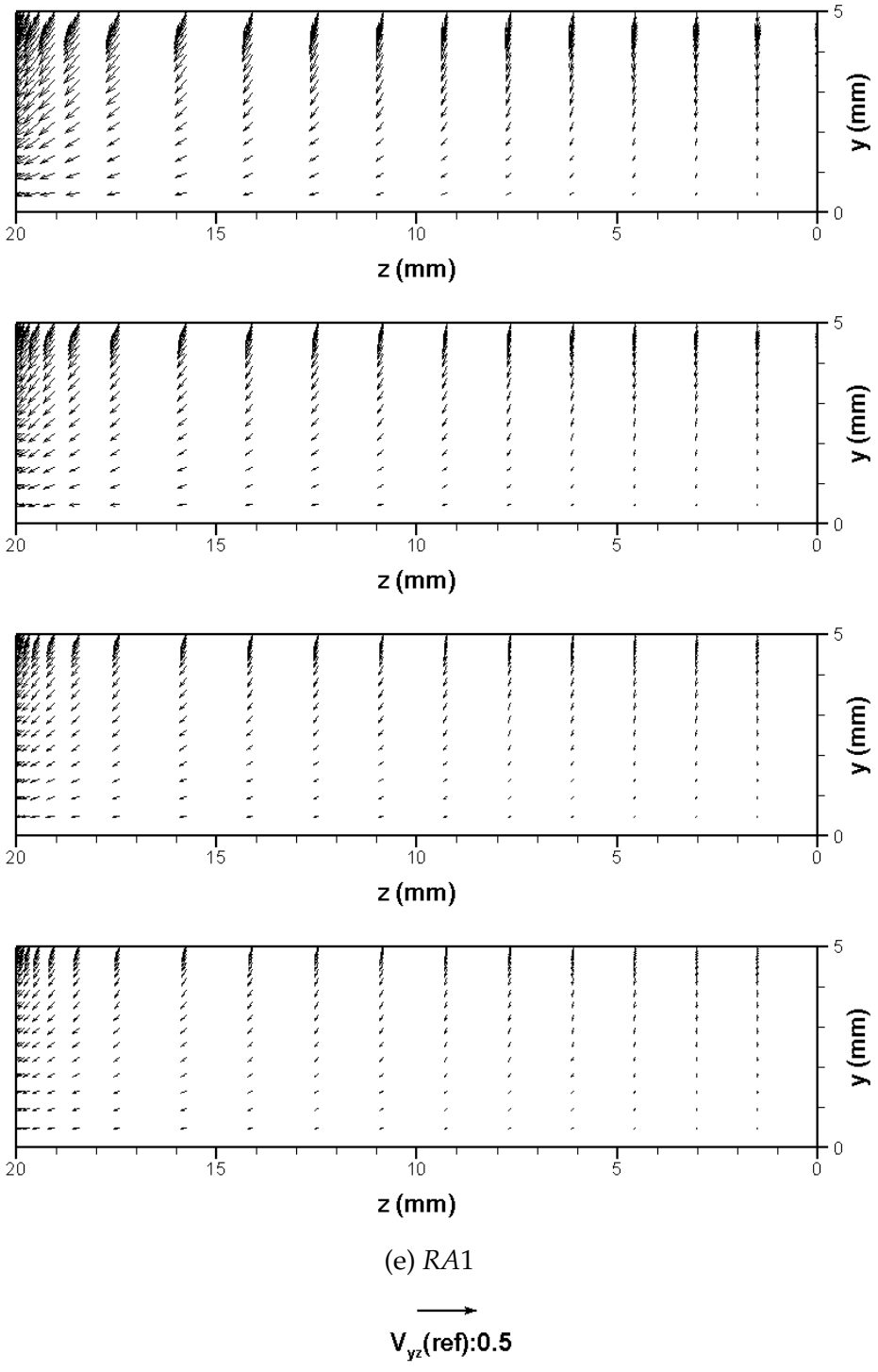

(e) *RA*1

Figure D.2: Continued

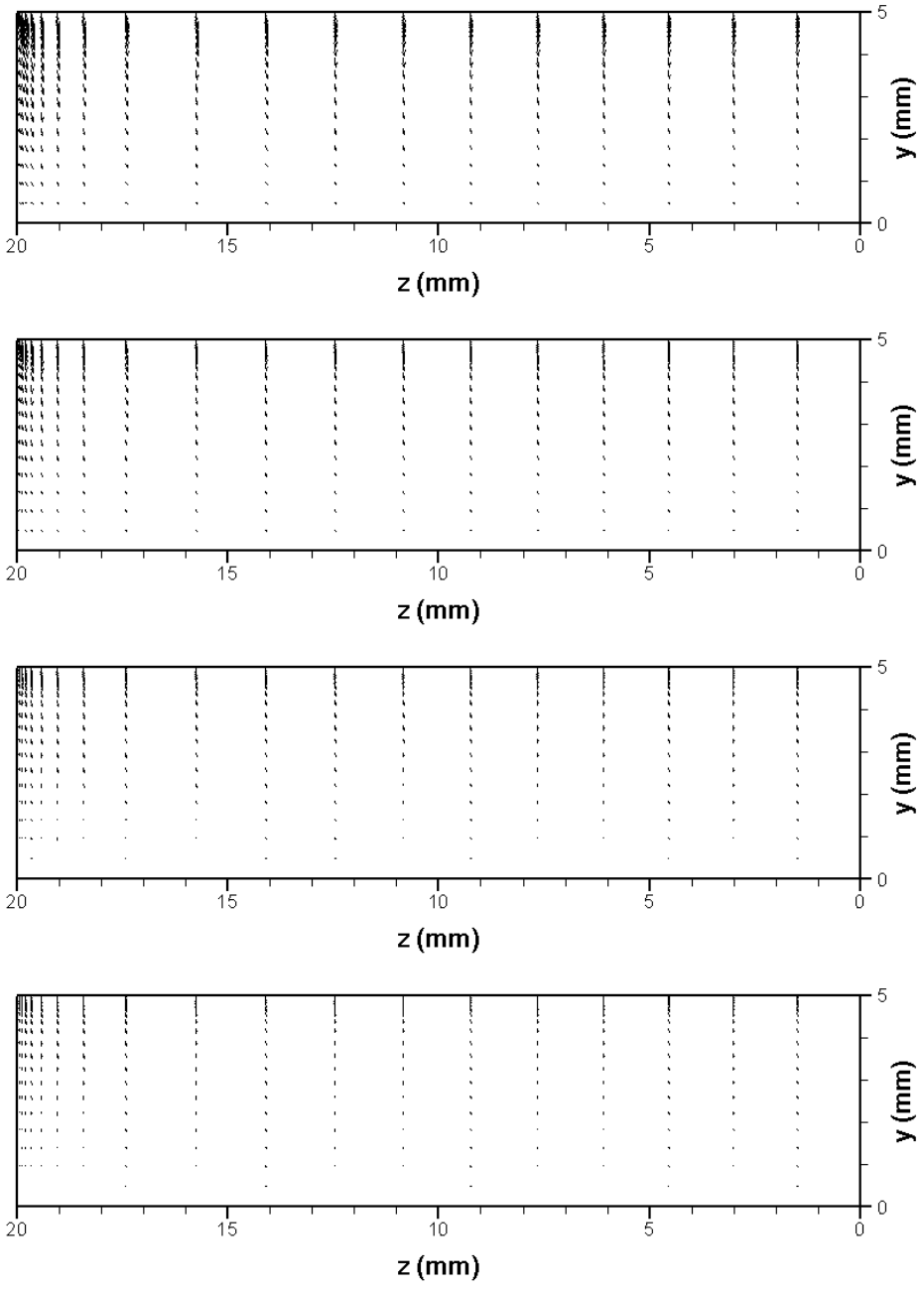

(f) *RA*2

Figure D.2: Continued

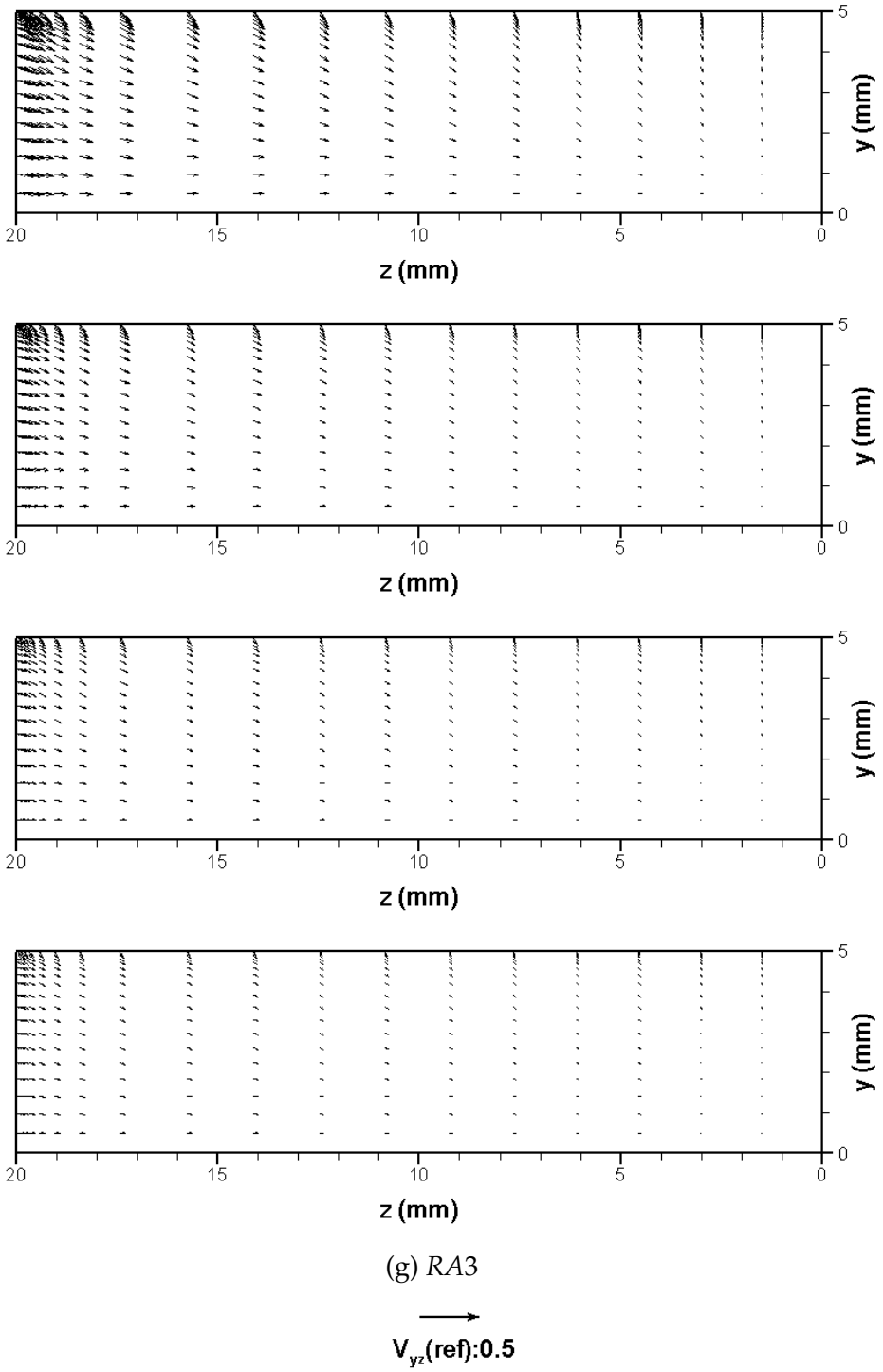

(g) *RA*3

Figure D.2: Continued

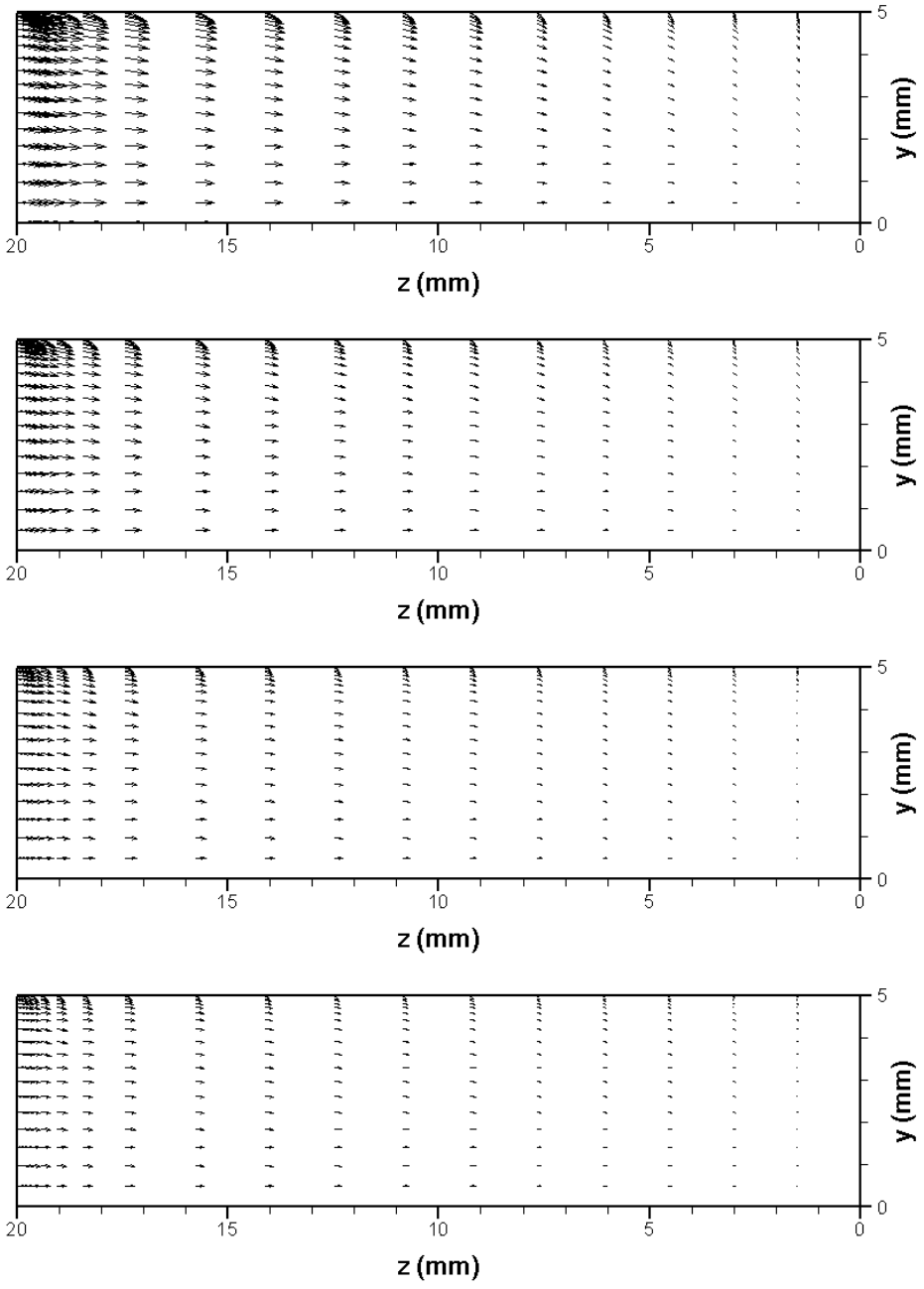

(h) *RA*4

Figure D.2: Continued

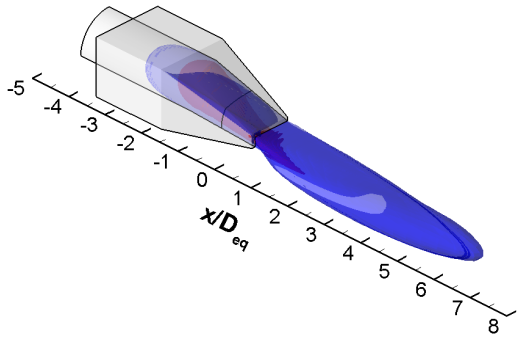

(a) *EA1C1*

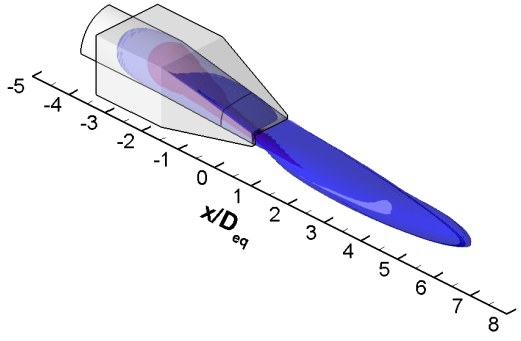

(b) *EA1C2*

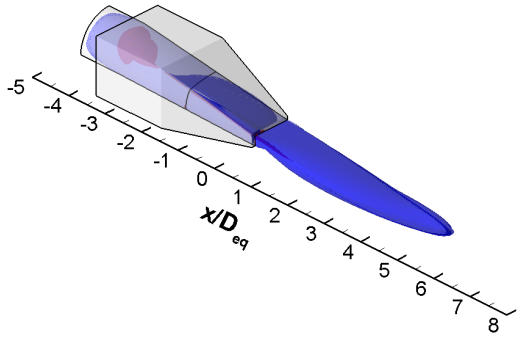

(c) *EA1C3*

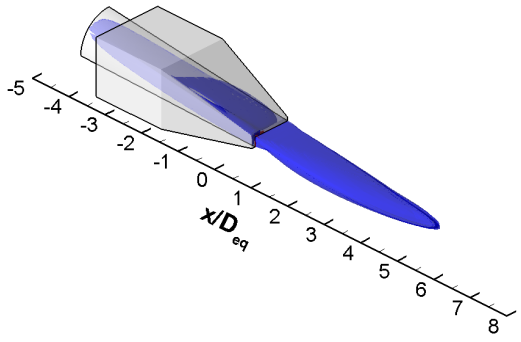

(d) *EA1C4*

Figure D.3: Development of normalised streamwise vorticity ($\omega_x D_{eq}/V_{exit}$) inside the nozzle for the E−series; iso-surface of +0.1 are shown in red and that of −0.1 are shown in blue (Note: only one quadrant is shown for all cases)

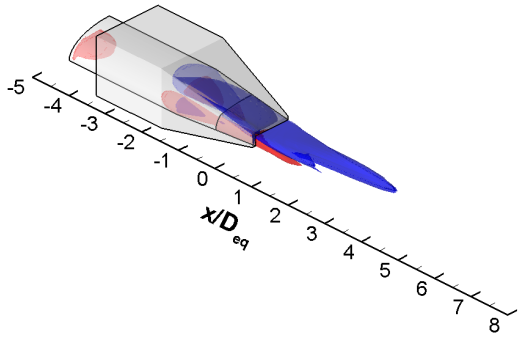

(e) *EA2C1*

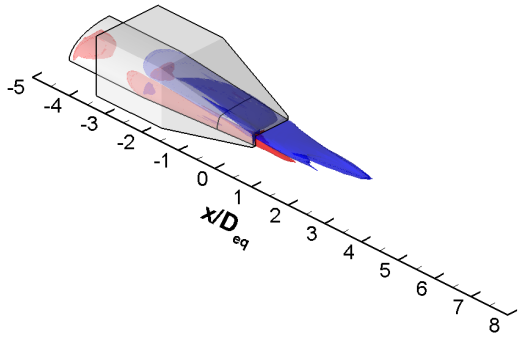

(f) *EA2C2*

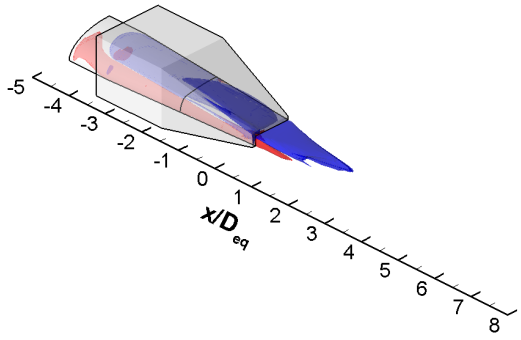

(g) *EA2C3*

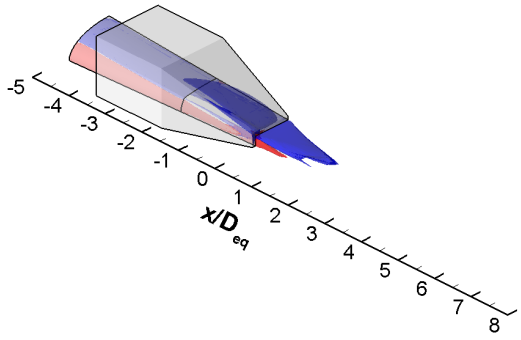

(h) *EA2C4*

Figure D.3: Continued

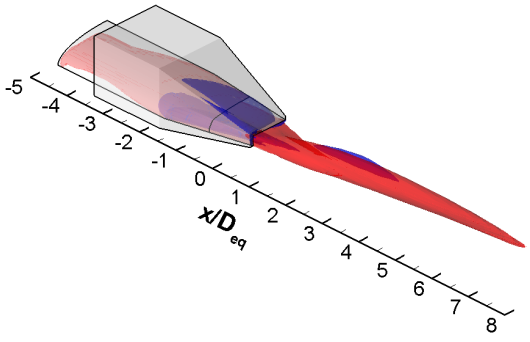

(i) *EA3C1*

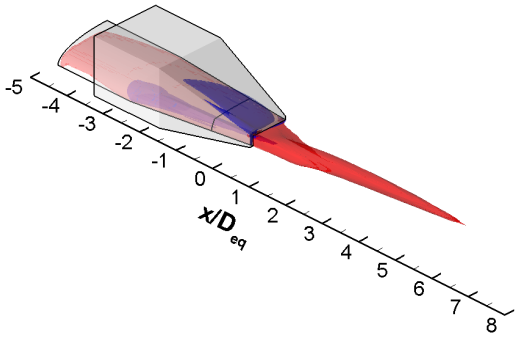

(j) *EA3C2*

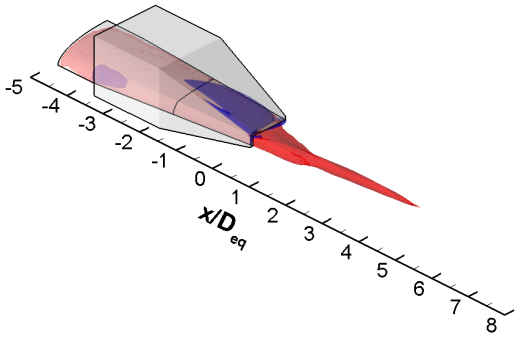

(k) *EA3C3*

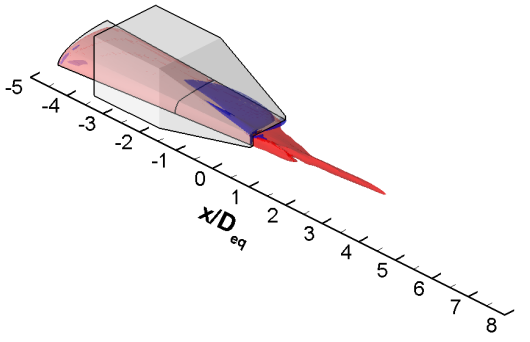

(l) *EA3C4*

Figure D.3: Continued

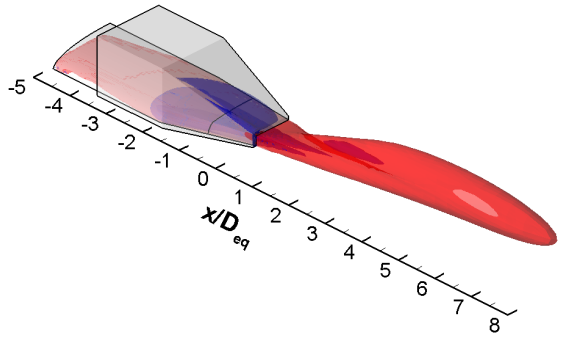

(m) *EA4C1*

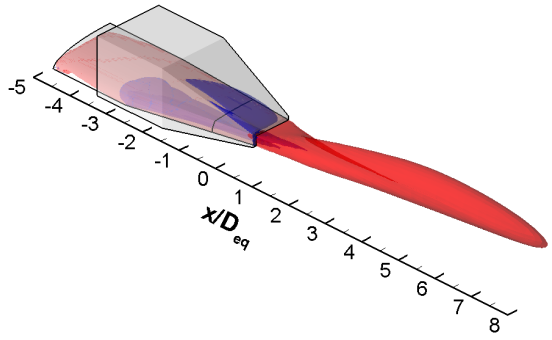

(n) *EA4C2*

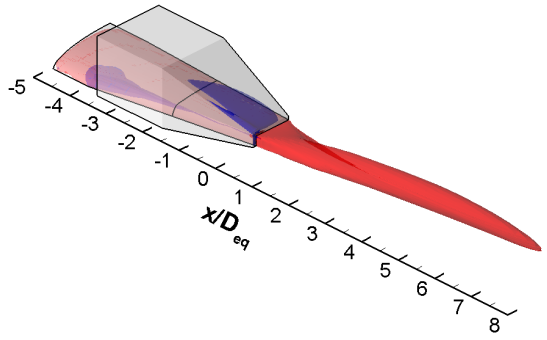

(o) *EA4C3*

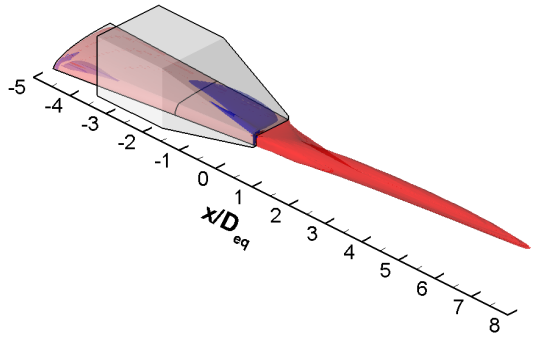

(p) *EA4C4*

Figure D.3: Continued

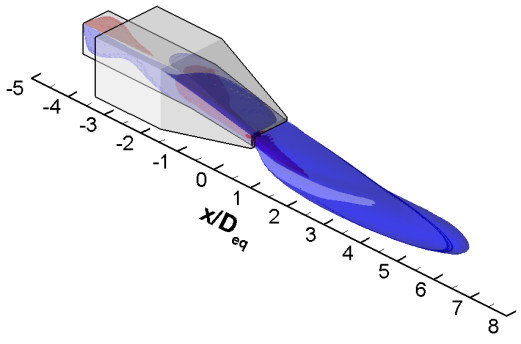

(a) *RA*1*C*1

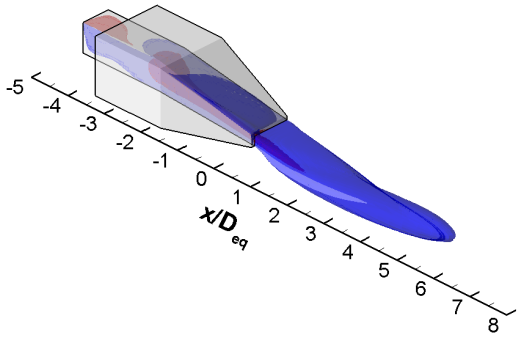

(b) *RA*1*C*2

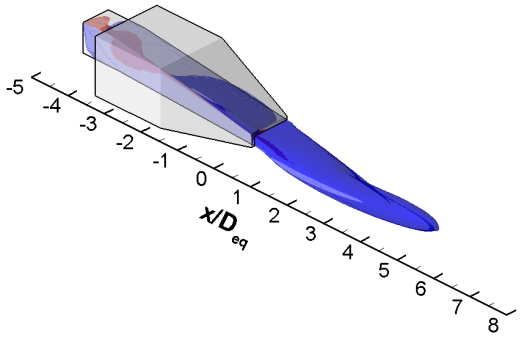

(c) *RA*1*C*3

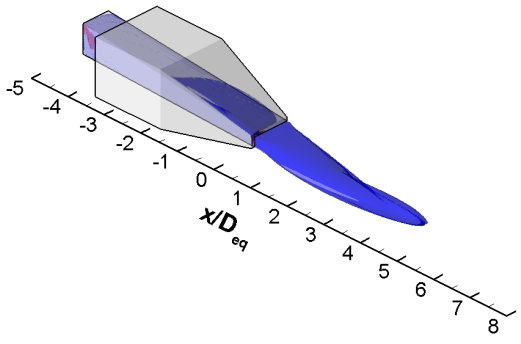

(d) *RA*1*C*4

Figure D.4: Development of normalised streamwise vorticity ($\omega_x D_{eq}/V_{exit}$) inside the nozzle for the R−series; iso-surface of +0.1 are shown in red and that of −0.1 are shown in blue (Note: only one quadrant is shown for all cases)

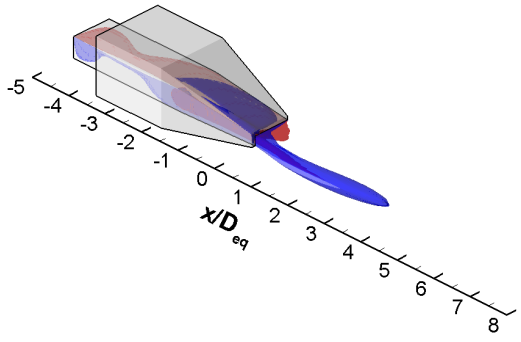

(e) *RA2C1*

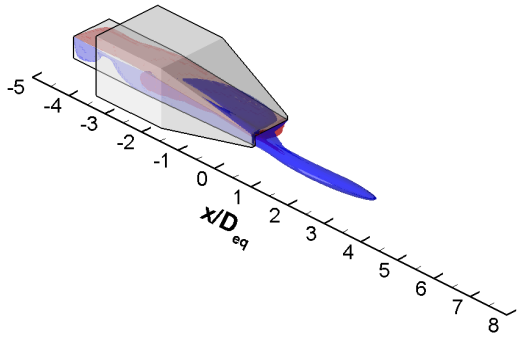

(f) *RA2C2*

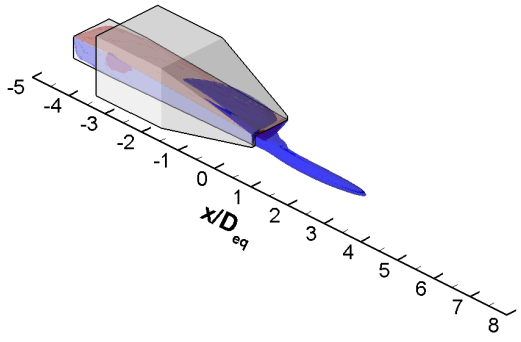

(g) *RA2C3*

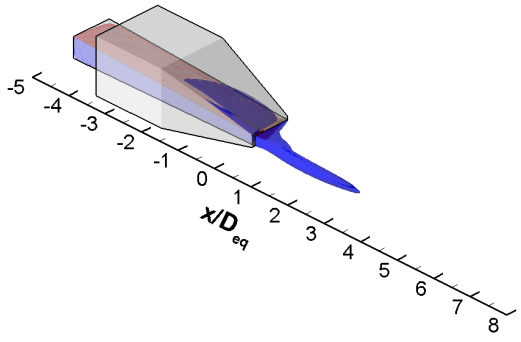

(h) *RA2C4*

Figure D.4: Continued

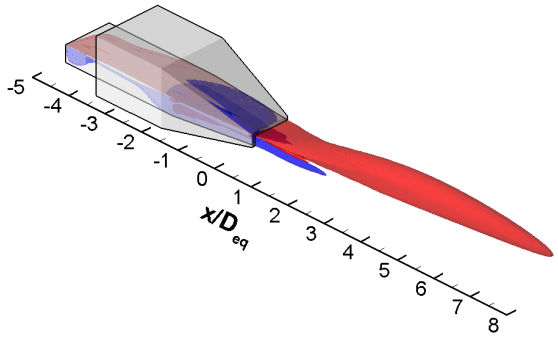

(i) *RA3C1*

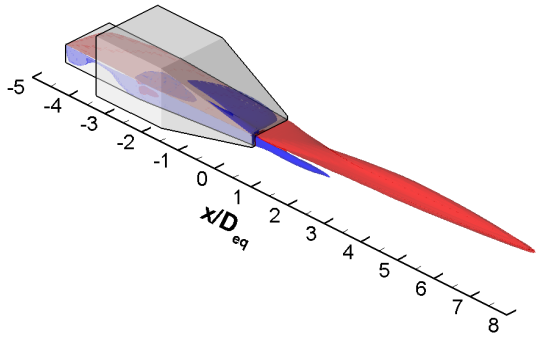

(j) *RA3C2*

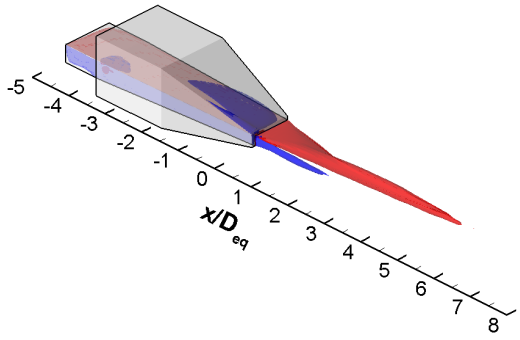

(k) *RA3C3*

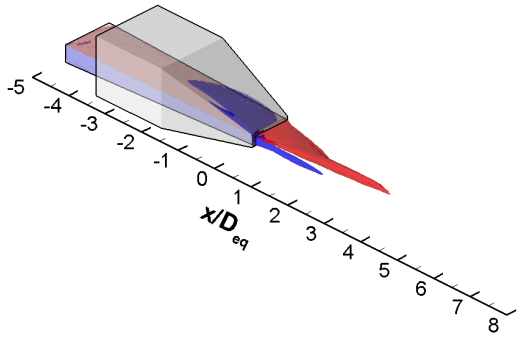

(l) *RA3C4*

Figure D.4: Continued

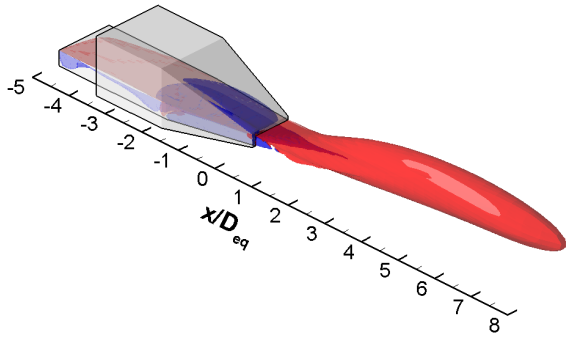

(m) *RA*4*C*1

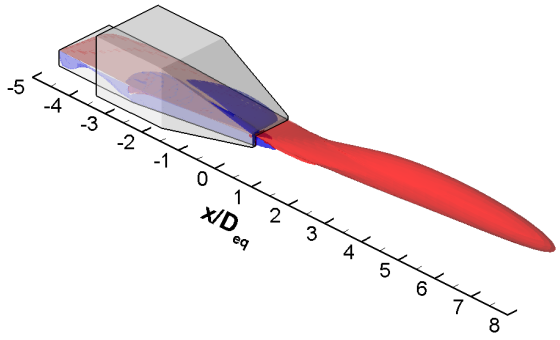

(n) *RA*4*C*2

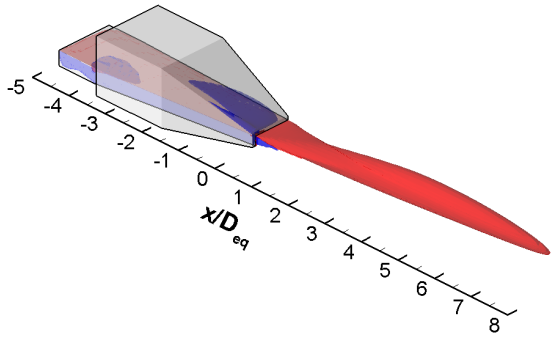

(o) *RA*4*C*3

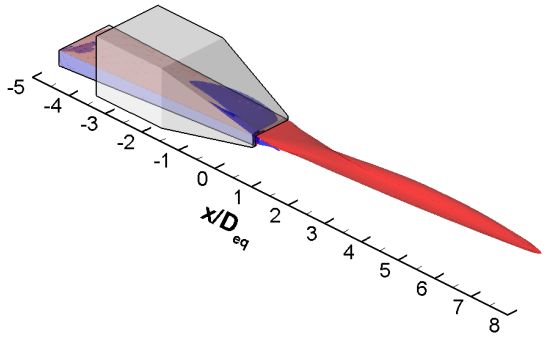

(p) *RA*4*C*4

Figure D.4: Continued

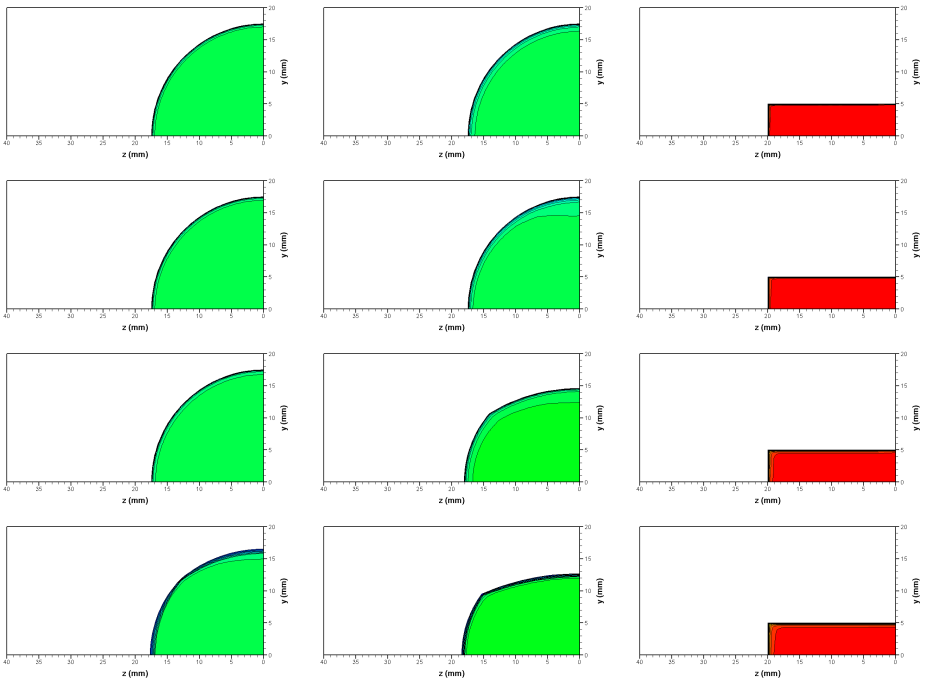

(a) *EA*1; from top to bottom, *CSR* = 1, 2, 3, 4

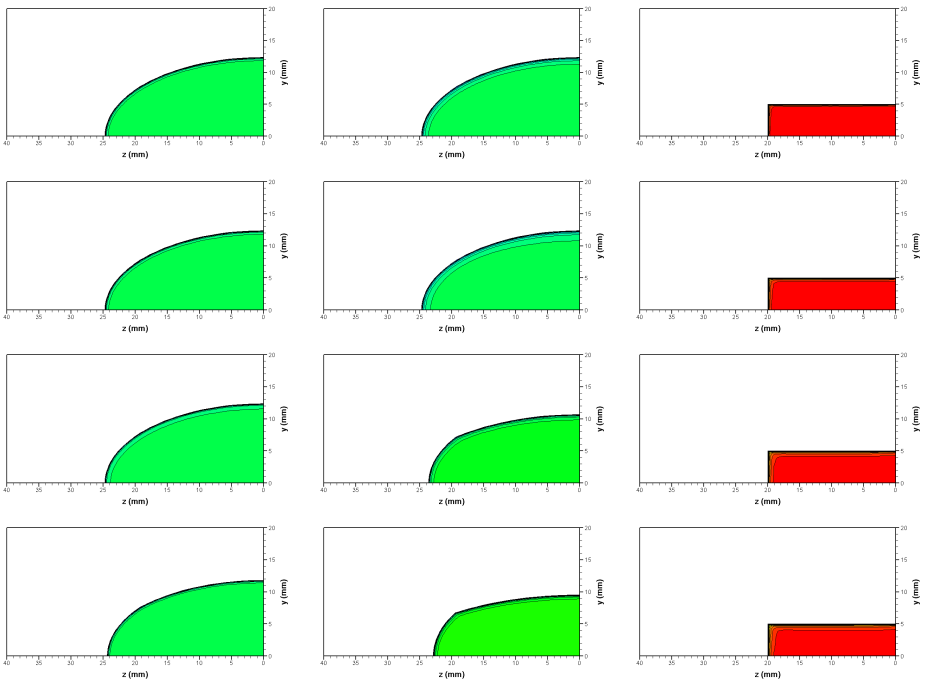

(b) *EA*2; from top to bottom, *CSR* = 1, 2, 3, 4

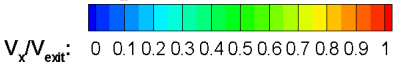

Figure D.5: Contours of normalised streamwise velocity (V_x/V_{exit}) for E−series configurations at planes 4.5 D_{eq} upstream (left), 3 D_{eq} upstream (centre) and at the nozzle exit (right)

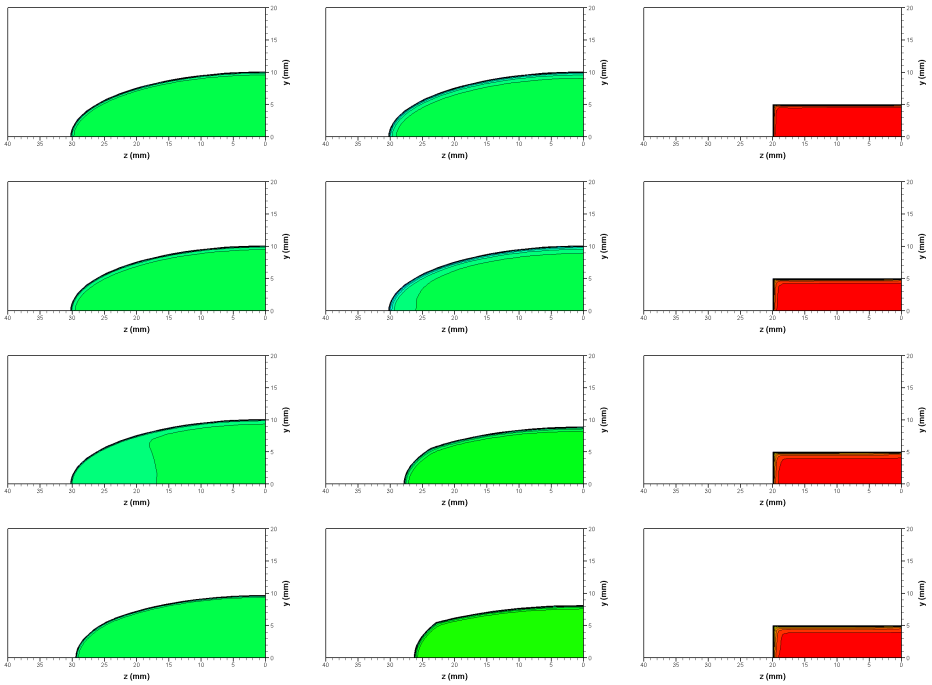

(c) *EA*3; from top to bottom, *CSR* = 1, 2, 3, 4

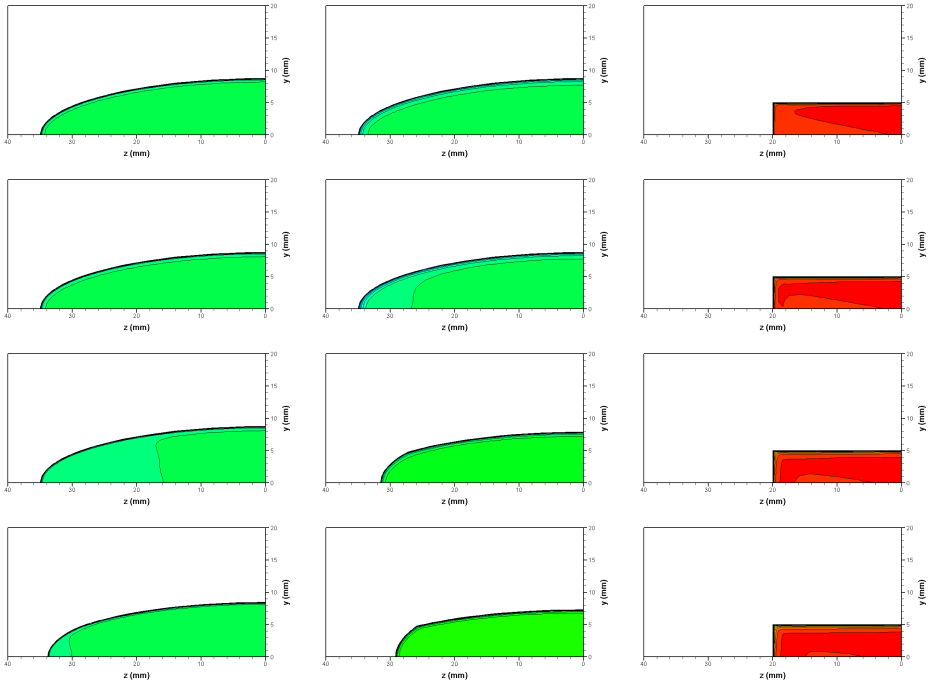

(d) *EA*4; from top to bottom, *CSR* = 1, 2, 3, 4

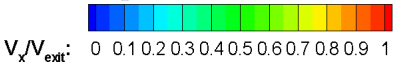

Figure D.5: Continued

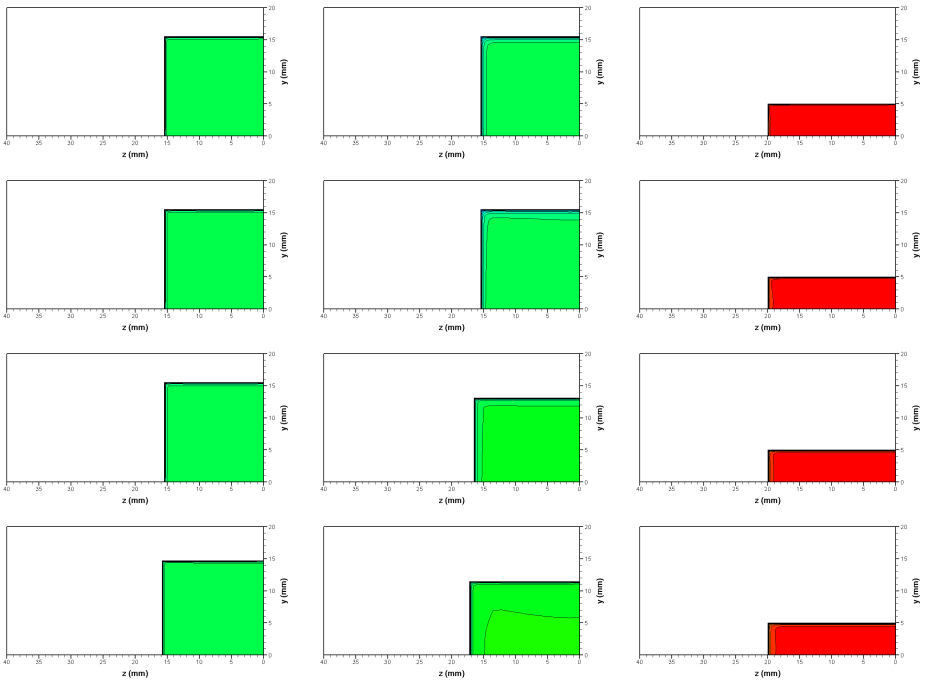

(a) *RA*1; from top to bottom, *CSR* = 1, 2, 3, 4

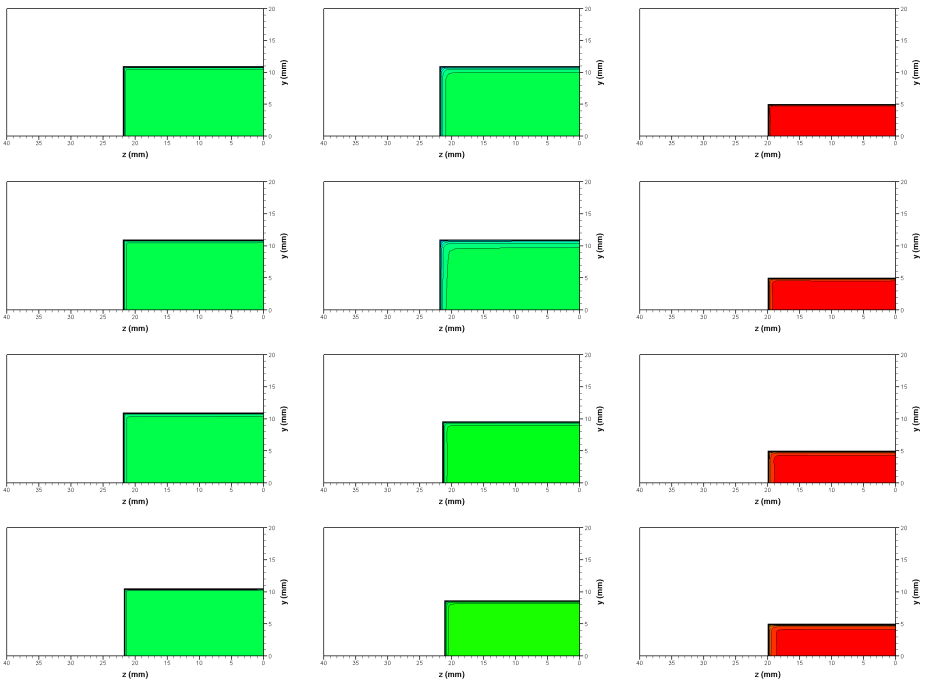

(b) *RA*2; from top to bottom, *CSR* = 1, 2, 3, 4

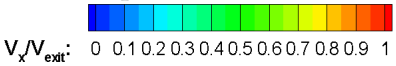

Figure D.6: Contours of normalised streamwise velocity (V_x/V_{exit}) for R−series configurations at planes 4.5 D_{eq} upstream (left), 3 D_{eq} upstream (centre) and at the nozzle exit (right)

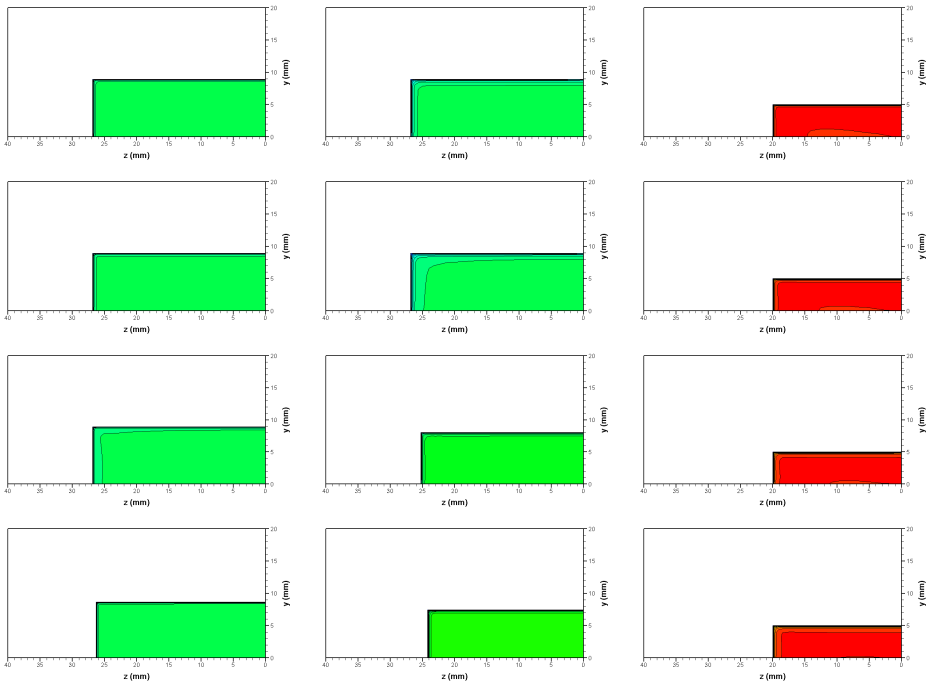

(c) *RA*3; from top to bottom, *CSR* = 1, 2, 3, 4

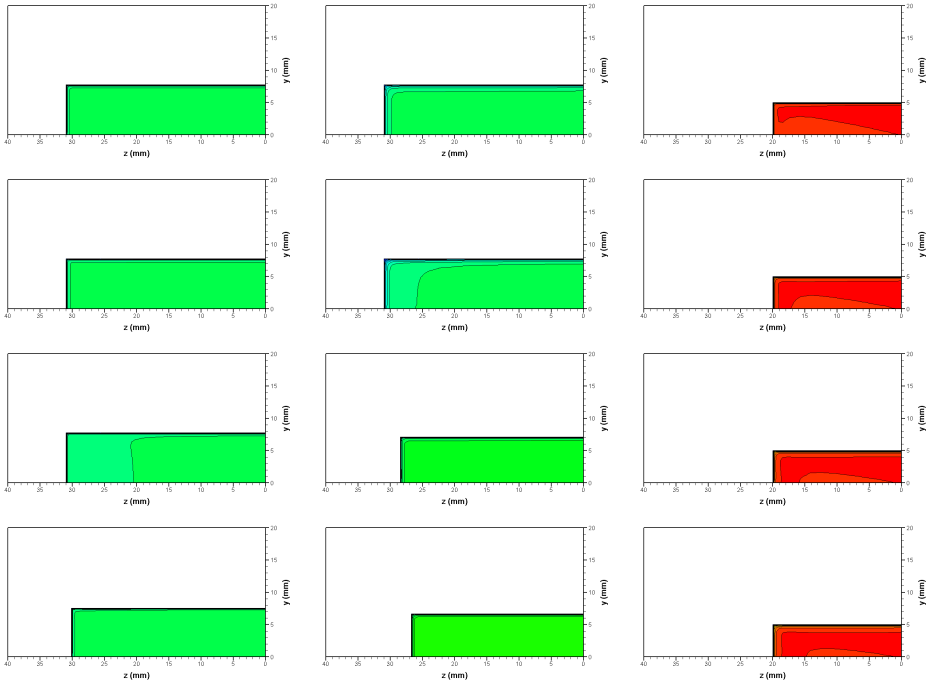

(d) *RA*4; from top to bottom, *CSR* = 1, 2, 3, 4

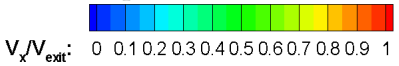

Figure D.6: Continued

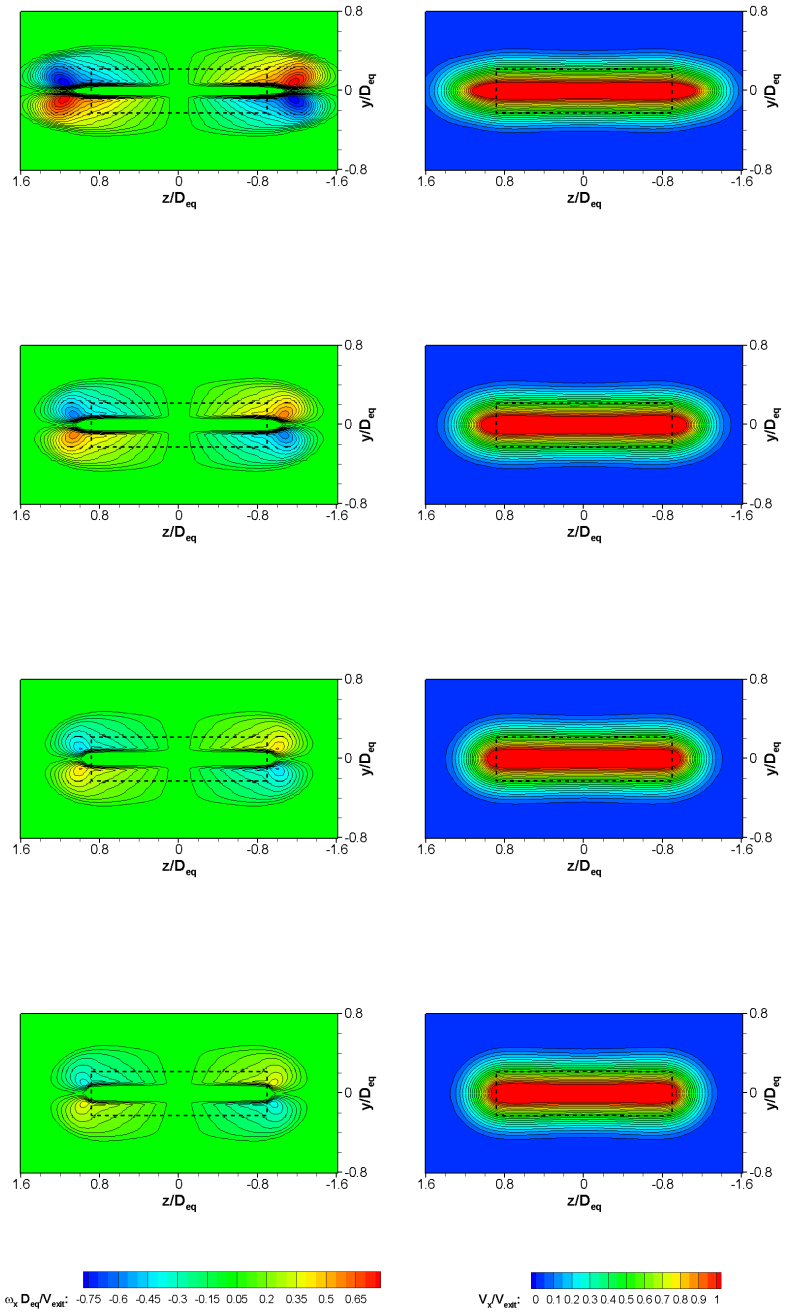

(a) *EA*1

Figure D.7: Contours of normalised streamwise vorticity ($\omega_x D_{eq}/V_{exit}$) (left) and normalised streamwise velocity (V_x/V_{exit}) (right) for the E−series configurations at a plane 2 D_{eq} downstream of the exit; from top to bottom in each configuration, C1, C2, C3, C4; the dashed outline represents the nozzle exit

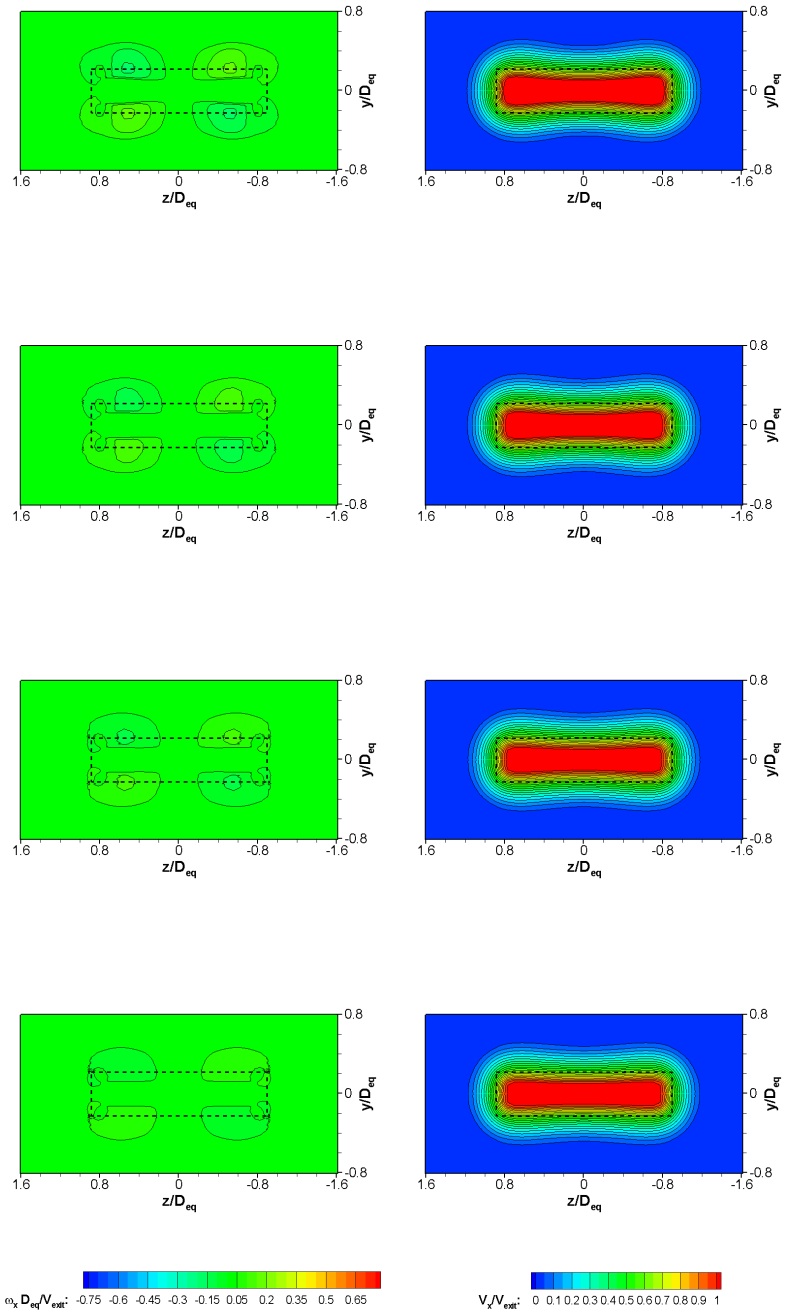

(b) *EA*2

Figure D.7: Continued

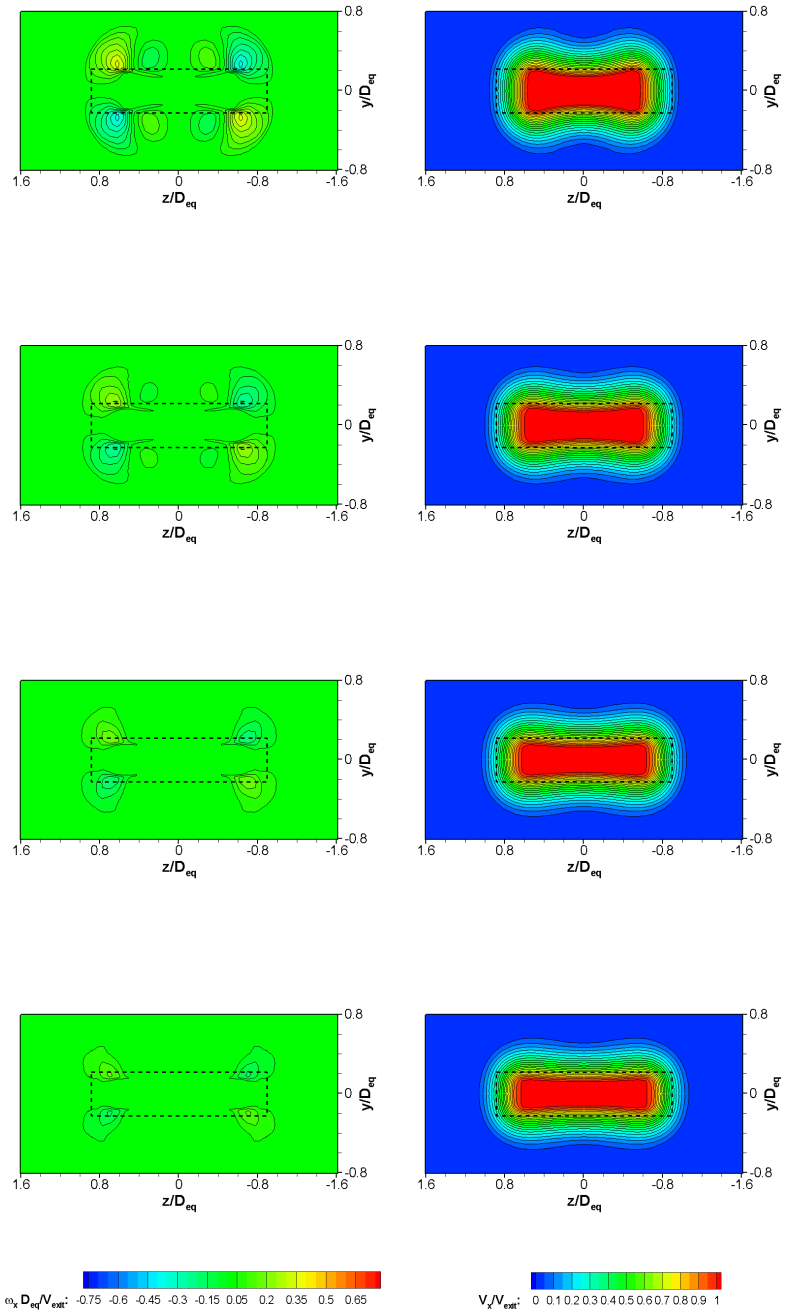

(c) *EA*3

Figure D.7: Continued

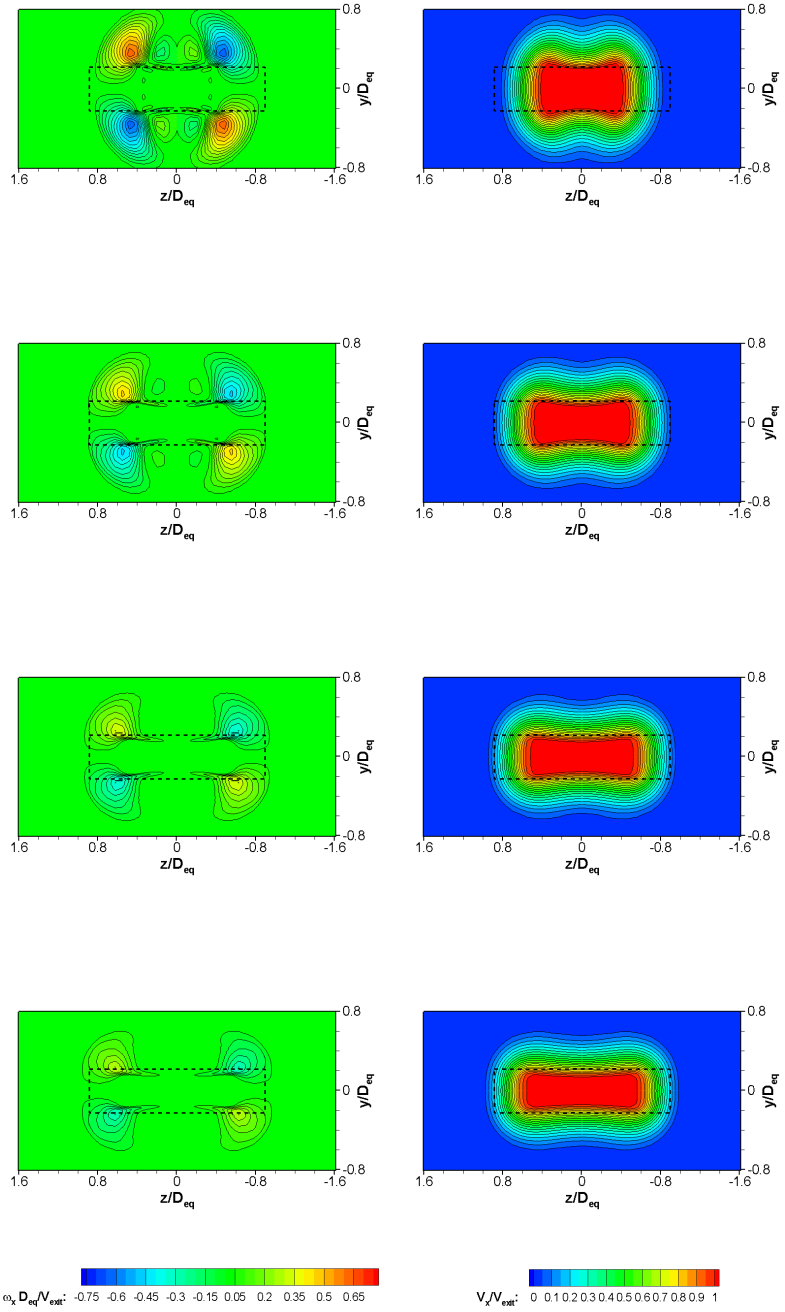

(d) *EA*4

Figure D.7: Continued

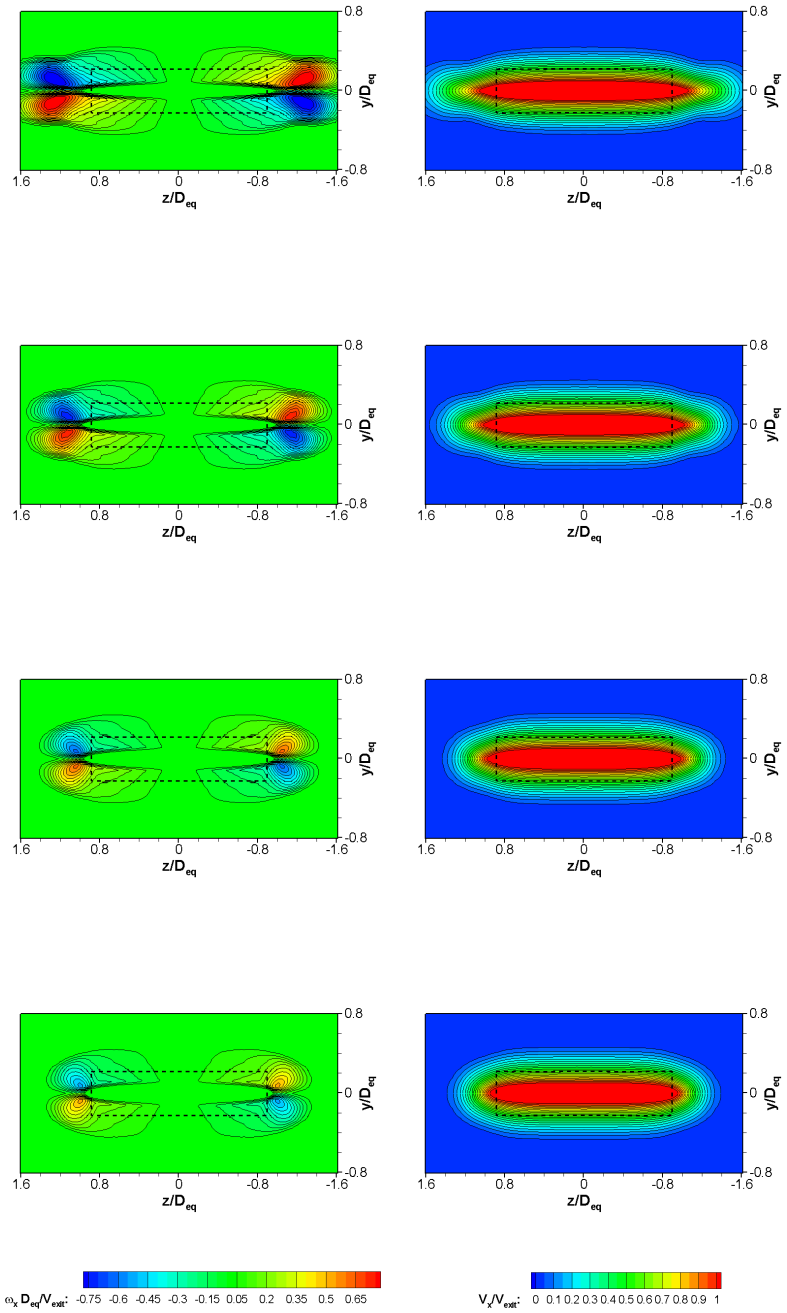

(a) *RA*1

Figure D.8: Contours of normalised streamwise vorticity ($\omega_x D_{eq}/V_{exit}$) (left) and normalised streamwise velocity (V_x/V_{exit}) (right) for the R−series configurations at a plane 2 D_{eq} downstream of the exit; from top to bottom in each configuration, C1, C2, C3, C4; the dashed outline represents the nozzle exit

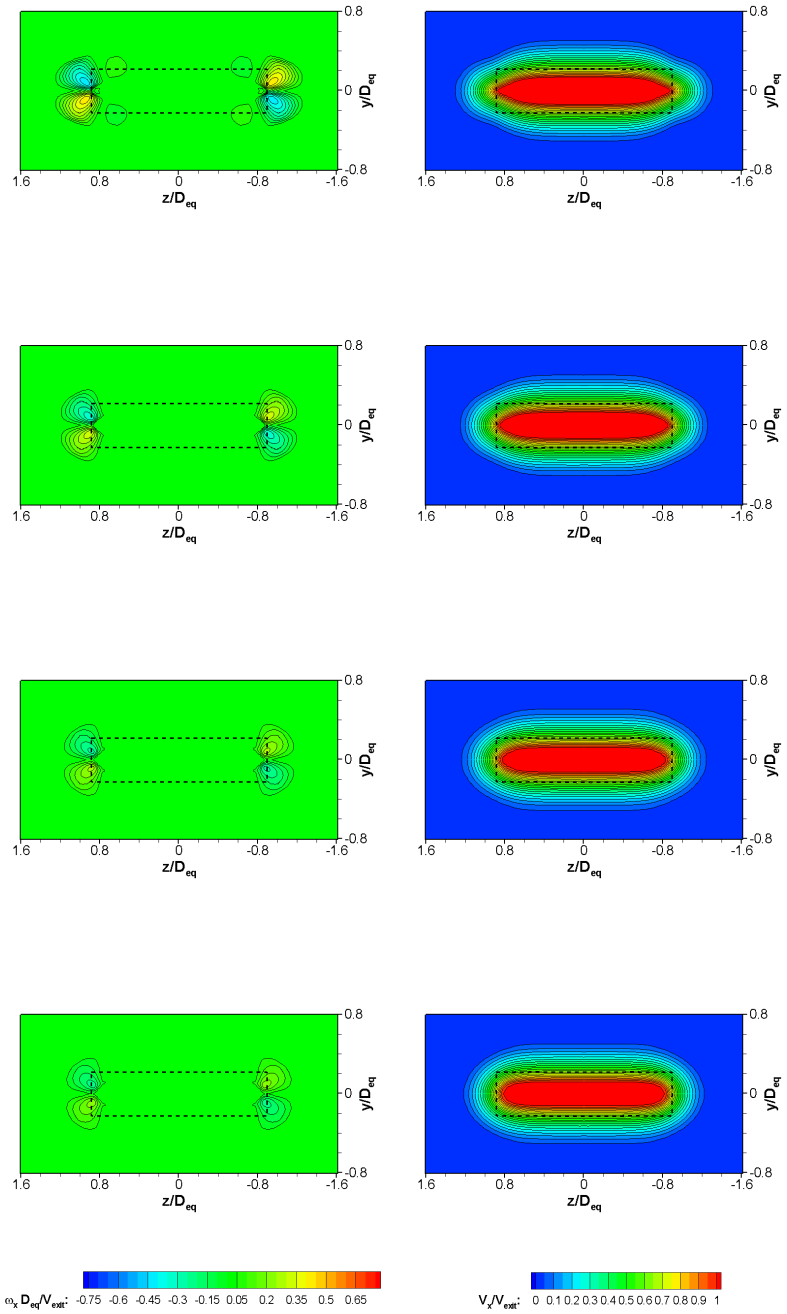

(b) *RA*2

Figure D.8: Continued

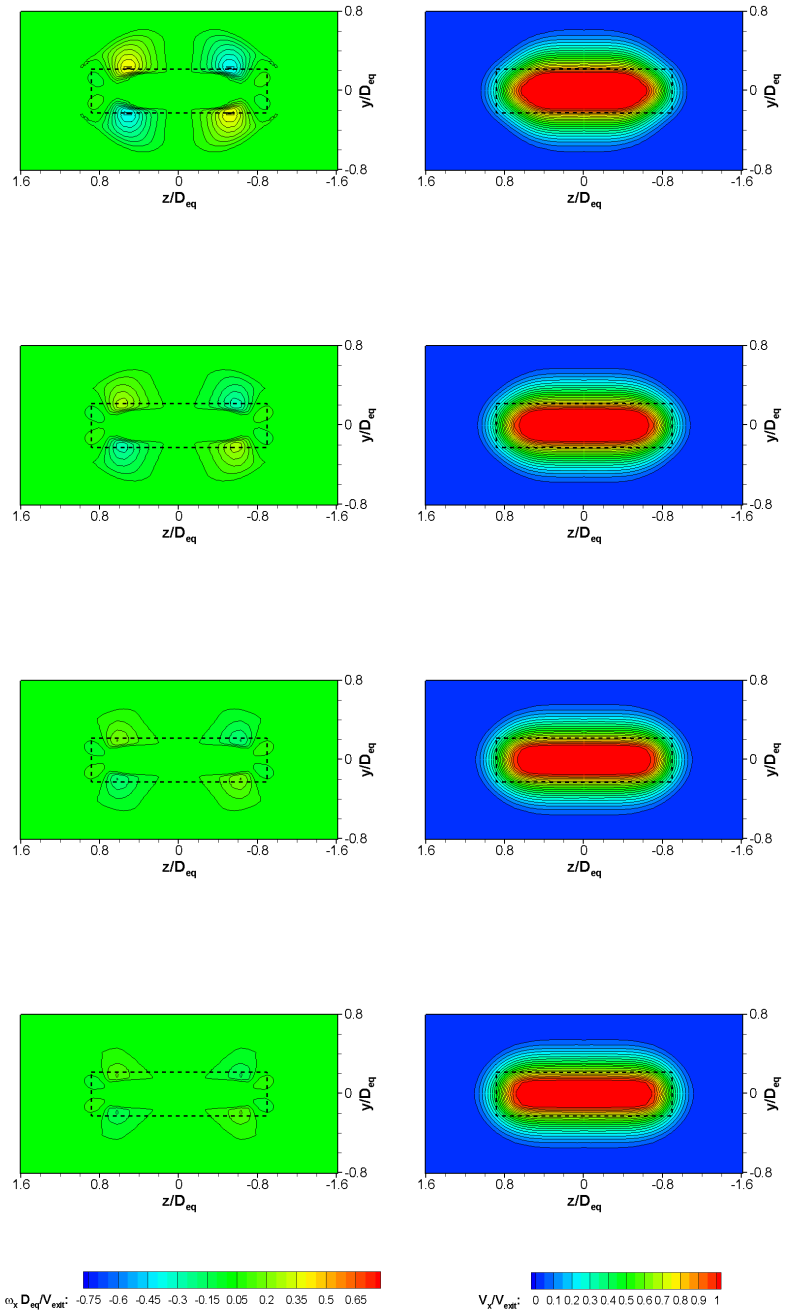

(c) *RA*3

Figure D.8: Continued

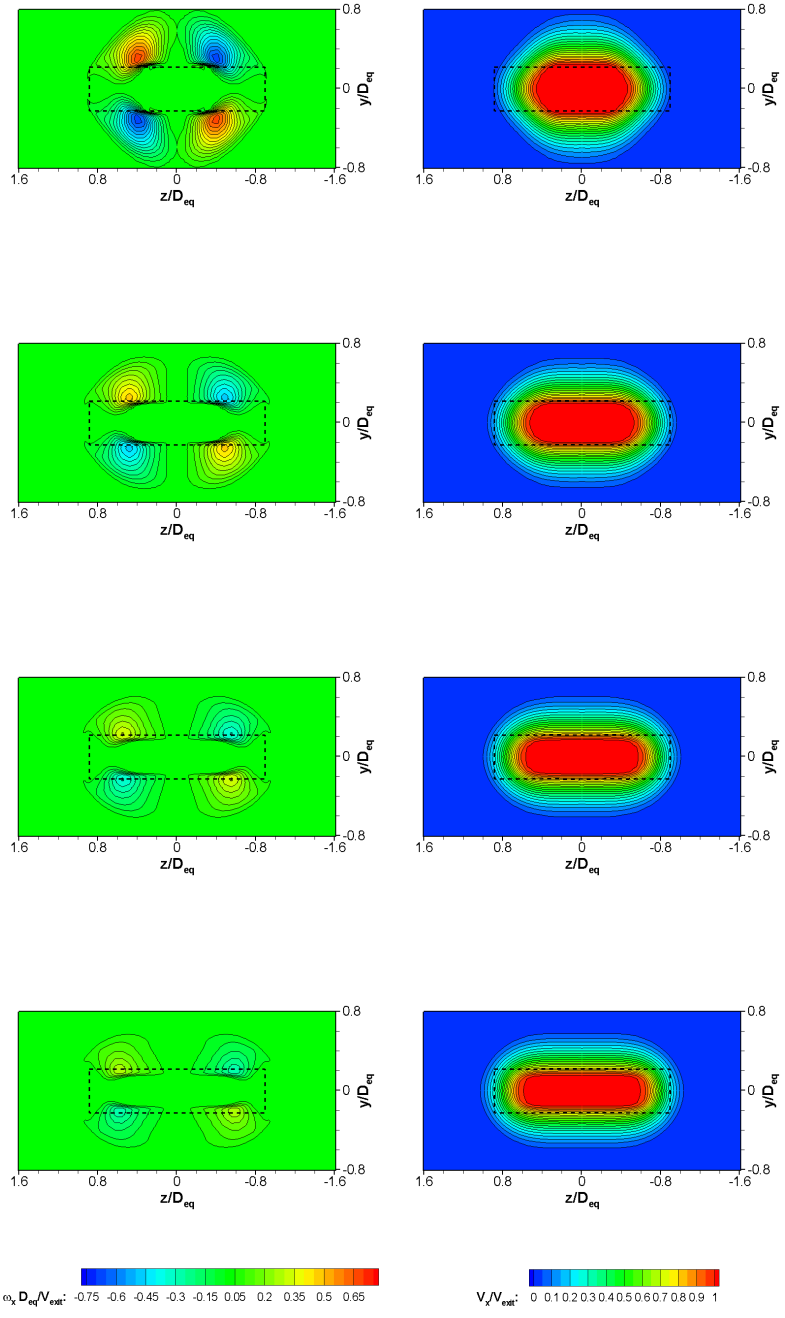

(d) *RA*4

Figure D.8: Continued

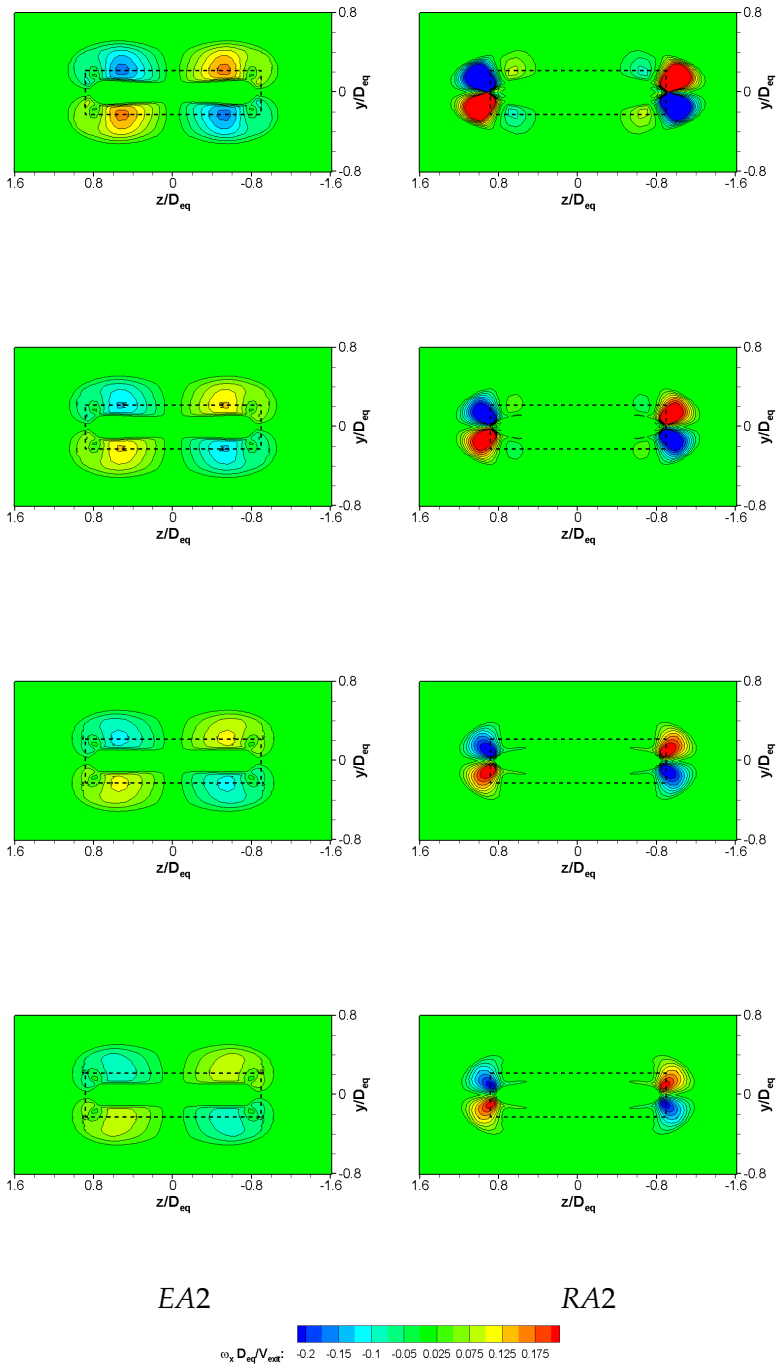

Figure D.9: Contours of normalised streamwise vorticity ($\omega_x D_{eq}/V_{exit}$) for E− and R−series configurations at a plane 2 D_{eq} downstream of the exit presented with a different contour scale; from top to bottom in each configuration, C1, C2, C3, C4; the dashed outline represents the nozzle exit

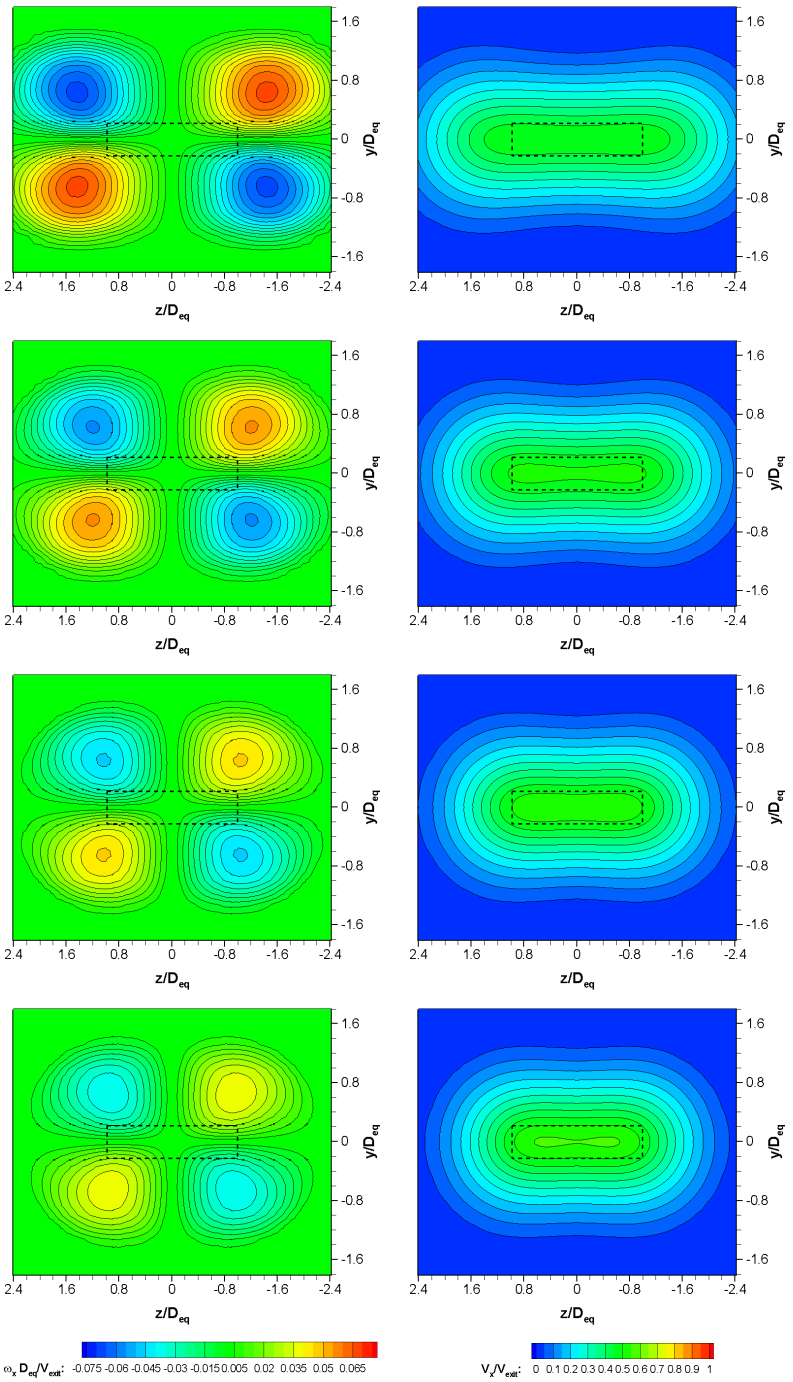

(a) *EA*1

Figure D.10: Contours of normalised streamwise vorticity ($\omega_x D_{eq}/V_{exit}$) (left) and normalised streamwise velocity (V_x/V_{exit}) (right) for the E−series configurations at a plane 8 D_{eq} downstream of the exit; from top to bottom in each configuration, C1, C2, C3, C4; the dashed outline represents the nozzle exit

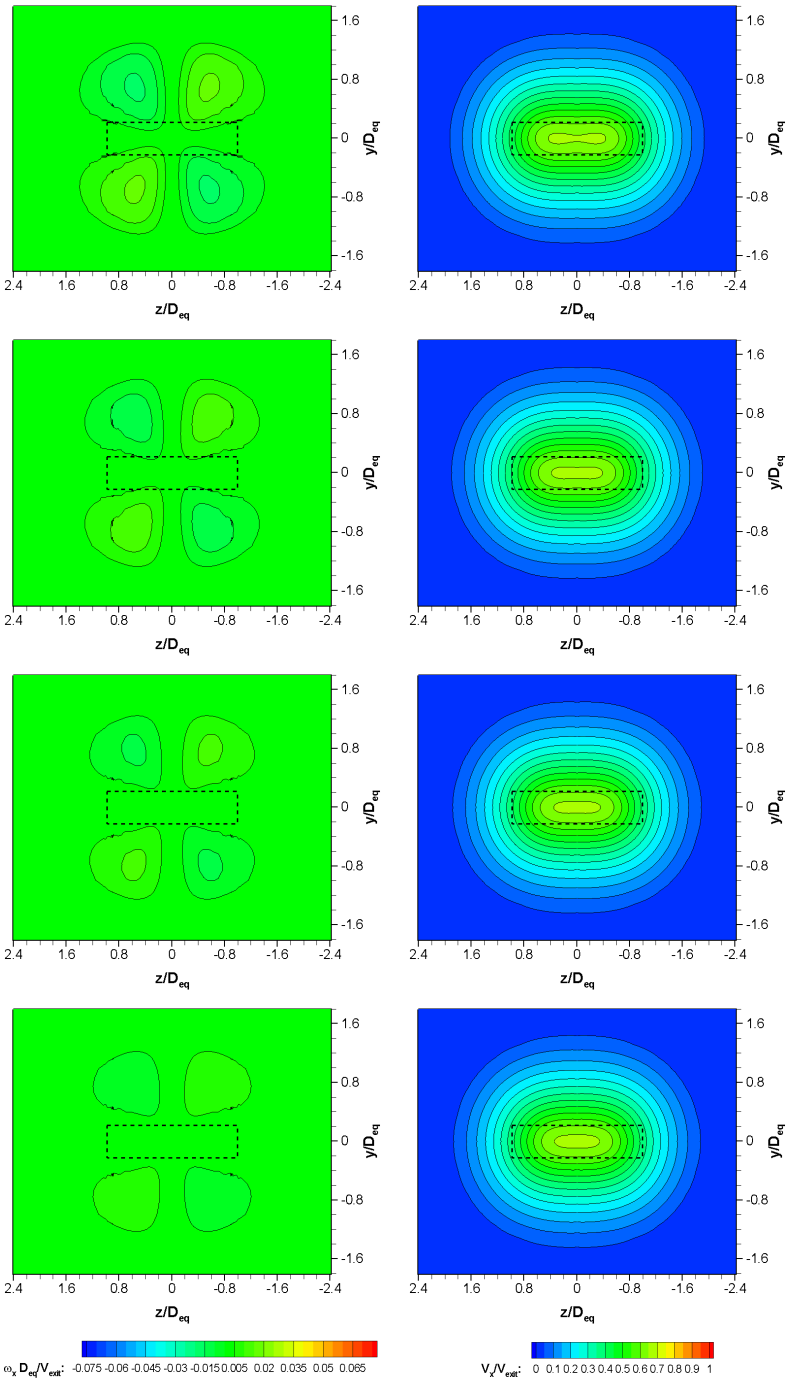

(b) *EA*2

Figure D.10: Continued

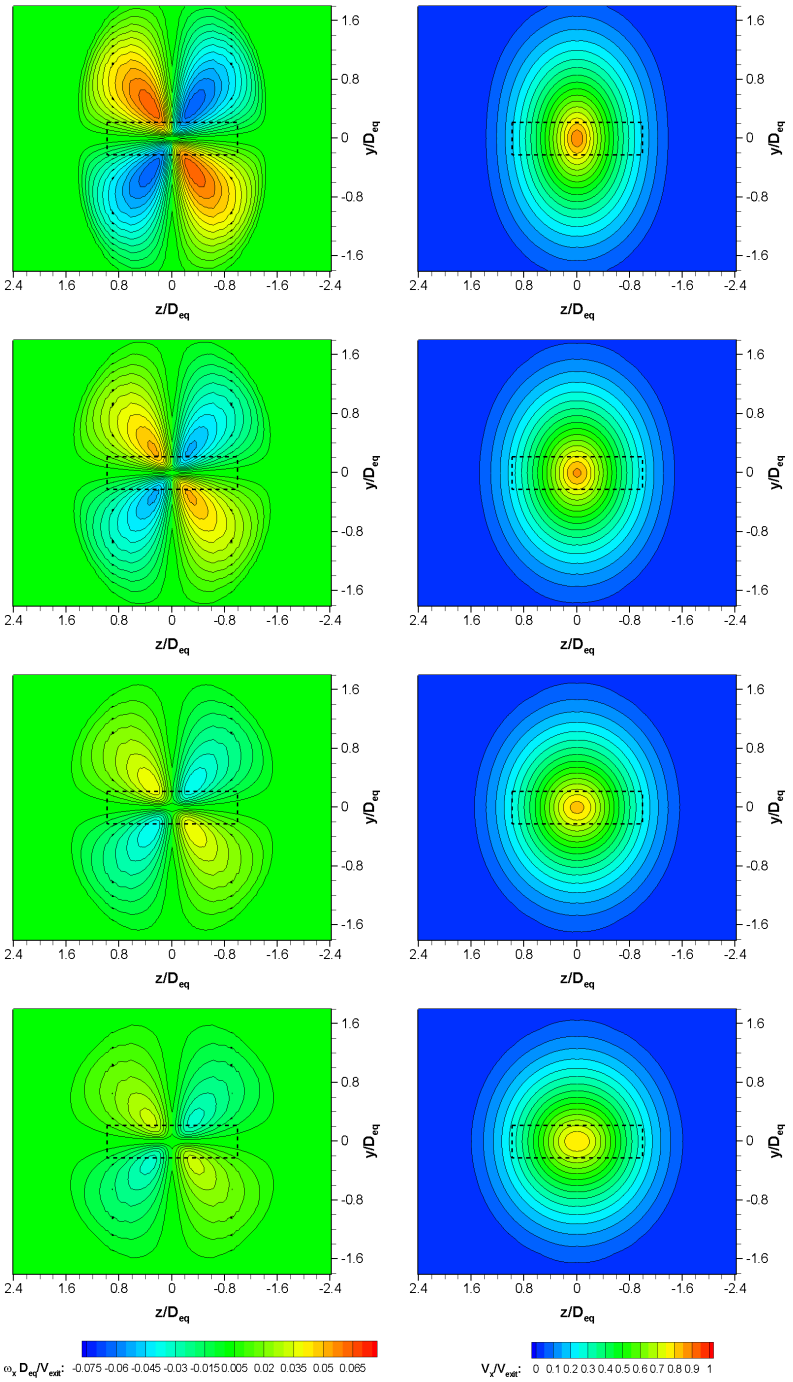

(c) *EA*3

Figure D.10: Continued

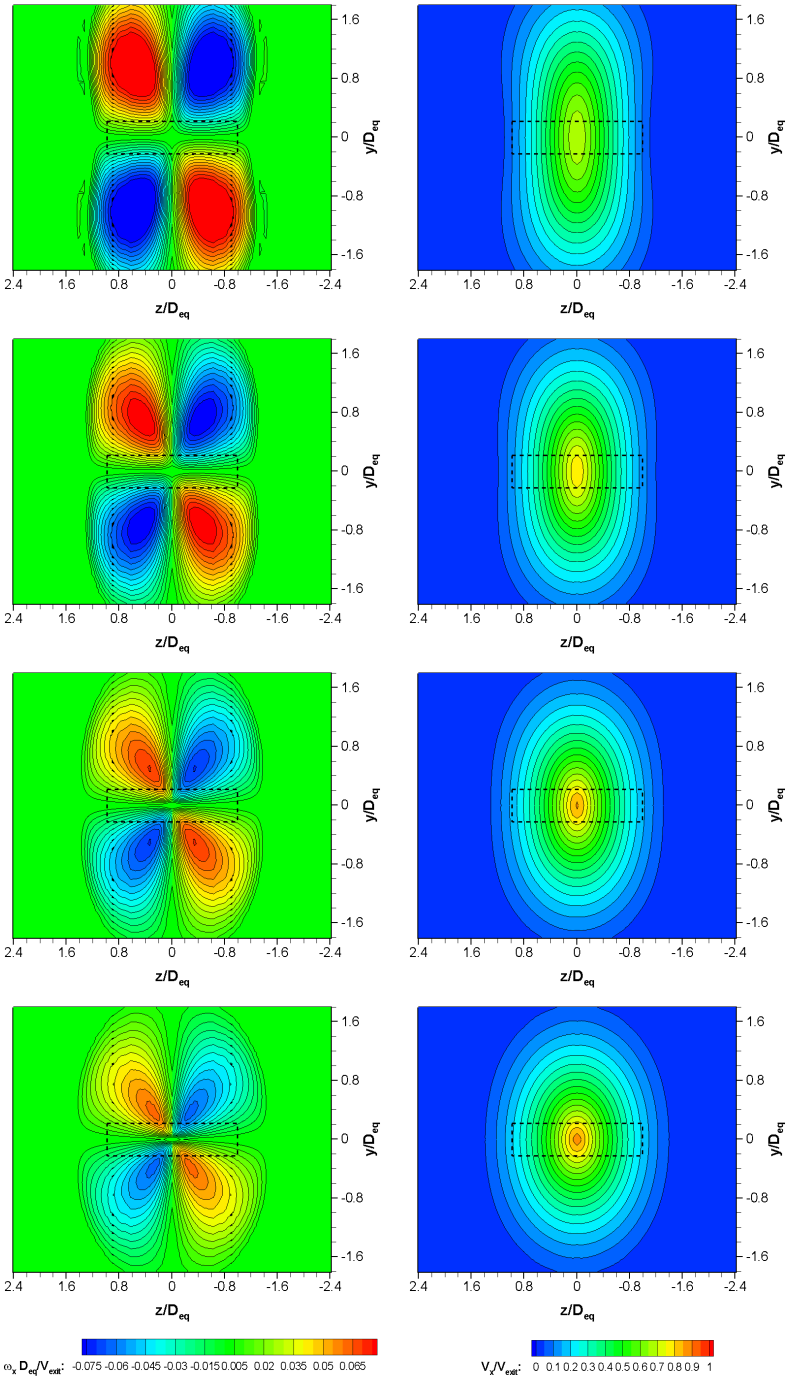

(d) *EA*4

Figure D.10: Continued

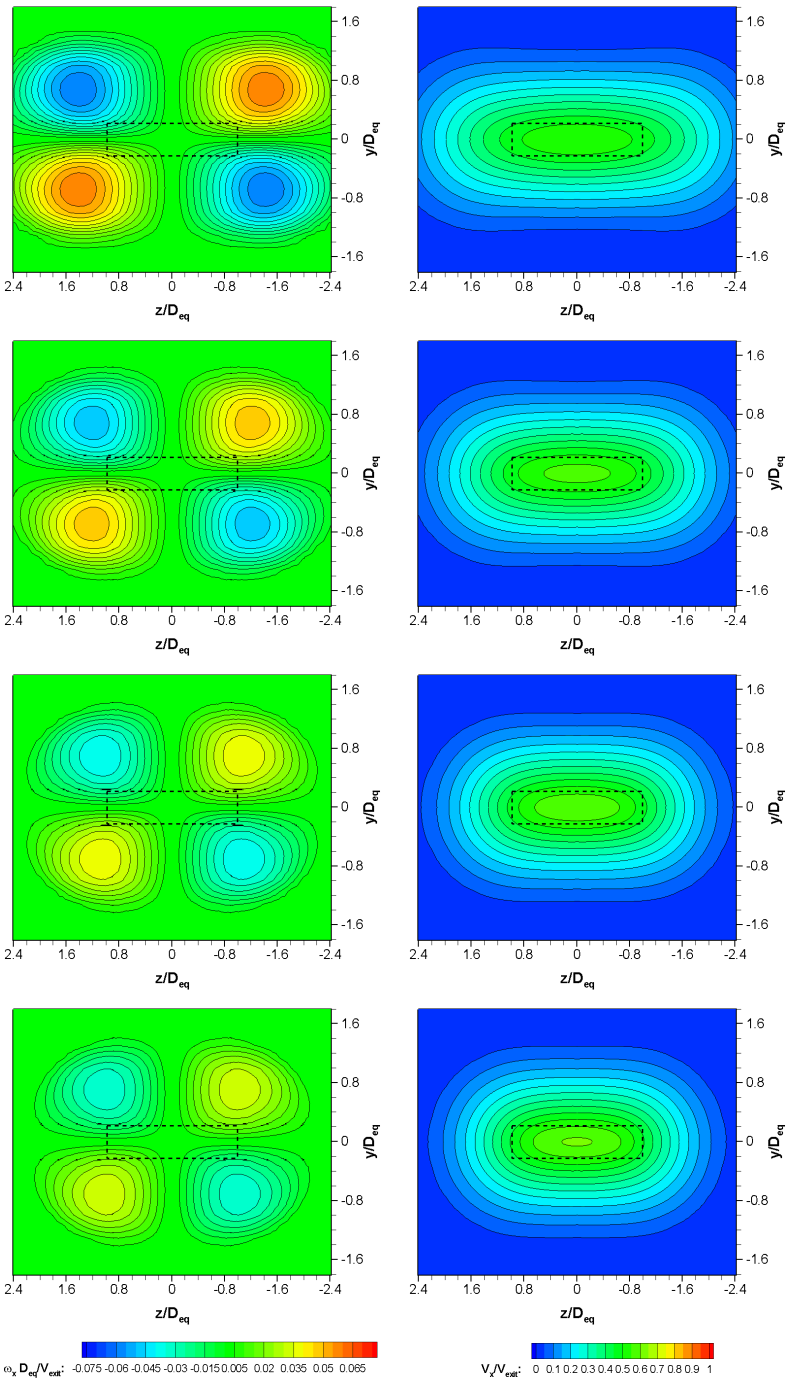

(a) *RA*1

Figure D.11: Contours of normalised streamwise vorticity ($\omega_x D_{eq}/V_{exit}$) (left) and normalised streamwise velocity (V_x/V_{exit}) (right) for the R−series configurations at a plane 8 D_{eq} downstream of the exit; from top to bottom in each configuration, C1, C2, C3, C4; the dashed outline represents the nozzle exit

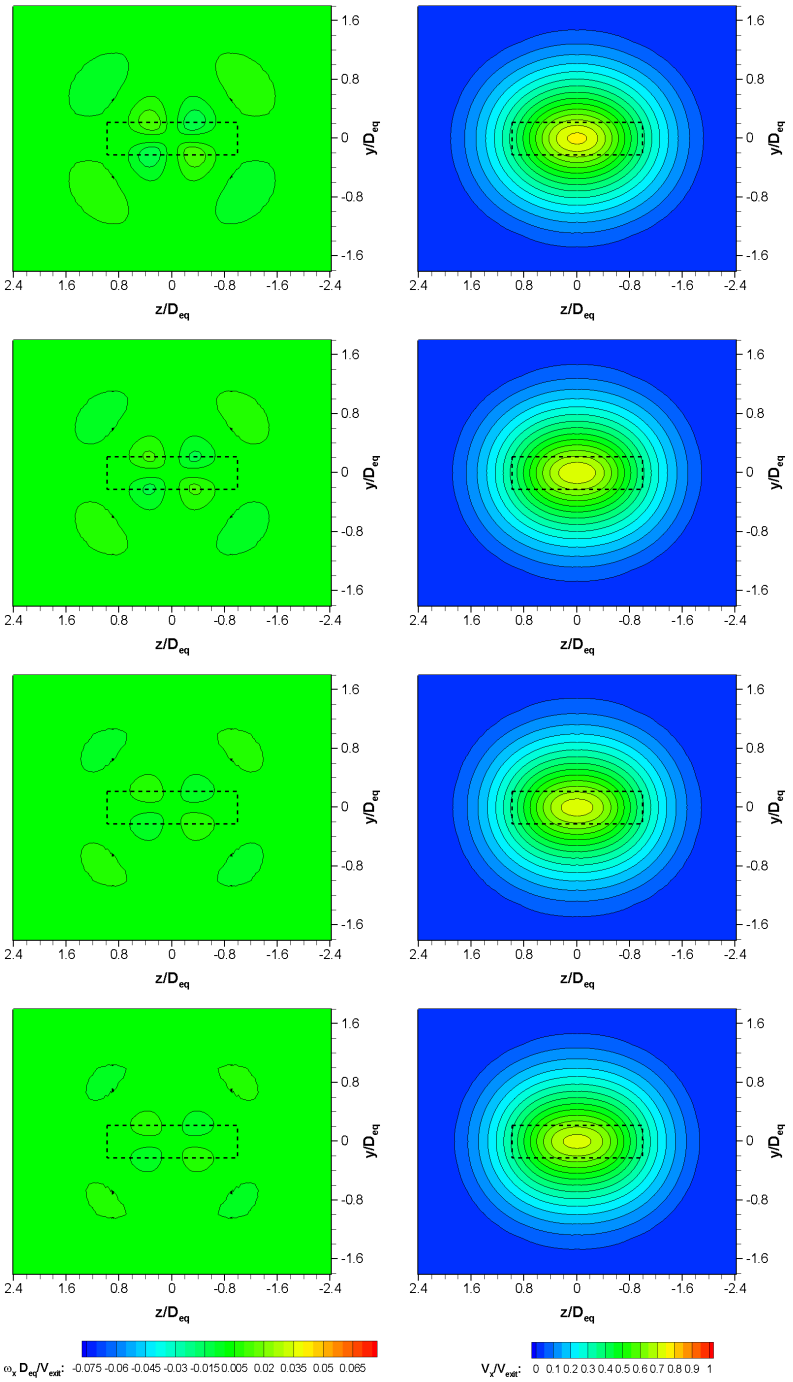

(b) *RA*2

Figure D.11: Continued

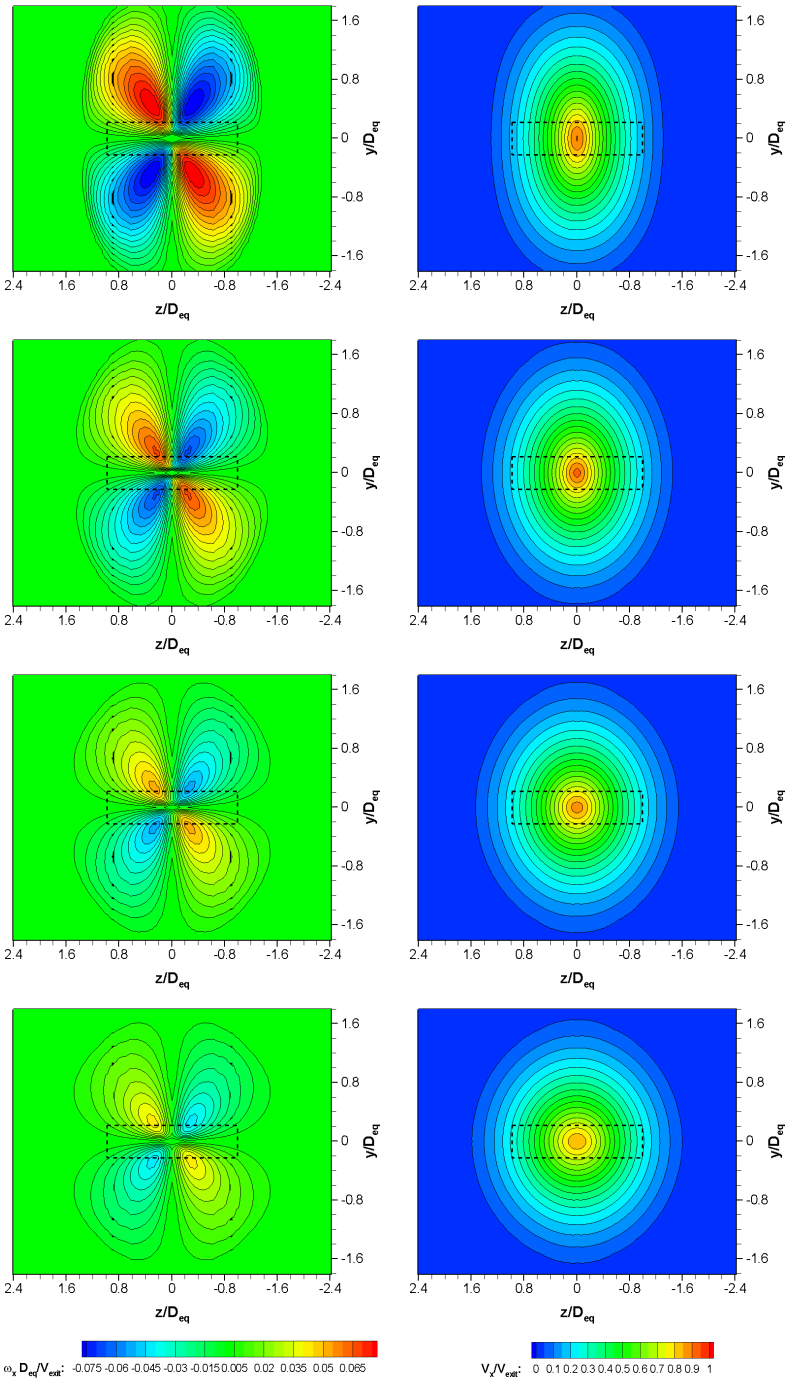

(c) *RA*3

Figure D.11: Continued

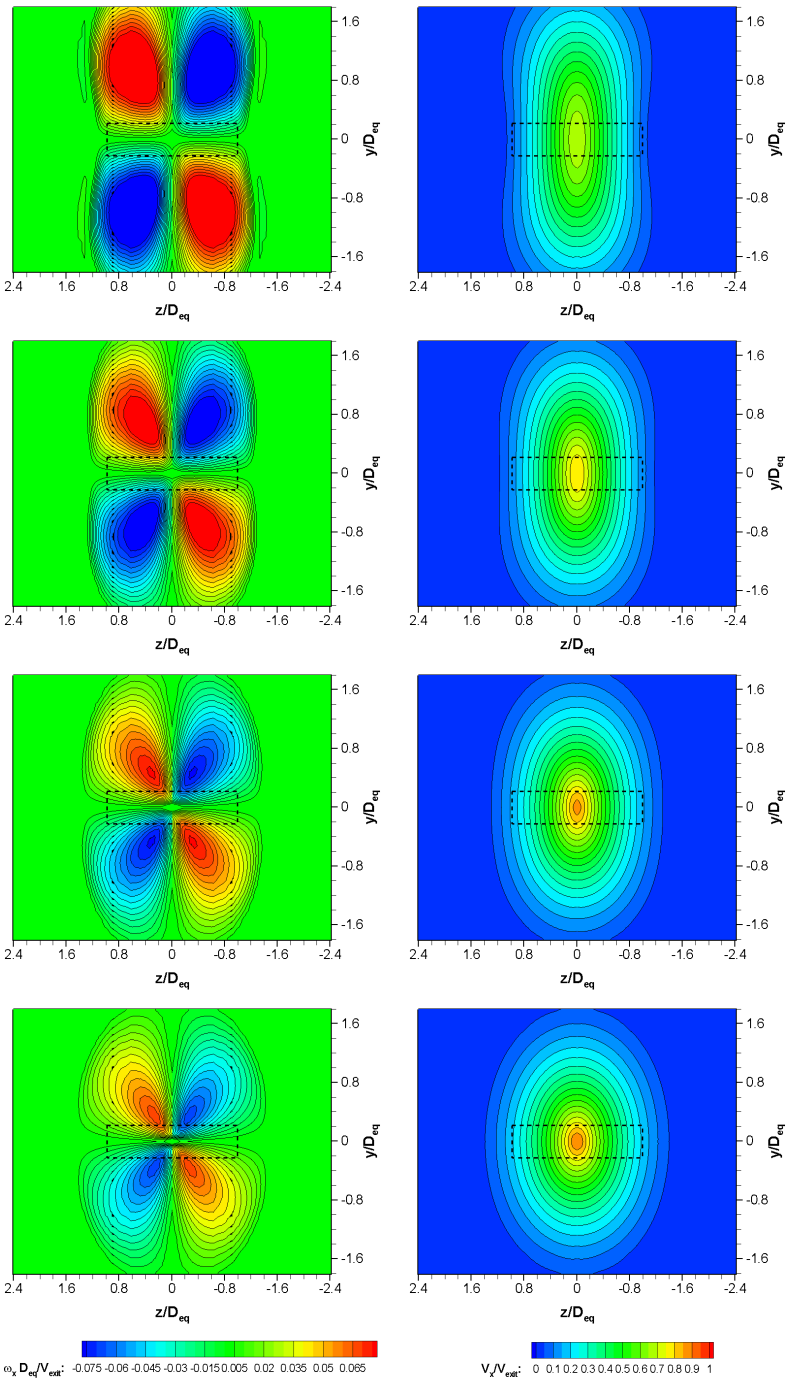

(d) *RA*4

Figure D.11: Continued

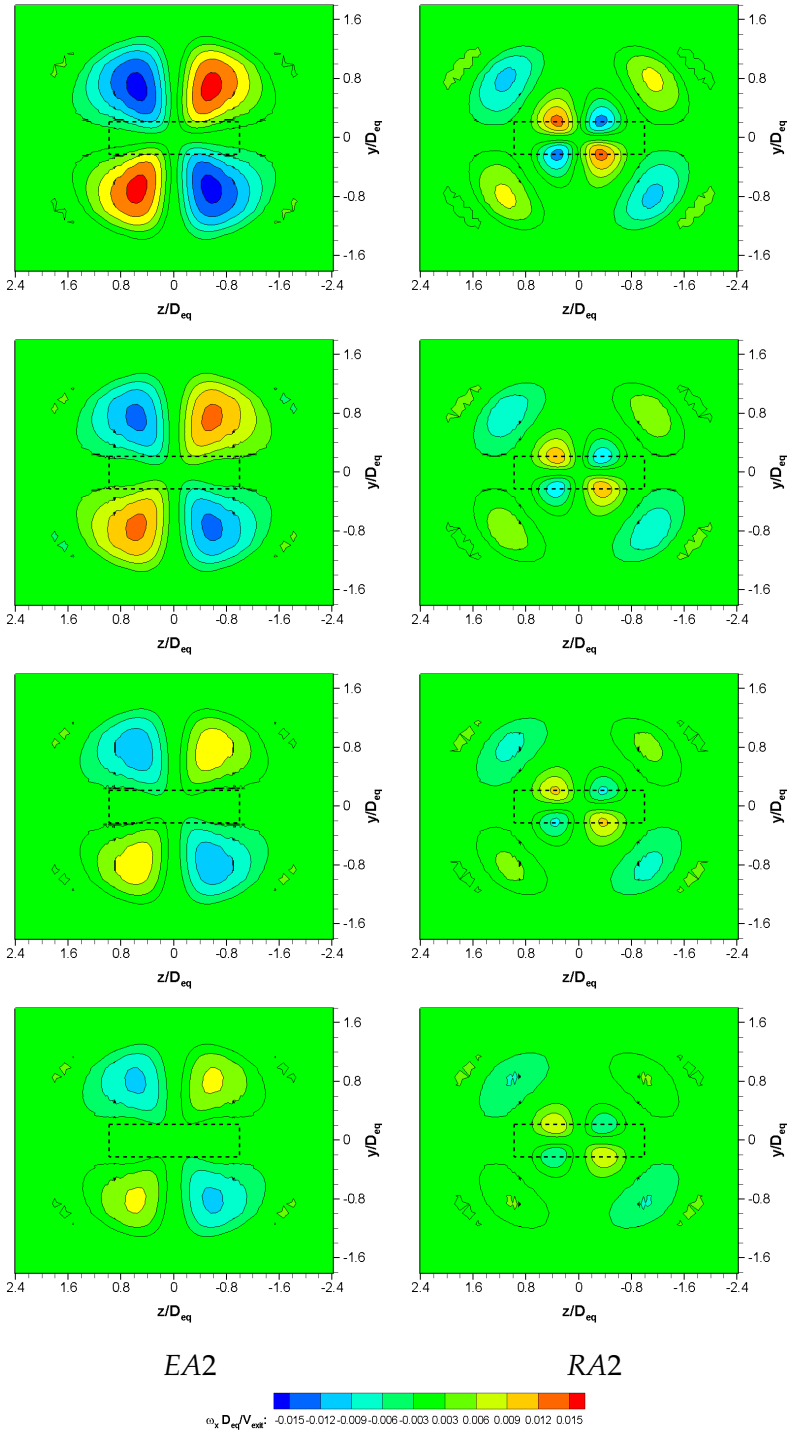

Figure D.12: Contours of normalised streamwise vorticity ($\omega_x D_{eq}/V_{exit}$) for E− and R−series configurations at a plane 8 D_{eq} downstream of the exit presented in a different scale; from top to bottom in each configuration, C1, C2, C3, C4; the dashed outline represents the nozzle exit

Appendix E

Results for $AR4$ Nozzle: Supersonic Flow

The results and analysis pertaining to the supersonic jet flow issuing from the $AR4$ nozzle at NPR = 2.50 and 3.50 are presented in this appendix. Use is made of a quantitative visualisation technique called background-oriented schlieren (*BOS*) to understand the density field of the jet at NPR = 2.50 and for comparison with the relevant *CFD* results. Qualitative data in terms of conventional schlieren images are also presented for comparison at both NPR values.

E.1 Validation of BOS

The background-oriented schlieren method is validated for its application for the current supersonic study of rectangular jets. The FORTRAN code developed by Dr. Mark Finnis (Cranfield University) and the image-processing code written in Matlab had to be tested before accepting the results from the *BOS* setup. A pre-validated *CFD* simulation based on a circular Stratford nozzle running at NPR = 2.50 was used for this purpose. A brief description about the experimental setup and image capture has been provided in Section 4.2.2.3 earlier. The process of acquiring *BOS* data is explained in more details here.

With the setup in place, an image was captured without flow through the nozzle (Figure E.1(a)). This aimed to serve as a base image for cross-correlation with the first image captured for the nozzle running at NPR = 2.50 (Figure E.1(b)). The process was repeated over to get a total of 8 image pairs. These image pairs were then analysed with the FORTRAN code. The FORTRAN code incorporates a cross-correlation algorithm which produces a vector field of the density gradients obtained from each image pair. It then averages the data from these eight pairs and outputs a single text file in ASCII format with the values of the density gradients along the two axes at each point in the grid. Internally, the code then uses the data from the ASCII file to generate a projected density image by solving

the Poisson equation. The values of the integral at the boundary are provided through the code and utilised by the solver to return a grayscale value for each pixel of the image file generated. A typical projected density image generated by this code is shown in Figure E.2.

The next step was to collect all the necessary projections (as image pairs), average them and create a projected density image field for each. This is a basic requirement for tomographic reconstruction. Each projection contains information about the whole field compressed in a single plane as viewed from a particular direction or orientation. Now consider a number of projections of this field such that each is looking at the centre of the field from a different orientation. If this information is projected back from the different projections into an empty field, the distinctive features of the original field should be visible. Clearly, the more the number of projections, the better is the quality of the reconstructed field and the higher are the details of the distinctive features. For this study, a small code was written in Matlab making use of the 'Inverse Radon Transform' function that is available in its image processing toolbox. The inverse radon transform function retrieves information from the projections and constructs the features of the field as viewed from that direction. This process is repeated for all the available projections. The subsequent three-dimensional field can then be sliced along any direction, as required, to see the actual details for the given plane. In the case of the density field under consideration, the projected density images are analysed and then stored in a 3-D matrix with the grayscale pixel values now representing a density value in the 3-D flow field. Each grayscale value can then be subsequently normalised using a known density value (e.g. centreline density at the nozzle exit, ρ_c) to get a quantitative density field.

The circular Stratford nozzle used for validation of the background-oriented schlieren was sufficient to test all the necessary features of both codes. Since it was an axial flow-field, projections along a single direction were sufficient for reconstruction of the actual density field; the same image could be used as many number of times as required to create the density field. In this particular case, the same projected density field image was used 180 times, for projection angles in steps of 1° from 0°–179°.

The normalised density contours obtained from the simulation were compared to the results from the *BOS* analysis (Figure E.3). The two images in Figure

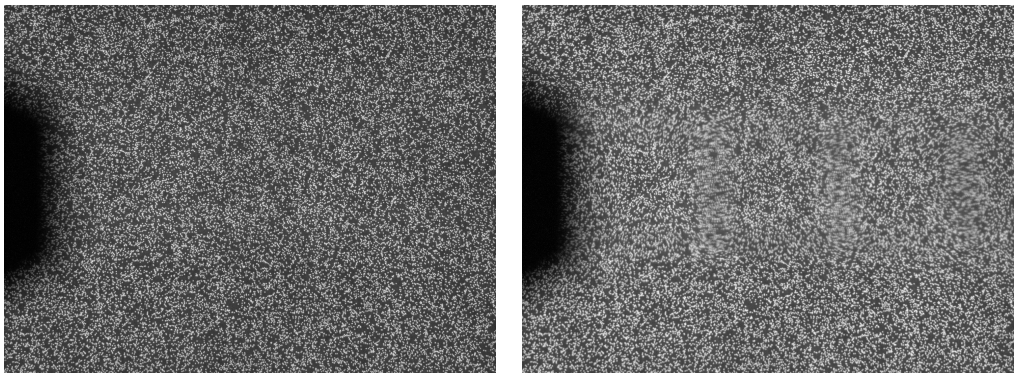

(a) Without flow (b) With flow

Figure E.1: The background dot pattern image pair used for creating the vector field

E.3 show a very favourable agreement. The overall shock-structure and the corresponding density variation is effectively captured by the *BOS* analysis. There is, however, the presence of slightly distorted values, possibly due to noise while performing the image reconstruction using the filtered backprojection technique. It can also be seen that the shock-cell spacing is different for the *CFD* compared to the *BOS* results; the shock-cells corresponding to the *CFD* simulation are about 1 diameter long, whilst those for the case of the *BOS* are ≈1.17 diameters long. These minor differences are, however, deemed to be acceptable and do not exhibit a departure from the similar behaviour that can be seen from the *CFD* and *BOS* data. This suggests that the *BOS* analysis that has been done for the circular Stratford nozzle can now be confidently extended for use with the rectangular *AR*4 nozzle.

E.2 *AR*4 Nozzle: *BOS* Technique

Following the acceptance of the background-oriented schlieren technique for assessing the density field quantitatively, using the available codes, it was employed for the rectangular nozzle running at $NPR = 2.50$. Since the flow-field was no longer axisymmetric, a number of different projections had to be taken along different angular orientations with respect to the nozzle. Since the complete *BOS* setup could not be rotated around a fixed nozzle, the dual-flange arrangement was used to rotate the *AR*4 nozzle in specific steps, keeping the *BOS* setup fixed.

Figure E.2: The projected density field, as computed from the Poisson equation using the in-house FORTRAN code

This ensured that all the necessary projections could be obtained with ease and with minimum change necessary to the experimental setup. Also, since the flow straighteners inside the settling chamber worked more efficiently at supersonic *NPR*, it was expected that the flow deviation encountered for low *NPR* flows would be absent for choked flow conditions. This meant that, taking advantage of the symmetry of the nozzle about major and minor axes, image data for $0^\circ - 90^\circ$ could be captured and duplicated to that for $90^\circ - 180^\circ$. The number of projections was set at 24 for this particular case, resulting in rotation of the nozzle in steps of 7.5° for each projection. The process of obtaining the projected density field using

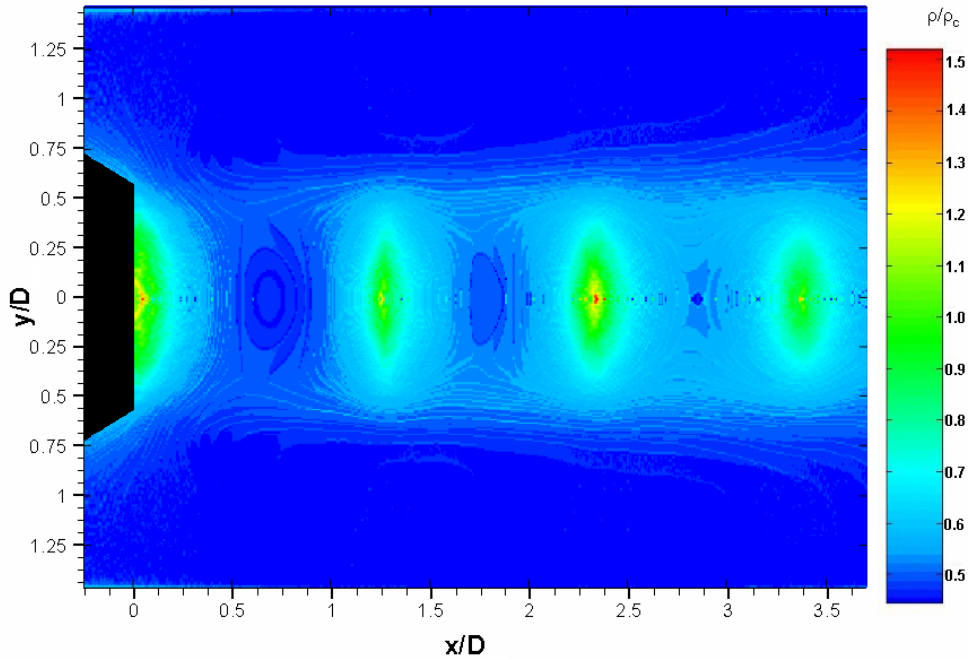

(a) Background Oriented Schlieren

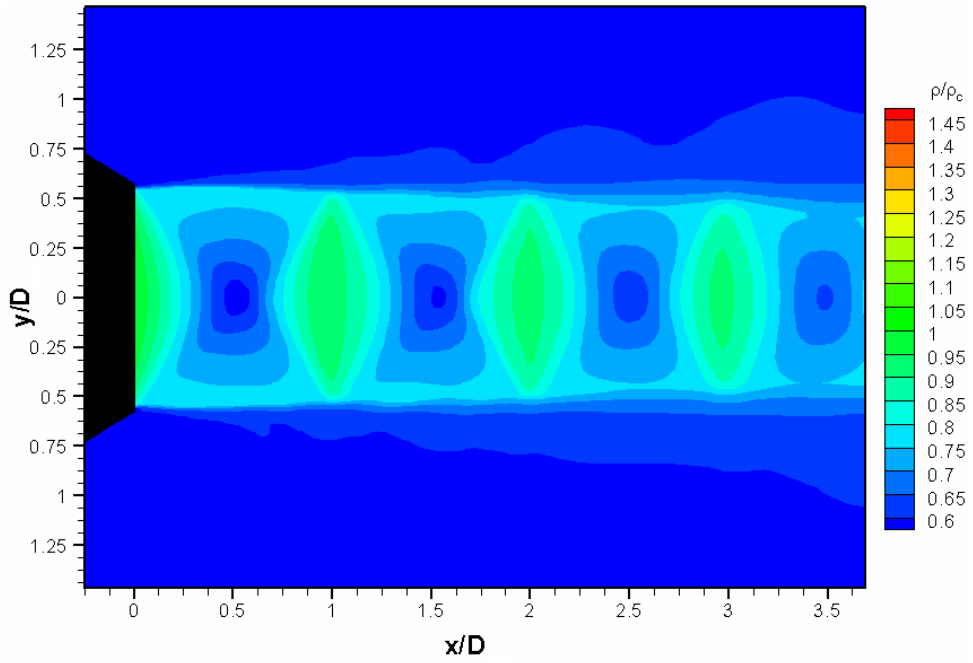

(b) *CFD* results from Fluent™

Figure E.3: Comparison of normalised density contours for circular Stratford nozzle running at NPR = 2.50; ρ_c is the exit centreline density

the FORTRAN code remained similar to the axisymmetric nozzle case. The projected density images, thus obtained, were then further analysed with the Matlab code after a few modifications to the code used for the Stratford nozzle. All the images were individually read into the code and assigned to the projection angles for which they were created. The image reconstruction process was similar to that explained earlier for the Stratford nozzle. The normalised density contours at the major and minor axis planes are compared with the simulation results in Figure E.4.

The shock-cell structure and density variation shows a very good agreement for the rectangular nozzle flow as well. The actual values of the density contours are slightly higher for the *BOS*; the existence of the very high density regions is more likely to be due to the presence of noise which distorts the actual values. The actual shock-cell spacing is greater in the case of experiments compared to *CFD*, again mirroring the results seen for the axisymmetric case; both show that it is ≈10% more for experiments with respect to *CFD*.

E.3 Conclusions of the *BOS* study

The background-oriented schlieren method is easy to set up compared to many other quantitative measurement techniques. It is a completely non-intrusive method of measuring a flow-field property, and with proper calibration, ideal for measurement of axisymmetric flow experiments. It is, however, limited in its application. For measurement of non-axisymmetric flow, there has to be an appropriate arrangement to move the background and the camera set-up without disturbing their positions with respect to each other. Alternatively, the same result might be achieved if the flow-field to be measured can be rotated about a fixed axis without affecting the flow structures developing, as was done for the current experiment. It also requires a sufficiently large space unobstructed by any other equipment so that the images captured exhibit only the flow and its development.

In spite of these inherent drawbacks, it still shows a big promise for non-intrusive measurement. The current FORTRAN code is being further developed to incorporate the image processing. This is aimed at improving the overall results and providing them in a single stage of analysis.

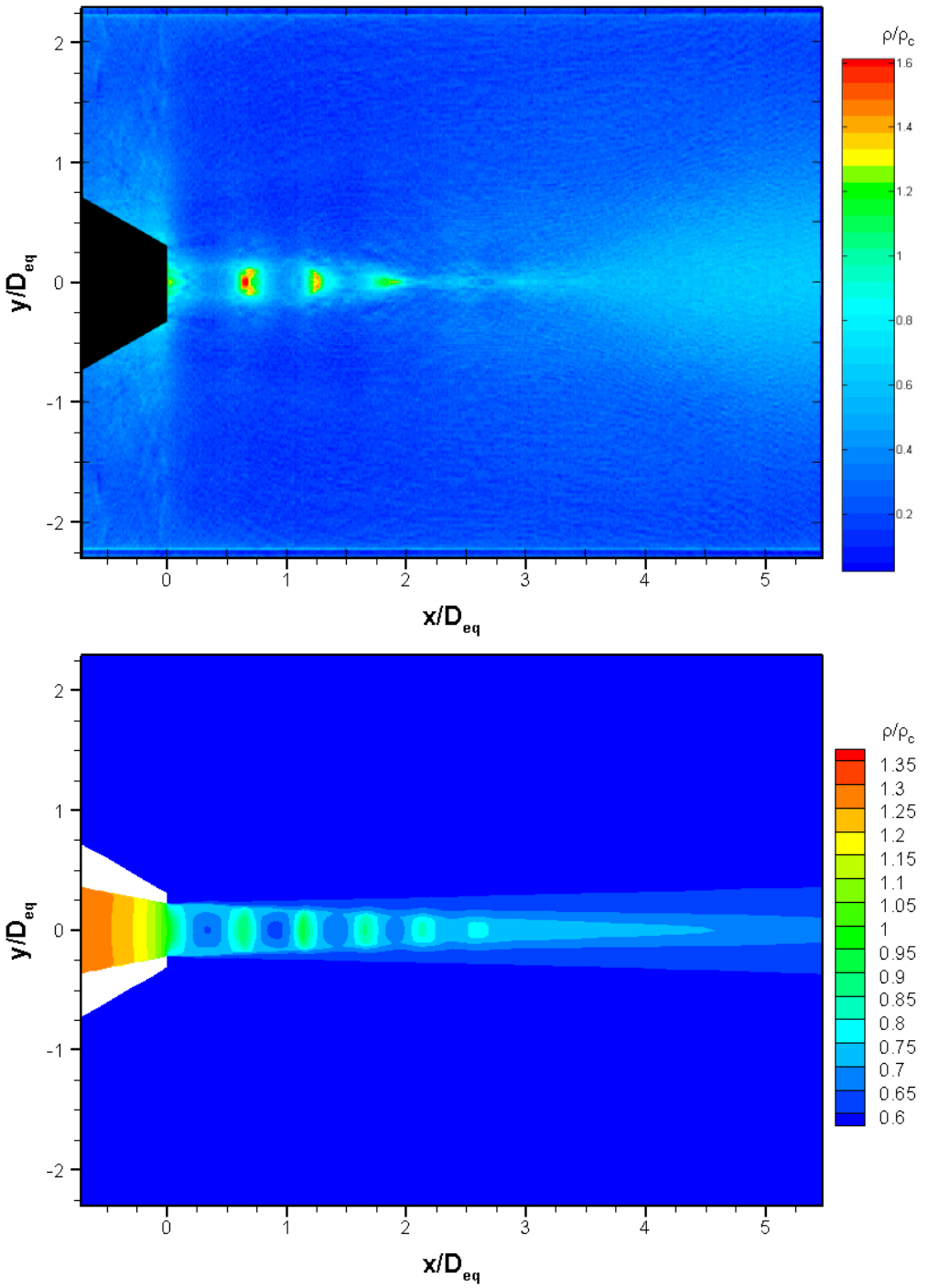

(a) Minor axis plane; background-oriented schlieren (top), *CFD* simulation (bottom)

*Figure E.4: Comparison of normalised density contours for AR*4 *nozzle running at NPR* = 2.50*;* ρ_c *is the exit centreline density*

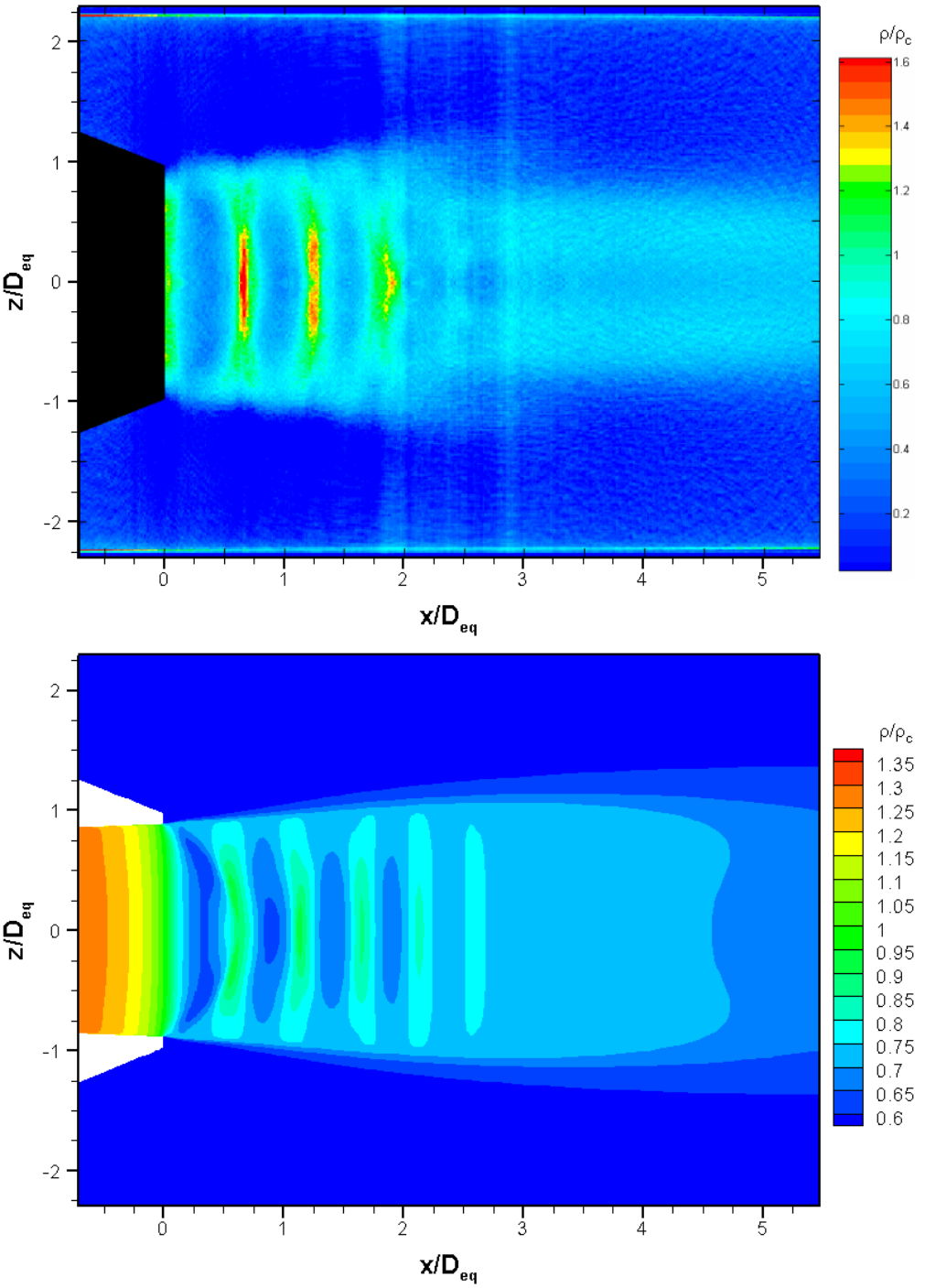

(b) Major axis plane; background-oriented schlieren (top), *CFD* simulation (bottom)

Figure E.4: Continued

E.4 $AR4$ Nozzle: Other results

Further to the NPR = 2.50 simulations, data were also collected for NPR = 3.50 simulations. These were compared with conventional schlieren images for qualitative analysis, as shown in Figure E.5. These show a similar trend with the experimental (schlieren) results, indicating a shock-cell spacing 10% greater than the *CFD* results. The half-velocity-widths for the two NPR values, as calculated from *CFD*, are given in Figure E.6. Since these simulations have been run for a steady-state solution, the effect of screech on the flow development cannot be seen. The two half-velocity-width plots, however, clearly show a distinct difference. While the spread along the major axis is greater, at the same time, the spread along the minor axis is lesser, for NPR = 2.50 compared to NPR = 3.50. This reflects the observations of Papamoschou & Roshko (1988); higher NPR results in lower spreading rates due to compressibility effects. The spreading rates along the major and minor axes for NPR = 2.50 are almost uniform from ≈4.5 D_{eq} to 16 D_{eq}; the spreading rate is slightly higher along the minor axis. After ≈16 D_{eq}, the spreading rates decrease along both the axes as the jet moves towards self-similarity. However, it now seems to spread faster along the major axis. The NPR = 3.50 case, on the other hand, shows a different behaviour compared to this. The spreading rate along the major axis is very low from ≈3 D_{eq} to 8 D_{eq}; it then rises steadily upto ≈20 D_{eq} after which it reduces slowly. Along the minor axes, for similar locations as for the major axis, the spreading rate rises rapidly and continues to do so until ≈20 D_{eq}, by which time, it is almost equal to the spreading rate along the major axis. This indicates that the jet has possibly achieved self-similarity.

This difference in the spreading rates might be explained by looking at the streamwise vorticity distribution (Figure E.7). The dominance of the 'out-flow' pairs resisting axis-switching can be clearly seen for both the NPR cases at 2 and 8 D_{eq} planes. There is, however, the presence of a weaker 'in-flow' pairs that exist for the NPR = 3.50 case (Figure E.7 (a), bottom). This might be responsible for the lower jet spread along the major axis and simultaneous increase in the spreading along the minor axis. By 8 D_{eq} downstream, the 'in-flow' pair is very weak and, thus, cannot influence the jet spread as much; the spreading rate starts rising along the major axis since stronger 'out-flow' pairs still exist, although their effect

along the minor axis is not clearly visible. Around 16 to 20 D_{eq} downstream, the jet spreads for both the *NPR* cases tend towards self-similarity. The corresponding normalised velocity contours are shown in Figure E.8. The velocity magnitudes are clearly higher in the case of $NPR = 3.50$, which is expected; the velocity contours show that the jet spread is greater along the minor axis for $NPR = 3.50$.

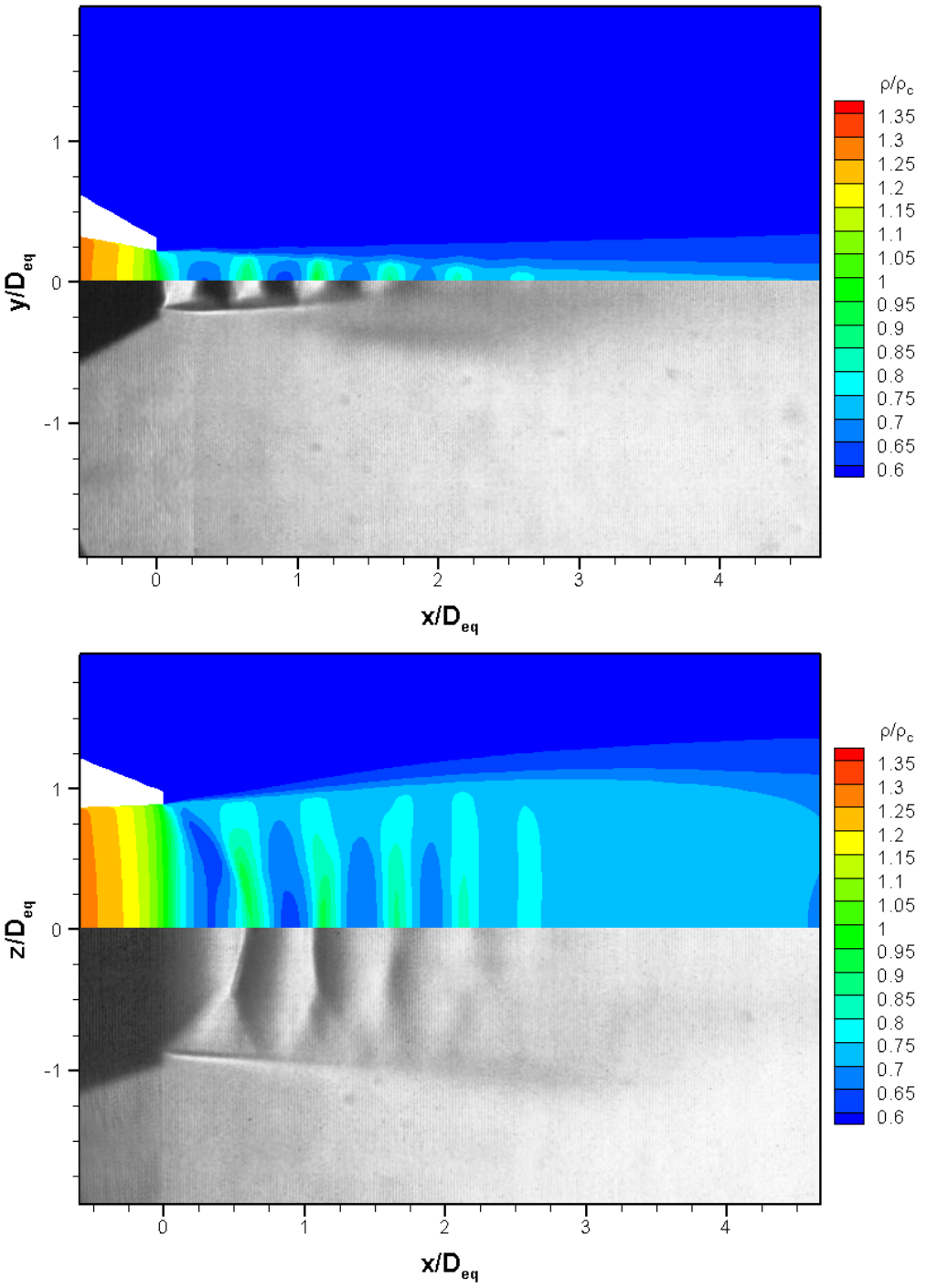

(a) *NPR* = 2.50; Minor axis plane (top), Major axis plane (bottom)

Figure E.5: Qualitative comparison of normalised density contours for AR4 nozzle with conventional schlieren; ρ_c is the exit centreline density

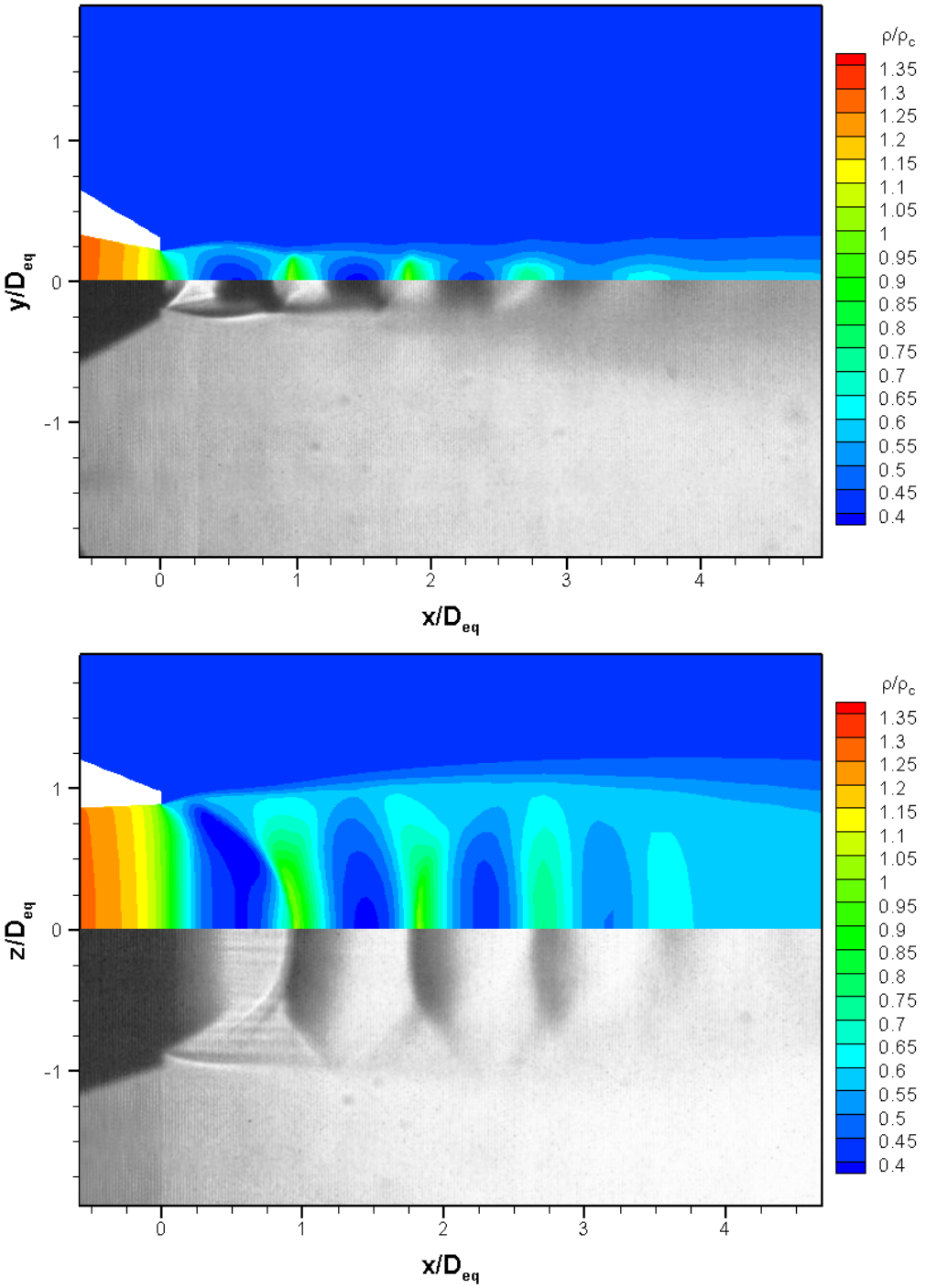

(b) *NPR* = 3.50; Minor axis plane (top), Major axis plane (bottom)

Figure E.5: Continued

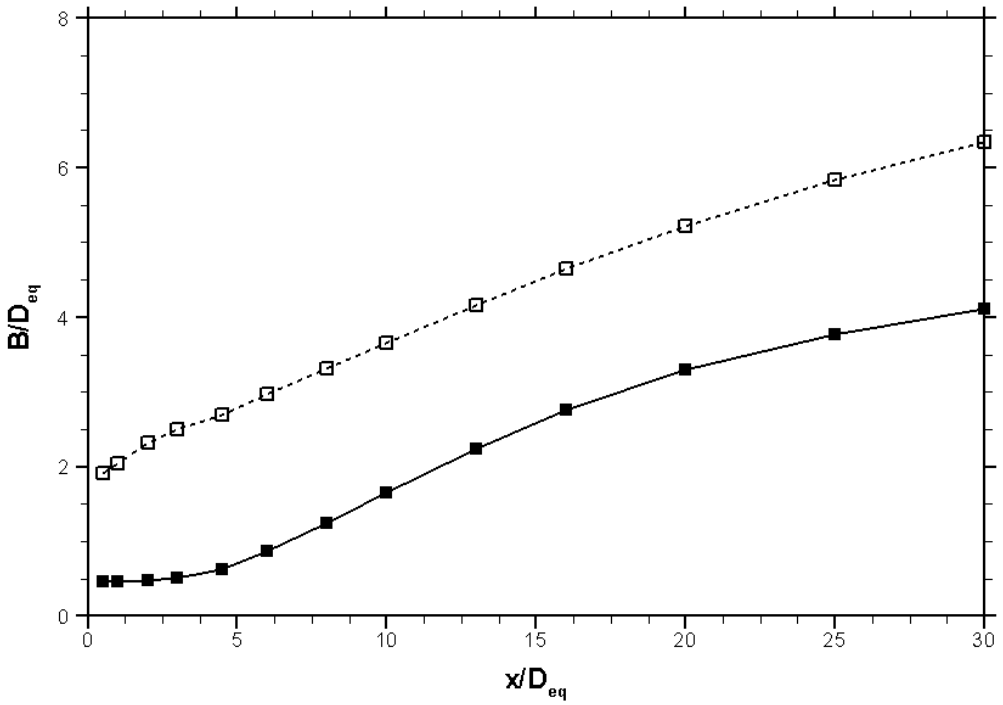

(a) $NPR = 2.50$

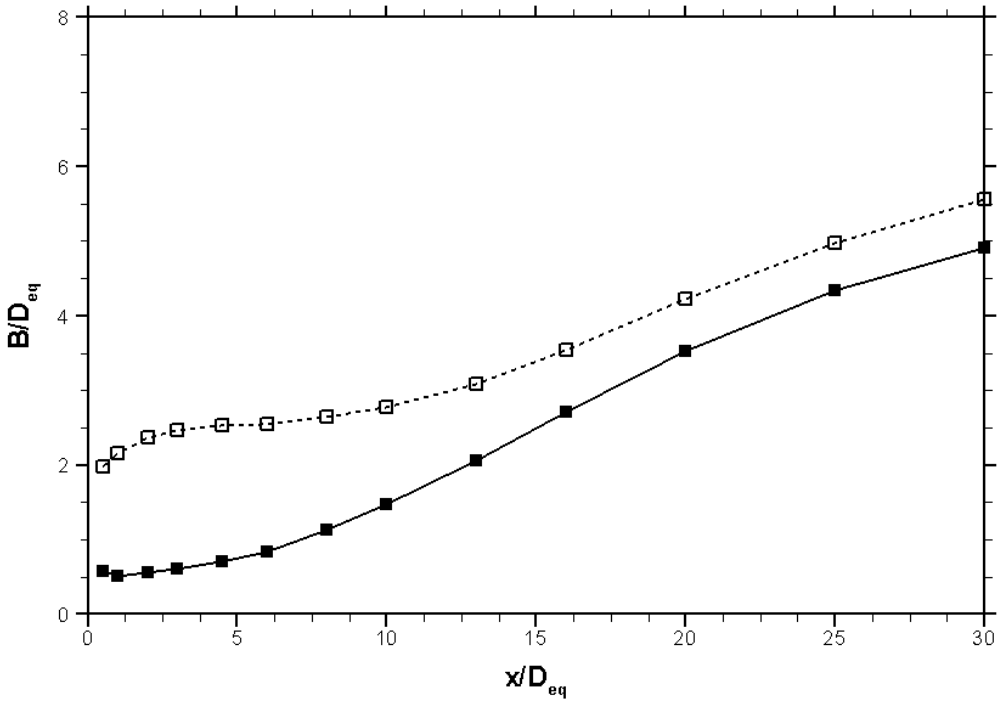

(b) $NPR = 3.50$

Figure E.6: Streamwise variation of jet half-velocity-width for computed supersonic cases: —■—, B_y/D_{eq}; – – □ – –, B_z/D_{eq}

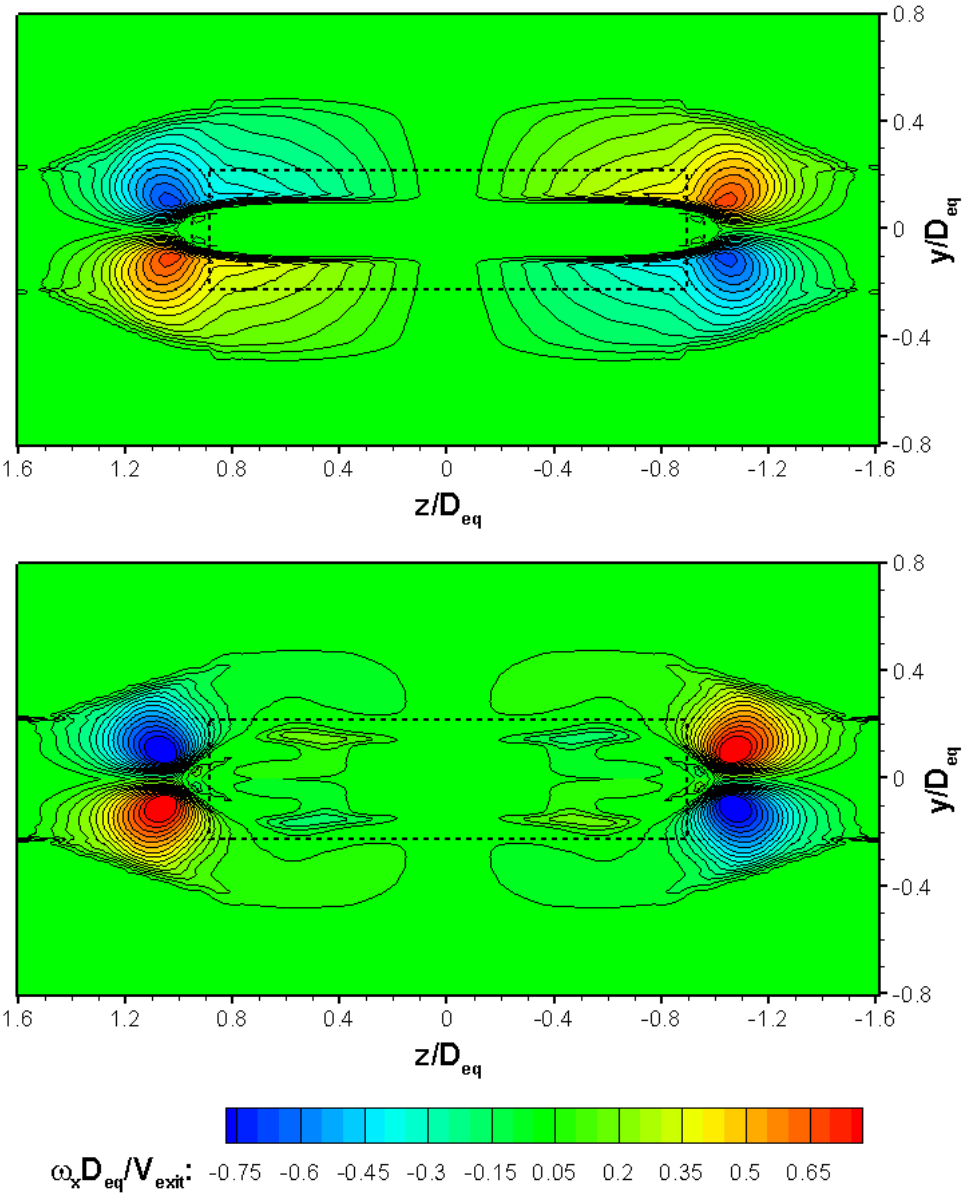

(a) Normalised streamwise vorticity at 2 D_{eq}

Figure E.7: Contours of normalised streamwise vorticity ($\omega_x D_{eq}/V_{exit}$) at planes 2 and 8 D_{eq} downstream of the exit; NPR = 2.50 (top), and NPR = 3.50 (bottom)

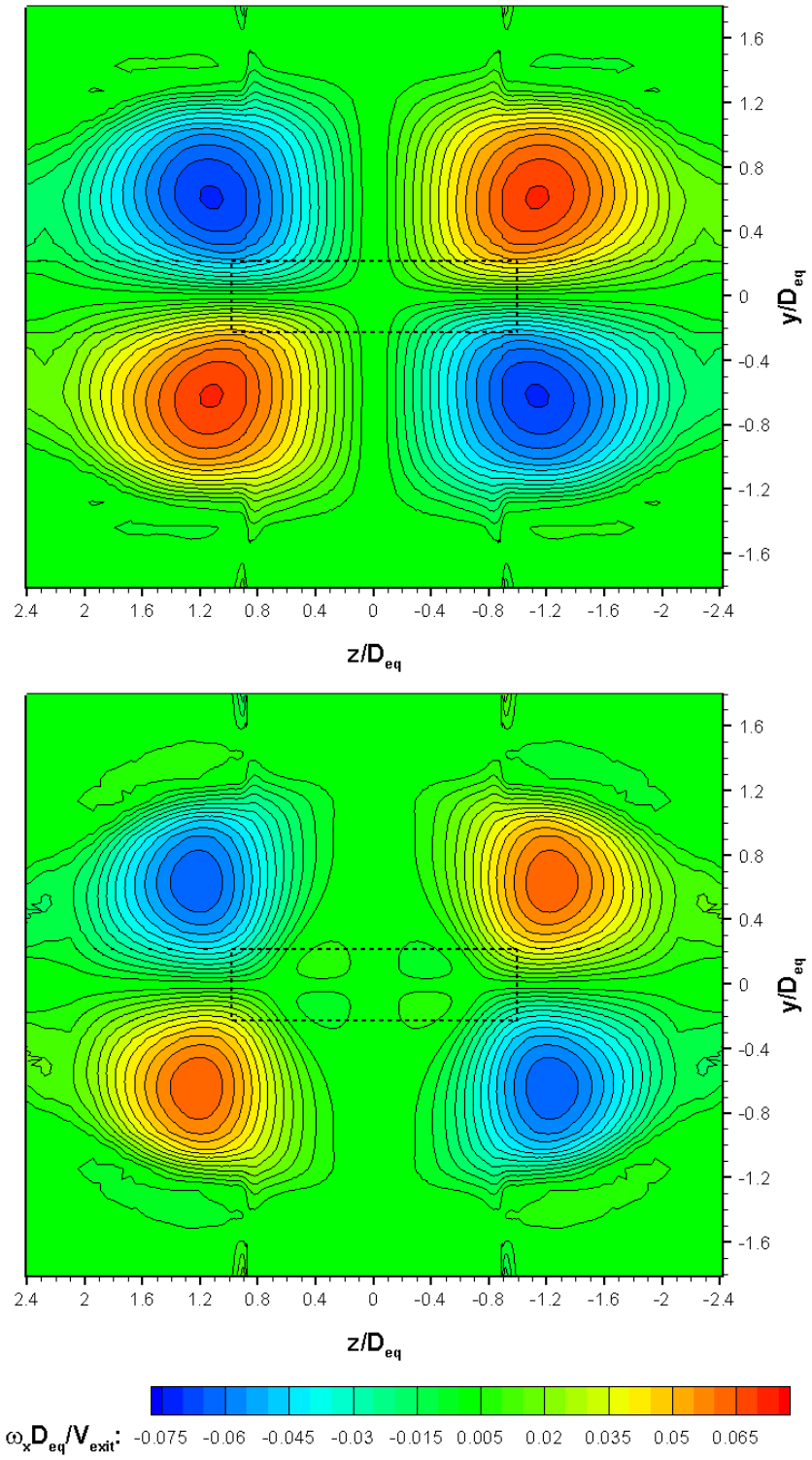

(b) Normalised streamwise vorticity at 8 D_{eq}

Figure E.7: Continued

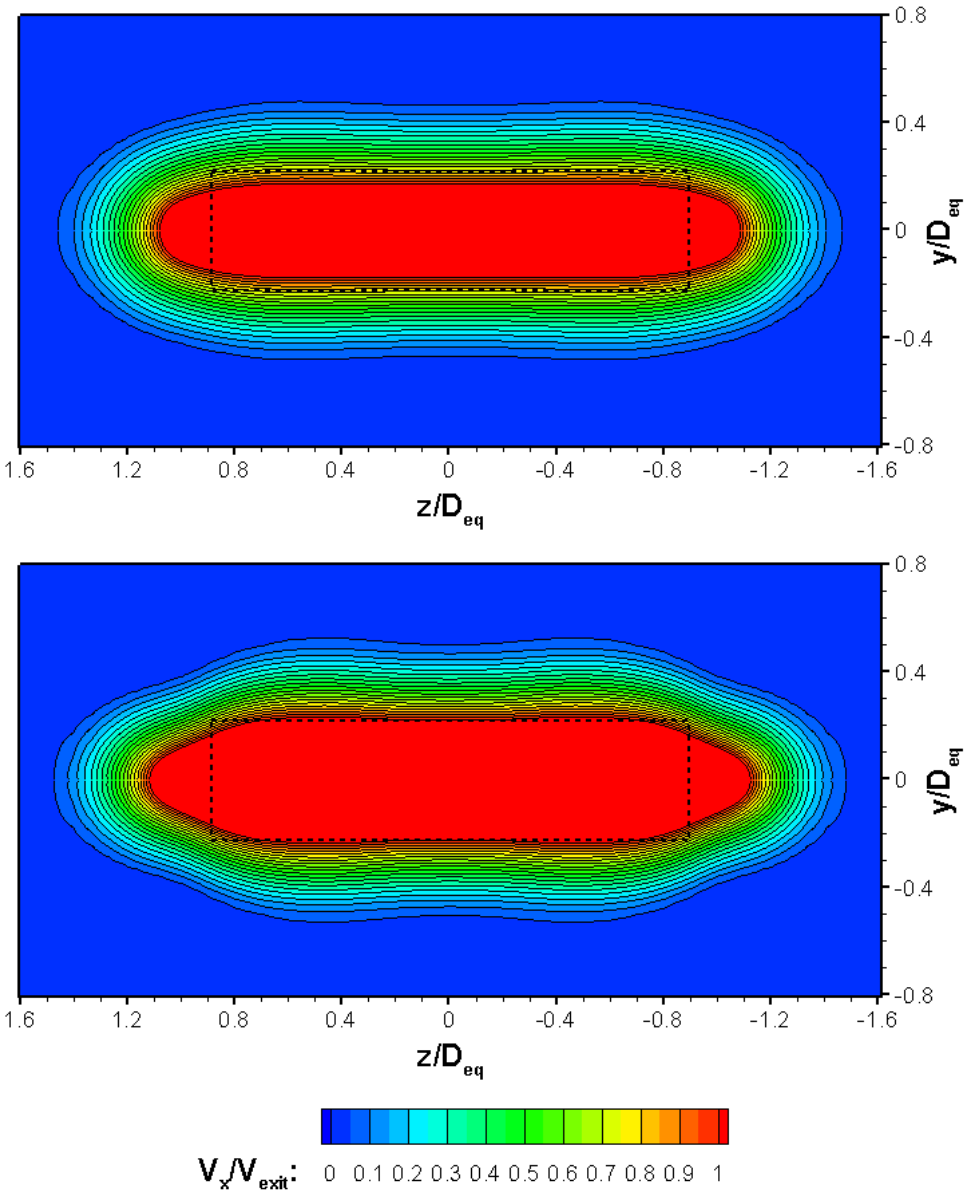

(a) Normalised streamwise velocity at 2 D_{eq}

Figure E.8: Contours of normalised streamwise velocity (V_x/V_{exit}) at planes 2 and 8 D_{eq} downstream of the exit; NPR = 2.50 (top), and NPR = 3.50 (bottom)

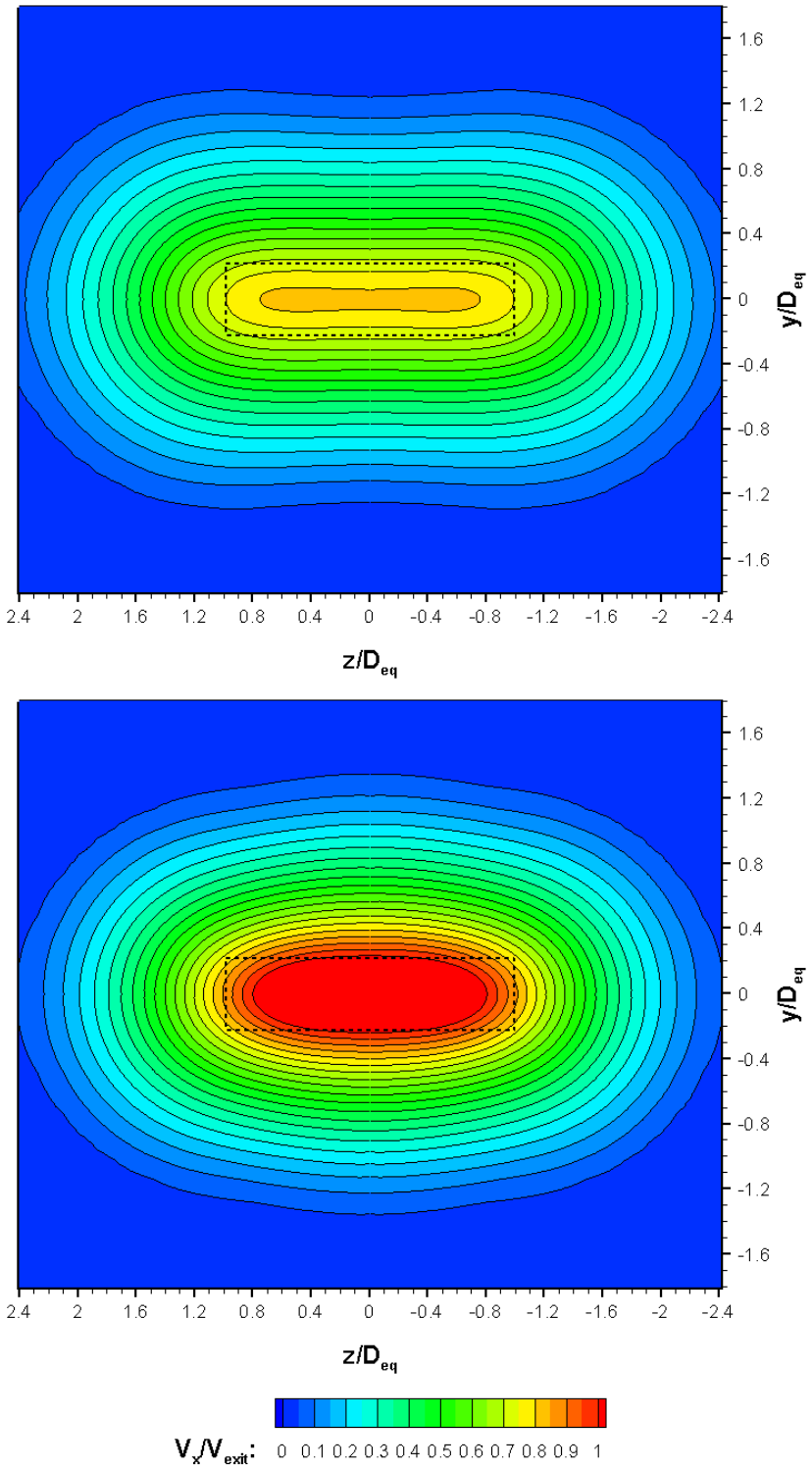

(b) Normalised streamwise velocity at 8 D_{eq}

Figure E.8: Continued